Design, modelling, and experiments of mid-infrared supercontinuum generation in soft-glass photonic crystal fibers

Amar Nath Ghosh

▶ **To cite this version:**

Amar Nath Ghosh. Design, modelling, and experiments of mid-infrared supercontinuum generation in soft-glass photonic crystal fibers. Optics / Photonic. Université Bourgogne Franche-Comté, 2020. English. NNT : 2020UBFCD035 . tel-03141438

HAL Id: tel-03141438

https://theses.hal.science/tel-03141438

Submitted on 15 Feb 2021

HAL is a multi-disciplinary open access archive for the deposit and dissemination of scientific research documents, whether they are published or not. The documents may come from teaching and research institutions in France or abroad, or from public or private research centers.

L'archive ouverte pluridisciplinaire **HAL**, est destinée au dépôt et à la diffusion de documents scientifiques de niveau recherche, publiés ou non, émanant des établissements d'enseignement et de recherche français ou étrangers, des laboratoires publics ou privés.

UBFC
UNIVERSITÉ
BOURGOGNE FRANCHE-COMTÉ

UNIVERSITÉ DE FRANCHE-COMTÉ

THÈSE DE DOCTORAT DE L'ÉTABLISSEMENT UNIVERSITÉ BOURGOGNE FRANCHE-COMTE

PRÉPARÉE À L'UNIVERSITÉ DE FRANCHE-COMTE

École doctorale n°37

Sciences Pour l'Ingénieur et Microtechniques

Doctorat d'Optique et Photonique

par

AMAR NATH GHOSH

Design, modelling, and experiments of mid-infrared supercontinuum generation in soft-glass photonic crystal fibers

Désign, simulations et expériences de générations de supercontinuum dans l'infrarouge moyen dans des fibres à cristaux photoniques en verre souple

Thèse présentée et soutenue à Besançon, le 5 Octobre 2020
Composition du Jury :

JACQUOT MAXIME	Professeur, Université de Franche-Comté, Besançon	President
HANNA MARC	Chargé de recherche, CNRS, Laboratoire Charles Fabry, Institut d'optique, Paris	Rapporteur
BRÈS CAMILLE-SOPHIE	Associate Professeur, EPFL, Lausanne	Rapporteur
BUCZYNSKI RYSZARD	Professeur, Université de Varsovie, Pologne	Examinateur
TROLES JOHANN	Professeur, Université des Rennes 1, Institut des Sciences chimiques de Rennes, Rennes	Examinateur
SYLVESTRE THIBAUT	Directeur de recherche, CNRS, Institut FEMTO-ST, Besançon	Directeur de thèse
DUDLEY JOHN	Professeur, Université de Franche-Comté, Institut FEMTO-ST, Besançon	Co-directeur de thèse

Title: Design, modelling, and experiments of mid-infrared supercontinuum generation in soft-glass photonic crystal fibers

Keywords: Supercontinuum generation, photonic crystal fibers, mid-infrared, heavy metal-oxide glass, chalcogenide glasses, polarization-maintaining.

Abstract:

This doctoral thesis, funded within the framework of a European Marie-Curie H2020 SUPUVIR project, focuses on the design and fabrication of new photonic crystal fibers from infrared soft glasses making it possible to produce a wide emission spectrum in the mid-infrared (IR) wavelength region through generation of supercontinuum (SC). Applications of mid-IR SC sources cover infrared spectroscopy, optical detection of chemical and molecular species, materials processing, and biomedical imaging. An alternative to conventional thermal light sources, mid-IR SC sources have broad spectral bandwidth like a lamp or Globar and high brightness, which is more than 20 times of the sun focussed in a small spot similar to a laser. Several optical fibers with different photonic structures and different soft glasses have been produced and studied. In collaboration with the Institute of Electronic Materials Technology in Warsaw, heavy metal-oxide glass (PBG81) microstructured fibers were first developed and with these fibers we demonstrated the efficient generation of SC from 0.89 to 2.5 µm, limited by the absorption of the glass. Then, in partnership with the University of Rennes and the Technical University of Denmark, we fabricated microstructured fibers based on chalcogenide glasses ($As_{38}Se_{62}$) with polarization-maintaining property. These fibers have made it possible to generate a linearly polarized 3.1 to 6 µm supercontinuum. SC bandwidth was further extended between 1 µm and 7.4 µm in taper fibers produced from $Ge_{10}As_{22}Se_{68}$ glass. The laser power handling capacities of these chalcogenide fibers were also analyzed. Finally, we have developed a compact mid-IR SC system using a fiber cascade comprising of silica, fluoride, and chalcogenide fiber, pumped by a fiber laser at 1.55 µm, and making it possible to extend the emission range from 2 to 10 µm. This research work thus constitutes an important step towards the development of stable and compact fiber SC sources for various applications in the mid-infrared.

Titre : Design, modelling, and experiments of mid-infrared supercontinuum generation in soft-glass photonic crystal fibers

Mots-clés : Génération de supercontinuum, fibres microstructurées, verre d'oxyde de métal, verres chalcogénures, maintien de la polarisation

Résumé :

Cette thèse de doctorat, financée dans le cadre d'un projet Européen Marie-Curie H2020 SUPUVIR, porte sur la conception et la fabrication de nouvelles fibres optiques de verres infrarouges permettant de produire un large spectre d'émission dans l'infrarouge moyen par génération de supercontinuum. Les applications couvrent la spectroscopie, la détection optique d'espèces chimiques et moléculaires, le traitement des matériaux et l'imagerie biomédicale. Plusieurs fibres optiques avec différents structures photoniques et différent matériaux infrarouges ont été réalisées et étudiées. En collaboration avec l'Institut de technologie des matériaux électroniques à Varsovie, nous avons dans un premier temps développé des fibres microstructurées en verre d'oxyde de métal (PBG81) et nous avons démontré avec ces fibres la génération efficace de supercontinuum de 0.89 µm à 2.5 µm, limité par l'absorption du verre. Ensuite, nous avons conçu en partenariat avec l'Université de Rennes et l'Université Technique du Danemark des fibres microstructurées à base de verres chalcogénures ($As_{38}Se_{62}$) avec un maintien de la polarisation. Ces fibres ont permis de générer un supercontinuum de 3.1 à 6 µm linéairement polarisé. Les capacités de tenue à la puissance laser de ces fibres chalcogénures ont été également analysées. Afin d'étendre cette bande d'émission, des fibres étirées en verre $Ge_{10}As_{22}Se_{68}$ à très petit cœur ont été ensuite réalisées. Enfin, nous avons développé un système compact comprenant une série de fibres de silice, de verre fluoré, et de verre chalcogénure, pompé par un laser à fibre à 1.55 µm, et permettant d'étendre la gamme d'émission de 2 à 10 µm. Ces travaux de recherche constituent ainsi une étape importante vers le développement de sources fibrées, stables et compactes pour diverses applications dans l'infrarouge moyen.

UBFC UNIVERSITÉ BOURGOGNE FRANCHE-COMTÉ

Université Bourgogne Franche-Comté
32, avenue de l'Observatoire
25000 Besançon, France

ACKNOWLEDGEMENTS

FIRST of all I wish to express my gratitude to my supervisors at the FEMTO-ST Institute, Dr. Thibaut Sylvestre and Prof. John Dudley for their thorough guidance and instructions during the years of research and giving me the opportunity to conduct such an exciting research activity for my thesis. Besides the invaluable theoretical and experimental aid, both of them also provided me the encouraging support and motivation to complete this thesis. I thank the reviewers Dr. Marc Hanna and Prof. Camille-Sophie Brès for their insightful comments and suggestions in a very quick time. I am grateful to Prof. Ryszard Buczynski, Prof. Johann Troles, and Prof. Maxime Jacquot for accepting to be my examiners.

I thank my co-authors Dr. Mariusz Klimczak, Prof. Ryszard Buczynski, Dr. Marcello Meneghetti, and Sébastien Venck for their contribution and sharing their valuable practical knowledge while performing experiments together. I would like to express my gratitude to Dr. Laurent Brilland from the SelenOptics company, Prof. Johann Troles from the university of Rennes, Dr. Christian R. Petersen and Prof. Ole Bang from the Technical University of Denmark for organizing several secondments about chalcogenide fiber fabrication and characterization for me in their respective institutions and also for providing me the guidance during those internships. I would like to thank Prof. Gil Fanjoux for sharing his valuable knowledge with me about COMSOL simulation which was very helpful in this work. I wish to thank the members of nonlinear optics group of the FEMTO-ST Institute, Alex, Jean-Charles, Kien, and Vincent for providing me several technical supports in the laboratory. I would like to thank CNRS and European Union's Horizon 2020 Research and Innovation Programme under grant agreement n°722380 project SUPUVIR for providing me the funding for this work. I also thank Aline, Sarah, and Valérie for taking care of all the work related travel and reimbursements during my PhD thesis.

I wish to thank my fellow group members from SUPUVIR consortium, Abba, Chetan, Etienne, Fathima, Gaoyuan, Ivan, Kyei, Manoj, Marcello, Shreesha, Tanvi, Xavier, Zahra for their professional support during the workshops and training events as well as the social fun we had together. I would like to specially thank my colleague Solveig for providing me the support with French language, administrative work and mental courage throughout my PhD years. I would further like to thank my coworkers from the FEMTO-ST Institute, Antonio, Benoit, Clement, Riccardo, Thomas and Vincent and all others for the good time we have had in or outside the laboratory.

Last, but certainly not the least, my deepest gratitude goes to my parents, elder sisters, and sister-in-laws for their love and constant support they have provided in every sphere of my life. I convey my heartiest love to my nephew Sovon and niece Rohini.

Besançon, August 03, 2020 Amar Nath Ghosh

CONTENTS

LIST OF SYMBOLS AND ACRONYMS

LIST OF SYMBOLS

Symbol	Unit	Description
a	[µm]	Core radius of a fiber
a_1		Sellmeier coefficient
a_2		Sellmeier coefficient
A_0		Sellmeier coefficient
A_1		Sellmeier coefficient
A_2		Sellmeier coefficient
A_{eff}	[µm^2]	Effective mode area
A_i	[V m^{-1}]	Electric field amplitude of idler wave
A_j		Sellmeier coefficient
A_p	[V m^{-1}]	Electric field amplitude of pump wave
A_s	[V m^{-1}]	Electric field amplitude of signal wave
b	[µm]	Cladding radius of an optical fiber
B	[T]	Magnetic flux density
B_{group}		Group birefringence
B_1		Sellmeier coefficient
B_2		Sellmeier coefficient
B_3		Sellmeier coefficient
B_j	[µm^2]	Sellmeier coefficient
B_{phase}		Phase birefringence
$C_{\%}$		Percentage coupling efficiency
C_1	[µm^2]	Sellmeier coefficient
C_2	[µm^2]	Sellmeier coefficient
C_3	[µm^2]	Sellmeier coefficient
D	[C m^{-2}]	Electric flux density
D	[ps nm^{-1}km^{-1}]	Dispersion parameter
d	[µm]	Diameter of air-capillary of a photonic crystal fiber
E	[V m^{-1}]	Electric field
f_R		Fraction of Raman response to the total response
F	[V m^{-1}]	Transverse spatial distribution of electric field

h_R		Delayed Raman response
H	[A m^{-1}]	Magnetic field strength
J	[A m^{-2}]	Electric current density
k_0	[m^{-1}]	Wave number
k_m		Modified Bessel function of second kind
L	[m]	Length of an optical fiber
L_B	[m]	Beat length
L_D	[m]	Dispersion length
L_{eff}	[m]	Effective length
L_{fiss}	[m]	Fission length
L_{NL}	[m]	Nonlinear length
M	[A m^{-1}]	Magnetic polarization/Magnetization
n		Refractive index
n_0		Refractive index of air
n_2	[m^2 W^{-1}]	Nonlinear index coefficient
n_{clad}		Refractive index of the cladding of an optical fiber
n_{core}		Refractive index of the core of an optical fiber
n_{eff}		Effective refractive index of optical modes in an optical fiber
n_L		Linear part of refractive index
N		Soliton order
P	[C m^{-2}]	Electric polarization
$P^{(1)}$	[C m^{-2}]	First-order polarization
$P^{(2)}$	[C m^{-2}]	Second-order nonlinear polarization
$P^{(3)}$	[C m^{-2}]	Third-order nonlinear polarization
P_0	[W]	Peak power of an optical pulse
P_{c}	[W]	Coupled power in an optical fiber
P_{in}	[W]	Power at the input of an optical fiber
P_k	[W]	Relative peak power of fundamental soliton
P_L	[W]	Launched pump power in an optical fiber
P_L	[C m^{-2}]	Linear polarization
P_{NL}	[C m^{-2}]	Nonlinear polarization
P_{out}	[W]	Transmitted power at the output of an optical fiber
P_s	[W]	Peak power of a soliton
P_p	[W]	Pump power
R	[m]	Radius of inner surface of air-capillaries
R_c	[C m^{-2}]	Critical bending radius of curvature
R_{F}		Fresnel reflectance
s		Self-steepening
T_0	[s]	Half-width of an optical pulse

T_{FWHM}	[s]	Full-width at half-maximum of an optical pulse
T_k	[s]	Temporal width of fundamental soliton
v_g	[m s^{-1}]	Group velocity of an optical mode
$v_{g,s}$	[m s^{-1}]	Group velocity of a soliton
V		V number/Normalized frequency
V_c	[s^{-1}]	Cut-off frequency
V_{PCF}		V number/Normalized frequency for photonic crystal fiber
α	[dB m^{-1}]	Attenuation constant
$\alpha_{\text{confinement}}$	[dB m^{-1}]	Confinement loss in an optical fiber
β	[m^{-1}]	Propagation constant of an optical mode
β_0	[m^{-1}]	Propagation constant at centre frequency
β_1	[s m^{-1}]	Fist order dispersion
β_2	[s^{2}m^{-1}]	Group-velocity dispersion
β_3	[s^{3}m^{-1}]	Third order dispersion
β_m	[s^{m}m^{-1}]	mth order disperion
γ	[W^{-1}m^{-1}]	Nonlinear coefficient
γ	[N m^{-1}]	Surface tension
Δ		Relative refractive index difference
ΔP	[Pa]	Pressure difference across the internal and external surface of air-capillaries
Δn		Perturbation to the refractive index
ΔT	[s]	Time delay between two orthogonally polarization components of an optical pulse
ε_r		Relative permittivity of a material
θ_c	[rad]	Critical angle for total internal reflection
θ_{in}	[rad]	Angle of incidence
θ_t	[rad]	Angle of refraction
κ	[rad]	Effective phase mismatch
λ	[m]	Wavelength
λ_0	[m]	Vacuum wavelength
λ_p	[m]	Pump wavelength
Λ	[µm]	Pitch or the distance between two air holes in a photonic crystal fiber
ν_{SSFS}		Dynamics of soliton self-frequency shift
ϕ	[rad]	Phase of a wave
ϕ_{NL}	[rad]	Phase induced by self-phase modulation
ρ	[C]	Electric charge density
ρ		Radial coordinate
τ_1	[s]	Relaxation parameter related to Raman gain spectrum
τ_2	[s]	Relaxation parameter related to Raman gain spectrum

τ_{shock}	[s]	Shock time scale
χ		Material's susceptibility
$\chi^{eff}_{(3)}$		Effective nonlinear parameter
ω	[rad s^{-1}]	Angular frequency
ω_0	[rad s^{-1}]	Angular frequency at the centre of bandwidth
ω_i	[rad s^{-1}]	Idler frequency
ω_p	[rad s^{-1}]	Pump frequency
ω_s	[rad s^{-1}]	Signal frequency
ω_S	[rad s^{-1}]	Stokes frequency
ω_{AS}	[rad s^{-1}]	Anti-Stokes frequency
ω_{DW}	[rad s^{-1}]	Frequency of dispersive wave
Ω	[rad s^{-1}]	Frequency of a photon
Ω	[rad s^{-1}]	Frequency shift between soliton and dispersive wave
Ω_s	[rad s^{-1}]	Frequency shift between pump and idler frequencies or pump and signal frequencies

LIST OF PHYSICAL CONSTANTS

Symbol	Value	Description
c	2.998×10^{8} m s^{-1}	Speed of light
$\hbar$	1.0545×10^{-34} J s	Reduced Planck constant
k_B	1.3807×10^{-23} J K^{-1}	Boltzmann's constant
ϵ_0	1.256×10^{-6} H m^{-1}	Vaccuum permittivity
μ_0	8.854×10^{-12} F m^{-1}	Vaccuum permeability

LIST OF ACRONYMS

Abbreviation	Description
ANDi	All-normal-dispersion
AR	Anti-reflection
ARF	Anti-resonant fiber
As	Arsenic
As_2S_3	Arsenic trisulfide
As_2Se_3	Arsenic triselenide
Bi_2O_3	Bismuth trioxide
BPM	Beam propagation method
C	Carbon

CCl_4	Carbon tetrachloride
CdO	Cadmium monoxide
CGNLSE	Coupled generalized nonlinear Schrödinger equation
CW	Continuous wave
DFWM	Degenerate four-wave mixing
DW	Dispersive wave
DXPM	Degenerate cross-phase modulation
FDM	Finite difference method
FEM	Finite element method
FFT	Fast Fourier transform
FROG	Frequency-resolved optical gating
FTIR	Fourier-transform infrared spectroscopy
FWHM	Full-width at half-maximum
FWM	Four-wave mixing
Ga_2O_3	Gallium trioxide
Ge	Germanium
GeTe	Germanium telluride
GNLSE	Generalized nonlinear Schrödinger equation
GVD	Group-velocity dispersion
H	Hydrogen
H2020	Horizon 2020
HCl	Hydrochloric acid
HF	Hydrofluoric acid
H_2O	Water
ICF	Inhibited coupling fiber
InF_3	Indium trifluoride
IPRS	Intrapulse Raman scattering
IR	Infrared
ITN	Innovative training network
$LiNbO_3$	Lithium niobate
LPF	Long-pass filter
MSCA	Marie Skłodowska-Curie actions
MCT	Mercury-cadmium-tellurite
MF	Microstructured fiber
MgO	Magnesium oxide
MI	Modulation instability
MIR	Mid-infrared
MMF	Multimode fiber

MOPA	Master oscillator power amplifier
NA	Numerical aperture
NANF	Nested capillary anti-resonant nodeless fiber
ND	Neutral density
NIR	Near-infrared
NLSE	Nonlinear Schrödinger equation
OCT	Optical coherence tomography
OH	Hydroxide
OPO	Optical parametric oscillator
PBF	Photonic band-gap fiber
PBO	Lead monoxide
PCF	Photonic crystal fiber
PM	Polarization-maintaining
PMD	Polarization-mode dispersion
PPLN	Periodically poled lithium niobate
RF	Radio frequency
RHS	Right-hand side
RS	Raman scattering
S	Sulfur
Sb	Antimony
SC	Supercontinuum
SC-PCF	Suspended core photonic crystal fiber
Se	Selenium
SEM	Scanning electron microscope image
Si	Silicon
SiO_2	Silica
SIF	Step-index fiber
SMF	Single-mode fiber
SPM	Self-phase modulation
SRS	Stimulated Raman scattering
SSFS	Soliton self-frequency shift
SUPUVIR	SUPercontinuum broadband light sources covering UV to IR applications
Te	Tellurium
TeO_2	Tellurite
$TeCl_4$	Tellurium chloride
THG	Third harmonic generation
TIR	Total internal reflection
TOD	Third-order dispersion

TPA	Two photon absorption
UV	Ultraviolet
XPM	Cross-phase modulation
Yb: KYW	Potassium yttrium tungstate
ZBLAN	ZrF_4-BaF_2-LaF_3-AlF_3-NaF

LIST OF PUBLICATIONS

PEER REVIEWED JOURNAL PAPERS

(I) E. Genier, **A. N. Ghosh**, S. Bobba, P. Bowen, O. Bang, P. M. Moselund, J. M. Dudley, and T. Sylvestre, "Cross-phase modulation instability in PM ANDi fiber-based supercontinuum generation", *Opt. Lett.* **45**(13), 3545–3548 (2020).

(II) S. Venck, F. St-Hilaire, L. Brilland, **A. N. Ghosh**, R. Chahal, C. Caillaud, M. Meneghetti, J. Troles, F. Joulain, S. Cozic, S. Poulain, G. Huss, M. Rochette, J. M. Dudley, and T. Sylvestre, "2-10 µm mid-infrared fiber-based supercontinuum laser source: experiment and simulation", *Laser Photonics Rev.***14**(6), 2000011 (2020).

(III) S. Perret, C. Poudel, **A. N. Ghosh**, G. Fanjoux, L. Provino, T. Taunay, A. Monteville, D. Landais, C. Kaminski, J. M. Dudley, and T. Sylvestre, "A Silica-based Photonic Crystal Fiber for the generation of broad band UV radiation", *OSA Continuum* **3**(1), 31–42 (2020).

(IV) **A. N. Ghosh**, M. Meneghetti, C. R. Petersen, O. Bang, L. Brilland, S. Venck, J. Troles, J. M. Dudley, and T. Sylvestre, "Chalcogenide-glass polarization-maintaining photonic crystal fiber for mid-infrared supercontinuum generation", *J. Phys.: Photonics* **1**(4), 044003 (2019).

(V) C. R. Petersen, M. B. Lotz, G. Woyessa, **A. N. Ghosh**, T. Sylvestre, L. Brilland, J. Troles, M. H. Jakobsen, R. Taboryski, and O. Bang, "Nanoimprinting and tapering of chalcogenide photonic crystal fibers for cascaded supercontinuum generation", *Opt. Lett.* **44**(22), 5505–5508 (2019).

(VI) M. Klimczak, D. Dobrakowski, **A. N. Ghosh**, G. Stepniewski, D. Pysz, T. Sylvestre, and R. Buczynski, "Nested-capillary anti-resonant silica fiber with mid-infrared transmission and low bending sensitivity at 4000 nm", *Opt. Lett.* **44**(17),4395–4398 (2019).

(VII) **A. N. Ghosh**, M. Klimczak, R. Buczynski, J. M. Dudley, and T. Sylvestre, "Supercontinuum generation in heavy-metal oxide glass based suspended-core photonic crystal fibers", *J. Opt. Soc. Am. B* **35**(9), 2311–2316 (2018).

NATIONAL AND INTERNATIONAL CONFERENCE PAPERS

(i) S. Rao D. S., T. Karpate, **A. N. Ghosh**, M. Klimczak, D. Pysz, R. Buczynski, C. Billet, O. Bang, J. M. Dudley, and T. Sylvestre, "Real-time noise measurement in supercontinuum generation in PM and Non-PM ANDi tellurite fibers", in *2020 Conference on Laser and Electro-Optics (CLEO)*, Paper STh3P.4, (San Jose, USA), May 2020.

(ii) S. Venck, F. St-Hilaire, L. Brilland, **A. N. Ghosh**, R. Chahal, C. Caillaud, M. Meneghetti, J. Troles, F. Joulain, S. Cozic, S. Poulain, G. Huss, M. Rochette, J.

M. Dudley, and T. Sylvestre, "2-10 µm mid-infrared all-fiber supercontinuum laser source: experiment and simulation", in *SPIE Photonics West, Nonlinear Frequency Generation and Conversion: Materials and Devices XIX*, paper 11264-8, (California, USA), Feb. 2020.

(iii) G. Genty, Z. Eslami, **A. N. Ghosh**, T. Sylvestre, M. Klimczak, R. Buczynski, and J. M. Dudley, "Supercontinuum generation in the near and mid-infrared using soft-glass fibers", in *OSA Advanced Photonics Congress (AP) 2019 (IPR, Networks, NOMA, SPPCom, PVLED)*, paper NoM4B.2, (California, USA), August 2019.

(iv) S. Perret, C. Poudel, **A. N. Ghosh**, G. Fanjoux, L. Provino, T. Taunay, A. Monteville, D. Landais, C. Kaminski, J. M. Dudley, and T. Sylvestre, "Generation d'un spectre ultraviolet de 350 a 391 nm dans une fibre optique a cristal photonique en slice UV-grade", in *Journees nationales d'Optique Guidee (JNOG), Société Française d'Optique*, (Paris, France), July 2019.

(v) **A. N. Ghosh**, M. Meneghetti, C. R. Petersen, O. Bang, L. Brilland, S. Venck, J. Troles, J. M. Dudley, and T. Sylvestre, "Chalcogenide-glass polarization-maintaining photonic crystal fiber for mid-infrared supercontinuum generation", in *2019 Conference on Lasers and Electro-Optics Europe & European Quantum Electronics Conference (CLEO/Europe-EQEC)*, paper cj_5_4, (Munich, Germany), June 2019.

(vi) S. Perret, **A. N. Ghosh**, G. Fanjoux, L. Provino, T. Taunay, A. Monteville, D. Landais, J. M. Dudley, and T. Sylvestre, "UV-grade silica-based photonic crystal fibers for broadband UV generation over 350–395 nm", *2019 Conference on Lasers and Electro-Optics Europe & European Quantum Electronics Conference (CLEO/Europe-EQEC)*, paper cj_8_4, (Munich, Germany), June 2019.

(vii) M. Klimczak, D. Dobrakowski, **A. N. Ghosh**, G. Stepniewski, D. Pysz, T. Sylvestre, and R. Buczynski, "Nested-capillary anti-resonant silica fiber with mid-infrared transmission and low bending sensitivity at 4000 nm", in *2019 Conference on Laser and Electro-Optics (CLEO)*, Paper STh1L.5, (San Jose, USA), May 2019.

(viii) **A. N. Ghosh**, M. Klimczak, R. Buczynski, J. Dudley, and T. Sylvestre, "Supercontinuum generation in suspended-core heavy-metal oxide glass photonic crystal fibers", in *OSA Advanced Photonic Congress, Specialty Optical Fibers*, Paper SoTh3H.2, (Zurich, Switzerland), July 2018.

(ix) **A. N. Ghosh**, M. Klimczak, R. Buczynski, J. Dudley, and T. Sylvestre, "Supercontinuum generation in a suspended core heavy metal oxide glass photonic crystal fiber", in *SPIE Photonics Europe, Micro-Structured and Specialty Optical Fibres V*, vol. 10681, paper 106810U, (Strasbourg, France), Apr. 2018 (*Invited*).

FUTURE PLANNED CONTRIBUTION

(a) S. Rao D. S., T. Karpate, **A. N. Ghosh**, M. Klimczak, R. Buczynski, C. Billet, O. Bang, J. M. Dudley, and T. Sylvestre, "Comparison of noise properties of the supercontinuum generated in PM and non-PM all-normal dispersion tellurite fibers using dispersive Fourier transform", 2020 (Under preparation).

TRAINING COURSES AND SUMMER SCHOOLS

(1) "Entrepreneurship in Technical Science" at DTU Fotonik, Department of Photonics Engineering, Technical University of Denmark, Copenhagen, Denmark, 12–17 August, 2019.

(2) "Microscopy and Sensing Workshop" at University of Cambridge, Department of Chemical Engineering and Biotechnology, Cambridge, UK, 26–28 November, 2018.

(3) "First Workshop on Photonic Crystal Fiber Technology for Ultrafast Optics Applications" at Institute of Electronic Materials Technology, Warsaw, Poland, 9–12 April, 2018.

(4) Training event on "Supercontinuum broadband light sources for UV and IR applications" at Femto-st Institute, France, 19–21 September, 2017.

(5) 9^{th} International Summer School "New Frontiers in Optical Technologies" at Optoelectronics Research Centre, Tampere University of Technology, Tampere, Finland, 7–11 August, 2017.

AUTHOR'S CONTRIBUTION

THE scientific results presented in this thesis have been carried out in the nonlinear optics group at the FEMTO-ST Institute and in the DTU Fotonik at the Technical University of Denmark. Out of 7 journal paper publications referred as (I)-(VII), presented earlier in the list of publications, this thesis is mostly based on papers (IV), (V), and (VII). All the simulations and characterizations (except the one related to paper (V)) presented in this thesis have been performed by the author. The author has written papers (IV) and (VII). The author's further contribution in paper (IV) includes drawing and fabrication of polarization-maintaining PCF and tapers (as a part of secondment in the SelenOptics company and the University of Rennes, France), characterization of the PCFs for mid-IR supercontinuum generation (as a part of secondment in the DTU Fotonik, Denmark), numerical computation and simulation in COMSOL and MATLAB, respectively. In paper (VII), author has also performed the numerical simulation and characterization of photonic crystal fiber for supercontinuum generation. Among the remaining 5 coauthored papers, author's contribution in paper (I) is some part of the experiment regarding SC generation in PM-ANDi fiber, in paper (II) is a part of numerical computation in COMSOL regarding the chalcogenide fiber, in paper (III) is design and numerical computation of UV-grade silica-based photonic crystal fiber in COMSOL, in paper (v) is fabrication of tapered chalcogenide photonic crystal fiber and in paper (VI) is some part of the experiment regarding the mid-IR transmission and bending sensitivity measurements in nested-capillary anti-resonant silica fiber. All the 7 journal papers are attached at the end of this thesis.

1

GENERAL INTRODUCTION

INFRARED (IR) light, positioned beyond the red limit of the visible band in the electromagnetic spectrum, was first discovered by astronomer Sir Frederick William Herschel in 1800 while studying the difference in temperature induced by the individual colors of light [190]. He created a spectrum of different colours by directing sunlight through a prism and then by using a thermometer he measured each color's temperature, which found to be increasing from violet to the red part of the spectrum. He further found that beyond the red part of the spectrum surprisingly had the highest temperature of all, which led to the discovery of IR radiation. According to the ISO 20473 scheme, IR spectrum can be divided into three regions: near-infrared (0.78-3 µm), mid-infrared (3-50 µm), and far-infrared (50-1000 µm).

1.1/ MOTIVATION

In this thesis we are mostly interested in the properties and applications of light in the mid-IR spectral region, particularly, 2-20 µm mid-IR band, which is often referred as the molecular "fingerprint region". This region contains highly distinctive absorption features from the fundamental vibrational resonances of molecules. For example, vibration frequencies of different greenhouse gases, toxic chemicals and explosives lie in this fingerprint region as shown in Fig. 1.1. When IR light is incident on such substances, the

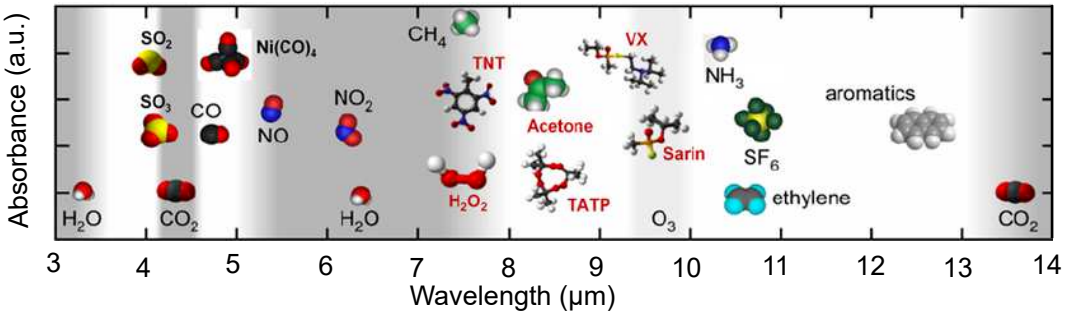

Figure 1.1: The absorption of various molecules in the mid-IR region, reproduced from [173].

interaction between IR light and the vibration of molecules leads to the absorption of some part of the light, which creates a unique fingerprint for that specific molecule and thus allow us to identify them. This leads to numerous spectroscopic applications such

as early cancer diagnostics [142, 158, 220], protein dynamics [46, 164], trace gas detection [60, 174], atmosphere pollutant monitoring [148], and explosive detection [161]. Furthermore, the mid-IR spectral region contains the atmospheric transparent windows (3–5 µm) and (8–12 µm) where both military and civilian thermal imaging can take place [205].

Supercontinuum (SC) generation, which is one of the most spectacular and visually perceptible nonlinear effects, is produced by a cascade of linear and nonlinear processes in transparent nonlinear media such as specially designed optical fibers made from special type of glasses, where a high intensity laser pulse undergoes extreme spectral broadening while propagating through the fiber [128]. SC generation was first reported in bulk glass by Alfano et al. in 1970 [8]. Since then SC generation has enormously attracted a great deal of scientific and technological interest and it has been widely studied in various nonlinear media or materials such as solids, liquids, gases and different types of waveguides [126, 204].

With the new technological advances, the development of novel laser sources, extensive research on highly nonlinear materials and upgraded design and fabrication technique of optical fibers and waveguides are continuously leading to new studies on SC generation extended to the yet unexplored parts of the electromagnetic spectrum. In recent times, spatially coherent, single-mode output, deliverable through fiber system, broadband, and high brightness SC sources with their multioctave wide spectral bandwidth have shown very high potential to replace the traditional thermal sources like incandescent bulb and Globar (silicon carbide thermal emitter), which provide broadband IR radiation. Another alternative to thermal sources providing broadband IR radiation is synchrotron IR beamlines, however, its widespread use is limited due to its extremely large size and high installation and operational cost. The brightness of SC sources are found to be 5–6 orders of magnitude higher than Globars and 1–2 orders of magnitude higher than synchrotron IR beamlines [242].

Fiber-based SC sources are the broadband light sources based on the principle of SC generation. For over a decade, SC sources are commercially available for the visible and near-IR spectral range, where they have been used in numerous applications like optical coherence tomography (OCT) [175, 218], various advanced microscopy techniques, such as stimulated emission depletion (STED) microscopy and multiphoton microscopy, interference reflection microscopy, and multispectral photoacoustic microscopy [153, 182, 225, 256]. Currently, a significant amount of research effort is focused on extending the spectral width of SC sources toward the mid-IR in the 2–20 µm molecular fingerprint region, which offers numerous practical applications of SC sources, such as material processing, gas monitoring, absorption spectroscopy, biomedical imaging, chemical sensing, and OCT [135, 207, 212, 213, 215, 217, 227, 236, 239, 242, 243, 246, 248, 251].

1.2/ STATE-OF-THE-ART FOR MID-INFRARED SUPERCONTINUUM (SC) GENERATION

Development of mid-IR SC sources through mid-IR SC generation, which is the goal of this thesis, suffers a significant challenge due to requirement of exotic glasses, complex fabrication techniques, and new pump laser wavelengths. Various soft glasses based on chalcogenide (As_2S_3, As_2Se_3,GeAsSe) [207, 236], tellurite (TeO_2)[230], telluride (GeTe,

GeAsTeSe) [195, 238], and ZBLAN (ZrF_4–BaF_2–LaF_3–AlF_3–NaF) [130, 235, 181] have been used for drawing highly nonlinear infrared fibers. SC sources with their spectra reaching up to 4 µm (in some cases up to 4.8 µm) have already become commercially available by leading photonics companies like NKT Photonics, Le Verre Fluoré, and Leukos [257, 258]. Norblis recently launched an SC source up to 10 µm with 50 mW of output power [259]. Although much progress in this field has been reported recently, state-of-the-art mid-IR SC systems are still in their infancy and considerable effort is required before mature broadband IR SC light sources beyond 10 µm with high output power are made available for industrial applications.

We present a brief state-of-the-art for mid-IR SC generation, which can be classified into two types: direct pumping and cascaded pumping. Direct pumping is based on bulky and extremely expensive mid-IR pump sources such as, tunable optical parametric oscillator (OPO) and optical parametric amplifier (OPA). On the other hand, cascaded pumping uses less expensive near-IR fiber lasers and amplifiers, and in most of the cases they do not require free-space propagation, thus making all-fiber SC system possible.

Among the direct pumping SC generation systems, Zhao et al. recently demonstrated mid-IR SC generation spanning from 2 to 16 µm in a 14 cm long low-loss step-index telluride (Ge–Te–AgI) fiber pumped in the normal dispersion regime at 7 µm by 150 fs pulses emitted from an OPA system [238]. Cheng et al. reported SC generation in the range 2-15.1 µm in a 3 cm long step-index As_2Se_3 fiber. The fiber with a core diameter of 15 µm was pumped at 9.8 µm with peak power of 2.89 MW delivered from a mid-IR pump source comprising of a Ti:Sapphire mode-locked seed laser, a traveling-wave optical parametric amplifier of superfluorescence (TOPAS), and a difference frequency generation (DFG) unit [217]. Lemière et al. most recently demonstrated SC generation spanning from 2 to 14 µm in arsenic- and antimony-free chalcogenide glass fiber [251]. Here, a 40 mm long 10 µm core step-index fiber, made from glass pair: $Ge_{20}Se_{60}Te_{20}$/$Ge_{20}Se_{70}Te_{10}$, was pumped by 65 fs pulses in the mid-IR. The pulses were delivered from a non-collinear optical parametric amplifier (NOPA) pumped by chirped pulse amplified (CPA) Ti:sapphire system and the NOPA was then followed by a DFG module [251]. Ou et al. also reported a mid-IR SC spectrum spanning from 1.8 to 14 µm in a 20 cm long and 23 µm core diameter $Ge_{15}Sb_{25}Se_{60}$/$Ge_{15}Sb_{20}Se_{65}$ step-index fiber pumped by 150 fs pulses at 6 µm delivered by an OPA system [223]. C. R. Petersen et al. demonstrated the generation of a SC spectrum covering from 1.4 to 13.3 µm using ultra-high numerical aperture chalcogenide step-index fiber [207]. They pumped a 16 µm core diameter fiber made from $As_{40}Se_{60}$/$Ge_{10}As_{23.4}Se_{66.6}$ (core/cladding) glass at 6.3 µm using a Ti:sapphire laser pumped tunable OPA and a noncollinear difference frequency generation (NDFG) module, which generated the above mentioned continuum with output power of 150 µW that can be scaled up by increasing the repetition rate or the pulse duration [207]. Yu et al. reported a widest spectrum in step-index chalcogenide fibers with low peak power of 3 kW [215]. By pumping an 11 cm long $Ge_{12}As_{24}Se_{64}$/$Ge_{10}As_{24}S_{66}$ fiber with 330 fs pulses at 4.0 µm emitted from an OPA system, they obtained a SC spectrum spanning from 1.8 to 10 µm [215].

On the other hand, among the most advanced fiber-based SC systems, Martinez et al. recently reported a mid-IR SC generation from 1.6 to 11 µm with an average output power of 139 mW in a cascaded fiber system using concatenated step-index ZBLAN, As_2S_3, and As_2Se_3 fibers, pumped at 1.553 µm by a master oscillator power amplifier (MOPA) system and three thulium-doped fiber amplifier stages [241]. Hudson et al. demonstrated a SC spectrum spanning from 1.8 to 9.5 µm with an average output power of around 30

mW in a polymer coated As_2Se_3/As_2S_3 taper fiber pumped by 4.2 kW peak power pulses emitted from a holmium based fiber laser at 2.9 µm [232]. Kubat et al. reported SC generation spanning from 0.9 to 9 µm with an average output power of 15 mW above 6 µm in a ZBLAN-As_2Se_3 fiber cascade pumped by a thulium laser at 2 µm. The thulium laser pumped ZBLAN step-index fiber generated a SC from 0.9 to 4.1 µm, which is then injected into a 5 µm As_2Se_3 microstructured PCF that generated the long wavelength edge [203]. C. R. Petersen et al. demonstrated mid-infrared cascaded SC generation beyond 7 µm in a silica-fluoride-chalcogenide fiber cascade pumped by a 1.55 µm seed laser and a thulium-doped fiber amplifier [224]. They pumped a commercially available $Ge_{10}As_{22}Se_{68}$-glass photonic crystal fiber with 135 mW of the pump continuum spanning from 3.5–4.4 µm and obtained a SC spectrum up to 7.2 µm with a total output power of 54.5 mW [224]. SC spectrum with record 565 mW of output power spanning from 1.9 to 4.8 µm at -20 db level was demonstrated by pumping a fiber cascade comprising of step-index silica and As_2S_3 fibers with a multistage MOPA system by Gattass et al. in 2012 [183]. In our European project, we also recently demonstrated mid-IR SC generation from 2 to 10 µm in a cascaded silica-ZBLAN-$As_{38}Se_{62}$ fiber system directly pumped with a commercially available 460-ps pulsed fiber laser at 1.55 µm without any fiber amplifier stage [260]. This technique paves the way for low cost, practical, and robust broadband SC sources in the mid-IR without the requirement of mid-infrared pump sources or Thulium-doped fiber amplifiers.

1.3/ STRUCTURE OF THE THESIS

The main focus of this thesis is the research of mid-IR SC generation in soft-glass microstructured PCFs for the development of mid-IR SC sources with high average output power, capability of maintaining stable and linear polarization, and spectral bandwidth extended beyond 6 µm for applications in optical sensing, absorption spectroscopy, and optical coherence tomography. This thesis is organised as follows:

In **Chapter 2**, the basic theory of light propagation in an optical fiber which includes both the linear and nonlinear effects leading to SC generation is presented. Linear effects include the processes such as linear loss, chromatic dispersion, and polarization-mode dispersion and the nonlinear effects include processes like optical Kerr effect, self-phase modulation, cross-phase modulation, four-wave mixing, modulation instability, Raman scattering, solitons, and dispersive waves, to name a few. Finally, the generalized nonlinear Schrödinger equation governing all the linear and nonlinear processes in an optical fiber that is useful for the numerical investigation of SC generation, is further presented.

Chapter 3 starts with an overview of soft-glass materials that offer mid-IR transmission and are appropriate for mid-IR SC generation. Then the stack-and-draw method for fabrication of heavy metal-oxide glass based suspended-core PCFs, which was manufactured at the Institute of Electronics Material Technology (ITME) in Warsaw, is further demonstrated here. The chapter continues with computation of group velocity dispersion parameters, which are very important for the numerical analysis of SC generation. A brief introduction of the experimental setup including the generation and measurements of SC light is presented and followed by the analysis of obtained results. A detailed numerical analysis of SC generation based on the generalized nonlinear Schrödinger equation and its comparison with experimental results are further provided here. The results was published in journal paper (VII). The chapter ends with a conclusion of the overall work.

In **Chapter 4**, a detailed fabrication process of high purity chalcogenide glass using the standard melt-quenching method is presented in the beginning. The chapter then continues with the fabrication of polarization-maintaining (PM) and non-PM PCFs and tapers using casting method, as a part of author's secondment in the University of Rennes and the SelenOptics company. Transmission and attenuation characteristics of the drawn PCFs and tapers are shown further in this chapter. Numerical computations of the group-velocity dispersion and the birefringence properties of the fibers are then discussed to show in particular how both the birefringence and the dispersion can be tailored to enhance SC generation by tapering the PCF down to a few µm core diameter. Then the results of mid-IR SC generation with various fiber and pump configurations, obtained at the DTU Fotonik as a part of author's secondment, is presented. First the results of journal paper [IV] is presented, which at the time of publication represented the broadest spectrum ever recorded in a polarization-maintaining PCF with direct pumping. Then the results of both direct and cascaded pumped SC generation in a non-PM taper fiber is presented where the cascaded pumped SC, at the time of publication, represented the broadest SC recorded in a taper PCF generated in cascaded configuration and the result was published in journal paper (V). Finally, power damage threshold measurement of chalcogenide photonic crystal fiber (delivered by the University of Rennes) is presented.

Chapter 5 deals with general conclusion, where the accomplished results are summarized along with all the major issues and an outlook presents the possibilities to further overcome the issues and enhance the efficiency of mid-IR SC sources in the future.

2

LIGHT PROPAGATION IN AN OPTICAL FIBER

THIS chapter introduces the building block of nonlinear optics in connection to the supercontinuum (SC) generation in optical fibers. Like the electromagnetic wave in radio frequency (RF) domain, optical waves can only interact with each other indirectly through an optical medium. In the first section, we start with linear propagation of light inside an optical fiber through the introduction of Maxwell's equations and the wave equation. Optical pulses in fiber experience linear changes from linear loss, chromatic dispersion, and polarization-mode dispersion. Once the linear effects have been established, the readers in the second section have been introduced to the nonlinear effects, which are mostly relevant to SC generation. Furthermore, in an optical fiber, the linear and nonlinear optical phenomenon have combine effect on pulse propagation, which is modelled using the generalized nonlinear Schrödinger equation.

2.1/ LINEAR PROPAGATION OF LIGHT IN OPTICAL FIBERS

2.1.1/ MAXWELL'S EQUATIONS AND THE WAVE EQUATION

Propagation of an electromagnetic field in an optical medium is described by one of the most successful set of equations ever written in the history of physics: the Maxwell equations. In the absence of free charges (i.e., current $\vec{J} = 0$ and charge density $\rho = 0$) in an optical fiber, Maxwell's equations can be expressed as (in SI units) [61]

$$\nabla \cdot \vec{D} = \rho = 0, \tag{2.1.1}$$

$$\nabla \cdot \vec{B} = 0, \tag{2.1.2}$$

$$\nabla \times \vec{E} = -\frac{\partial \vec{B}}{\partial t}, \tag{2.1.3}$$

$$\nabla \times \vec{H} = \vec{J} + \frac{\partial \vec{D}}{\partial t}, \tag{2.1.4}$$

where $\vec{D}$ and $\vec{B}$ represent electric and magnetic flux densities, respectively and $\vec{E}$ and $\vec{H}$ are the corresponding electric and magnetic field vectors. The rate of changes of electric and magnetic flux densities in response to the electric and magnetic fields propagating

inside a fiber are related by the following equations [61]

$$\vec{D} = \epsilon_0 \vec{E} + \vec{P}, \tag{2.1.5}$$

$$\vec{B} = \mu_0 \vec{H} + \vec{M}, \tag{2.1.6}$$

where ϵ_0 and μ_0 are the vacuum permittivity and permeability, respectively and $\vec{P}$ and $\vec{M}$ are the electric and magnetic polarizations, respectively. The effect of magnetic polarization disappears ($\vec{M} = 0$) in an optical fiber, which is a nonmagnetic medium. From Eqs. 2.1.1- 2.1.6, the wave equation, which describes the light propagation in an optical fiber, can be derived as

$$\nabla \times \nabla \times \vec{E} = -\frac{1}{c^2}\frac{\partial^2 \vec{E}}{\partial t^2} - \mu_0 \frac{\partial^2 \vec{P}}{\partial t^2}, \tag{2.1.7}$$

where $c = 1/\sqrt{\mu_0 \epsilon_0}$ is the speed of light in vacuum. Using the relations $\nabla \times \nabla \times \vec{E} = \nabla(\nabla \cdot \vec{E}) - \nabla^2 \vec{E} = -\nabla^2 \vec{E}$ and $\nabla \cdot \vec{D} = \nabla \cdot \epsilon_0 \vec{E} = 0$, Eq. 2.1.7 can be rewritten in the following form

$$\nabla^2 \vec{E} = \frac{1}{c^2}\frac{\partial^2 \vec{E}}{\partial t^2} + \mu_0 \frac{\partial^2 \vec{P}}{\partial t^2}. \tag{2.1.8}$$

Induced electric polarization $\vec{P}$ is not linear with the strength of applied electric field and it can be expressed by the general relation [28, 45, 143]

$$\begin{aligned} \vec{P} &= \epsilon_0 [\chi^{(1)} \vec{E} + \chi^{(2)} \vec{E}^2 + \chi^{(3)} \vec{E}^3 + \cdots + \chi^{(n)} \vec{E}^n], \\ &\equiv \vec{P}^{(1)} + \vec{P}^{(2)} + \vec{P}^{(3)} + \cdots, \end{aligned} \tag{2.1.9}$$

where $\vec{P}^{(1)}$, $\vec{P}^{(2)}$, and $\vec{P}^{(3)}$ are referred to as first-order polarization, second-order nonlinear polarization, and third-order nonlinear polarization, respectively. $\chi^{(n)}$ is a rank $n+1$ material response tensor known as the susceptibility, which is defined by the material's composition and molecular structure. Usually, tensor χ is time-dependent, which will be neglected in the further mathematical derivations. The first term of right-hand side of Eq. 2.1.9 accounts for the linear response which dominates on P at low electromagnetic field interacting with the material. The effect of linear susceptibility $\chi^{(1)}$ includes through the refractive index n and attenuation coefficient α, which will be discussed in the later part of this section. For a strong field, we have to take account the higher-order susceptibilities, which cause different nonlinear effects. The second-order susceptibility term $\chi^{(2)}$, which is responsible for nonlinear effects such as second-harmonic generation and sum or difference-frequency generation [28], vanishes along with other even terms of susceptibility for isotropic centro-symmetric materials, such as glasses. Thus, the third-order susceptibility term $\chi^{(3)}$ is the very first and most significant higher-order polarization term for glass fiber, referred as third-order nonlinearity. $\chi^{(5)}$, the next higher-order nonlinear term being approximatively 10^{-24} times higher than $\chi^{(3)}$ [143], is neglected in this thesis. Therefore, the induced polarization $\vec{P}$ can be split into the linear contribution, $\vec{P}_L$ from $\chi^{(1)}$ and nonlinear contribution, $\vec{P}_{NL}$ from $\chi^{(3)}$, such that

$$\vec{P}(\vec{r}, t) = \vec{P}_L(\vec{r}, t) + \vec{P}_{NL}(\vec{r}, t). \tag{2.1.10}$$

In the linear propagation regime, we can only focus on $\vec{P}_L$, which can be expressed in terms of electric field as

$$\vec{P}_L(\vec{r},t) = \epsilon_0 \int_{-\infty}^{t} \chi^{(1)}(t-t')\vec{E}(\vec{r},t')dt'. \tag{2.1.11}$$

The Fourier transform of $\vec{P}_L(\vec{r},t)$ is $\tilde{\vec{P}}_L(\vec{r},\omega)$ which is given by

$$\tilde{\vec{P}}_L(\vec{r},\omega) = \tilde{\chi}^{(1)}(\omega)\tilde{E}(\vec{r},\omega), \tag{2.1.12}$$

where $\tilde{\chi}^{(1)}(\omega)$ is the Fourier transform of $\chi^{(1)}(t)$ and $\tilde{E}(\vec{r},\omega)$, which represents the Fourier transform of $\vec{E}(\vec{r},t)$, can be defined as

$$\tilde{E}(\vec{r},\omega) = \int_{-\infty}^{\infty} \vec{E}(\vec{r},t)\exp(i\omega t)dt. \tag{2.1.13}$$

Therefore, the wave equation (Eq. 2.1.8) can now be expressed in the frequency domain as

$$\nabla^2\tilde{E}(\vec{r},\omega) = -\epsilon(\omega)\frac{\omega^2}{c^2}\tilde{E}(\vec{r},\omega), \tag{2.1.14}$$

where $\epsilon(\omega)$ is the frequency-dependent dielectric constant that can be defined for lossless medium as

$$\epsilon(\omega) = 1 + \tilde{\chi}^{(1)}(\omega) = n^2(\omega), \tag{2.1.15}$$

where $n(\omega)$ is the refractive index, which often does not depend on the spatial coordinates in core and cladding of a step-index fiber. Therefore, Eq. 2.1.14 takes the form of Helmholtz equation [141] as

$$\nabla^2\tilde{E} + n^2(\omega)\frac{\omega^2}{c^2}\tilde{E} = 0. \tag{2.1.16}$$

The solution to Eq. 2.1.16 will be discussed in the following sections.

2.1.2/ OPTICAL FIBERS AND PROPAGATION MODES

The development of optical fibers has been tremendously growing since the demonstration of low loss propagation in silica fibers in 1970 [9], and therefore, their possible application for the telecommunication industry. The simplest type of optical fiber is step-index fiber (SIF) in which a central glass core (circular) with refractive index n_{core} is surrounded by a circular cladding whose refractive index n_{clad} is lower than n_{core} as shown in Fig. 2.1. a and b are the core and cladding radius, respectively. There is another type of fiber known as gradient-index fiber in which n_{core} decreases gradually from the centre of the core to its boundary [21, 24]. Based on the theory of ray optics, according to Snell's law of refraction, light in optical fiber is guided by the physical effect of total internal reflection (TIR). At the air-fiber interface, we can have

$$n_0\sin(\theta_{\text{in}}) = n_{\text{core}}\sin(\theta_t), \tag{2.1.17}$$

where θ_{in} is the angle of incidence of a ray of light on the fiber face and θ_t is the refracted angle in the core of the fiber, both being taken with respect to the normal and n_0 is the

refractive index of air, which is 1 in case of air, as shown in Fig. 2.1. TIR occurs up to a maximum angle of incidence such that the core/cladding refraction is greater than a certain limiting angle, called the critical angle, which is defined as

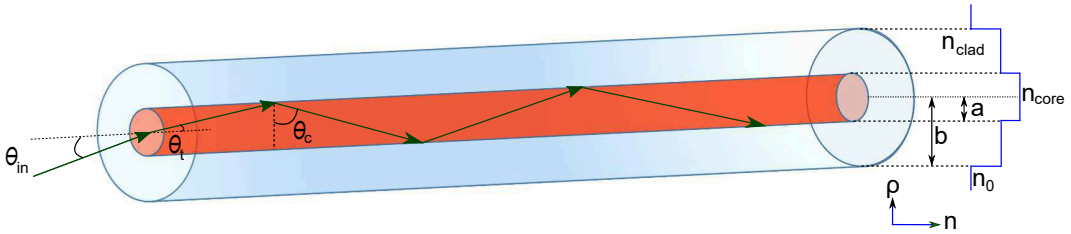

Figure 2.1: Schematic of the geometric structure of an optical fiber. Refraction at the air-glass interface and total internal reflection at the core-cladding interface are shown by the ray diagram. The step-index refractive index profile showing the contrast between the refractive index of core (n_{core}) and cladding (n_{clad}) is presented as a function of radial coordinate ρ. a and b are the core and cladding radius, respectively.

$$n_0 \sin(\theta_c) = \frac{n_{\text{clad}}}{n_{\text{core}}}. \tag{2.1.18}$$

From trigonometry, the acceptance angle of the fiber for which the above condition is fulfilled is then given by the numerical aperture (NA), which can be expressed by Pythagorean subtraction of core and cladding refractive indices as [141, 162]

$$\sin(\theta_{\text{in}}) = \sqrt{{n_{\text{core}}}^2 - {n_{\text{clad}}}^2} = \text{NA}. \tag{2.1.19}$$

Another important parameter that characterizes an optical fiber is the relative refractive index difference Δ of n_{core} and n_{clad}:

$$\Delta = \frac{n_{\text{core}} - n_{\text{clad}}}{n_{\text{core}}}. \tag{2.1.20}$$

In the context of wave optics, we can have more accurate understanding of guiding properties of a SIF by solving the wave equation (2.1.16), derived in Section 2.1.1. It is done by adopting a scalar approach along with slowly varying envelope approximation, where the quasi-monochromatic optical field is assumed to be linearly polarized with polarization unit vector $\hat{x}$ along the fiber length and the rapidly varying part of electric field is separated such that

$$\vec{E}(\vec{r}, t) = \frac{1}{2}\hat{x}[E(\vec{r}, t)\exp(-i\omega_0 t) + c.c.], \tag{2.1.21}$$

where $\vec{E}(\vec{r}, t)$ is a slowly varying function of time (relative to optical period), ω_0 is carrier central frequency, and c.c. denotes the complex conjugate. It is more convenient to work in the Fourier domain while obtaining wave equation for amplitude $E(\vec{r}, t)$. Therefore, Eq. 2.1.16 can be solved by using the method of separation of variables such that it gives a solution of the form

$$\tilde{E}(\vec{r}, \omega - \omega_0) = F(x, y)\tilde{A}(z, \omega - \omega_0)\exp(i\beta_0 z), \tag{2.1.22}$$

where $F(x,y)$ represents the transverse spatial distribution of electric field, $\tilde{A}(z,\omega)$ is a slowly varying function of z, and β_0 is the propagation constant of the wave. The spatial modes in optical fiber are generally described by their effective area, which is defined as [131]

$$A_{\text{eff}} = \frac{\left(\iint_{-\infty}^{\infty} |F(x,y)|^2 dxdy\right)^2}{\iint_{-\infty}^{\infty} |F(x,y)|^4 dxdy}. \tag{2.1.23}$$

The effective mode area is evaluated using the modal distribution $F(x,y)$ of the fundamental mode (can also be done for all other modes) and it depends on the structural parameters of fiber such as the radius of the core and the core-cladding refractive index difference. In case of highly nonlinear fiber on which this thesis is based on, the nonlinear effects are enhanced by reducing the effective mode area. It is an important factor while considering nonlinear effects on pulse propagation as described in Section 2.2. Since, the SIF (see Fig. 2.1) has cylindrical symmetry, therefore, the modal distribution can be expressed using cylindrical coordinate system as [131]

$$\frac{d^2F}{d\rho^2} + \frac{1}{\rho}\frac{dF}{d\rho} + \left(n^2k_0^2 - \beta^2 - \frac{m^2}{\rho^2}\right)F = 0, \tag{2.1.24}$$

where refractive index $n = n_{\text{core}}$ for $\rho \leq a$ (within the core) and $n = n_{\text{clad}}$ for $\rho \geq a$ (within the cladding). Eq. 2.1.24 is a well-known differential equation for the Bessel functions. In the core region ($\rho \leq a$), solutions to Eq. 2.1.24, by using the boundary condition that $\vec{E}$ and $\vec{H}$ should be continuous at the core-cladding interface with increasing radial distance (ρ), can be written as

$$F(\rho) = J_m(p\rho), \tag{2.1.25}$$

where $J_m(x)$ is the Bessel function and $p = ({n_{\text{core}}}^2k_0^2 - \beta^2)^{1/2}$. In the cladding region ($\rho \geq a$), the solution $F(\rho)$, which is represented by the modified Bessel function k_m, decays exponentially with increasing radial distance (ρ). Therefore,

$$F(\rho) = k_m(q\rho), \tag{2.1.26}$$

where $q = (\beta^2 - {n_{\text{clad}}}^2k_0^2)^{1/2}$ gives the following important relation

$$p^2 + q^2 = k_0^2({n_{\text{core}}}^2 - {n_{\text{clad}}}^2). \tag{2.1.27}$$

Using Eq. 2.1.27, the eigenvalue equation can be directly written as [24, 50]

$$\left[\frac{J_m'(pa)}{pJ_m(pa)} + \frac{k_m'(qa)}{qk_m(qa)}\right]\left[\frac{J_m'(pa)}{pJ_m(pa)} + \frac{{n_{\text{clad}}}^2}{{n_{\text{core}}}^2}\frac{k_m'(qa)}{qk_m(qa)}\right] = \left(\frac{m\beta k_0({n_{\text{core}}}^2 - {n_{\text{clad}}}^2)}{an_{\text{core}}p^2q^2}\right)^2, \tag{2.1.28}$$

where the notation prime represents the differentiation with respect to the argument. The eigenvalue equation (2.1.28) has several solutions for β for each integer values of m. Each eigenvalue β_{ms}, where s is an integer, describes a specific mode, which is guided by the fiber that fulfils the condition, $k_0n_{\text{clad}} < \beta < k_0n_{\text{core}}$. There are two types of fiber modes: HE_{ms} and EH_{ms}. The number of modes that is supported by a specific fiber generally depends on several parameters such as the radius of fiber core (a), numerical aperture (NA), and the excitation wavelength. In this respect, an important parameter is the normalized frequency or V-parameter, which can be used along with the eigenvalue

equation (2.1.28) to determine the cut-off of different modes in the fiber. Therefore, V can be expressed as [131]

$$V = p_c a = a k_0 ({n_{\text{core}}}^2 - {n_{\text{clad}}}^2)^{1/2} = \frac{2\pi a}{\lambda}\text{NA}, \tag{2.1.29}$$

where p_c is obtained from Eq. 2.1.27 at $q = 0$. Since, in this thesis, we are mainly interested in single-mode fiber, therefore, we only discuss about the cut-off condition that allows only one mode to be guided in the fiber. A single mode fiber only supports the fundamental mode HE_{11} for which the cut-off condition is $V < V_c$, where the cut-off frequency V_c is found to be the smallest solution to the Bessel function, $J_0(V_c) = 0$, which occurs when $V_c = 2.405$ [131].

2.1.3/ PHOTONIC CRYSTAL FIBER

A particular fiber design that revolutionized the field of nonlinear fiber optics and supercontinuum generation is the photonic crystal fiber (PCF), also known as holey fiber. In the 1970s, Kaiser et al. suggested the possibility to modify the light guidance properties of optical fibers by introducing a microstructure in its refractive index profile [14]. However, fabrication of such fibers has become technologically well known since the work done by Philip Russell's group in 1996 [55]. PCF's technology has matured extremely during the last two decades. In particular, the control of the fiber drawing process with extreme precision has enabled to produce a great variety of complex structures.

Photonic crystal fibers exhibit some unique features in comparison to the standard optical fibers [55, 69, 72, 78, 80, 82, 108]. Cross-section of PCFs consists of glass materials and hollow air channel along the longitudinal direction. Introduction of these air-holes allows us to tailor the modal, dispersive and nonlinear properties of the fiber more flexibly compared to standard fibers. For examples, it is possible to design endlessly single-mode PCFs with different core sizes, which guide light in a single transverse mode from the near-ultraviolet to infrared wavelength range [57, 62, 72, 108, 118]. Mechanically robust PCFs with extremely small core diameter around 1 µm [72] are feasible for enhancing nonlinear optical processes along the fiber [68, 108, 213]. On the other hand, large core single mode PCFs can also be manufactured enabling the useful features like reduced nonlinearities and the ability to sustain high peak power from an amplifier system or high power lasers [62, 108, 79, 116, 109, 123]. It is possible to design PCFs that exhibit very low dispersion values with a flat profile over a broad wavelength range for application like optical parametric amplification and supercontinuum generation in the infrared [70, 99, 112, 115, 104]. Moreover, using proper arrangement and size of the air holes, the waveguide dispersion of PCFs can also be tailored to push the zero-dispersion wavelength close to the pumping wavelength for efficient supercontinuum generation in the infrared [163, 145, 168, 252], Furthermore, it is possible to maintain the polarization of guided light along the fiber by introducing large amount of birefringence in the core of the fiber [76, 81, 85, 88, 105, 114]. However, due to various phenomena such as bending, micro-deformation, and glass-impurities, PCFs have propagation losses which are an order of magnitude higher than the conventional all-solid fibers [84, 89, 86, 92, 103, 102, 107, 110] and this point will be discussed in the next section.

Depending on the nature of the core, PCFs can be classified in two categories: microstructured fibers (MFs) and photonic band-gap fibers (PBFs). Most of the widely used

PBFs exhibit a hollow core at the centre of the structure and a periodic air-hole lattice which forms the cladding [63, 66, 100, 139]. There are also soild core PBFs, which consist a 1D or 2D periodic structure in the cladding and a solid core whose refractive index is lower than that of cladding [155, 159]. Therefore, confinement of the light in such fibers cannot be explained by the total internal reflection mechanism but it can be interpreted as a consequence of the cladding periodicity. For example, light guidance in a hollow core PBF occurs through genuine photonic band-gap i.e., the periodicity of the air-hole lattice enables to trap the light in the core by a two-dimensional photonic band-gap. Only light with a certain wavelength range can fulfill the guidance condition, therefore, it results in rather narrow transmission bandwidths for such hollow core fibers. Transmission in these PBFs can be broadened by introducing a Kagomé lattice design in the cross-section of the fiber [127, 138]. These Kagomé fibers are considered to be one type of inhibited coupling fibers (ICFs) as the light guidance in such fibers occurs through a so-called inhibited-coupling guidance, which is based on a strong phase mismatch of core and the cladding modes preventing the leakage of the core modes into the inner cladding [91, 133]. Another type of ICFs with a more simplified structure is the anti-resonant fiber (ARF) whose cladding consists of only one ring of circular capillaries offering low loss transmission in the mid-IR wavelength regime [167, 180, 194, 197, 211]. A recent study has been demonstrated a mid-IR transmission up to 4.2 µm with an attenuation of 1.5 dB/m within 3.6-4 µm wavelength range and a bending loss of 0.5 dB/m at a bending radius of 40 mm at around 3.8 µm in a nested capillary anti-resonant nodeless fiber (NANF), which is a variant of ARFs [250]. The Hollow-core PBFs have attracted much interest due to their potential for lossless and distortion-free transmission, optical sensing, and other novel applications in nonlinear optics [91, 106, 111, 113]. However, they are not that much used in SC generation experiments, therefore, are beyond the scope of this thesis. On the other hand, SC generation is mainly observed in solid-core MFs, which will be discussed in details in this thesis in the following paragraphs.

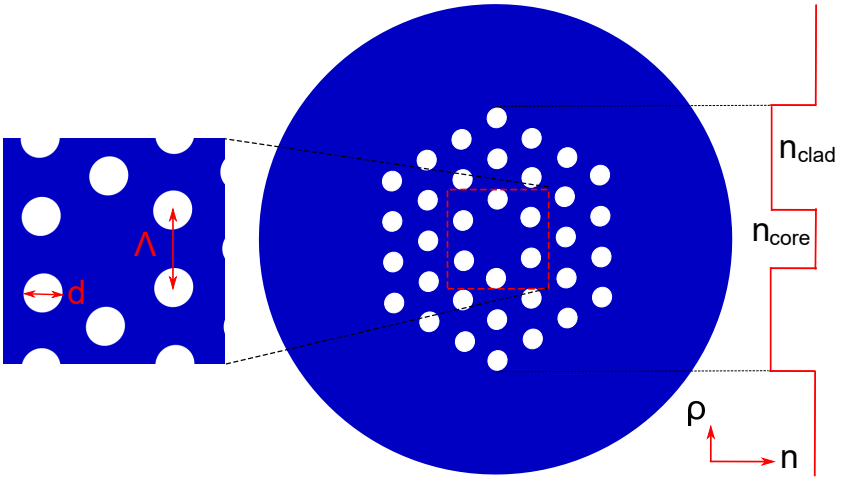

Figure 2.2: Schematic of a solid-core index-guiding PCF with a cladding consisting of triangular lattice of air-holes, which guides light through modified total internal reflection. The diameter (d) of air-capillary and the pitch (Λ) are defined in the zoomed-in region of the core in the left. The refractive index profile of the PCF, shown on the right, indicates that the resulting effective refractive index of air hole-glass cladding is lower than the core.

Microstructured fibers possess a solid core in the centre of the structure made from silica [65, 67, 96] or non-silica glasses [75, 95, 97]. The typical design of a solid core microstructured photonic crystal fiber is based on a periodic, hexagonal lattice of air-capillaries forming a cladding region (also referred as the photonic crystal cladding) with one or more missing capillaries in the center forming the core, as shown in Fig. 2.2. The air-capillaries are maintained down the longitudinal direction of the fiber to create a low-index region, thus, the effective refractive index of the central core region of the PCF is higher than that of the surrounding air-hole cladding region. These fibers, also known as index-guiding PCFs, guide light through modified total internal reflection, conceptually similar to the standard SIFs guiding [57, 100, 139]. However, unlike SIFs, the effective refractive index of the photonic crystal cladding is highly wavelength dependent, and is determined by the properties of the fundamental space filling mode (β_{fsm}), i.e. cladding mode [74, 90]. The modal properties of MFs can be analyzed using the corresponding normalized frequency defined as [100]

$$V_{\text{PCF}} = a\sqrt{k^2 {n_{\text{core}}}^2 - \beta_{fsm}^2}, \tag{2.1.30}$$

where a and n_{core} are the radius and refractive index of MF's core, respectively. In comparison to Eq. 2.1.29, the primary difference is that, in the high frequency limit, value of V_{PCF} converges towards a stationary value due to a vanishing core-cladding index contrast and therefore, depends only on the air-capillary diameter d and the distance between two adjacent air-capillaries, also known as lattice pitch Λ [100]. The second-order cut-off in MFs occurs at $V_{\text{PCF}} < 4.2$, therefore, for a PCF with $d/\Lambda < 0.45$, V_{PCF} converges towards a value below the cut-off that makes the PCF endlessly single-moded [100]. In MFs, dispersion can be altered significantly through the appropriate selection of d and Λ.

2.1.4/ Losses in optical fiber

In an optical fiber, there are several linear losses such as propagation loss and Fresnel loss, which affect the transmission of light inside the fiber. If P_L amount of power is launched in the beginning of the fiber having a length L, then the transmitted power at the output of the fiber will be given by

$$P_{\text{out}} = P_L \exp(-\alpha L), \tag{2.1.31}$$

where α (km^{-1} in linear unit) is known as the attenuation constant, which is the measure of losses from all sources. The relationship between α in dB unit and linear unit (which will be used in numerical simulation later in the thesis) is given by

$$\alpha_{\text{dB}} = -\frac{10}{L}\log\left(\frac{P_{\text{out}}}{P_L}\right) = 4.343\alpha. \tag{2.1.32}$$

The linear propagation loss inside the fiber usually originates from material absorption, scattering at the interfaces between different materials of the fiber, and bending loss.

2.1.4.1/ Bending loss

Light inside a fiber experiences two types of bending loss: macrobending and microbending. Macrobending loss associates with bending or wrapping of the fiber. In a bent fiber, in order to maintain the wavefront, the outer side of guided mode needs to travel faster than inner side, which becomes difficult in case of small bending radius of curvature, resulting

leakage of some part of energy out of the fiber. The critical bending radius of curvature (R_c), for which bending loss can be neglected, is given by [172].

$$R_C = \frac{3n_{\text{clad}}\lambda}{4\pi(\text{NA})^3}, \tag{2.1.33}$$

where n_{clad} is refractive index of cladding and NA is the numerical aperture of the fiber. Macrobending loss becomes insignificant in case of highly nonlinear fiber (requires short length), when the fiber is kept straight or the bending radius is large enough. On the other hand, microbending loss arises from random axial distortions of the core-clad interface generated from mechanical tensile forces during fiber drawing. This loss can be avoided by using efficient drawing parameters. Therefore, in highly nonlinear microstructured fiber like chalcogenide fiber or heavy metal-oxide fiber, contribution of material absorption loss and interface scattering loss are dominant.

2.1.4.2/ SCATTERING LOSS

For microstructured photonic crystal fiber (as shown in Fig. 2.2) from soft glasses such as heavy metal-oxide or chalcogenide glass, scattering loss originates from the scattering at interfaces between fiber material and air due to imperfect smoothness, which is the cause for aging of the fiber and increase in loss during storage [206, 210]. Such problem can be avoided by storing the fibers in dry atmosphere. Since, Rayleigh scattering is inversely proportional to fourth power of wavelength, therefore, attenuation due to Rayleigh scattering can be reduced by operating at the longer wavelength. Mie scattering, which is proportional to the square of wavelength, originates from the refractive index fluctuation in the core and cladding of the fiber due to inhomogeneity, impurities and defects in the glass. It can be removed by using highly purified glass for fiber drawing.

2.1.4.3/ MATERIAL ABSORPTION LOSS

Another source of linear propagation loss comes from the material absorption. There are two types of absorption loss: intrinsic absorption and extrinsic absorption. Intrinsic absorption originates from the interaction between the guided light and the glass materials of the fiber. Modifying the glass material is a good way to reduce these losses, which determine the fundamental minimum possible losses. On the other hand, extrinsic absorption is caused by the interaction between the guided light and the impurities present in the glass or atmosphere. Soft glass like chalcogenide glass-based optical fibers (composed of S, Se or Te) support transmission in the mid-IR region. Figure 2.3 shows the transmission spectra of microstuctured hexagonal suspended-core $Ge_{10}As_{22}Se_{68}$, $As_{38}Se_{62}$, $As_{40}S_{60}$, and $Te_{20}As_{30}Se_{50}$ fibers [210]. All these fibers show good transmission from 2 µm up to the mid-IR region with several attenuation peaks due to impurities in the glass and atmosphere.

Using standard stack-and-draw method (which will be discussed in Chapter 3), a single-mode fiber shows a minimum optical loss (α) of 10 dB/m at 1.55 µm [156] and a multi-mode fiber shows a minimum loss of 3 dB/m at the same wavelength [144]. Attenuation lower than 1 dB/m have been obtained by using moulding method, which will be later discussed in Chapter 4 [170, 165]. The lowest attenuation of < 0.05 dB/m at 3.7 µm was observed in a $As_{38}Se_{62}$ glass-based six air holes suspended-core photonic crystal fiber (SC-PCF), which offers multi-mode propagation [170]. This attenuation is close to the record of 0.012 dB/m measured in a As_2S_3 glass-based classical step-index fiber

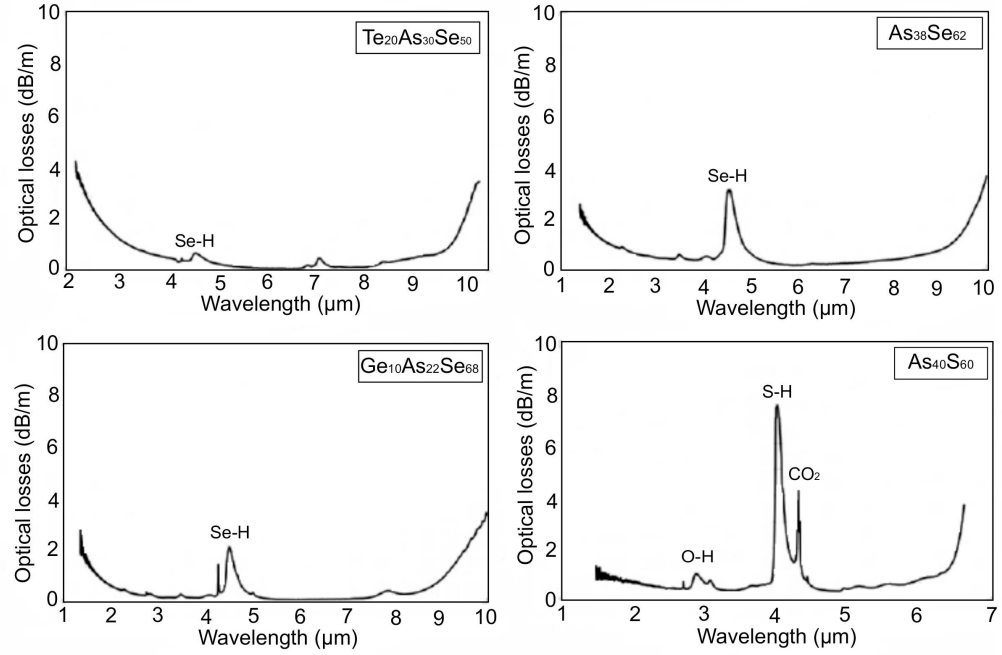

Figure 2.3: Linear loss of chalcogenide glass based microstuctured optical fibers after drawing. Figure reproduced from [210].

[160]. The best attenuation for a single-mode fiber at telecom wavelength is 0.35 dB/m in a $As_{40}S_{60}$ glass-based SC-PCF [163] and 1 dB/m in a $Ge_{10}As_{22}Se_{68}$ glass-based PCF [189].

2.1.4.4/ COUPLING LOSS

When a light beam is launched into a fiber core, it experiences Fresnel reflection loss from the input facet of the fiber and only a percentage of input power (P_{in}) is coupled to the fiber. The coupled power (P_{c}) is then transmitted at the output of the fiber as output power (P_{out}), after experiencing propagation loss (α) and another Fresnel reflection loss from fiber's output facet as shown in Fig. 2.4. Fresnel reflectance (R_{F}) for normal incidence is given by

$$R_F = \left|\frac{n_1 - n_2}{n_1 + n_2}\right|^2, \tag{2.1.34}$$

where n_1 is the refractive index of air and n_2 is the refractive index of the glass used to draw the fiber. If the length (L) of the fiber, R_{F}, and α are known, then the coupling efficiency can be estimated from the measured P_{in} and P_{out}. We neglected any kind of outcoupling losses to measure P_{out}. The coupled power is defined by

$$P_{\text{c}} = \frac{P_{\text{out}}}{(1 - R_{\text{F}})} 10^{\frac{\alpha L}{10}}. \tag{2.1.35}$$

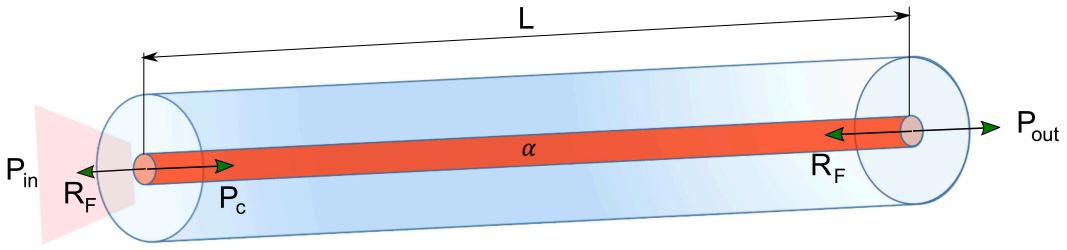

Figure 2.4: Schematic representation of coupling model to estimate coupling efficiency.

The factor $(1-R_F)$ takes into account the contribution of Fresnel reflection from the output facet of the fiber. The percentage coupling efficiency is then defined by Eq. 2.1.36 as

$$C_{\%} = \frac{P_c}{P_{in}} \times 100. \tag{2.1.36}$$

2.1.5/ CHROMATIC DISPERSION

The response of a dielectric medium depends on the optical frequency ω when the bound electrons of that medium interact with an incident electromagnetic wave leading to different refractive index. Thus the phase velocity and group velocity will be also frequency dependant. This frequency dependence property of refractive index of a medium is known as chromatic dispersion. Medium's refractive index can be described using the Lorentz model [179, 247]. Far from the resonant frequency of the medium, one can calculate the refractive index of a material using the Sellmeier equation with the following form [29]

$$n^2(\lambda) = 1 + \sum_{j=1}^{k} \frac{A_j \lambda^2}{\lambda^2 - B_j^2}, \tag{2.1.37}$$

where n is the refractive index at wavelength λ, B_j is the material resonance wavelength and A_j is the strength of j^{th} resonance. The Sellmeier formula is one of the most accurate formula, when absorption is negligible, i.e., in the transparent region of the glass. It is capable of fitting the refractive index data to similar accuracy level of measured such data with currently available methods. It has been found that the necessary and sufficient value for satisfactorily fitting of almost all the practical materials within their transparency region is $k = 3$ [3, 5]. For soft glasses like heavy metal oxide (PbO-Bi_2O_3-Ga_2O_3-SiO_2-CdO) or chalcogenide (As_2S_3, As_2Se_3, GeAsSe), these parameters B_j and A_j had been reported in the previous literatures [152, 191, 216, 236].

The effective refractive index (n_{eff}) of the modes guided in a step-index fiber can be obtained by analysing the propagation mode using COMSOL software. Three types of beam propagation method (BPM) do exists, which are based on the fast Fourier transform (FFT)[17], finite difference method (FDM) [47] and finite element method (FEM) [47, 59], respectively. In particular, FEM is an efficient tool for the most general i.e., arbitrarily-shaped, inhomogeneous, dissipative, anisotropic, and nonlinear optical waveguide problem with advantage of renewing the finite element mesh at each propagation step according to the optical power distribution [53]. The commercial COMSOL software is based on finite element method. The basic equations that COMSOL uses are described here.

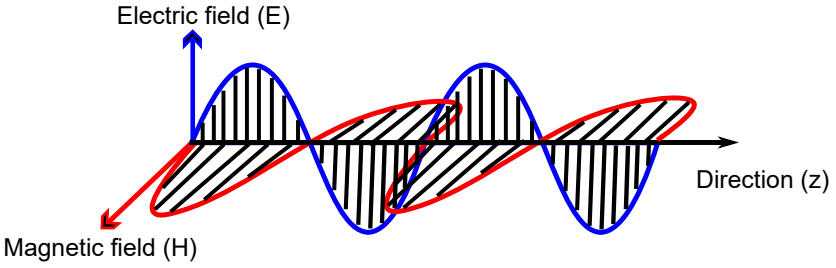

Figure 2.5: Propagation of electric and magnetic field (TEM modes).

In a 3D optical waveguide, the propagation of transverse electric and magnetic field along the propagation direction z is shown in Fig. 2.5. For a monochromatic wave with frequency ω and propagation constant β, the electric field ($\vec{E}$) and the magnetic field ($\vec{H}$) are given by

$$\vec{E}(x,y,z,t) = \vec{E}(x,y)e^{j(\omega t-\beta z)}, \qquad (2.1.38) \qquad \vec{H}(x,y,z,t) = \vec{H}(x,y)e^{j(\omega t-\beta z)}, \qquad (2.1.39)$$

where $\phi = \omega t - \beta z$ is the phase of the wave. When the relative permeability of the medium is constant, the Helmholtz's equation for the electric field can be expressed as

$$\nabla_\perp^2 E + (k^2 - \beta^2)E = 0, \quad \text{or,} \quad \nabla_\perp^2 E + k_0^2(\varepsilon_r - {n_{\text{eff}}}^2)E = 0, \qquad (2.1.40)$$

and for the magnetic field, the equation can be summarized as

$$\nabla_\perp^2 H + (k^2 - \beta^2)H = 0, \quad \text{or,} \quad \nabla_\perp^2 H + k_0^2(\varepsilon_r - {n_{\text{eff}}}^2)H = 0, \qquad (2.1.41)$$

where $\nabla_\perp^2 = \frac{\partial^2}{\partial x^2} + \frac{\partial^2}{\partial y^2}$. The optical waveguide has uniform structure along z direction which leads to $\frac{\partial}{\partial z} = -j\beta$. Furthermore, for the magnetic field, the eigenvalue of the equation can be obtained by deriving the Helmholtz's equation as

$$\nabla \times (n^{-2}\nabla \times H) - k_0^2 H = 0, \qquad (2.1.42)$$

where ∇ represents the Laplace operator. Here Helmholtz's equation is solved for the eigen value $\lambda = -j\beta$. The chromatic dispersion originates from both material dispersion and waveguide dispersion and effective refractive index (n_{eff}) is used to represent their combined effect. The effective refractive index of the modes in an optical waveguide is expressed by the ratio between the propagation constant β and the wavenumber in vacuum k_0 as

$$n_{\text{eff}} = \frac{\beta}{k_0}. \qquad (2.1.43)$$

Therefore, propagation constant β becomes

$$\beta = \frac{2\pi}{\lambda_0} n_{\text{eff}}, \qquad (2.1.44)$$

where λ_0 is the vacuum wavelength. The imaginary part of the effective refractive index obtained from the FEM analysis gives the confinement loss in the optical fiber. It is defined

as

$$\alpha_{\text{confinement}} = \frac{40\pi \times \text{Im}[n_{\text{eff}}]}{\lambda \times \ln(10)}. \tag{2.1.45}$$

Normally, the effect of chromatic dispersion on light propagation in an optical fiber is included by expanding the propagation constant β around some centre frequecy ω_0 as [131]

$$\beta(\omega) = \beta_0 + \beta_1(\omega - \omega_0) + \frac{1}{2}\beta_2(\omega - \omega_0)^2 + \frac{1}{6}\beta_3(\omega - \omega_0)^3 + ... + \frac{1}{m!}\beta_m(\omega - \omega_0)^m, \tag{2.1.46}$$

where

$$\beta_m = \left(\frac{d^m\beta}{d\omega^m}\right)_{\omega=\omega_0}, \qquad (m = 0, 1, 2, 3, ...). \tag{2.1.47}$$

The term β_0 in Eq. 2.1.46 represents the propagation constant at center frequency ω_0. The relationship between the parameters β_1 and β_2 with effective refractive index $n_{\text{eff}}(\omega)$ is given by

$$\beta_1 = \frac{1}{v_g} = \frac{1}{c}\left(n_{\text{eff}} + \omega\frac{dn_{\text{eff}}}{d\omega}\right), \tag{2.1.48}$$

$$\beta_2 = \frac{1}{c}\left(2\frac{dn_{\text{eff}}}{d\omega} + \omega\frac{d^2n_{\text{eff}}}{d\omega^2}\right). \tag{2.1.49}$$

The envelope of an optical pulse can be said to travel as a wave packet with group velocity v_g, which is the inverse of parameter β_1. The parameter β_2 is responsible for pulse broadening in optical fiber and known as group-velocity dispersion (GVD) parameter, which is often expressed through the dispersion parameter D, given by

$$D = \frac{d\beta_1}{d\lambda} = -\frac{2\pi c}{\lambda^2}\beta_2 = -\frac{\lambda}{c}\frac{d^2n_{\text{eff}}}{d\lambda^2}. \tag{2.1.50}$$

Figure 2.6 shows the variation of β_2 with wavelength λ for microstructured PCFs drawn from PBG81 glass (red curve), $Ge_{10}As_{22}Se_{68}$ glass (black curve), and $As_{38}Se_{62}$ glass (blue curve) using Eqs. 2.1.37 and 2.1.49. There are two types of dispersion depending on the sign of the GVD parameter:normal and anomalous. When $\beta_2 > 0$, the dispersion is known as normal in which low-frequency (red-shifted) components of an optical pulse travel faster than high-frequency (blue-shifted) components of the same pulse. The exact opposite phenomena occurs in anomalous dispersion when $\beta_2 < 0$. The wavelength at which $\beta_2 = 0$ is known as zero-dispersion wavelength (ZDW). However, at ZDW, effect of dispersion does not disappear completely. Therefore, inclusion of the parameter β_3 in Eq. 2.1.46, which is known as the third-order dispersion (TOD) parameter, is necessary for pulse propagation near ZDW and it is responsible for asymmetric pulse broadening [131]. The third-order dispersion has an important impact on SC generation of introducing a perturbation to the stability of solitary waves, known as solitons, which then break-up and generate resonant radiation, known as dispersive waves (DW) [128].

It is evident from chromatic dispersion that due to group velocity mismatch, pulses at different wavelength travel at different speed inside a fiber. This feature leads to a

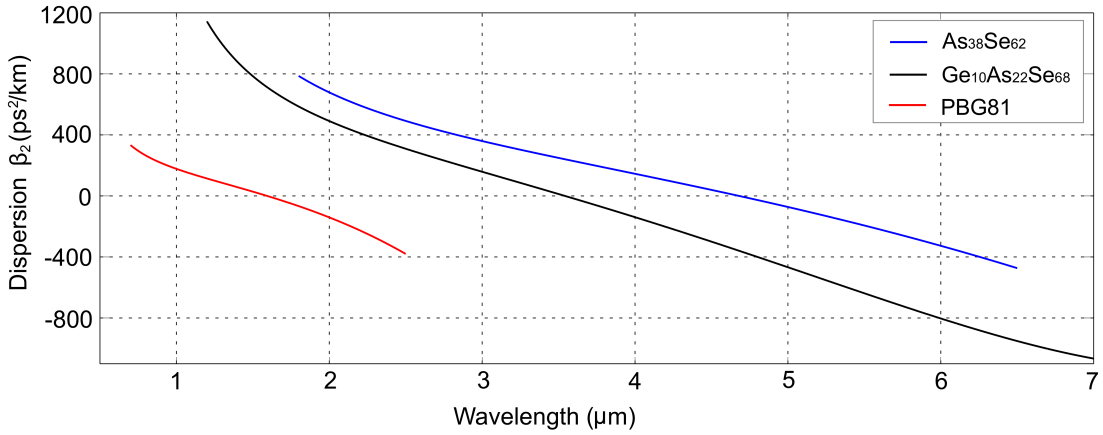

Figure 2.6: Variation of numerically computed group-velocity dispersion parameter β_2 with wavelength. Red curve:suspended-core PCF from PBG81 glass with 4.3 μm core diameter (described in Chapter 3), black curve:microstructured PCF from $Ge_{10}As_{22}Se_{68}$ glass with 6 μm core diameter (described in Chapter 4), and blue curve:microstructured PCF from $As_{38}Se_{62}$ glass with 8.11 μm core diameter (described in Chapter 4).

walk-off effect, which affects nonlinear interaction between two optical pulses in a way such that when the faster moving pulse completely walk through the slower pulse, the nonlinear interaction between them disappears. The propagation length after which the pulse interaction becomes negligible is known as walk-off length L_W, which is defined by the following Eq. 2.1.51 for pulses with width T_0 as [131]

$$L_W = \frac{T_0}{|\beta_1(\omega_2) - \beta_1(\omega_1)|}, \tag{2.1.51}$$

where ω_1 and ω_2 are the center frequencies of two pulses and the parameter β_1 at these frequencies are calculated using Eq. 2.1.48. Another characteristic length scale from the impact of dispersion that should be mentioned here is the dispersion length L_D, which is defined by the relation

$$L_D = \frac{T_0^2}{|\beta_2|}. \tag{2.1.52}$$

It describes the length of a fiber over which dispersion causes a pulse with width T_0 to broaden by a factor of $\sqrt{2}$.

2.1.6/ Polarization-mode dispersion

A single-mode fiber, not being truly single mode, can support two orthogonally polarized degenerate modes, which do not couple with each other when excited under ideal conditions like perfect cylindrical symmetry and absence of fiber stress. However, in real fiber with random variation of core shape along its length, two degenerate modes polarized in orthogonal x and y directions mix with each other having different propagation constant β due to the modal birefringence or phase birefringence B_{phase}, whose strength is defined

by [131]

$$B_{\text{phase}}(\lambda) = \frac{|\beta_x(\lambda) - \beta_y(\lambda)|}{k_0} = \left| n^x_{\text{eff}}(\lambda) - n^y_{\text{eff}}(\lambda) \right|, \tag{2.1.53}$$

where $n^x_{\text{eff}}(\lambda)$ and $n^y_{\text{eff}}(\lambda)$ are the effective refractive indices of x-polarized and y-polarized states. The axis with larger and smaller mode effective refractive index are known as slow axis and fast axis, respectively. The group birefringence can be expressed as [176]

$$B_{\text{group}}(\lambda) = B_{\text{phase}}(\lambda) - \lambda \frac{dB_{\text{phase}}(\lambda)}{d\lambda}. \tag{2.1.54}$$

The difference between group and phase birefringence is often neglected except for elliptical core fiber where the difference is quite significant and hence, both birefringence are measured to characterize the fiber [22, 34]. Two orthogonal modes exchange their power in a periodic fashion while propagating inside a fiber with beat length L_B, which is given by [131]

$$L_B = \frac{2\pi}{|\beta_x(\lambda) - \beta_y(\lambda)|} = \frac{\lambda}{B_{\text{phase}}(\lambda)}. \tag{2.1.55}$$

In a standard optical fiber, when an optical pulse is excited, random change in phase birefringence broadens the pulse at the output as both orthogonal components of that pulse having different group velocities travel with different speed along the fiber. This phenomena is known as polarization-mode dispersion (PMD). For an optical fiber with length L and a constant phase birefringence B_{phase}, the amount of pulse broadening can be obtained from the time delay between two orthogonally polarization components of the optical pulse, also know as differential group delay (DGD), which is defined as

$$\text{DGD} = L|\beta_{1x} - \beta_{1y}| = L(\Delta\beta_1), \tag{2.1.56}$$

where $\Delta\beta_1$ is related to group-velocity mismatch. Eq. 2.1.56 can be used to estimate PMD only for short length fibers and fibers which maintain the initial polarization of incident light. For fibers which do not maintain polarization, DGD is proportional to $\sqrt{L}$ for $L > 0.1$ km. PMD can be minimized using polarization-maintaining or polarization-preserving fibers [19, 23, 44, 77, 81]. The polarization-maintaining fibers are discussed in details in Chapter 4.

2.1.7/ DISPERSIVE PULSE PROPAGATION

In the solution to the Helmholtz equation expressed in Eq. 2.1.22 in Section 2.1.2, we assumed the amplitude term $\tilde{A}(z, \omega)$ to be slowly varying function of z compared to the carrier frequency. In the time domain, slowly varying approximation represents the condition in which the carrier frequency is higher than the bandwidth of the optical field. Therefore, $\partial^2\tilde{A}/\partial z^2$ can be neglected and it leads to [131]

$$2i\beta_0 \frac{\partial \tilde{A}}{\partial z} + (\beta^2 - \beta_0^2)\tilde{A} = 0. \tag{2.1.57}$$

Using the approximation $\beta^2 - \beta_0^2 = 2\beta_0(\beta - \beta_0)$, Eq. 2.1.57 can be written as [131]

$$\frac{\partial \tilde{A}}{\partial z} = i[\beta(\omega) - \beta_0]\tilde{A}. \tag{2.1.58}$$

Now we return to the time domain by performing inverse Fourier transform of Eq. 2.1.58 in order to obtain the propagation equation for $A(z,t)$. If we include the Taylor series expansion term of propagation constant β (as shown in Eq. 2.1.46) up to second order, which means β_0 vanishes, and considering the losses (α) in fiber, Eq. 2.1.58 for linear propagation therefore becomes

$$\frac{\partial A}{\partial z} = -\frac{\alpha}{2}A - \beta_1\frac{\partial A}{\partial t} - \frac{i\beta_2}{2}\frac{\partial^2 A}{\partial t^2}. \tag{2.1.59}$$

Eq. 2.1.59 can be used to demonstrate the effect of GVD on optical pulse propagating in a linear dispersive medium. Therefore, in a retarded time frame moving with the pulse at the group velocity ($T = t - z/v_g = t - \beta_1 z$), Eq. 2.1.59 for lossless propagation becomes

$$\frac{\partial A}{\partial z} = -\frac{i\beta_2}{2}\frac{\partial^2 A}{\partial T^2}. \tag{2.1.60}$$

Eq. 2.1.60 is solved in the frequency domain by using Fourier transform method. Fourier transform (FT) of $A(z,T)$ is $\tilde{A}(z,\omega)$ such that

$$A(z,T) = \frac{1}{2\pi}\int_{-\infty}^{\infty}\tilde{A}(z,\omega)\exp(-i\omega T)d\omega, \tag{2.1.61}$$

which leads to $\partial^2 A/\partial T^2 = \mathrm{FT}(-\omega^2\tilde{A})$. Therefore, in frequency domain, Eq. 2.1.60 becomes

$$\frac{\partial \tilde{A}}{\partial z} = \frac{i\beta_2}{2}\omega^2\tilde{A}, \tag{2.1.62}$$

with the following solution,

$$\tilde{A}(z,\omega) = \exp\left(\frac{i\beta_2}{2}\omega^2 z\right)\tilde{A}(0,\omega). \tag{2.1.63}$$

From Eq.2.1.63, it can be seen that the effect of GVD is to impose a phase shift on the spectral component of the pulse depending on both the frequency and propagation length. Although this kind of phase change does not affect the spectral shape of the pulse, however, it can modify the temporal shape of the pulse. Therefore, the general solution for Eq. 2.1.60 becomes

$$A(z,T) = \frac{1}{2\pi}\int_{-\infty}^{\infty}\tilde{A}(0,\omega)\exp\left(\frac{i}{2}\beta_2\omega^2 z - i\omega T\right)d\omega, \tag{2.1.64}$$

where $\tilde{A}(0,\omega)$, which is the FT of the incident field (at $z = 0$), can be obtained as

$$\tilde{A}(0,\omega) = \int_{-\infty}^{\infty}A(0,T)\exp(i\omega T)dT. \tag{2.1.65}$$

Eq. 2.1.64 may be used for any input pulses of arbitrary shapes. However, in this thesis, we have worked with only Gaussian pulses. For a Gaussian pulse, the incident field can

be written as

$$A(0,T) = \exp\left(-\frac{T^2}{2T_0^2}\right), \tag{2.1.66}$$

where T_0 is pulse's half-width ($1/e$ of maximum $|A|^2$). It is related to full-width at half-maximum (FWHM) by the following relation

$$\Delta T = T_{\text{FWHM}} = 2(ln2)^{1/2}T_0 \approx 1.665T_0. \tag{2.1.67}$$

If we use Eqs. 2.1.65 and 2.1.66 on Eq. 2.1.64 and perform integration over ω using the following identity [136],

$$\int_{-\infty}^{\infty} \exp(-ax^2 + bx)dx = \sqrt{\frac{\pi}{a}}\exp\left(\frac{b^2}{4a}\right), \tag{2.1.68}$$

the amplitude $A(z,T)$ at a certain point z along the fiber length can be written as

$$A(z,T) = \frac{T_0}{(T_0^2 - i\beta_2 z)^{1/2}}\exp\left[-\frac{T^2}{2(T_0^2 - i\beta_2 z)}\right]. \tag{2.1.69}$$

Eq. 2.1.70 shows that a propagating Gaussian pulse maintains its shape. However, the width T_1 of the Gaussian pulse broadens with z due to GVD as given by

$$T_1(z) = T_0[1 + (z/L_D)^2]^{1/2}, \tag{2.1.70}$$

where L_D is the dispersion length described in Eq. 2.1.52. For a Gaussian pulse having

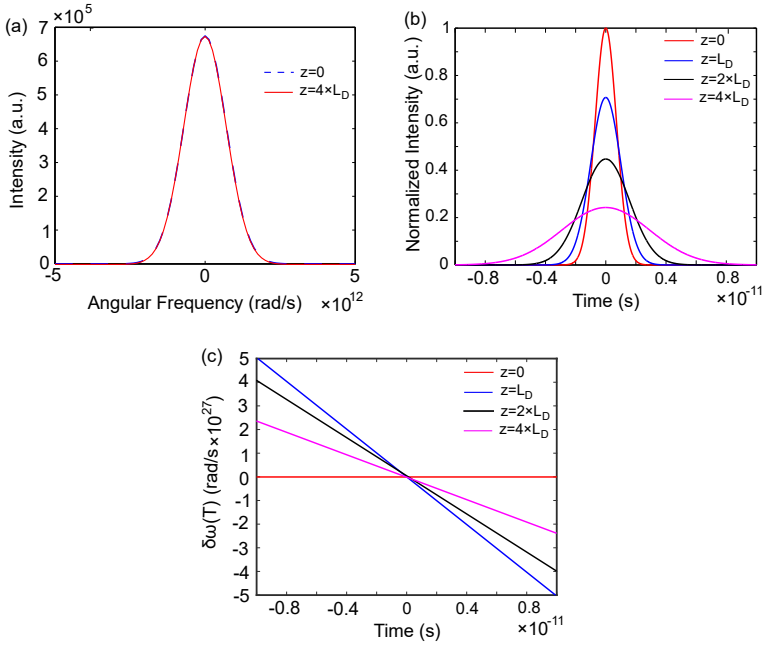

Figure 2.7: (a) Calculated spectrum of a 1 ps Gaussian pulse before and after propagating a distance $z = 4 \times L_D$, demonstrating the preservation of its spectral shape. (b) Normalized intensity $|A|^2$, showing the temporal pulse broadening and (c) frequency chirp $\delta\omega/\delta t$ as a function of time for $z = 0$, $z = L_D$, $z = 2 \times L_D$, and $z = 4 \times L_D$.

a pulse width $T_0 = 1$ ps, pulse intensity $|A|^2$ and spectrum was calculated at different propagating length along z at zero and four times the dispersion length. The preservation of spectral shape of the Gaussian pulse is shown in Fig. 2.7(a). Figure 2.7(b) shows the extent of dispersion induced broadening of its temporal shape. The fiber imposes a linear frequency chirp across the broadened pulse as shown in Fig. 2.7(c), which is calculated using the following [131]

$$\delta\omega(T) = \frac{sgn(\beta_2)(z/L_D)}{1+(z/L_D)^2}\frac{T}{T_0^2}. \tag{2.1.71}$$

2.2/ NONLINEAR EFFECTS

This section provides a brief introduction into the basic nonlinear-optical phenomena in optical medium. The area of nonlinear optics is related to the analysis of the interaction between light and matter where the material's response to the applied field in nonlinear. Propagation of high-intensity light beam through an optical medium results in some incredible physical phenomena, known as nonlinear optical effects. The typical properties of a nonlinear medium, such as absorption and refractive index, can be altered due to the intense pump beam. The interaction of light with the nonlinear medium leads to a complex coupling between the spectral and spatial components of light through the optical medium. Optical fibers have been accepted as an ideal optical medium due to their strong light confinement capabilities. These nonlinear effects have been exploited in optical fibers for all-optical processing applications in telecommunication and fiber laser industries. The nonlinear effects in optical fiber can occur in two ways. The first one is due to instantaneous intensity dependence of the refractive index of the medium from the distortion of electronic structure of the molecules of fiber material. The second one is due to the inelastic-scattering phenomenon. They will be discussed in details in this section.

The bandwidth of supercontinuum generation is related to the nonlinear response of a dielectric material to an applied electric field with high optical intensity, for example high power laser pulses. Furthermore, a time varying polarization acts as the source of new components of electromagnetic field. Nonlinear wave equation for an isotropic material can be written as [143]

$$\nabla^2\vec{E} - \frac{\epsilon_r}{c^2}\frac{\partial^2\vec{E}}{\partial t^2} = \frac{1}{\epsilon_0 c^2}\frac{\partial^2\vec{P_{NL}}}{\partial t^2}, \tag{2.2.1}$$

where ϵ_r is the dimensionless relative permittivity of the material. As it is discussed earlier in Eq. 2.1.10 that the induced polarization ($\vec{P}$) is a combination of linear ($\vec{P}_L$) and nonlinear ($\vec{P}_{NL}$) contribution from $\chi^{(1)}$ and $\chi^{(3)}$, respectively, therefore, $\vec{P}_{NL}$ can be expressed in terms of electric field as [131]

$$\vec{P}_{NL}(\vec{r},t) = \epsilon_0 \iiint_{-\infty}^{t} \chi^{(3)}(t-t_1, t-t_2, t-t_3) \vdots \vec{E}(\vec{r},t_1)\vec{E}(\vec{r},t_2)\vec{E}(\vec{r},t_3)dt_1dt_2dt_3. \tag{2.2.2}$$

Eq. 2.2.2 provides a general description of third-order nonlinear effects in optical fibers. Due to its complexity, it is necessary to assume the nonlinear response to be instantaneous and also only from electronic origin as the electron's response to optical field is faster than that of nuclei. Therefore, the third-order nonlinear polarization $\vec{P}^{(3)}$, when the

rapidly varying part of electric field is separated as in Eq. 2.1.21, becomes [131]

$$\vec{P}^{(3)} = \epsilon_0 \chi^{(3)} \frac{1}{8} [\vec{E}_1 \exp(-i\omega_1 t) + \vec{E}_2 \exp(-i\omega_2 t) + \vec{E}_3 \exp(-i\omega_3 t) + c.c.]^3, \tag{2.2.3}$$

where ω_1, ω_2, and ω_3 are the three frequency components of applied electric field. Expansion of Eq. 2.2.3 leads to a large number of combination terms, 44 different frequency components to be exact if the negative and positive frequencies are considered to be distinct. All of these 44 terms are not shown in this thesis explicitly as they are long, however, it is possible to find them in most of the general nonlinear optics books like ref [143]. These terms describe multiple nonlinear processes, including: the optical Kerr effect, which is responsible for self-phase modulation (SPM) [18, 131], cross-phase modulation (XPM) [131], four-wave mixing (FWM) [131], and third harmonic generation (THG) [56] and the last two processes require phase-matching to be efficient [56, 131]. All these processes are termed as elastic nonlinear processes, which correspond to photon-photon interactions where total energy remains constant because of the absence of any kind of energy exchange between the medium and the electric field. On the other hand, inelastic nonlinear processes correspond to photon-phonon interactions in which a small portion of optical energy is converted into phonon energy. Such effects include Raman and Brillouin scattering [131]. Since, in the assumption of instantaneous nonlinear response earlier, we neglected the contribution of molecular vibration to $\chi^{(3)}$, therefore, Eq. 2.2.3 does not include those inelastic processes like Raman or Brillouin scattering, but will be introduced later in the chapter. All the above mentioned nonlinear processes are described separately in the following sections except THG and Brillouin scattering, which have negligible effects in short-pulsed SC generation in optical fibers due to phase matching requirements and long electrostrictive response time [143], respectively.

2.2.1/ KERR EFFECT AND THE NONLINEAR SCHRÖDINGER EQUATION

Most of the nonlinear effects in optical fibers originate from nonlinear refraction, which is also known as the optical Kerr effect. It is a phenomenon that refers to the intensity dependance of refractive index, i.e., the change in refractive index caused by a high optical intensity, I. In such conditions, the refractive index of an optical material can be written as [131, 143]

$$n(\omega, I) = n_L(\omega) + n_2^I I = n_L(\omega) + n_2 |\vec{E}|^2, \tag{2.2.4}$$

where n_L is the linear part of the refractive index given by Eq. 2.1.37, $I = (n\epsilon_0 c_0 |\vec{E}|^2)/2$ is the optical intensity inside the fiber, and n_2 represents the nonlinear index coefficient, which is directly related to real (Re) part of $\chi^{(3)}$. For a linearly polarized electric field and assuming $\chi^{(3)}$ contains only one component in its tensor, n_2 and n_2^I can be calculated from $\chi^{(3)}$ using the following relations as [131]

$$n_2^I = \frac{3}{4n_L^2 \epsilon_0 c_0} \mathrm{Re}(\chi^{(3)}) \quad \text{and} \quad n_2 = \frac{3}{8n_L} \mathrm{Re}(\chi^{(3)}). \tag{2.2.5}$$

Nonlinear refraction can be included in Eq. 2.1.59 by considering the Kerr effect as a small perturbation Δn to the refractive index that is given by

$$\Delta n = n_2 |\vec{E}|^2 + \frac{i\tilde{\alpha}}{2k_0}, \tag{2.2.6}$$

where $\tilde{\alpha}$ is the intensity dependent absorption coefficient. If we neglect losses, then second term on the right hand side of Eq. 2.2.6 disappears. According to the first-order perturbation theory [2], Δn does not affect the modal distribution $F(x,y)$. However, it modifies the propagation constant as [131]

$$\tilde{\beta}(\omega) = \beta(\omega) + \Delta\beta(\omega), \tag{2.2.7}$$

where

$$\Delta\beta(\omega) = \frac{\omega^2 n(\omega)}{c^2\beta(\omega)} \frac{\iint_{-\infty}^{\infty} \Delta n(\omega)|F(x,y)|^2 dxdy}{\iint_{-\infty}^{\infty} |F(x,y)|^2 dxdy}. \tag{2.2.8}$$

Due to the quasi-monochromatic assumption ($\Delta\omega \ll \omega_0$), Taylor expansion of $\Delta\beta$ can be omitted and the perturbation reduces to $\Delta\beta \approx \Delta\beta_0$. Therefore, Eq. 2.1.59 becomes

$$\frac{\partial A}{\partial z} + \frac{\alpha}{2}A + \beta_1\frac{\partial A}{\partial t} + \frac{i\beta_2}{2}\frac{\partial^2 A}{\partial t^2} = i\Delta\beta_0 A. \tag{2.2.9}$$

Now using Eq. 2.2.6 and $\beta(\omega) \approx n(\omega)\omega/c$ and assuming that $F(x,y)$ in Eq. 2.2.8 does not vary much over the bandwidth of the pulse, then the perturbation is further reduced to

$$\Delta\beta_0(\omega) = \gamma|A|^2, \tag{2.2.10}$$

where the nonlinear parameter γ can be defined by

$$\gamma = \frac{n_2^I \omega_0}{cA_{\text{eff}}}. \tag{2.2.11}$$

The parameter A_{eff} represents the effective mode area as defined in Eq. 2.1.23. Therefore, for lossless propagation and using the transformation $T = t - \beta_1 z$, Eq. 2.2.9 can be written as

$$\frac{\partial A}{\partial z} + \frac{i\beta_2}{2}\frac{\partial^2 A}{\partial T^2} = i\gamma|A|^2 A. \tag{2.2.12}$$

The pulse propagation Eq. 2.2.12 is referred to as the nonlinear Schrödinger equation (NLSE) as it resembles the Schrödinger equation with a nonlinear potential.

Another consequence of the Kerr effect is the intensity dependence of the group velocity that leads to the phenomena of self-steepening and optical shock wave formation [6, 12]. The intensity dependence of group velocity causes the peak of the pulse to slow down more than the edges of the pulse, leading to steepening of the trailing edge of the pulse. When the edge becomes infinitely steep, the intensity changes instantaneously, and eventually it leads to form an optical shock wave and wave-breaking. However, optical shocks with an infinitely sharp trailing edge never occur in practice as group velocity dispersion acts against the steepening, and therefore, it requires numerical simulations to investigate further. Self-steepening also affects self-phase modulation induced spectral broadening, which will be discussed in Section 2.2.2. Blue frequency components broadens more than the red ones when self-steepening is combined with SPM. Self-steepening also substantially reduces process like soliton self-frequency shift (will be discussed in Section 2.2.6) due to the decrease of the nonlinearity as the center wavelength of the soliton shifts towards the red. Self-steepening will be included into the NLSE in Section

2.2.7.

2.2.2/ SELF-PHASE MODULATION AND CROSS-PHASE MODULATION

Self-phase modulation (SPM) is a phenomenon that leads to spectral broadening of optical pulses. It refers to the self-induced nonlinear phase shift over the temporal envelope that an optical pulse experiences from the nonlinear refractive index of the fiber through which it propagates [7, 13, 16, 18]. The accumulated phase of a propagating pulse over a fiber length L due to nonlinear refraction is given by [131]

$$\phi = \frac{2\pi}{\lambda_0} nL = (n_L + n_2^I I)\frac{2\pi}{\lambda_0} L. \tag{2.2.13}$$

Therefore, the intensity dependent nonlinear phase-shift induced by SPM becomes,

$$\phi_{NL} = \frac{2\pi}{\lambda_0} L n_2^I I = \gamma P_0 L, \tag{2.2.14}$$

where P_0 is the peak power of the pulse and γ is the nonlinear coefficient, defined in Eq. 2.2.11. Due to its time-dependence, this nonlinear phase-shift translates into broadening of the optical spectrum as the pulse propagates inside the fiber. However, the temporal pulse shape remains unaffected by SPM. The effective propagation distance at which the maximum phase-shift becomes equals to 1 is known as nonlinear length (L_{NL}). It is defined as

$$L_{NL} = \frac{1}{\gamma P_0}. \tag{2.2.15}$$

The spectral content of the transmitted pulse can be intuitively described by introducing the concept of the instantaneous frequency $\omega(t)$, i.e., the frequency of the pulse at a specific time instance of the pulse envelope. SPM leads to a shift in the instantaneous frequency, which is described by [143]

$$\omega(T) = \omega_0 + \delta\omega(T), \tag{2.2.16}$$

where

$$\delta\omega(T) = -\frac{\partial \phi_{NL}}{\partial T} \tag{2.2.17}$$

represents the variation of the instantaneous frequency. The minus sign is due to the choice of the factor $\exp(-i\omega_0 t)$ in Eq. 2.1.21. At the leading edge of the pulse, intensity and nonlinear phase increase which in turn decrease the instantaneous frequency and vice versa for the trailing edge. The time dependence of the variation of instantaneous frequency ($\delta\omega$) is referred to as frequency chirping. The nonlinear frequency chirp induced by SPM continuously generates new frequency components, therefore, producing a symmetric spectral broadening as the pulse propagates along the fiber [166]. The SPM-induced chirp $\delta\omega(T)$ for a Gaussian pulse of the form $P = P_0 \exp(-T^2/T_0^2)$ is given by [131]

$$\delta\omega(T) = \frac{2T}{T_0^2}\frac{L_{\text{eff}}}{L_{NL}} \exp\left(-\frac{T^2}{T_0^2}\right), \tag{2.2.18}$$

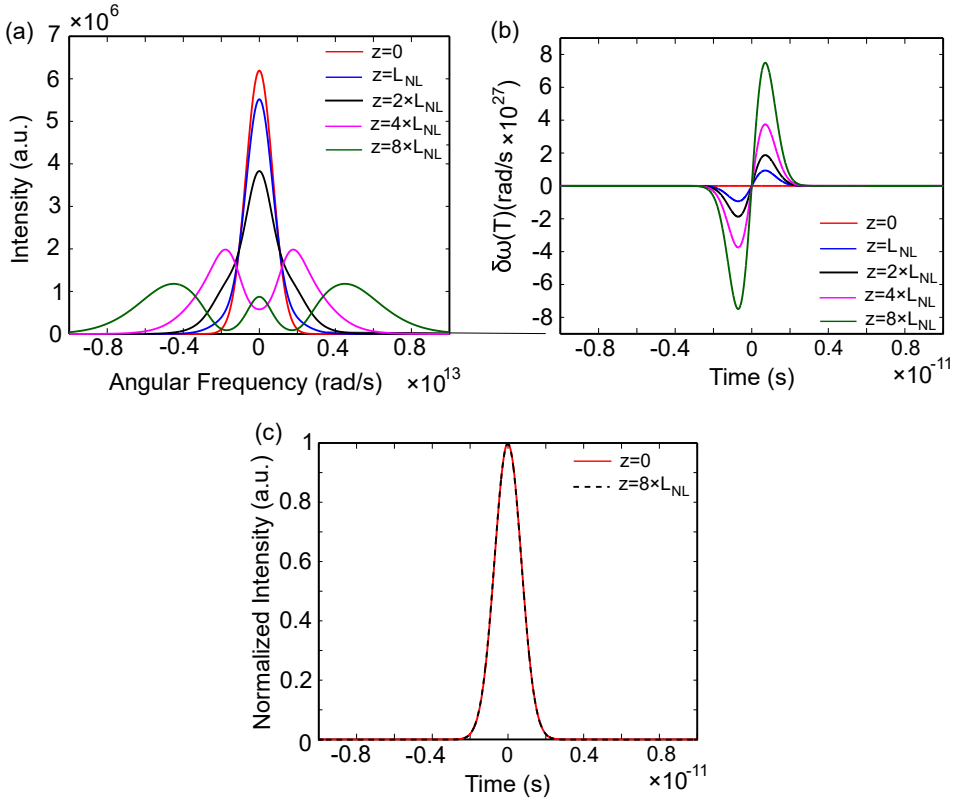

Figure 2.8: (a) Illustration of SPM-induced spectral broadening of a 1 ps Gaussian pulse with increasing propagation length from $z = 0$ to $z = 8 \times L_{NL}$ in an optical fiber. (b) Demonstration of the evolution of frequency chirp $\delta\omega(T)$ over the pulse envelope with increasing propagation length from $z = 0$ to $z = 8 \times L_{NL}$. (c) Preservation of the temporal shape of the pulse during propagation.

where $L_{\text{eff}} = [1 - \exp(-\alpha L)]/\alpha$ is the effective length, which becomes equals to fiber length L in the absence of fiber losses. The chirp of SPM can also be comparable to positive GVD, where shorter wavelength components of the spectrum are shifted towards the trailing edge of the pulse. By solving Eq. 2.2.12 with $\beta_2 = 0$, the SPM-induced spectral broadening and frequency chirp of a 1 ps Gaussian pulse with propagation distance in an optical fiber are illustrated in Figs. 2.8(a) & (b), respectively. The preservation of temporal shape of the pulse is shown in Fig. 2.8(c). As discussed earlier, self-steepening leads to an asymmetry in SPM-induced spectral broadening of ultrashort pulses [30, 31]. The effect of self-steepening (s) is defined by [131]

$$s = \frac{1}{\omega_0 T_0}, \tag{2.2.19}$$

where T_0 and ω_0 are initial pulse width and central frequency, respectively. The shock time scale is defined as $\tau_{\text{shock}} = \tau_0 = 1/\omega_0$. The distance at which the shock is formed can be obtained as

$$z_s = \left(\frac{e}{2}\right)^{1/2} \frac{L_{NL}}{3s}. \tag{2.2.20}$$

As a result, for femtosecond pulses, a significant amount of self-steepening of the pulse can occur in few-cm long nonlinear fiber. It is noted that, additional dispersion of the nonlinearity arises from the frequency dependence of the effective area of the mode A_{eff}, which is defined in Eq. 2.1.23 [48, 101, 117]. The frequency dependence of A_{eff} can be included to first order through a simple correction to the value of shock time scale τ_{shock}. Therefore, the corrected τ_{shock} becomes [42, 83, 122]

$$\tau_{\text{shock}} = \tau_0 - \left[\frac{1}{n_{\text{eff}}(\omega)}\frac{dn_{\text{eff}}(\omega)}{d\omega}\right]_{\omega_0} - \left[\frac{1}{A_{\text{eff}}(\omega)}\frac{dA_{\text{eff}}(\omega)}{d\omega}\right]_{\omega_0}. \tag{2.2.21}$$

Eq. 2.2.21 is obtained by neglecting the frequency dependence of the nonlinear refractive index n_2 [122]. The term in Eq. 2.2.21 that is dependent on the frequency derivative of n_{eff} can be neglected because the frequency dependence of n_{eff} is typically very small compared to that of the effective area. Furthermore, in a single-mode fiber, it seems clear that the effective mode area decreases with increasing frequency, which means $[dA_{\text{eff}}(\omega)/d\omega]_{\omega_0} < 0$. Therefore, the effective mode area correction quantitatively increases the τ_{shock} and it leads to a proportional increase in the dispersion of the nonlinear response.

Cross-phase modulation (XPM) refers to the nonlinear phase-shift of an optical pulse induced by another pulse with different wavelength that are overlapping in time. Therefore, Eq. 2.2.3 can be written in a modified form for two co-propagating pulses with carrier frequencies ω_1 and ω_2 as [131]

$$\vec{P}^{(3)} = \epsilon_0\chi^{(3)}\frac{1}{8}[\vec{E_1}\exp(-i\omega_1 t) + \vec{E_2}\exp(-i\omega_2 t) + c.c.]^3. \tag{2.2.22}$$

Expansion of Eq. 2.2.22 gives the following terms [131, 143],

$$\vec{P}^{(3)}(\omega_1) = \frac{\epsilon_0\chi^{(3)}}{8}(3\vec{E_1}\vec{E_1^*} + 6\vec{E_2}\vec{E_2^*})\vec{E_1} = \chi^{(3)}_{eff}(|\vec{E_1}|^2 + 2|\vec{E_2}|^2)\vec{E_1}, \tag{2.2.23}$$

$$\vec{P}^{(3)}(\omega_2) = \frac{\epsilon_0\chi^{(3)}}{8}(3\vec{E_2}\vec{E_2^*} + 6\vec{E_1}\vec{E_1^*})\vec{E_2} = \chi^{(3)}_{eff}(|\vec{E_2}|^2 + 2|\vec{E_1}|^2)\vec{E_2}, \tag{2.2.24}$$

$$\vec{P}^{(3)}(3\omega_1) = \frac{\chi^{(3)}_{eff}}{3}\vec{E_1}^3, \tag{2.2.25}$$

$$\vec{P}^{(3)}(3\omega_2) = \frac{\chi^{(3)}_{eff}}{3}\vec{E_2}^3, \tag{2.2.26}$$

$$\begin{aligned}\vec{P}^{(3)}(2\omega_1 + \omega_2) &= \chi^{(3)}_{eff}\vec{E_1}^2\vec{E_2},\\ \vec{P}^{(3)}(2\omega_1 - \omega_2) &= \chi^{(3)}_{eff}\vec{E_1}^2\vec{E_2}^*,\end{aligned} \tag{2.2.27}$$

$$\begin{aligned}\vec{P}^{(3)}(2\omega_2 + \omega_1) &= \chi^{(3)}_{eff}\vec{E_1}\vec{E_2}^2,\\ \vec{P}^{(3)}(2\omega_2 - \omega_1) &= \chi^{(3)}_{eff}\vec{E_1}^*\vec{E_2}^2,\end{aligned} \tag{2.2.28}$$

where $\chi^{(3)}_{eff} = (3\epsilon_0/8)\chi^{(3)}$ acts as an effective nonlinear parameter. Neglecting all the four terms (Eqs. 2.2.25- 2.2.28) that generate polarization at frequencies other than ω_1 and ω_2 because of their strong phase-mismatch, only two terms (Eqs. 2.2.23- 2.2.24)

with exclusively ω_1 and ω_2 are considered here. The two terms on the right hand side of Eqs. 2.2.23- 2.2.24 are due to SPM and XPM, respectively. Therefore, the induced nonlinear phase-shift of the two pulses can be expressed as [131]

$$\begin{aligned}\phi_{NL,\omega_1} &= k_0 L n_2^I(|\vec{E_1}|^2 + 2|\vec{E_2}|^2) = \gamma L(P_1 + 2P_2),\\ \phi_{NL,\omega_2} &= k_0 L n_2^I(|\vec{E_2}|^2 + 2|\vec{E_1}|^2) = \gamma L(P_2 + 2P_1),\end{aligned} \tag{2.2.29}$$

where P_1 and P_2 are the peak powers of the two pulses at frequency ω_1 and ω_2, respectively. From Eq. 2.2.29, the contribution of XPM to nonlinear phase-shift is seen to be twice that of SPM. Furthermore, XPM is also responsible for asymmetric spectral broadening of co-propagating pulses in optical fiber because of dispersion-induced pulse walk-off.

Degenerate cross-phase modulation (DXPM) occurs between the two orthogonal polarization components associated with a single-frequency optical wave [58]. For an arbitrary polarized optical wave, the electric field can be expressed as

$$\vec{E}(\vec{r},t) = \frac{1}{2}[\hat{x}E_x + \hat{y}E_y]\exp(-i\omega_0 t) + c.c., \tag{2.2.30}$$

where E_x and E_y are the complex amplitudes of the polarization components of the field and the longitudinal component E_z is neglected for being small compared to E_x and E_y. Therefore, the induced polarization's nonlinear part P_{NL} may be written as [131]

$$P_{NL}(\vec{r},t) = \frac{1}{2}[\hat{x}P_x + \hat{y}P_y]\exp(-i\omega_0 t) + c.c., \tag{2.2.31}$$

where

$$P_x = \frac{3\epsilon_0\chi^{(3)}}{4}\left[\left(|E_x|^2 + \frac{2}{3}|E_y|^2\right)E_x + \frac{1}{3}(E_x^* E_y)E_y\right], \tag{2.2.32}$$

$$P_y = \frac{3\epsilon_0\chi^{(3)}}{4}\left[\left(|E_y|^2 + \frac{2}{3}|E_x|^2\right)E_y + \frac{1}{3}(E_y^* E_x)E_x\right], \tag{2.2.33}$$

where the last term in Eqs. 2.2.32 and 2.2.33 leads to vector four-wave mixing process, which is discussed in the next section. XPM will be further explained in Section 2.2.6 during the discussion of soliton dynamics.

2.2.3/ FOUR-WAVE MIXING

From the expansion of Eq. 2.2.22, the four neglected terms (Eqs. 2.2.25- 2.2.28), which contain either third harmonics or combination of ω_1 and ω_2, represent four-wave mixing (FWM). FWM is a third-order nonlinear parametric recombination process, where two or more pump photons at one or more frequencies are annihilated to create photons at new frequencies through the third-order susceptibility $\chi^{(3)}$ while conserving the net momentum and energy during the parametric interaction [15, 27, 56, 131]. In addition, the nonlinear change on the refractive index of the material would also impact the momentum of the system. Here, momentum and energy of photons can be treated as propagation constant and angular frequency, respectively. Therefore, this process requires matching of both frequency and wave vector between four interacting waves. The latter requirement is known as phase matching. Significant FWM occurs only if phase-mismatch nearly vanishes. There are two types of phase matched FWM. In the first one, three photons

at frequencies ω_1, ω_2, and ω_3 transfer their energy to a single photon at the frequency $\omega_4 = \omega_1 + \omega_2 + \omega_3$. This term is responsible for THG ($\omega_1 = \omega_2 = \omega_3$) or frequency conversion ($\omega_1 = \omega_2 \neq \omega_3$). However, due to dispersion walk-off in this process, it is difficult to satisfy the phase matching with $\Delta\beta = \beta_{\omega_1} + \beta_{\omega_2} + \beta_{\omega_3} - \beta_{\omega_4} = 0$. In the second case, two photons at frequencies ω_1 and ω_2 are annihilated and simultaneously two new photons at frequencies ω_3 and ω_4 are generated such that $\omega_3 + \omega_4 = \omega_1 + \omega_2$. It is easier to satisfy the phase matching in this process since the requirement is $\Delta\beta = \beta_{\omega_3} + \beta_{\omega_4} - \beta_{\omega_1} - \beta_{\omega_2} = 0$ [131].

Figure 2.9 demonstrates the degenerate four-wave mixing (DFWM) case of $\omega_1 = \omega_2$, which is the most relevant to SC generation. This process is also very interesting as FWM here can be initiated with a strong single pump beam at frequency ω_p that creates two sidebands located symmetrically at frequencies ω_s (signal) and ω_i (idler) with a frequency shift Ω_s, given by [131]

$$\Omega_s = \omega_p - \omega_s = \omega_i - \omega_p. \tag{2.2.34}$$

The low and high frequency sidebands at ω_s and ω_i are referred to as the Stokes and

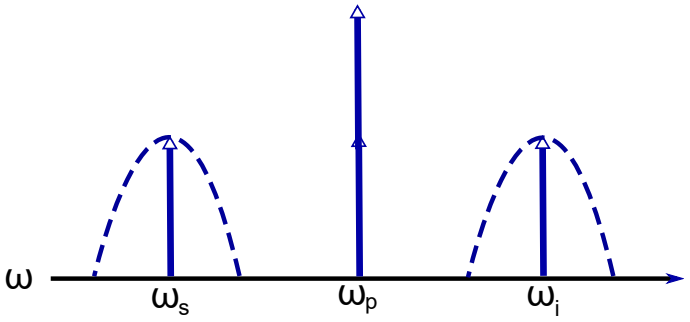

Figure 2.9: Illustration of DFWM where two pump photons at frequency ω_p are annihilated and two photons are simultaneously generated at signal (ω_s) and idler (ω_i) frequencies. The dashed curves illustrate the formation of lobes by the gain versus signal wavelength due to the non-zero peak gain at $\Delta\beta \neq 0$.

anti-Stokes bands, respectively. The requirement for phase matching condition in this case is $\Delta\beta = \beta_{\omega_s} + \beta_{\omega_i} - 2\beta_{\omega_p}$ [93]. The DFWM can also be used for optical parametric amplification where parametric gain (g) is provided to the weak signal at ω_s through the pumping at ω_p. The parametric gain g is defined as

$$g = \sqrt{(\gamma P_p)^2 - (\kappa/2)^2}, \tag{2.2.35}$$

where P_p is the pump power and $\kappa = \Delta\beta + 2\gamma P_p$ represents the effective phase mismatch. The maximum gain of the optical parametric amplification that occurs at $\kappa = 0$, is therefore given by [131]

$$g_{\text{max}} = \gamma P_p = \frac{2\pi n_2^I P_p}{\lambda_p A_{\text{eff}}}, \tag{2.2.36}$$

where λ_p is the pump wavelength.

From an electromagnetic point of view, we may consider the interaction of three stationary copolarized waves which are signal, idler and pump at frequencies ω_s, ω_i, and ω_p,

characterized by the slowly varying electric fields with complex amplitudes $A_s(z)$, $A_i(z)$, and $A_p(z)$, respectively. Assuming single transverse mode and including the losses, we can derive three coupled equations for the complex field amplitudes of the three waves as [15, 49, 93]

$$\frac{dA_p}{dz} = i\gamma\left[\left(|A_p|^2 + 2(|A_s|^2 + |A_i|^2)\right)A_p + 2A_sA_iA_p^*\exp(i\Delta\beta z)\right] - \frac{\alpha}{2}A_p, \tag{2.2.37}$$

$$\frac{dA_s}{dz} = i\gamma\left[\left(|A_s|^2 + 2(|A_i|^2 + |A_p|^2)\right)A_s + A_i^*A_p^2\exp(i\Delta\beta z)\right] - \frac{\alpha}{2}A_s, \tag{2.2.38}$$

$$\frac{dA_i}{dz} = i\gamma\left[\left(|A_i|^2 + 2(|A_s|^2 + |A_p|^2)\right)A_i + A_s^*A_p^2\exp(i\Delta\beta z)\right] - \frac{\alpha}{2}A_i, \tag{2.2.39}$$

where * denotes complex conjugate, z is the propagation length of the fiber, and α represents the attenuation coefficient. The first two terms on the right-hand side of Eqs. 2.2.37-2.2.39 describe SPM and XPM, respectively. The third term is responsible for the energy transfer between the three interacting waves that strongly depends on the phase-mismatch $\Delta\beta$. If we expand $\beta(\omega)$ in a Taylor series to the third order (neglecting fourth and higher order terms) around the zero-dispersion frequency ω_{ZDW}, then $\Delta\beta$ can be expressed as [93]

$$\Delta\beta = \beta_3(\omega_p - \omega_{ZDW})(\omega_p - \omega_s)^2. \tag{2.2.40}$$

When the pump wavelength is in the normal dispersion regime ($\Delta\beta > 0$), accumulated phase-mismatch will increase with the signal wavelength, thus decreasing the resulting efficiency of the process. Phase matching is possible to achieve even in normal dispersion regime in multimode or highly birefringent fibers due to the substantially different waveguide dispersion of different modes. On the other hand, when the pump wavelength is positioned in the anomalous dispersion regime ($\Delta\beta < 0$), the nonlinear phase-mismatch $2\gamma P_p$ can be compensated with linear phase-mismatch $\Delta\beta$. Therefore, the gain versus signal will form two lobes on each side of fixed pump with peak gain at $\Delta\beta = 2\gamma P_p$. This parametric process establishes a balance between GVD and the Kerr effect and it is identical to the phenomenon known as modulation instability [131], which will be discussed in the next section.

2.2.4/ MODULATION INSTABILITY

In optical fibers, modulation instability (MI) describes a process, where a CW or quasi-CW signal is unstable against perturbations of background noise, which then breaks up into a train of ultrashort pulses [25, 26, 35]. MI is therefore the exponential growth of a perturbation to the waveform, which can arise from e.g. pump noise or quantum noise. MI usually occurs in the anomalous dispersion region, where the leading and trailing edge of a pulse undergoes a frequency-upshift and frequency-downshift, respectively due to GVD [35], which is exactly the opposite to SPM. MI can generally be described as a degenerate FWM process phase matched by SPM that leads to a temporal modulation of the pulse which results two symmetric broad side lobes on each side of the pump. If the NLSE (Eq. 2.2.12) is solved for the steady state assuming $A(z,T)$ remains time independent during the propagation inside the fiber and furthermore, adding a perturbation to the steady state leads to the perturbation of the wavenumber (k) and frequency (Ω), which

satisfy the following dispersion relation as [131]

$$k = \pm\frac{1}{2}|\beta_2\Omega|[\Omega^2 + \mathrm{sgn}(\beta_2)4\gamma P_0/|\beta_2|]^{1/2}, \tag{2.2.41}$$

where $\mathrm{sgn}(\beta_2) = \pm 1$ depending on the sign of β_2. In the normal GVD region ($\beta_2 > 0$), steady state is stable against small perturbations as wavenumber k is real all Ω. However, in some cases, MI is possible to observe in normal GVD region, which is although outside the scope of this work. In the anomalous GVD region ($\beta_2 < 0$), the wavenumber k becomes imaginary, which leads to an exponential growth of the perturbation wave with z, similar to what was found in the analysis of SPM-phase-matched FWM. The gain spectrum of MI can be obtained by setting $\mathrm{sgn}(\beta_2) = -1$ and $g(\Omega) = 2\mathrm{Im}(k)$ in Eq. 2.2.41. The peak position (Ω_{max}) of the gain sidebands and maximum gain (g_{max}) are given by [131]

$$\Omega_{\mathrm{max}} = \pm\left(\frac{2\gamma P_0}{|\beta_2|}\right)^{1/2} \quad , \quad g_{\mathrm{max}} = 2\gamma P_0. \tag{2.2.42}$$

Peak gain does not depend on β_2, rather shows a linear increase with incident power. Fiber losses decrease the MI gain along the fiber length as they reduce incident power [25]. When the power of MI sidebands grows, they can further develop more sidebands, thus can create a cascade of MI peaks, which ultimately results to the total break-up of the pulse into a train of short sub-pulses. These sub-pulses are stable solutions known as solitons or solitary waves, which balance the effect of GVD and SPM for certain pulse energies and temporal pulse shapes of these sub-pulses throughout propagation inside the fiber. This concept will be further discussed in details in Section 2.2.6.

2.2.5/ RAMAN SCATTERING

Raman Scattering (RS) is an inelastic scattering, which comes from the photon-phonon interaction in an optical medium where the incident photons are scattered from the vibrational modes of the material molecules [1, 131]. Simply stated, it is a non-resonant process in which the material absorbs a photon and thereby creates an excitation to a virtual upper energy level and can occur irrespective of optical pump frequency. Figure. 2.10 illustrates the energy level diagram describing the basic principle of two possible spontaneous Raman scattering processes [131, 143]. In the Stokes process, pump photon (ω_p) excites the vibrational quanta in the medium, i.e., phonon. During the relaxation, a new phase matched photon (ω_S) is generated with an energy that is decreased by the energy of the phonon and whose spectrum is therefore red-shifted, i.e., the Stokes frequency shift. On the other hand, the anti-Stokes process involves scattering from the already excited vibrational state (Vib_S) and results a phase matched photon (ω_{AS}) with increased energy having blue-shifted spectrum, i.e., anti-Stokes frequency shift. The probability of the first one is much higher because the materials in thermal equilibrium have a higher population in ground state compared to excited state by the Boltzmann factor $\exp(\hbar\Omega/k_BT)$ [143]. Another reason for Stokes line to be stronger is the relaxed phase matching requirements between phonon and photon that results in an overall asymmetric gain profile. Raman scattering is spontaneous in the absence of any photon at the Stokes frequency. RS is further known as stimulated Raman scattering (SRS) when the process is stimulated by a seed through build-up from spontaneous Raman, which leads to the amplification of the seed [131]. The gain spectrum of SRS, being independent of the pump wavelength, offers a flexible possibility for power amplification at any wavelengths. SRS can be used to provide distributed amplification to a signal propagating in an optical

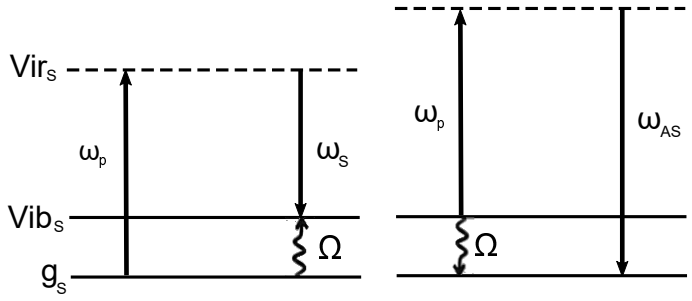

Figure 2.10: Illustration of spontaneous Raman scattering describing the principle of Stokes and anti-Stokes frequency shift. g_s, Vib_s, and Vir_s represent ground energy state, vibrational energy state, and virtual energy state, respectively. ω_p, ω_S, and ω_{AS} are the frequencies of pump, Stokes and anti-Stokes photons, respectively.

fiber along with a Stokes shifted high power continuous wave Raman pump. Following the similar argument, it seems apparent that Raman gain can amplify the low frequency components of a sufficiently broadband pulse by transferring energy from the high frequency components of that pulse. This effect is known as intrapulse Raman scattering (IPRS) [131]. IPRS is an important effect in SC generation that leads to red-shifting of sub-picosecond pulses, which will be further discussed in Section 2.2.6.

SRS contributes to the third-order nonlinear polarization through delayed Raman (vibrational) response. If we introduce the delayed response into the general form of time dependent nonlinear polarization given in Eq. 2.2.12, then the scalar form of nonlinear induced polarization becomes [131]

$$\vec{P}_{NL}(\vec{r},t) = \frac{3\epsilon_0}{4}\chi^{(3)}E(\vec{r},t)\int_{-\infty}^{t} R(t-t')\vec{E}^2(\vec{r},t')dt', \tag{2.2.43}$$

where $R(t)$ is the nonlinear response function, which includes both the instantaneous electronic (Kerr) response that normally modelled as a Delta function $\delta(t)$ and a delayed Raman response $h_R(t)$, is given by

$$R(t) = (1-f_R)\delta(t) + f_R h_R(t), \tag{2.2.44}$$

where f_R is the fractional contribution of the delayed Raman response to nonlinear polarization P_{NL}. $h_R(t)$ can be determined from the Raman gain spectrum, which is related to the imaginary part of Fourier transform of $h_R(t)$ [43]. In silica, delayed Raman response can be approximated by an exponentially-decayed sinusoidal function as [131]

$$h_R(t) = \frac{\tau_1^2+\tau_2^2}{\tau_1^2\tau_2^2}\exp(-t/\tau_2)\sin(t/\tau_1), \tag{2.2.45}$$

where τ_1 and τ_2 are the relaxation parameters taken to be 12.2 fs and 32 fs for fused silica, respectively, which were chosen to provide a good fit to the actual Raman gain spectrum of standard single-mode silica fibers [42]. Raman gain spectrum and delayed Raman response of soft-glass fibers including heavy metal-oxide and chalcogenide glasses are discussed in details in Section 3.6.2 in Chapter 3 and in Section 4.6.2 in Chapter 4, respectively. SRS is included in the NLSE in Section 2.2.7.

2.2.6/ SOLITONS AND DISPERSIVE WAVES

As discussed earlier in Section 2.2.4, solitons can be generated only when the effects of Kerr nonlinearity (SPM) and GVD can exactly cancel each other [11, 39, 51]. The chirp arising from GVD and SPM from Fig. 2.7(c) and Fig. 2.8(b), respectively, can cancel each other's effect when the right values of β_2 and P_0 are maintained such that $L_D = L_{NL}$. The soliton order N, which governs the relative importance of the SPM and GVD effects on pulse evolution inside an optical fiber, can be introduced here as [131]

$$N = \sqrt{\frac{L_D}{L_{NL}}} = \sqrt{\frac{\gamma P_0 T_0^2}{|\beta_2|}}. \tag{2.2.46}$$

The case $N = 1$ corresponds to a fundamental soliton, i.e., a state in which the effects of SPM and GVD are in balance and allow for the pulse to maintain its shape as it propagates inside an optical fiber. When $N \ll 1$, no soliton formation occurs as the nonlinearity from γP_0 is too weak and the pulse broadening is dominated by dispersion alone. In the case of $2 > N > 1$, the pulse will adjust itself its shape during the propagation in anomalous dispersion regime in order to achieve the above mentioned balance and irrespective of the initial shape, it eventually evolves into a secant-hyperbolic (sech) pulse. As a result, if the processes such as loss, Raman, and TOD are neglected, then the soliton is relatively stable against small perturbations and therefore, it will maintain its temporal and spectral shape throughout the propagation. The cases $N \geq 2$ corresponds to higher-order solitons that do not maintain their shapes. Here SPM and GVD can interact in such a way that the higher-order solitons follow a periodic evolution during propagation with their shape recovering at multiples of the soliton period (z_0), which is defined as $z_0 = \pi L_D/2$ [131]. Higher-order soliton actually consists of N fundamental solitons that propagate together due to the degeneracy of their group-velocities [38]. The relative peak power (P_k) and the temporal width (T_k) of these fundamental solitons are given by [38, 52, 131]

$$P_k = \frac{(2N - 2k + 1^2)}{N^2} P_0, \tag{2.2.47}$$

$$T_k = \frac{T_0}{2N - 2k + 1}, \tag{2.2.48}$$

where k is an integer from 1 to N. Therefore, the solitons, which are ejected first, have higher amplitudes, shorter durations, and propagate with faster group velocities, and the following solitons will be weaker and longer. Higher-order solitons periodically change their temporal shape and spectrum while propagating along the fiber due to interference between the fundamental solitons. Only the degeneracy of the group-velocities binds these fundamental solitons of a higher-order soliton together. However, if we assume that the N-order soliton behaves as a superposition of N fundamental solitons, then perturbation of the soliton steady-state though the effects such as third-order dispersion and intrapulse Raman effect will force the solitons to travel with different group velocity. As a result, N-order soliton is split up into N fundamental solitons. This non-instantaneous process is known as soliton decay or soliton fission [37, 38, 94]. For input pulses of duration exceeding 200 fs with sufficiently low bandwidth (which is the case of this thesis work), soliton fission is generally dominated by the Raman perturbation. On the other hand, dispersive perturbation dominates soliton fission process for the input pulses of duration

less than 20 fs. Soliton fission develops over fission length L_{fiss}, which is given by [128]

$$L_{\text{fiss}} = \frac{L_D}{N}. \tag{2.2.49}$$

From Eq. 2.2.48, it seems apparent that solitons with very short duration may be generated. For a soliton whose temporal width is 1 ps or shorter, the bandwidth of its optical spectrum is broad enough and consequently, the spectrum overlaps with the Raman gain. In that case, stimulated Raman scattering continuously transfers energy from the high frequency part of the pulse spectrum to its low frequency part. This energy transfer results an increasing red-shift of the soliton with propagation along the fiber. This process is commonly referred to as the soliton self-frequency shift (SSFS) and this prime process along with soliton fission cause strong spectral broadening towards longer wavelengths [33]. In the anomalous dispersion regime, the longer wavelengths correspond to smaller group velocities and therefore, the solitons continuously slow down with propagation inside the fiber [134]. The dynamics of the soliton self-frequency shift ν_{SSFS} can be expressed as [32]

$$\nu_{\text{SSFS}} \propto \frac{|\beta_2|}{T_0^4}. \tag{2.2.50}$$

Therefore the shorter-duration solitons that are ejected first in the fission process experience greater self-frequency downshifts due to the increased peak power and walk-off proportionally faster from the input pump wavelength. The following solitons will further experience a decreasing shift, thus forming a continuum of spectrally separated solitons.

On the other hand, the presence of higher-order dispersion modifies the soliton fission dynamics and generates the so-called dispersive waves (DWs). TOD leads to the transfer of energy from the soliton, which was generated in the fission process, to a narrow-band resonance in the normal GVD regime [36, 94, 128]. Each fundamental soliton generates a dispersive wave whose frequency can be calculated from a phase-matching argument involving the soliton linear and nonlinear phase and the linear phase of a continuous wave at a different frequency [54]. The initial DW is emitted primarily from the first ejected soliton having the broadest bandwidth and thus has maximum overlap with the resonance of the DW. For a soliton with peak power P_s and group velocity $v_{g,s}$ at a frequency ω_s, the DW is generated at the frequency ω_{DW}, which can be obtained from the following relation [128]:

$$\beta(\omega_s) - \frac{\omega_s}{v_{g,s}} + (1 - f_R)\gamma P_s = \beta(\omega_{DW}) - \frac{\omega_{DW}}{v_{g,s}}. \tag{2.2.51}$$

If we neglect the fourth-order dispersion, then the frequency shift (Ω) between soliton and dispersive wave may be approximated as [131]

$$\Omega = \omega_s - \omega_{DW} \approx -\frac{3\beta_2}{\beta_3} + \frac{\gamma P_s \beta_3}{3\beta_2^2}. \tag{2.2.52}$$

When the dispersion slope is positive ($\beta_3 > 0$), solitons propagating in that region experience positive frequency shift, therefore, the DWs are generated in the normal dispersion regime at shorter wavelengths. On the other hand, for negative dispersion slope ($\beta_3 < 0$), DWs are generated in the normal dispersion regime at longer wavelengths as the solitons in this case approach the normal dispersion regime on the long-wavelength side.

Initially DWs lag behind the solitons as they have group velocities smaller than those of solitons. However, continuous deceleration of solitons allow the DWs to catch up with them. Therefore, the generated DWs can overlap with the solitons in time, which leads to their interaction through XPM and FWM to generate new frequency components at even shorter wavelengths, but it may also lead to a soliton-like two-frequency soliton-DW state [125, 129, 131]. Furthermore, the Raman and Kerr effects with a varying local GVD may together lead to a localized non-dispersive trapped state of the DWs, in which they continuously blue-shift in response to the red-shifting solitons [134]. It is noted that the short-wavelength pulse is typically much weaker than the associated long-wavelength soliton, therefore, the nonlinear refractive-index change induced by the soliton is very significant. The previous mechanism therefore may be explained by the soliton imposing a potential on the DW that is trapped on one side by the nonlinear refractive-index change induced by the intense solitons, and on the other side by a linear potential originating from the fact that the soliton moves with changing group velocity dispersion. During the red-shift, soliton changes its group velocity. However, it can match its group velocity with the trapped DW if DW maintains its group velocity through blue-shifting. Furthermore, in long run, the DWs inevitably leak radiation with shifting and may completely dissociate from the solitons due to the finite trapping potential imposed on DWs by them. SPM, soliton generation, SSFS, and DWs generation are illustrated through numerical simulation and explained in details in Section 3.6 in Chapter 3 and in Section 4.6.2 in Chapter 4. The following section will briefly present a generalized form of the NLSE, which models the above mentioned higher-order effects.

2.2.7/ GENERALIZED NONLINEAR SCHRÖDINGER EQUATION

The generalized NLSE (GNLSE) is a more accurate model than the NLSE presented in Eq. 2.2.12. It includes higher-order dispersion terms, self-steepening through the $(i/\omega_0)\partial/\partial T$ term, and the vibrational contribution to the nonlinear induced polarization through the delayed Raman response function $R(T)$, can be written as [131]

$$\frac{\partial A}{\partial z} + \underbrace{\frac{\alpha}{2}A}_{Linear-loss} - \underbrace{\sum_{m\geq 2}\frac{i^{m+1}}{m!}\beta_m\frac{\partial^m A}{\partial T^m}}_{Dispersion} = \underbrace{i\gamma\left(1+\frac{i}{\omega_0}\frac{\partial}{\partial T}\right)}_{Kerr+Self-steepening} \times\left(A(z,T)\int_{-\infty}^{\infty}\underbrace{R(T')|A(z,T-T')|^2dT'}_{Raman}\right). \tag{2.2.53}$$

The terms in the left-hand side and right hand side of Eq. 2.2.7 represent linear and nonlinear effects, respectively. Each term is labeled with their physical representation. Inclusion of these terms in GNLSE simulation is much needed to explain the highly complex spectral and temporal evolution of SC generation. Details about the implementation of the GNLSE used in this work are given in Section 3.6 in Chapter 3 and a two-polarization code based on two coupled generalized nonlinear Schrödinger equations (CGNLSEs) are discussed and implemented in Section 4.6.2 in Chapter 4.

3

SUPERCONTINUUM GENERATION IN HEAVY METAL-OXIDE FIBER

BROADBAND and compact supercontinuum (SC) sources in the infrared (IR) are very attractive for sensing and spectroscopy applications [185, 169, 227] because this wavelength range contains chemical "fingerprints" of numerous molecules [207]. Soft glasses such as chalcogenide (As_2S_3) [207, 192, 198], tellurite [230, 193], and ZBLAN (ZrF_4–BaF_2–LaF_3–AlF_3–NaF) [130, 235, 181] have been widely used for drawing highly nonlinear fibers, and experiments have shown efficient SC generation in the mid-IR up to 15 µm [207, 192] and up to 11 µm using all-fiber systems [232, 241]. Another approach for mid-IR SC generation is gas-filled, hollow-core photonic crystal fiber, which provides low-loss guidance and much higher effective nonlinearity than capillary-based systems [208, 219]. Record output power of 1.4 W with broadest SC up to 3.2 µm have also been recently achieved in highly germanium-doped fibers [221]. An alternative to ZBLAN fibers that has recently received attention is small-core heavy metal oxide PCFs [209]. They possess a number of optical and mechanical properties that make them also attractive for SC generation, despite their limited transmission window from 0.55 to 2.8 µm compared to other soft glasses. The nonlinear index n_2 of this glass is one order of magnitude larger ($4.3 \cdot 10^{-19}$ m^2/W) than ZBLAN and silica glasses [209]. In particular, suspended core photonic crystal fibers (SC-PCFs) can be readily drawn in which the microstructures enable tight optical confinement and a small effective mode area in the order of few µm^2 [146, 202]. This results in a high nonlinear coefficient and zero-dispersion wavelength in the telecommunication C band. In recent years, suspended-core fibers have received less attention in the context of SC generation than regular lattice PCFs, although existing literature reports evidence about the versatility of this approach, including the choice of a glass platform (silica/soft glass), spectral coverage (near-IR/mid-IR), and the dispersion regime of SC generation (solitonic/allnormal) [150, 163, 201, 145, 184].

In this chapter, we experimentally demonstrated SC generation in lead-bismuth-gallium-cadmium-oxide glass (PBG81) based SC-PCFs pumped by 220 fs pulses around 1550 nm. We present a short overview of soft glasses for MIR SC generation and the motivation behind the selection of heavy metal-oxide glasses. The SC-PCFs containing six big air holes with large air fill fraction, are drawn from PBG-81 glass using stack-and-draw method. The group velocity dispersion for the fundamental mode of the fibers was computed from the scanning electron microscope (SEM) images of the fiber samples. We identify a number of nonlinear phenomena such as spectral broadening due to self-phase modulation, soliton generation, and Raman soliton self-frequency shift in the

fiber at the pumping wavelengths. The experimental spectra are compared with numerical simulations of the generalized nonlinear Schrödinger equation including the group velocity dispersion.

3.1/ SOFT GLASSES FOR MID-INFRARED SUPERCONTINUUM GENERATION

Development of optical materials that support transmission in mid-IR region as well as high optical nonlinearity, is essential due to the growing interest in the 2-20 µm molecular fingerprint region. Among other optical materials, glass plays very important role due to its unique structural and thermodynamic features. Moreover, glass has good stability, excellent homogeneity, good thermo-mechanical properties, and a viscosity–temperature relationship, which makes fiber drawing from it possible [98]. Silica based glasses are the most widespread material used for fiber systems, however, they exhibit high intrinsic absorption beyond 3.5 µm [228, 239] and also possess low nonlinear refractive index (e.g, $n_2 = 2.74 \cdot 10^{-20}$ m^2/W measured at the wavelength of 1053 nm for fused silica [64]) compared to soft glasses [229] or liquids [226] that limits their use in the mid-IR range. The limit of transmission window in silica glass for longer wavelengths, due to multi-photon absorption by Si–O bondings and vibrational resonances on OH–ions, motivates the search for other materials for PCF development that would allow for transmission in mid-IR. In past years, active research has been done on soft-glass chemistry to remove absorption bands while enhancing both transmission and nonlinearity. Most popular soft glasses

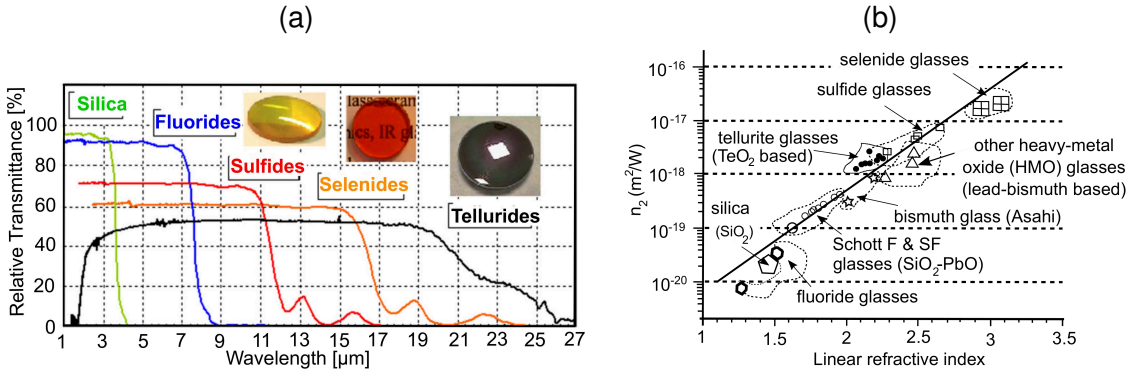

Figure 3.1: (a) Typical infrared transmission spectra of millimeter thick various bulk glass samples. The insets are examples of sulfide As_2S_3 (yellow), selenide As_2Se_3 (red), and telluride $Te_{20}As_{30}Se_{50}$ (black) glasses (taken from [228]). (b) Relation between the linear refractive index n and nonlinear refractive index n_2 in various glasses taken from [140].

such as chalcogenide (As_2S_3, As_2Se_3, GeAsSe), tellurite (TeO_2), chalcohalides (GeTe, GeAsTeSe), heavy metal oxide (PbO-Bi_2O_3-Ga_2O_3-SiO_2-CdO), and ZBLAN have been extensively used as mid-IR optical material for drawing highly nonlinear and widely transmissive optical fibers in the mid-IR for SC applications. Figure 3.1(a) shows the infrared transmission spectra of different glasses measured with 2-3 mm bulk sample [228, 239]. Tellurite and fluoride glasses offer transmission up to 4.5 µm and 8 µm, respectively, which is much higher than that of silica and chalcogenide glass offers the broadest transmission up to 25 µm range. Since, the variation of linear refractive index with wavelength depends on the glass composition and furthermore, according to Miller's rule (i.e., the

third-order nonlinear dielectric susceptibility $\chi^{(3)}$ is proportional to the fourth power of the linear susceptibility $\chi^{(1)}$ [4]), a high-intrinsic nonlinearity is usually associated with a high linear refractive index. Hence, the glasses composed of ions with high polarizibility supposed to have a high nonlinear refractive index. Figure 3.1(b) shows a summary of the relation between the linear refractive index n and the nonlinear refractive index n_2 in various glasses [140]. From this figure, we can see that, by introducing heavy atoms (i.e., heavy metal compounds) or ions with a large ionic radius (i.e., using chalcogen elements such as sulfur (S), selenium (Se), and tellurium (Te) to replace oxygen), it is possible to increase the polarizibility of the components in the glass matrix, which in turn increases the nonlinear refractive index n_2. In this thesis, we worked with heavy metal-oxide glasses in Chapter 3 and chalcogenide glasses in Chapter 4.

3.1.1/ HEAVY METAL-OXIDE GLASSES

Heavy metal-oxide glasses are very well known for their relatively high recrystallization resistance, ease of handling, and good mechanical properties compared to chalcogenide glasses and they also possess high nonlinearity and combination of visible to mid-infrared transmission window, compared to silica glass. The heavy metal-oxide glass described in this thesis was fabricated at the Institute of Electronic Materials Technology (ITME) in Warsaw, Poland. The chemical composition of this glass contains these oxides: PbO: 39.17, Bi_2O_3: 27.26, Ga_2O_3: 14.26, SiO_2: 14.06, and CdO: 5.26.

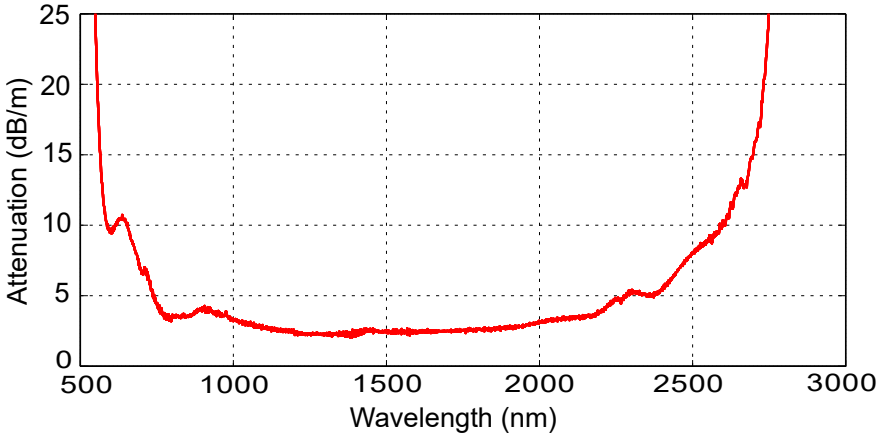

Figure 3.2: Attenuation spectrum of bulk lead-bismuth-gallium-cadmium-oxide glass used for drawing SC-PCFs, measured by our collaborator at ITME.

The glass has a high linear refractive index of 1.886 at 1550 nm. The glass transition temperature (T_g) of this glass is around 489 ℃. The nonlinear refractive index of PBG81 glass was measured as $n_2 = 4.3 \cdot 10^{-19}$ m^2/W, using standard Z-scan method at 1240 nm for bulk sample [119, 149], which is very high for oxide soft glasses and also much higher than that reported for any other oxide glass used in mid-IR supercontinuum generation. The attenuation spectrum of this PBG81 bulk glass was measured using standard cut-back method as shown in Fig. 3.2. This soft glass has a transmission window from 550 to 2800 nm with typical attenuation of around 2.5 dB/m within 1000–2000 nm. Above 2800 nm, this particular glass melt shows the onset of strong attenuation assigned to OH absorption and has been subject only to standard bubbling of the glass melt with dry air (<1000 ppm of OH). As Fig. 3.2 shows, the attenuation curve does not feature a local peak around 1380 nm, which is the main difference between PBG81 and previously used

PBG08 glass [209].

3.2/ FIBER FABRICATION

The SC-PCFs were fabricated at the Institute of Electronic Materials Technology in Warsaw, Poland. Here the fiber design is based on the traditional suspended-core geometry. The fiber was designed to have a central core, which is surrounded by 6 large air holes. Large air fill fraction was obtained by making the bridges/struts thinner and also increasing their number for better support of the core. High crystallization resistance of the glass allows fabrication of SC-PCFs via stack-and-draw method, which is a very well known technique for making PCFs. During the fiber drawing process, it is very important to maintain a precise pressure control, which in turn maintains a certain pressure difference across the internal and external surface and also to control the surface tension via furnace temperature at which the fiber is being drawn and they determine the final deformation of the holes. Luzi et al. experimentally and numerically investigated the effect of pressure and surface tension in six-hole fiber to inner holes enlargement and elongation along the radial direction during the fiber drawing process [187]. The relationship can be written as [187]

$$\Delta P = \frac{\gamma}{R}, \tag{3.2.1}$$

where ΔP represents the pressure difference, surface tension is denoted by γ, and R

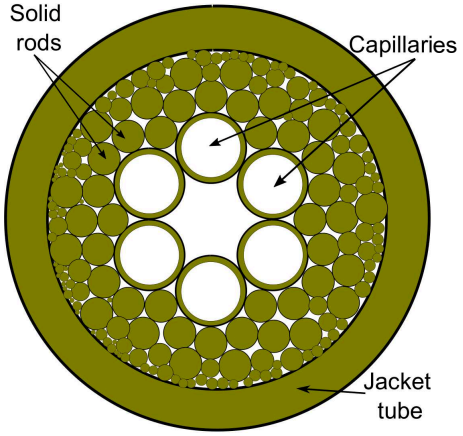

Figure 3.3: Stack containing capillaries and solid rods for preform drawing.

represents the radius of the internal surface. In this thesis, the fiber drawing parameters are not presented as they were not disclosed by the manufacturer. Here, the SC-PCFs are fabricated in four steps. In the first step, several capillary tubes and several solid rods were drawn from PBG81 glass. In the second step, stacking is performed with six big air hole capillaries in the middle and several solid glass rods surrounding those capillaries as shown in Fig. 3.3. The stack is then put inside a jacket tube made from same PBG81 glass and there after, a preform is drawn from the stacked form in the drawing tower at the third step. During this process, the air hole deformation in the preform was controlled by controlling the pressure inside the capillaries. In the last step, the final fiber was drawn from previously drawn preform. Here air hole structures are achieved by controlling the pressure inside the air hole during drawing. The diameter of the fiber is further controlled by the pulling speed of the fiber and the feeding speed of the preform into the furnace.

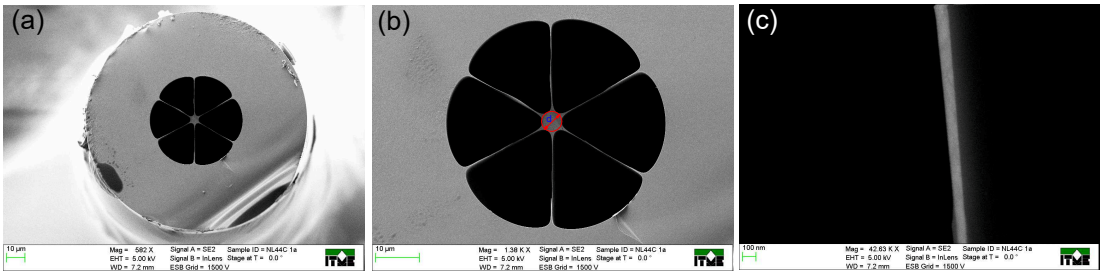

Figure 3.4: Cross-section SEM images of a SC-PCF: (a) Image of the fiber with outer diameter of 120.3 µm. (b) Expanded view of the microstructure region with core diameter of 4.5 µm. (c) One of the 6 struts supporting the core with thickness of 81 nm.

The microstructure of one of the five drawn PCFs is shown in scanning electron microscope (SEM) images in Figs. 3.4(a-c). Since, the SC-PCF has a hexagonal core shape, hence, the fiber core diameter d is defined as the diameter of the circle that is inscribed within the hexagonal core as shown in Fig. 3.4(b). The SC-PCF has outer diameter (d_{out}) of 120.3 µm and core diameter d of 4.5 µm. The hexagonal core is suspended in the outer glass region by six fine struts/bridges with thickness of about 81 nm. These thin struts result in a negligible modal confinement loss for the fundamental mode by ensuring a high degree of isolation in the core area. The small core and thin struts are protected by the outer glass region, which also provides sufficient mechanical strength for handling and cleaving of the fiber. Five different fibers were fabricated with dimensions chosen to yield zero-dispersion wavelengths (ZDWs) covering the range 1519-1653 nm. The opto-

Table 3.1: Geometric parameters of SC-PCFs used for dispersion computation and supercontinuum generation.

No.	Label	Core diameter [µm]	Strut thickness [nm]	ZDW [nm]
1	NL44C1a	4.5	81	1653
2	NL44C2a	4.3	99	1593
3	NL44C3a	3.95	90	1574
4	NL44C4b	3.8	40	1557
5	NL44C5c	3.51	47	1519

geometric parameters of the five fiber samples are given in Table 3.1. Here the labeling of the fiber sample was done according to the different fiber drawn in the drawing tower. The fibers have core diameter between 3.51 µm and 4.5 µm, and the strut thickness are in the range of 47 to 99 nm. The last column in this table represents ZDW of the five fiber samples, which are computed in the following section.

3.3/ COMPUTATION OF DISPERSION

Chromatic dispersion of optical fiber was presented in Chapter 2 from where several equations will be used to compute the effective refractive index and group velocity dispersion in this section. The dispersion properties of the SC-PCFs are computed from the cross-section SEM images of the fiber samples, one of which is shown in Fig. 3.4(b), using COMSOL software based on a full vector finite-element method. At first, based on

the processed SEM photo of the fiber cross section, the air hole structure was depicted accurately, and then, it was drawn in COMSOL. The refractive index of the air holes is set to 1. Considering the material dispersion, the refractive index for the PBG-81 glass is determined by a standard Sellmeier equation with the following form:

$$n^2(\lambda) = 1 + \frac{B_1\lambda^2}{\lambda^2 - C_1} + \frac{B_2\lambda^2}{\lambda^2 - C_2} + \frac{B_3\lambda^2}{\lambda^2 - C_3}, \tag{3.3.1}$$

Table 3.2: Sellmeier coefficients for PBG81 glass.

B_1	B_2	B_3	C_1 [µm^2]	C_2 [µm^2]	C_3 [µm^2]
2.30350920	0.21430548	1.73310331	0.02084623	0.08262994	183.5615768

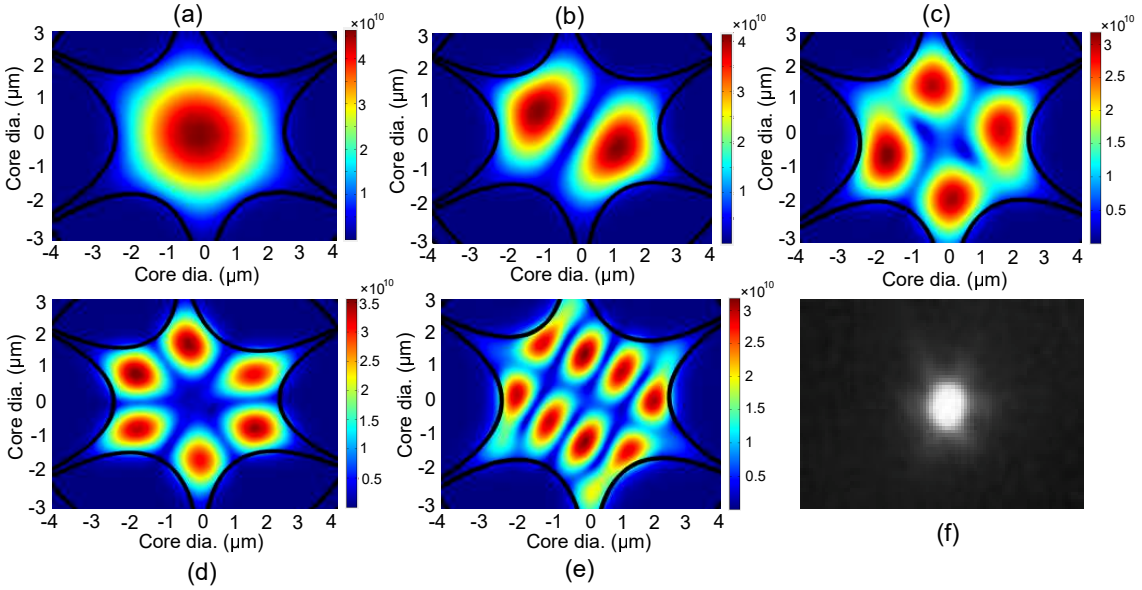

Figure 3.5: Computed mode field distribution inside the core of fiber sample NL44C2a at 1550 nm for (a) LP_{01} mode, (b) LP_{11} mode, (c) LP_{21} mode, (d) LP_{31} mode, (e) LP_{41} mode. (f) Experimentally obtained mode profile at the output end of the fiber sample NL44C2a at 1550 nm showing the fundamental LP_{01} mode.

where, B_1, B_2, and B_3 are dimensionless coefficients and C_1, C_2, and C_3 are the material resonant wavelengths. The measured Sellmeier coefficients for PBG81 glass that are used in the numerical modelling are given in Table 3.2.

According to the simulation, for the real (fabricated), asymmetric hexagonal core six-strut fiber, two orthogonally polarized fundamental modes (LP_{01}) and four LP_{11} modes, four LP_{21} modes, four LP_{31} modes, and four LP_{41} modes were found, which are shown in Figs. 3.5(a-e). Experimentally, we obtained a mode profile at the output end of a 60 cm long fiber sample using an IR camera as shown in Fig. 3.5(f). This image confirms that the light inside the fiber is guided in the fundamental LP_{01} mode for SC generation (described in the next section), which motivates to focus only on the fundamental mode guiding in our thesis. We further calculated the effective refractive index (n_{eff}) of the fundamental mode of five fiber samples, as shown in Fig. 3.6(a). The computed effective mode area are shown in Fig. 3.6(b) for 3 SC-PCF samples NL44C2a, NL44C5c, NL44C4b, which will

be later used for experimental demonstration. Using Eq. 2.1.50 from Chapter 2, the effective refractive index is then used to calculate the group velocity dispersion (GVD) for the fundamental mode, which are shown in Figs. 3.7(a)&(b). Figure 3.7(a) shows the group velocity dispersion curve of our five SC-PCF samples covering almost the entire transmission window of the fiber. As can be seen in Fig. 3.7(b), the zero-dispersion wavelength shifts from 1519 nm to 1653 nm as the core diameter increases from 3.51 µm to 4.5 µm. Since, for real (fabricated) structure, the air holes in the fibers are not symmetric, which introduces significant amount of phase birefringence. Hence, the phase birefringence is further calculated using Eq. 2.1.53 from Chapter 2 and they are shown in Fig. 3.7(c) for the five fiber samples. From this figure, it is seen that the phase birefringence varies between $1.6 \cdot 10^{-4}$ and $7.02 \cdot 10^{-5}$ at 1550 nm for the five SC-PCF samples with core diameter between 3.51 µm and 4.5 µm. We can also see that the phase birefringence is more dependent on the air hole structure than the core diameter of fiber samples. Among the five SC-PCF samples described above, we have used NL44C2a, NL44C5c, and NL44C4b for experimental demonstration as we obtained best results with these fibers.

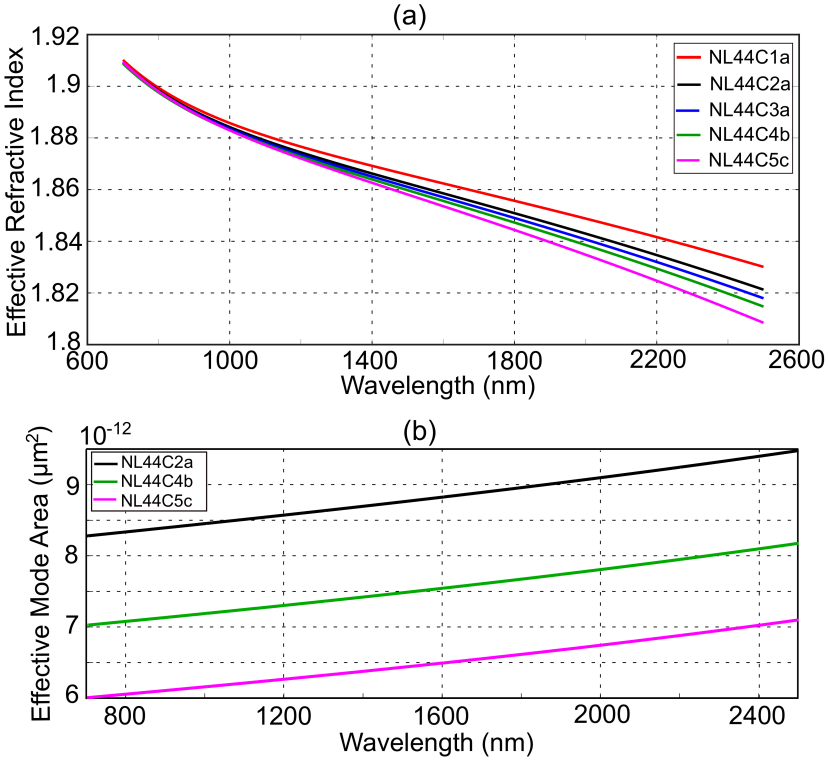

Figure 3.6: (a) Effective refractive index of 5 SC-PCFs calculated for the fundamental mode from SEM images. (b) Effective mode area for 3 SC-PCF samples, which are used for experimental demonstration.

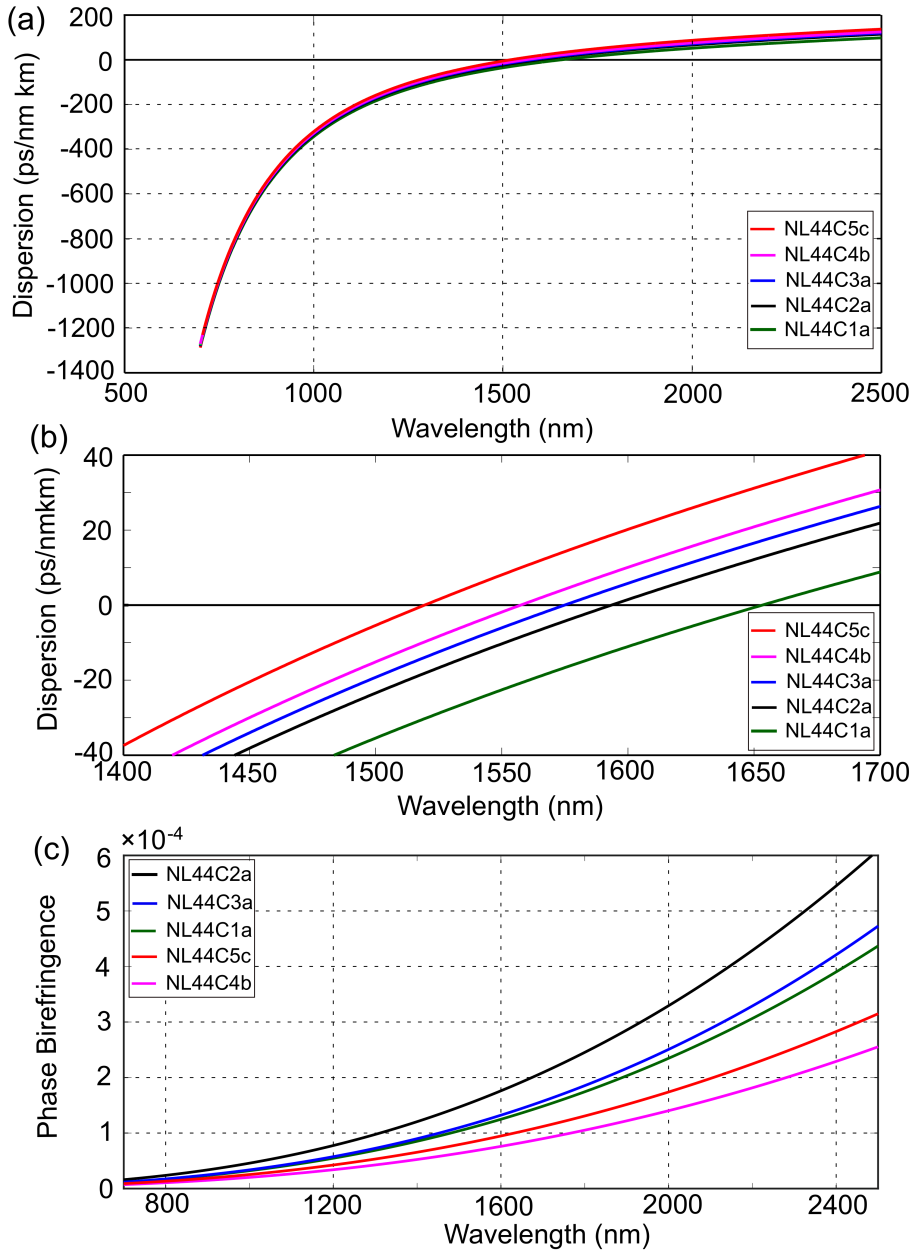

Figure 3.7: Dispersion and birefringence characteristics of 5 SC-PCFs computed for the fundamental mode: (a) Group velocity dispersion of SC-PCF samples. (b) Dispersion curve of the SC-PCFs showing zero-dispersion wavelength (ZDW). (c) Phase birefringence of the SC-PCFs.

3.4/ EXPERIMENTAL SETUP FOR SC GENERATION

The experimental setup for generating and measuring supercontinuum spectra is shown in Fig. 3.8. As a pump laser we used a 220-fs optical parametric oscillator (Chameleon Compact OPO-Vis), pumped by a Ti-Sapphire mode-locked laser (Chameleon Ultra II) at 80 MHz repetition rate having 140-fs pulse duration. The OPO signal is tunable in the range 1-1.6 µm with mean output powers 900 mW - 230 mW, and the idler from 1.7 µm

to 4 µm with powers from 250 mW to 80 mW. The signal (or the Idler in case of pumping above 1.7 µm) from the OPO was injected into the SC-PCF through an IR-coated focusing objective (40X magnification) and the coupling power was controlled via a variable attenuator. The light at the output of SC-PCF was collimated using a C-coated aspheric lens with a focal length of 3.5 mm. An IR camera was combined with neutral density (ND) filters to study the mode structure and guidance inside the fiber core. The generated SC light was measured using an IR spectrometer (Ocean Optics NIRQuest512-2.5) with sensitivity in the wavelength range of 900-2500 nm, combined with an imaging system (another focusing objective) and fluoride (InF_3) multimode fiber with a core diameter of 100 µm. The beam quality at OPO output was measured with a Thorlabs dual Scanning Slit Beam Profiler (900 - 2700 nm), as shown in the left inset of Fig. 3.8. The result of the IR imaging (right inset of Fig. 3.8) showed that the SC was generated in the fundamental mode over the full wavelength range and no evidence for the presence of multimode operation could be observed.

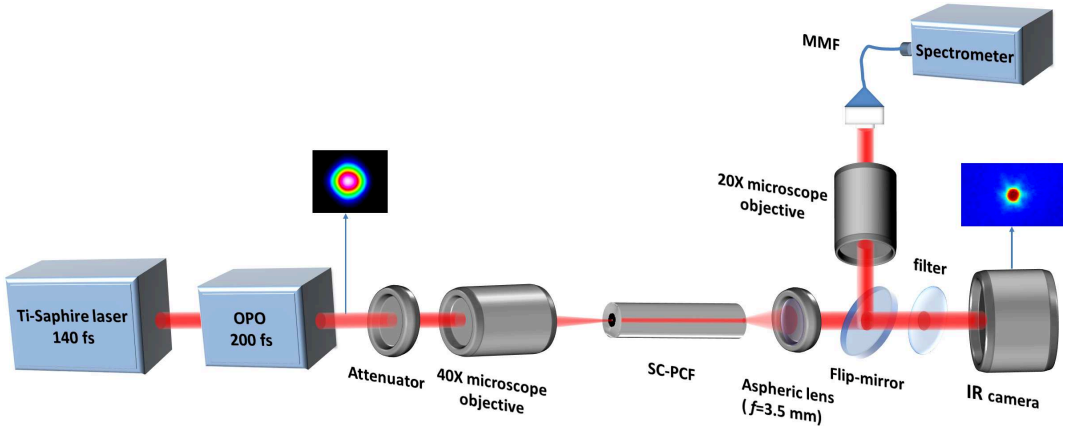

Figure 3.8: Schematic of the experimental setup for generating and measuring supercontinuum infrared light. SC-PCF, suspended core photonic crystal fiber; MMF, multimode fiber [inset-left: beam profile at OPO output, right: IR image at SC-PCF output].

3.5/ RESULTS

Figures 3.9(a-d) show the variation in the measured SC spectra for different fiber output powers as indicated for two SC-PCF samples NL44C2a (core diameter = 4.3 µm, length = 60 cm, ZDW = 1593 nm) and NL44C5c (core diameter = 3.51 µm, length = 180 cm, ZDW = 1519 nm), pumped using signal wavelengths of 1550 nm (in the normal dispersion regime) and 1580 nm (in the anomalous dispersion regime), respectively. The output spectra recorded for these two fiber samples show strong spectral broadening around the pump wavelength due to self-phase modulation at low input power. Note that, in addition to the peak contributed by pump wavelength, we have an additional peak due to the residual OPO idler that otherwise does not contribute to SC generation. As the power increases, we see red-shifted solitons beyond 2 µm and simultaneous generation of up-shifted dispersive waves down to 1 µm. At maximum coupling power, we obtained SC spectra of 1151 nm and 1575 nm bandwidths (at the -20 dB) for fiber samples NL44C2a and NL44C5c, respectively. The propagation loss was measured to be 4 dB/m at 1550 nm using standard cut-back method, where the loss in the glass at 1550 nm was 2.54

dB/m as can be seen from Fig. 3.2. Using the measured output power, Fresnel loss from the output facet of the fiber, and propagation loss inside the fiber in Eqs. 2.1.35 and 2.1.36 from Chapter 2, we estimated the coupling efficiency to be 38% and the coupling peak power to be 5.8 kW at 1550 nm.

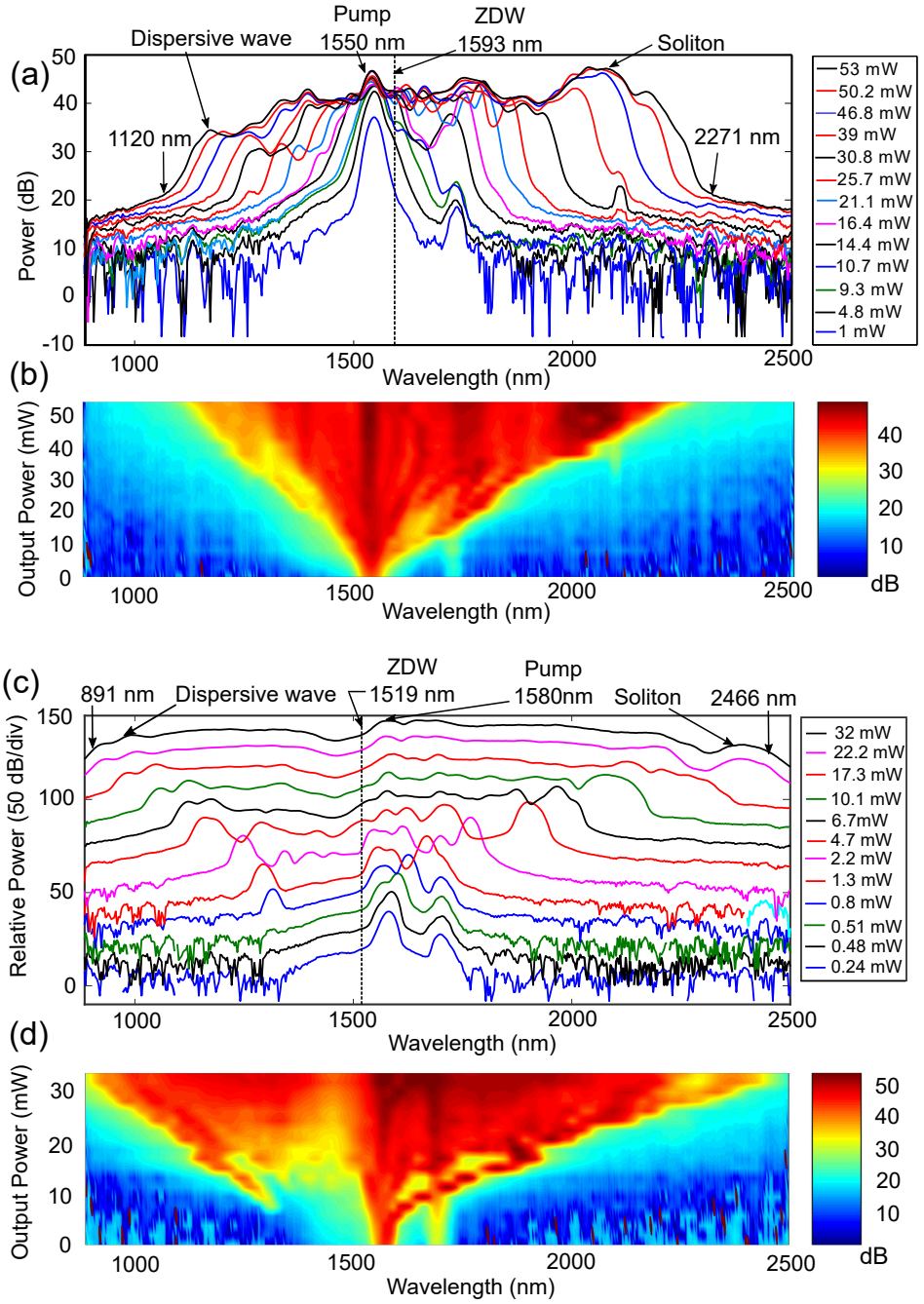

Figure 3.9: Supercontinuum spectra generated in two SC-PCF samples with 220 fs pulses pumped at 1550 nm and 1580 nm, respectively, as a function of mean output power. (a) and (c) Generation of SC spectra through spectral broadening, soliton ejection, and dispersive wave generation in two fiber samples NL44C2a and NL44C5c, respectively. (b) and (d) Evolution of SC spectrum with the fiber output power for the respective SC-PCF samples.

Another SC-PCF sample NL44C4b (core diameter = 3.8 µm, length = 183 cm, ZDW = 1557 nm) was also pumped at 1740 nm in the strong anomalous dispersion regime using the OPO's idler output. The variation in the measured SC spectra for different output powers for this fiber is shown in Figs. 3.10(a)&(b). As we pumped at a wavelength far away from the zero-dispersion wavelength of this fiber, we obtained three individual high power solitons beyond 2 µm and dispersive waves down to 1 µm instead of a smooth supercontinuum. At maximum power, the bandwidth of this broad spectrum is 1477 nm at the -20 dB level. The coupling efficiency and coupling peak power were estimated to be 38% and 3.8 kW, respectively. Furthermore, the SC-PCFs have six big air holes, which

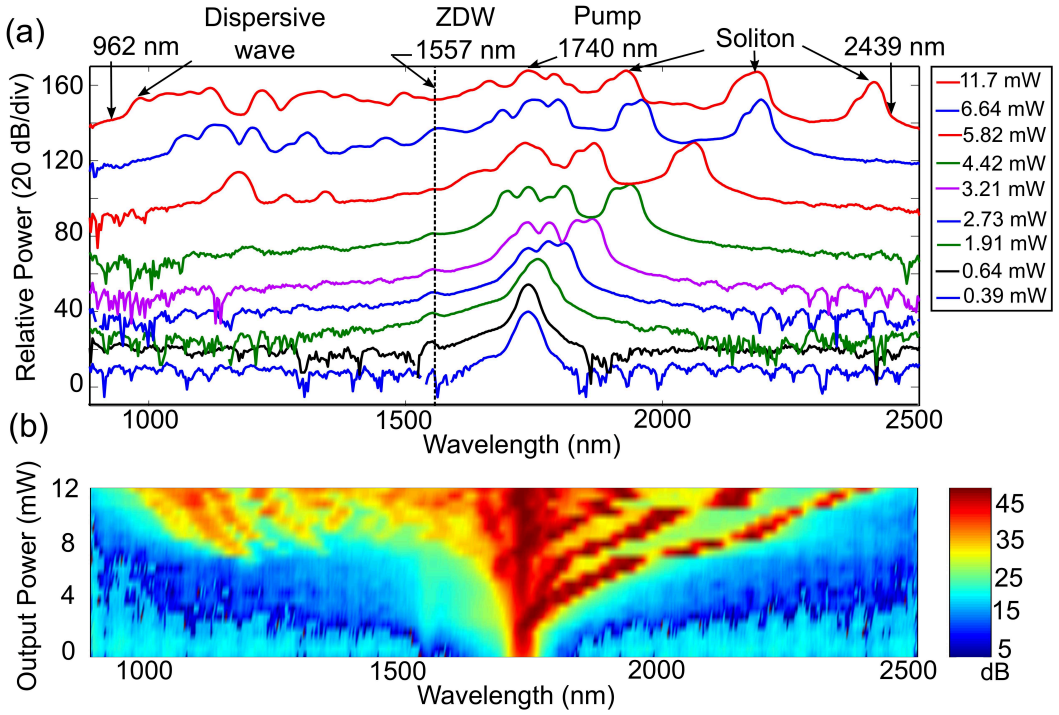

Figure 3.10: Spectra generated in SC-PCF sample NL44C4b with 220 fs pulses pumped at 1740 nm. (a) Generation of broad spectra through spectral broadening, soliton ejection, and dispersive wave generation. (b) Evolution of spectrum with the fiber output power.

are not symmetric in reality due to the fabrication process and it introduces some amount of birefringence in the fiber. From Fig. 3.7(c), NL44C4b sample shows a birefringence of $9.5 \cdot 10^{-5}$ at 1740 nm. Therefore, we investigated the effect of birefringence on SC spectra for SC-PCF sample NL44C4b at 1740 nm. Figure 3.11 shows the recorded SC spectra when tuning the input polarization from 0° till 240° with 20° steps and with constant output power of 11.7 mW. As it can be seen, the input pump polarization strongly affects the broadband SC generation. Since, from Fig. 3.10(a), pumping at 1740 nm results in a broad spectrum with three individual high power solitons, therefore, instead of SC bandwidth, we estimated the position of final soliton peak, which changes with input polarization angle due to birefringence of the fiber as shown in Fig. 3.12, with an angular periodicity of around 90°.

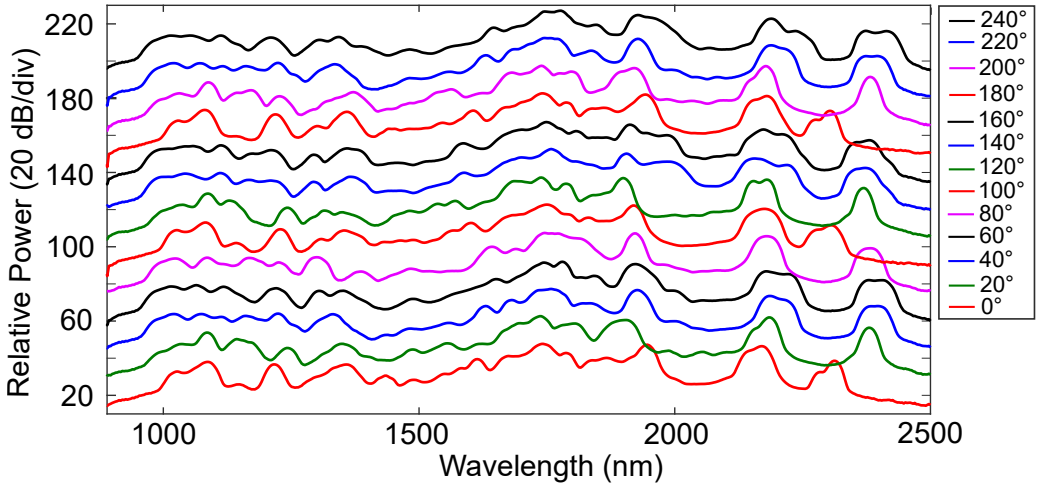

Figure 3.11: Dependency of SC spectra with incident angle of polarization from 0° to 240° for pumping at 1740 nm in SC-PCF sample NL44C4b.

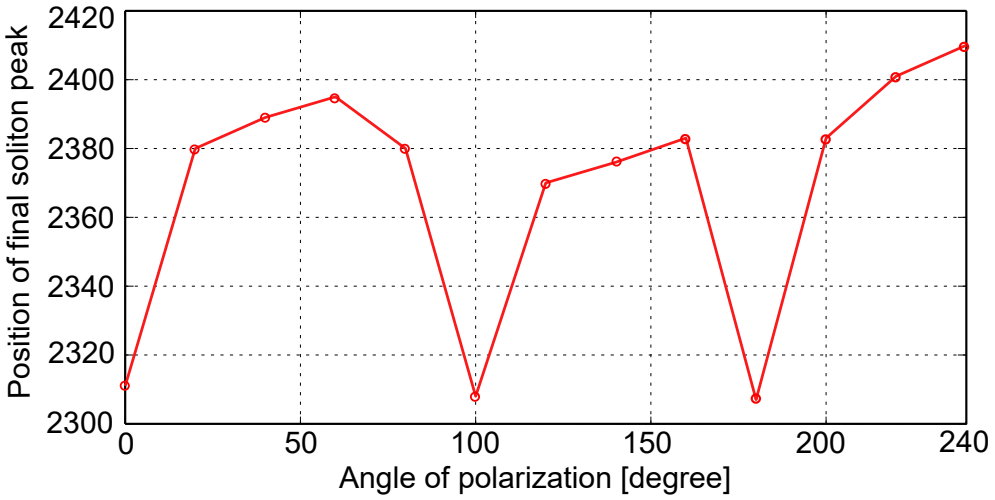

Figure 3.12: Position of final soliton peak at different polarization angle for 1740 nm pumping.

3.6/ COMPARISON WITH NUMERICAL SIMULATIONS

Nonlinear pulse propagation and supercontinuum generation was modelled using the generalized nonlinear Schrödinger equation (GNLSE) as shown below [128, 166]:

$$\frac{\partial A}{\partial z} + \frac{\alpha}{2}A - \sum_{k\geq 2}\frac{i^{k+1}}{k!}\beta_k\frac{\partial^k A}{\partial T^k} = i\gamma\left(1 + i\tau_{\text{shock}}\frac{\partial}{\partial T}\right)\times\left(A(z,T)\int_{-\infty}^{\infty}R(T')|A(z,T-T')|^2dT'\right). \tag{3.6.1}$$

Here the second term in the left-hand side of Eq. 3.6.1 accounts for linear loss with loss coefficient α. The third term represents the dispersion with dispersion coefficient β_k associated with Taylor series expansion of the propagation constant $\beta(\omega)$ about central frequency ω_0 and we have included the dispersion terms up to fourth order in the numerical simulation. In the simulation, we introduced a linear loss of 4 dB/m (measured using

standard cut-back method at 1580 nm). The second-order dispersion $\beta_2(\omega)$ is also shown in Fig. 3.7(a) as the D parameter, which was computed from the SEM image of SC-PCF samples. The right-hand side (RHS) of Eq. 3.6.1 models the nonlinear effects in the fiber: nonlinear coefficient $\gamma = 2\pi n_2/(\lambda_0 A_{\text{eff}})$, where nonlinear refractive index n_2 was $4.3 \cdot 10^{-19}$ m^2/W and effective mode area $A_{\text{eff}} = 8.8 \cdot 10^{-12}$ µm^2 at 1550 nm and $6.48 \cdot 10^{-12}$ µm^2 at 1580 nm for SC-PCF samples $NL44C2a$ and $NL44C5c$, respectively (see Fig. 3.6(b)). The time derivative term in RHS of Eq. 3.6.1 models the effects such as self-steepening and optical shock formation with $\tau_{\text{shock}} = 1/\omega_0$. The term $R(T) = (1 - f_R)\delta(t) + f_R h_R(t)$ represents the nonlinear response function which includes both instantaneous electronic and delayed Raman contribution. Fractional contribution of the delayed Raman response to

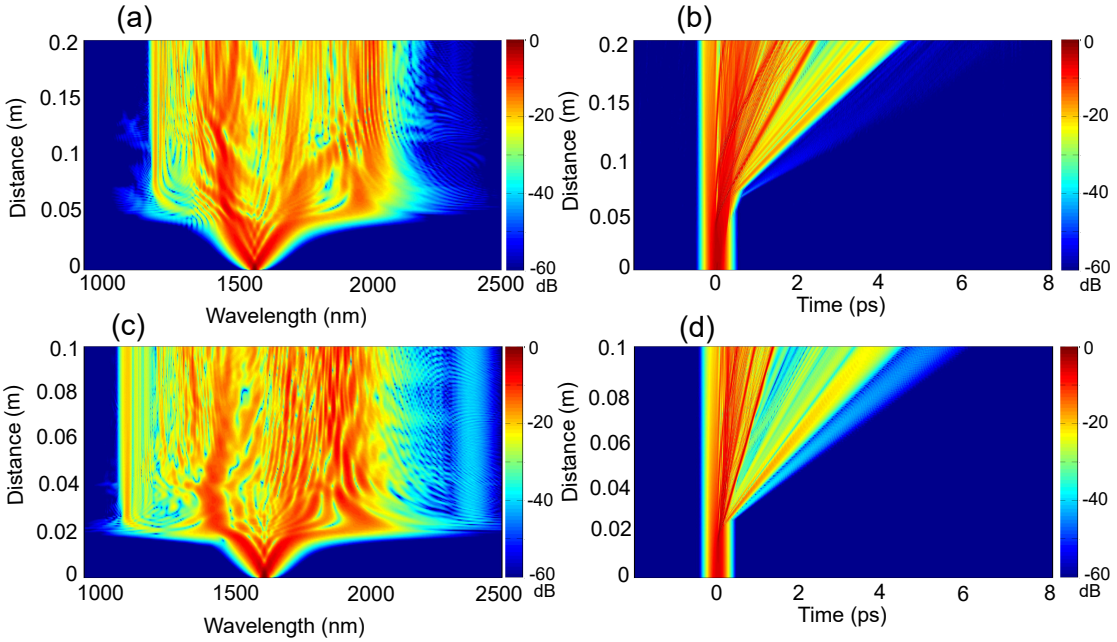

Figure 3.13: (a) & (c) Numerically generated evolution of SC spectra along the fiber length for NL44C2a & NL44C5c PCFs with 1550 nm and 1580 nm pumping, respectively. (b) & (d) Corresponding temporal distribution along the fiber length for NL44C2a & NL44C5c PCFs, respectively.

the Kerr nonlinearity, $f_R = 0.5$ was measured from Raman scattering spectra of bulk glass [244]. Raman response function $h_R(t)$ was fitted from a simulation for a different type of fiber made from the same glass where the first order Raman shift frequency was ±29 THz, and the Lorentzian fit to the first-order Raman scattering term provides the value of relaxation parameters τ_1 and τ_2 as 5.5 fs and 32 fs, respectively [244]. The input pulse was considered to be Gaussian. Frequency-resolved optical gating measurements of our input pulses (MeasPhotonics FROGscan) showed the presence of a linear chirp (parabolic phase), which was also included in the initial conditions. In the simulation for SC-PCF samples NL44C2a and NL44C5c, we used fiber lengths of 60 cm and 180 cm, and pump pulse duration of 225 fs and 220 fs, respectively. The peak power at the input of fiber was considered to be 2.5 kW for both SC-PCF samples NL44C2a and NL44C5c and they are in the same order to the experimental coupling peak powers estimated from the measured maximum output powers of 53 mW and 32 mW, corresponding to their respective maximum spectral broadening. Figures 3.13(a-d) show the evolution of numerically generated supercontinuum spectra along fiber length in spectral and time domain for the

two previously mentioned fiber samples pumped at 1550 nm and 1580 nm. Instead over the full fiber length, the pulse propagation inside the fiber is shown only up to 20 cm of fiber length in order to highlight the main nonlinear effects in SC generation as they mostly occurs in the beginning length (first few cm) of highly nonlinear fiber. In Figs. 3.13(a)&(c), strong spectral broadening can be seen in the beginning of fiber due to self-phase modulation. With increase in length, we can see soliton ejection and generation of dispersive waves. The soliton distributions as a function of time are shown in Figs. 3.13(b)&(d). We can clearly see the multiple soliton generation and time shift up to 4 ps due to soliton self frequency shift and dispersion.

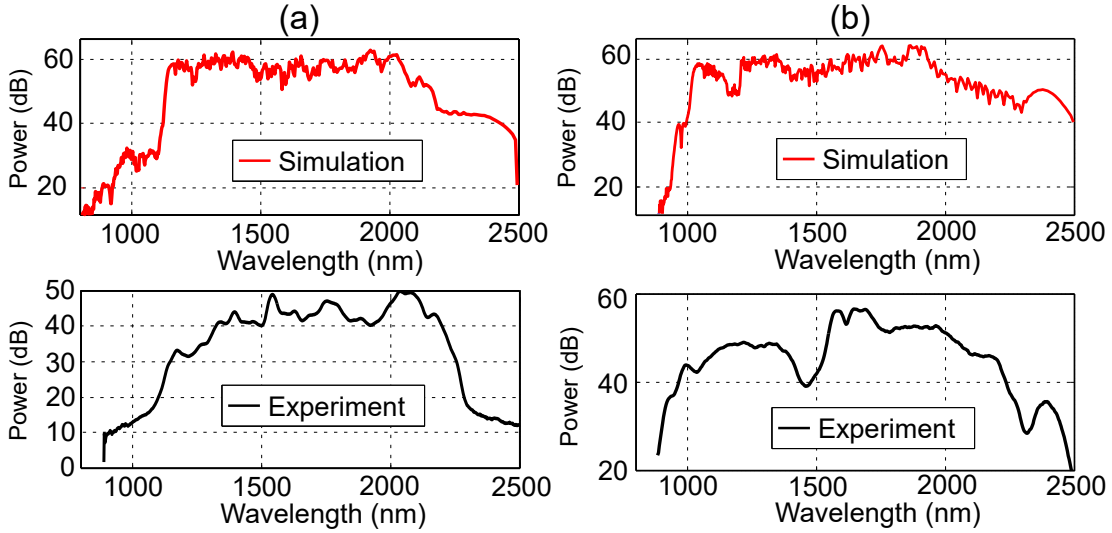

Figure 3.14: Comparison between numerically and experimentally generated SC spectra for 1550 nm and 1580 nm pumping in (a) NL44C2a and (b) NL44C5c PCFs, respectively.

The comparisons between simulation and experiment in the 1550 nm and 1580 nm pump case are shown in Fig. 3.14. Both the simulated and experimental SC spectra almost agree with each other in terms of SC bandwidth but they are quite different in terms of structure of the spectrum as can be seen from Fig. 3.14(a) for SC-PCF sample NL44C2a. We speculate that the observed discrepancy is accountable to some assumptions in the model. First, we did not take into account the wavelength-dependent losses over the full SC span and the higher-order optical modes. Second, the dispersion profile was numerically estimated from the cross-section image of the fiber structures. It is reasonable that small change of the slope of normal dispersion at wavelengths blue-shifted from the pump wavelength, would result in different dispersive wave phase matching conditions, which would be a plausible explanation to explain the short-wavelength discrepancies between the theoretical and measured spectra in Fig. 3.14. The relatively long fiber samples used in the experiment (for soft glass fibers and femtosecond pump pulses), would suggest significant contribution of the OH absorption loss, however, no such features are observed at around 1380 nm in spectra shown in Fig. 3.14. Bend loss of any higher-order mode-contained blue-shifted parts of the supercontinuum spectra could also be related to the observed discrepancies, but we did not observe such loss behavior for any reasonable bend radii in these fibers during the measurements.

3.7/ CONCLUSIONS

Wideband SC generation from 1120 nm - 2271 nm and from 891 nm - 2466 nm was demonstrated by pumping two suspended-core photonic crystal fibers in the both normal and anomalous dispersion regimes, respectively, with femtosecond pulses at 1550 nm and 1580 nm. These results demonstrate the strong potential of heavy metal-oxide SC-PCF for SC generation. Numerical simulations using nonlinear Schrödinger equation and the group velocity dispersion computed from the scanning electron microscope images of the SC-PCF samples show good qualitative agreement with the experimental one for 4.3 µm and 3.51 µm core diameter SC-PCF samples. It was further shown that strong anomalous dispersion pumping (1740 nm) of a SC-PCF sample with core diameter of 3.8 µm generates a broad spectrum from 962-2439 nm with individual high power solitons instead of a smooth SC spectrum. The SC-PCFs were drawn from high crystallization resistant heavy metal-oxide (PBG81) glass using standard stack-and-draw method. These SC-PCF structures offer tight light confinement and very small effective mode area of $8.8 \cdot 10^{-12}$ µm^2 at 1550 nm for one of these samples. The SC-PCFs show birefringence of the order of 10^{-5} to 10^{-4} due to the asymmetric six big air holes in the fiber microstructure. So, it has also been shown that tuning the input polarization angle with respect to the fiber axes affects the supercontinuum bandwidth. Since, the heavy metal-oxide glass has a high nonlinear index of $4.3 \cdot 10^{-19}$ m^2/W, short length of SC-PCF, e.g., around 60 cm is found to be enough for efficient SC generation as most of the nonlinear effects occur in the first few cm of highly nonlinear fiber. In spite of this, two out of our three experiments use a fiber length of around 180 cm. This is due to the fact that the fiber samples with an initial length of 2 meters used to get broke frequently while cleaving and handling during the experiment. Therefore, we perform the SC generation experiment with the maximum available fiber length for each samples to get the best SC spectrum at any account. It is important to stress that the SC spectra obtained using heavy metal-oxide (PBG81) glass SC-PCFs are limited by their transmission window up to 2.8 µm, which may limit their potential use for e.g., infrared spectroscopy. They are actually comparable to those can be obtained with highly nonlinear germanium-doped optical fibers [221]. The next chapter will be devoted to extending the SC in the mid-IR using chalcogenide glass based PCFs.

4

SUPERCONTINUUM GENERATION IN CHALCOGENIDE FIBERS

SUPERCONTINUUM (SC) generation towards the mid-infrared (MIR) range is a very active field of research motivated by a wide range of applications including optical coherence tomography (OCT), material processing, optical sensing and absorption spectroscopy. Among the wide variety of infrared fibers, chalcogenide-glass-based optical fibers (composed of S, Se or Te) are excellent photonic platforms for SC generation in the mid-IR due to their wider transmission window, tailorable dispersion in the mid-IR, and high optical nonlinearity up to hundred times greater than silica or ZBLAN glasses [207, 217, 236, 245, 251].

In order to obtain significant spectral broadening, the fiber should be pumped in the anomalous group velocity dispersion regime, which means the zero dispersion wavelength (ZDW) of the fiber should be close to the central wavelength of the pump laser as this will minimize the walk-off between different part of the generated spectrum allowing further broadening [166]. Most of the chalcogenide fibers have material zero group velocity dispersion far in the mid-IR. Therefore, for efficient SC generation with relatively short pump wavelengths (around 2 µm), the dispersion in chalcogenide fiber is tailored through specific waveguides as of small-core microstructured optical fibers [163, 145, 168], fiber tapering [177], or even both [178]. Furthermore, chalcogenide fiber has a little bit of disadvantage of having low damage threshold which is problematic while launching either high continuous power or high peak power pulses into the fiber. Scaling up of the fiber core is the simplest way to improve power handling capabilities in chalcogenide fiber. However, increase in core diameter comes with a cost. It results in low nonlinearity in the fiber and multimode propagation, which affect the further extension of SC spectrum. Therefore, one way to increase the nonlinearity while maintaining a moderate damage threshold is to reduce the core diameter of the fiber along the propagation distance through thermal tapering. Fiber tapering is a very well-known post-processing technology. Taper fiber increases the optical nonlinearity as well as enables dispersion engineering of the fiber. Birks et al. in 2000 first demonstrated that by tapering a large-core SMF-28 step-index silica fiber, efficient SC generation could be obtained with high coupling efficiency [71]. Since then, many researchers tried to implement this scheme in mid-IR using chalcogenide fibers. In 2007, Mägi et al. first reported the use of chalcogenide tapered fibers, where a 1.2 µm taper-waist core diameter As_2Se_3 taper offers a nonlinear coefficient γ of 68000 $W^{-1}km^{-1}$, which was 62000 times larger than that of silica single-mode fiber [137]. In 2011, Hudson et al. demonstrated an octave spanning

SC generation from 0.97 to 1.99 µm in an As_2S_3 tapered fiber with a core diameter of 1.3 µm by pumping at 1.55 µm with only 77 pJ of pulse energy [177]. Rudy et al. in 2013 reported a SC generation from 1-3.7 µm in an As_2S_3 tapered fiber pumped by a 2 µm thulium-doped fiber laser with about 300 pJ of pulse energy [196]. In 2014, Al-kadry et al. demonstrated a SC generation covering a bandwidth from 1.1 to 4.4 µm in a 10 cm long and 1.6 µm diameter As_2Se_3 microwire by pumping with 500 pJ of pulse energy at a wavelength of 1.94 µm [200]. Petersen et al. recently reported a broadband SC spanning from 1 to 11.5 µm with an average output power of 35.4 mW by pumping a 5.9 µm-diameter tapered $Ge_{10}As_{22}Se_{68}$ PCF at 4 µm [236]. Despite significant progress in this field, SC generation in the mid-IR beyond 6 µm with high average output power is still remains challenging in chalcogenide step-index tapered fibers.

On the other hand, there is particular interest in combining the chalcogenide fiber platform with polarization-preserving properties as this will enable polarization-dependent applications in interferometric techniques, gas and pressure sensing, integrated-optic devices and also polarization-sensitive OCT [40, 41, 147, 157, 171, 248]. Polarization-maintaining fibers also help in minimizing detrimental effects such as polarization noise and instability [240]. There are several ways of introducing strong birefringence in the fiber for polarization-maintaining propagation. For instance, birefringence can be obtained by applying mechanical stress in the cladding thus inducing anisotropy of the refractive index in the core region, which results in a modal birefringence up to $5 \cdot 10^{-4}$ for the so-called PANDA fibers [19, 23, 44] and close to 60% higher birefringence in bow-tie fibers [20]. Highly birefringent fibers can also be fabricated using the powder-in-tube process where two rods of glass material are placed on the sides of the core [234]. Another way of obtaining high birefringence is by breaking the symmetry of the fiber structure. This was achieved in photonic crystal fibers (PCFs) where an asymmetric arrangement of air holes is designed with two different diameter air holes located in orthogonal position near the core of the fiber, thus providing higher effective index difference between the two orthogonal polarization modes [77, 81, 105, 87, 216]. In addition to the alteration of air hole diameter in the core region of PCFs, an asymmetric structure can also be obtained by either introducing mechanical stress [124] or modifying the shape of air holes [132]. It has been shown that the birefringence of silica based polarization-maintaining photonic crystal fibers (PM-PCFs) can reach high values up to 10^{-3} [81, 87, 216], which is one order of magnitude higher than that of conventional PANDA or bow-tie silica fibers [19, 23, 44, 20].

In this chapter, we demonstrate SC generation in chalcogenide glass based polarization-maintaining photonic crystal fiber (PM-PCF) and non-PM-PCF tapers using femto second pulses. This work results from a collaboration between the FEMTO-ST Institute, the University of Rennes, the SelenOptics company, and the DTU Fotonik, in the framework of the European H2020-MSCA-ITN SUPUVIR project. The author of this thesis did a secondment in the University of Rennes and the SelenOptics company with Prof. Johann Troles and Dr. Laurent Brilland where he participated in chalcogenide glass fabrication, PCFs drawing, and fabrication of tapers. He did another secondment in the DTU Fotonik with Prof. Ole Bang and Dr. Christian R. Petersen where he characterized the chalcogenide PCFs and tapers to generate supercontinuum spectra. Here we outline the methods for fabrication of chalcogenide glass, polarization-maintaining photonic crystal fibers, and fiber tapers in Section 4.1 and 4.2. Optical transmission and attenuation of the fibers and tapers are provided in Section 4.3. In Section 4.4, we discuss the numerical computations of the group-velocity dispersion and the birefringence of the fibers.

We show in particular how we can tailor both the birefringence and the dispersion by tapering the PCF down to a few µm core diameter. The experimental setup for mid-IR SC generation is explained in Section 4.5. In Section 4.6, we show experimental results of broadband SC spectra in PM-PCF and non-PM-PCF tapers at different pump wavelength. The effect of pump polarization angle is finally investigated in the PM-PCF both experimentally and numerically using two-coupled generalized nonlinear Schrödinger equations (GNLSEs). The effect of taper-waist core diameter and taper-waist length on the SC bandwidth by both direct pumping and pumping in cascaded system is further shown here. Finally, power damage threshold measurement of chalcogenide fiber, a colaboration work between the Femto-st Institute and the University of Rennes, is described in Section 4.7.

4.1/ CHALCOGENIDE GLASSES

Chalcogenide glasses are very attractive optical photonic materials due to their wide transparency range, low optical losses, stability to atmospheric moisture, and high optical non-linearity (typically ~ 500 times more than traditional silica glasses)[199, 186]. Chalcogenide glasses contain at least one chalcogen elements such as S, Se, and Te. Depending on the composition, chalcogenide glasses can be transparent from visible up to 12 µm for sulfide, up to 16 µm for selenide, and up to 25 µm for telluride glass [239]. These glasses also have high linear refractive indices such as between 2.2 and 2.6 for sulfide, 2.4 and 3.0 for selenide, and 2.6 and 3.5 for telluride glasses [154]. Because of these unique properties, chalcogenide glasses are excellent candidates for SC generation towards the mid-IR and their applications.

4.1.1/ GLASS FABRICATION

The chalcogenide glass ($As_{38}Se_{62}$), which will be described in this thesis in details, was made at the University of Rennes and the SelenOptics company in France, where the author of this thesis participated in the glass fabrication process as a part of his PhD secondment. It was produced using the conventional melt-quenching method through several steps, which includes two stages of synthesis, annealing, quenching, and distillation [253, 233, 214]. Before the main synthesis process, we will discuss about the preparation of all necessary materials. During the glass preparation process, hydrogen and oxygen may be produced due to the presence of some water content in the glass. Therefore, the water needs to be removed in order to increase the purity of the glass and to remove absorption peak due to water contamination. We used tellurium chloride ($TeCl_4$), and magnesium to remove hydrogen and oxygen, respectively. $TeCl_4$ with hydrogen produces hydrocloric acid (HCl) and magnesium with oxygen produces magnesium-oxide (MgO), which were removed during dynamic distillation process later. Since, magnesium stored in plastic container gets oxidized very easily, it was treated with HCl and distilled water before we mix it with other materials. Next the silica ampoule (i.e., the housing of prepared glass) was also treated with hydrofluoric acid (HF) and distilled water. Then inside a glove box, the silica ampoule was filled with high purity arsenic (As) (99.999), Se (99.999), $TeCl_4$ (200 mg) and magnesium (20 mg). After that the silica ampoule was taken out of the glove box and placed in a two-stage vacuum pump, which is shown in Fig. 4.1. The primary pump is an oil pump to create vacuum inside the silica ampoule in the first stage and the second one is a turbo molecular pump to achieve ultra-vacuum. The blue cylinder contains a cylindrical glass trap, inside which, there is a spiral tube in

Figure 4.1: A two-stage vacuum pump, consisting of an oil pump and a turbo molecular pump where the silica ampoule (filled with glass materials as highlighted by the red circle) is pumped to achieve vacuum.

order to make extra space for the gas/impurities to cool down. This trap works as a condensation trap, which blocks both the flow of liquid from vacuum pump to silica ampoule (or the distillation tube during the case of distillation process later) and the flow of impurity gases into the vacuum pump. Outside of the glass trap, i.e., the rest of the blue cylinder is filled with liquid nitrogen that cools down the impurity gases. The silica ampoule was then pumped here for approximately 3 hours to create vacuum inside the ampoule. During the filling of silica ampoule in the glove box, selenium was poured at the top along with arsenic and $TeCl_4$ at the bottom, and magnesium in the middle so that after achieving the vacuum, selenium at the top can be melt using an external heater in order to make more space inside of it. Finally, the top end of the silica ampoule was sealed with a glass blower.

4.1.1.1/ FIRST SYNTHESIS

At this stage, we will start the first synthesis process. Here the previously filled silica ampoule will be put inside a furnace, which is shown in Fig. 4.2(a). Before putting into furnace, the ampoule was covered with an iron net to block the broken silica glass pieces and other material from spreading in case of an explosion inside the furnace. The ampoule was then inserted inside the furnace and the remaining part of the furnace is blocked with an insulating glass wool (can tolerate high temperature), which prevents the heat leakage from the furnace. The furnace has a rotational motion that enables uniform mixture of molten materials. The furnace's temperature was initially at 450 °C when the silica am-

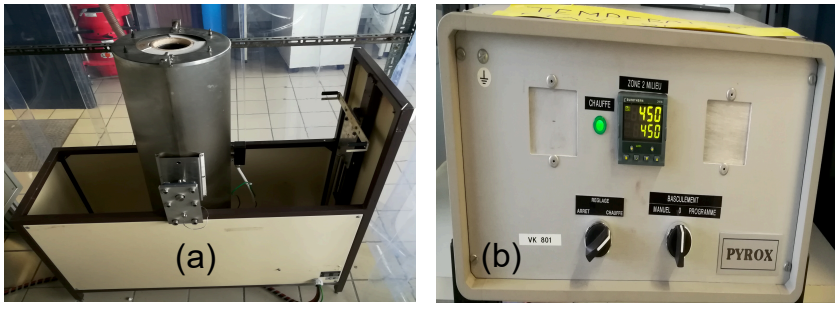

Figure 4.2: (a) Furnace for the synthesis of our glass. (b) Synthesis-furnace controller.

poule was being inserted into it. The temperature of the furnace was then programmed using the furnace controller as shown in Fig. 4.2(b). The evolution of the temperature inside the furnace progresses was as follows: temperature increased from 450℃ to 850℃ in 4 hours and maintained this temperature for 30 minutes, then decreased to 810℃ in one hour, again maintained this temperature for 30 minutes, and finally decreased to 700℃ in 2 hours. After the first synthesis was done in 8 hours, the silica ampoule was kept inside the furnace at 700℃ for 4 hours and then it was taken out of the furnace and placed into a water bucket for 15-20 seconds. This process is called quenching, which prevents crystallisation. In order to relieve the thermal stresses caused by quenching, the ampoule was then annealed at a temperature slightly below the glass transition temperature (T_g) around 165℃ for 30 minutes inside an annealing furnace and after that, it was gradually cooled down to room temperature in 6 hours. Finally, the resultant chalcogenide glass was retrieved by breaking and removing the silica ampoule. In order to reduce absorption due to different impurities in the glass and to have a better transmission window, the resultant chalcogenide glass was purified through two distillation processes namely dynamic distillation, which was performed in an open setup and static distillation, which was performed in a sealed tube setup.

4.1.1.2/ DYNAMIC DISTILLATION

In the first step, the impurity gases like HCl and CCl_4 were removed from the chalcogenide glass using dynamic distillation [253]. This distillation process is called dynamic distillation as it is performed with the dynamic two-stage vacuum pump. At first, the retrieved chalcogenide glass (including impurities) from the silica ampoule was filled in one chamber of a two-chamber distillation tube (properly treated with HF and distilled water). Then the distillation tube was mounted on a settings attached with a two-stage vacuum pump and a localized heater in a way such that the half portion of the empty batch chamber (considered as first chamber) and the full portion of the filled batch chamber (considered as second chamber) stays inside the localized heater as shown in Fig. 4.3. The rest part

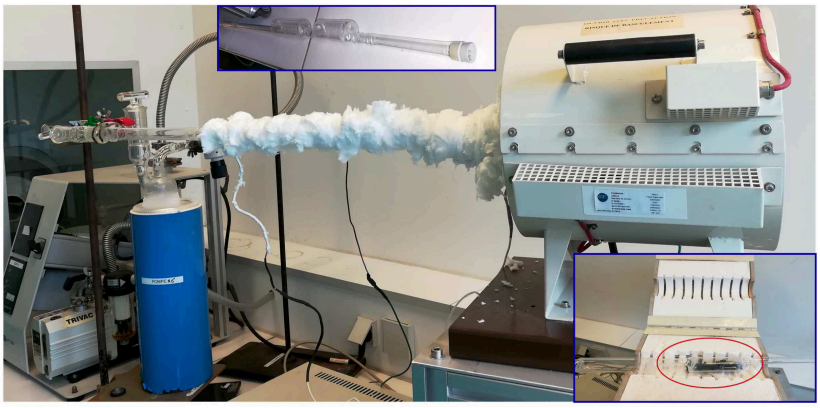

Figure 4.3: Dynamic distillation setup. Inset(top-middle): two-chamber distillation tube. Inset (bottom-right): the inner part of the localized heater where the half portion of the empty chamber and the full portion of the filled chamber (with chalcogenide glass as highlighted by the red circle) of the distillation tube is placed.

of the distillation tube was covered with an insulating glass wool to trap the heat from the localized heater. The temperature of the heater was initially kept at 400℃ for 30 minutes and then gradually increased to 600℃ in 12 hours. During the distillation process, at first,

all the impurity gases (HCl gas and CCl_4) will pass through the distillation tube and be sucked into the condensation trap. Then all the distilled material/glass from the second batch chamber will come to the first batch chamber and also in the lower part of the beginning length of the distillation tube as the upper part/cross section of the tube will be empty, which was used to create vacuum. The remaining impurities like MgO, which did not go through the distillation process due to high melting temperature of around 2852℃ will stay at the second batch chamber.

4.1.1.3/ STATIC DISTILLATION

In the second step, static distillation was performed to remove carbon, silica and other refractory oxides from the glass. It is called static distillation as it is performed without the vacuum pump. After the dynamic distillation, the second batch chamber filled with impurities was removed by sealing the distillation tube from one end of first batch chamber to first few cm of the distillation tube (i.e., the region covered with white cotton like substance where the distilled glass was deposited) on the other side of the first batch chamber using a glass blower. Then the sealed distillation tube was placed inside a furnace. The furnace was initially fixed at an inclined position and it has a hot zone and a cold zone as shown in Fig. 4.4. The position of distillation tube inside the furnace is also shown in the same figure. The furnace was heated at 640℃ for 10 minutes in order to melt the chalcogenide glass inside the distillation tube. After 10 minutes, the distillation tube inside the furnace was rotated to place the batch chamber in downward direction and a small part of the distillation tube was placed outside the furnace to expose it to cold environment i.e., at room temperature instead of using the cold zone of the furnace. Now the position of the furnace was changed from inclined to vertical state and its temperature was increased to near 700℃. During the static distillation process, the distilled glass will travel from the batch chamber to the cold part of the distillation tube outside the furnace in vapour form and will be deposited there leaving behind the impurities like carbon, silica and other refractory oxides in the batch chamber inside the furnace.

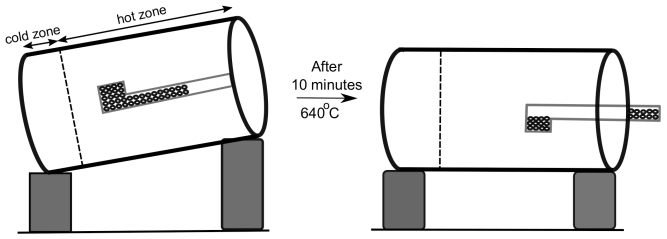

Figure 4.4: Different states of static distillation process

4.1.1.4/ SECOND SYNTHESIS

Since, during the two distillation processes, different materials from the chalcogenide glass were distilled at different speed due to their different melting point, which in turn separates the glass into different compounds physically. For this reason, the resultant distilled glass needs a second synthesis process in order to homogenize the glass material. Hence, after second distillation, the silica ampoule filled with distilled glass was sealed with a glass blower to remove the batch chamber with impurities and then it was placed inside the same furnace (as shown in Fig. 4.2(a)) for a second synthesis, where the glass was again homogenously heated for 10 hours at 850℃. Then the ampoule was

cooled down to 500℃, quenched and finally annealed below T_g to remove any mechanical constraints. Finally, the $As_{38}Se_{62}$ glass was retrieved from silica ampoule and stored in glove box to avoid contamination and water exposure. Using the similar procedure as above, a $Ge_{10}As_{22}Se_{68}$ glass (T_g is around 180℃) was also prepared with slightly different heating time and temperature of the furnaces than the $As_{38}Se_{62}$ glass.

4.1.2/ GLASS PROPERTIES

The nonlinear refractive index of $As_{38}Se_{62}$ glass and $Ge_{10}As_{22}Se_{68}$ glass are $1.1 \cdot 10^{-17}$ m^2/W and $8.8 \cdot 10^{-18}$ m^2/W, which are approximately 420 times and 350 times higher than silica value, respectively [73, 151]. The linear refractive index of $As_{38}Se_{62}$ glass and

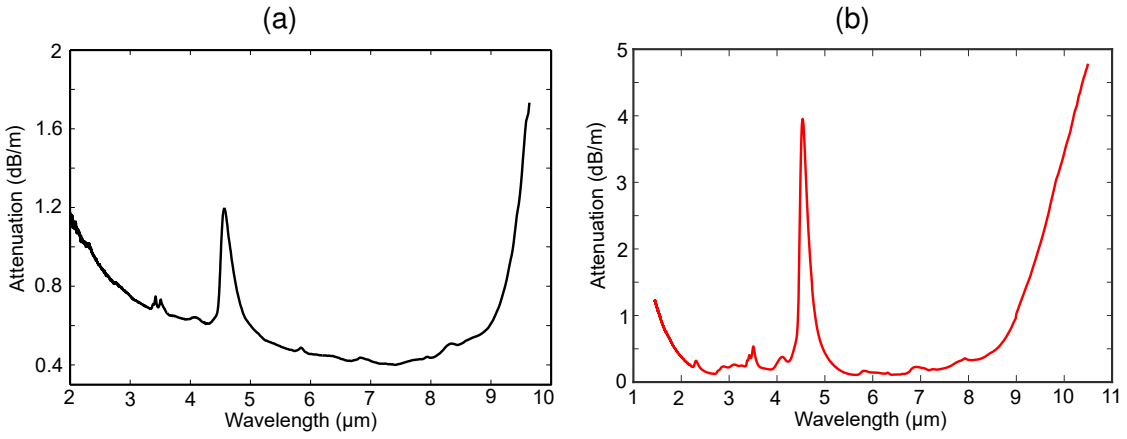

Figure 4.5: Attenuation spectrum of (a) $As_{38}Se_{62}$ glass and (b) $Ge_{10}As_{22}Se_{68}$ glass.

$Ge_{10}As_{22}Se_{68}$ glass at 1550 nm are given by 2.818 and 2.622, respectively [189]. The attenuation spectrum of bulk glass measured with a Bruker Tensor 37 FTIR spectrometer is shown in Fig. 4.5(a) for $As_{38}Se_{62}$ glass and in Fig. 4.5(b) for $Ge_{10}As_{22}Se_{68}$ glass. From Fig. 4.5(a), we can see that $As_{38}Se_{62}$ glass offers light transmission from 2 to 9.4 μm range with a minimum attenuation of 0.40 dB/m at 7.42 μm and an absorption peak at 4.56 μm due to the presence of Se-H chemical bonds. For $Ge_{10}As_{22}Se_{68}$ glass, the light transmission window covers from 1.5 to 10 μm with a minimum attenuation of 0.19 dB/m at 5.61 μm and it also has an absorption peak at 4.54 μm due to the presence of Se-H chemical bonds as can be seen from Fig. 4.5(b). Both of the glasses also show a very small absorption peak at 3.5 μm due to surface contamination by C–H bonds of non-cyclic organic compounds.

4.2/ FABRICATION OF CHALCOGENIDE PHOTONIC CRYSTAL FIBER (PCF)

In this section, we will describe the drawing procedure of microstructured photonic crystal fibers from chalcogenide glass. The fibers were drawn at the University of Rennes and the SelenOptics company in France. We fabricated two different type of fibers: highly birefringent polarization-maintaining photonic crystal fiber (PM-PCF) from $As_{38}Se_{62}$ glass and regular lattice PCF (non-PM) from $Ge_{10}As_{22}Se_{68}$ glass. Several tapers from both type of PCFs were further fabricated directly on the drawing tower. Since, both types of PCFs and PCF tapers from two different glasses were fabricated through similar process,

only the fabrication process of PM-PCF and tapers are reported in this section. Brilland et al. in [144] reported that drawing of microstructured PCFs from chalcogenide glass using conventional stack-and-draw method is not efficient as defects appear at the glass interfaces when the interstitial holes are collapsed during drawing, which results in strong optical losses above 20 dB/m without depending on the glass composition (Ge-Sb-S, As-Se, Te-As-Se). Therefore, here the PCFs were drawn from a preform, which was fabricated with an alternative method known as moulding method as described below.

4.2.1/ PREFORM FABRICATION

The PM microstructure preform containing 36 air holes organized in 3-rings, shown in Fig. 4.7(a), was prepared using the molding method [165]. In this method, the highly purified $As_{38}Se_{62}$ glass (as described in Section 4.1.1) is heated and flowed into a silica mold, which has the negative shape of the final preform. The silica mold is made of silica-glass capillaries with a thickness of 30 µm. These capillaries are organized in a hexagonal periodical pattern, using slices of a silica microstructured preform to keep them in place. The hole diameter (d_{hole}) is 460 µm and the pitch (Λ) is 1350 µm. In order to make a PM preform, the geometry of slices is modified (from regular lattice PCF) by placing two larger holes with a diameter of 650 µm in diametrically-opposed positions in the first ring, while maintaining the diameter of small air holes (d_{SA})/Λ ratio. Both the $As_{38}Se_{62}$ glass rod and the silica mold are placed in a silica ampoule. The ampoule is then heated in a rocking furnace at 600℃ for one hour so the chalcogenide glass can flow down in to the mold having a glass viscosity about 10^{-4} Pa.s. After that, air quenching is performed on the full mold for four minutes before annealing it at 165℃ for one hour. The silica tube around the preform is then removed with a diamond tool. At the final step, the chalcogenide preform is obtained by removing the embedded silica capillaries with a hydrofluoric acid treatment. The final $As_{38}Se_{62}$ glass preform has a diameter of around 16 mm and a length of 80 mm.

4.2.2/ FIBER FABRICATION

PM-PCF is drawn from the preform through the following procedure. At first, $As_{38}Se_{62}$ preform is installed in the drawing tower inside a silica glass enclosure, through which helium gas is flowed to remove any remaining moisture from inside it, as shown in Fig. 4.6(a). An annular electrical furnace is placed around the preform in such a way that it helps to heat the lower part of the preform. Both the preform chamber and the furnace chamber were filled with helium gas. The temperature of the annular furnace is increased until a drop of glass fall down from the preform due to the gravitational force (around 340℃) as shown in Fig. 4.6(b). Then the fiber accompanying the drop is attached to a rotating drum to continue the drawing while the preform is being fed gradually inside the annular furnace in the same time. During the drawing process, the desired air-hole diameter is obtained by controlling the helium gas pressure inside the enclosure. For a given feeding speed of the preform into the furnace, the diameter of the fiber is further controlled by the pulling speed of the rotating drum. Figures 4.7(b)&(c) show the scanning electron microscope (SEM) images of the $As_{38}Se_{62}$ PM-PCF drawn from the preform. As can be seen, it consists of 36 circular air holes in 3 rings with 2 larger air holes adjacent to the core that provides strong birefringence and polarization maintaining guiding. The distance between the closest points of the two large air holes, known as core diameter (d_{core}), is 8.11 µm and the outer diameter (d_{out}) of the PCF is 125 µm. The diameter of the large air holes (d_{LA}) and small air holes (d_{SA}) are 5.8 µm and 3.35 µm, respectively. The distance between two small air holes, also known as the pitch (Λ) is 7.025 µm, which gives a d_{SA}/Λ

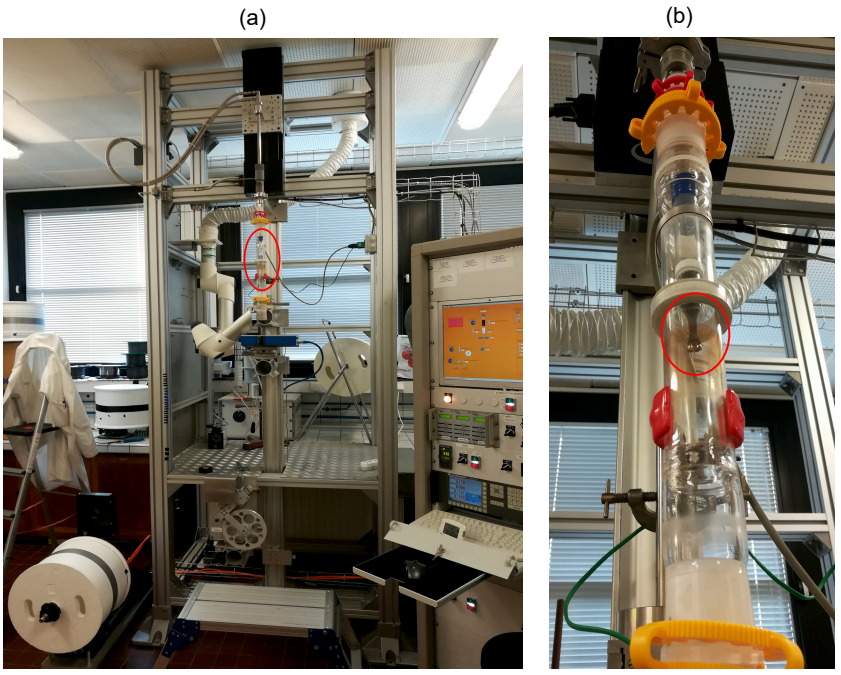

Figure 4.6: (a) Fiber drawing tower with the preform mounted on it inside an annular furnace (marked in red circle). (b) The event of neck down and the first drop from the preform at around 340℃ due to the gravitational force, highlighted by a red circle in the image.

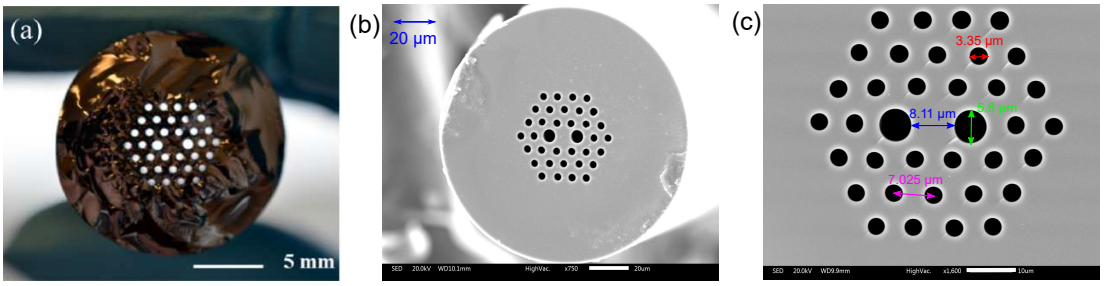

Figure 4.7: Cross-section images of $As_{38}Se_{62}$ preform and solid-core microstructured fiber. (a) Preform of $As_{38}Se_{62}$ glass. (b) SEM image of $As_{38}Se_{62}$ PM-PCF with an outer diameter (d_{out}) of 125 µm. (c) Expanded view of the microstructure region showing core diameter (d_{core} = 8.11 µm), small air hole diameter (d_{SA} = 3.35 µm), and pitch (Λ = 7.025 µm).

ratio of 0.477 that makes the PCF with uniform holes endlessly single-mode in the mid-IR [118].

4.2.3/ TAPER FABRICATION

$As_{38}Se_{62}$ PM-PCF tapers were directly made on the drawing tower (see Fig. 4.6(a)) using the following method. One end of a previously drawn PM fiber (as described in Section 4.2.2) with a length of 80 cm is glued (a special kind of glue which is dried using a UV lamp) with the fixing rod of the drawing tower. Then the annular electrical furnace is placed in the middle portion of the fiber. The other end of the PM fiber is glued with a silica fiber, which is fixed with the rotating drum. Then helium flow is being started inside

the furnace and a suction pump attached to the furnace is enabled to suck moisture and chalcogenide vapour from the furnace. In this case, the outer fibre diameter was 162 µm. Finally, the taper is obtained by drawing a second time the fiber at around 210 ℃ with a

Table 4.1: Fabrication parameters and taper-waist length of different tapers.

Taper type	Taper d_{core} (µm)	Taper d_{out} (µm)	Pulling speed (m/min)	Feeding speed (mm/min)	Taper length (cm)
$As_{38}Se_{62}$ PM-PCF	1.77	28.74	0.05	1.6	27,40,53
$Ge_{10}As_{22}Se_{68}$ PCF	2.5	28.53	0.05	1.5	5,12
	3	34.24	0.05	2.1	12,28
	4	45.65	0.05	3.8	16,26,34
	5	57.06	0.05	5.9	20,30
	6	68.47	0.05	8.5	11,30

Table 4.2: Mean structural parameters of $As_{38}Se_{62}$ PM-PCF and $Ge_{10}As_{22}Se_{68}$ PCF measured in the untapered fiber and in the taper-waist using SEM image.

	Initial fiber					Taper waist				
Taper type	d_{core} (µm)	d_{out} (µm)	d_{SA} (µm)	Λ (µm)	d_{SA}/Λ	d_{core} (µm)	d_{out} (µm)	d_{SA} (µm)	Λ (µm)	d_{SA}/Λ
AsSe	10	162	4.25	8.51	0.499	1.77	28.74	0.808	1.69	0.478
GeAsSe	14.59	166.5	5.23	10.36	0.504	6	68.47	2.04	4.13	0.494

tensile strength around 30 g. Since the initial PM fiber has an d_{out} of 162 µm and d_{core} of 10 µm, the output diameter of the waist should be 28.74 µm, which corresponds to an approximate core diameter of 1.77 µm in the taper-waist region. For this purpose, for a given pulling speed (0.05 m/min) of the rotating drum, the feeding speed of the preform into the furnace is calculated as 1.6 mm/min as reported in Table. 4.1.

For the $Ge_{10}As_{22}Se_{68}$ PCF tapers, d_{out} and d_{core} of the normal region were 166.5 µm and 14.59 µm. Therefore, similarly, d_{out} and d_{core} of the taper-waist region, fixed pulling speed, and calculated feeding speed for different tapers with different taper-waist core diameter are reported in Table 4.1. The obtained tapers from both glass compositions have a down-taper section length (L_{DT}) of 2–3 cm, uniform taper-waist section length (L_W) of 27–53 cm for $As_{38}Se_{62}$ PM-PCF and 5-34 cm for $Ge_{10}As_{22}Se_{68}$ PCF, and up-taper section length (L_{UT}) of 2–3 cm as shown in Figs. 4.8(a)&(b), respectively. Figures 4.8(c-g) represent the SEM images of the normal section and tapered section of $As_{38}Se_{62}$ PM-PCF taper and $Ge_{10}As_{22}Se_{68}$ PCF taper.

It was not possible to take SEM images of taper-waist section of all individual tapers having different taper-waist d_{core} without destroying them. Therefore, we have reported the geometrical parameters of only one $Ge_{10}As_{22}Se_{68}$ PCF taper and one $As_{38}Se_{62}$ PM-PCF taper with taper-waist of 6 µm and 1.77 µm, respectively, as given in Table 4.2.

Proper maintenance of d_{SA}/Λ ratio during the taper fabrication provides closer values of

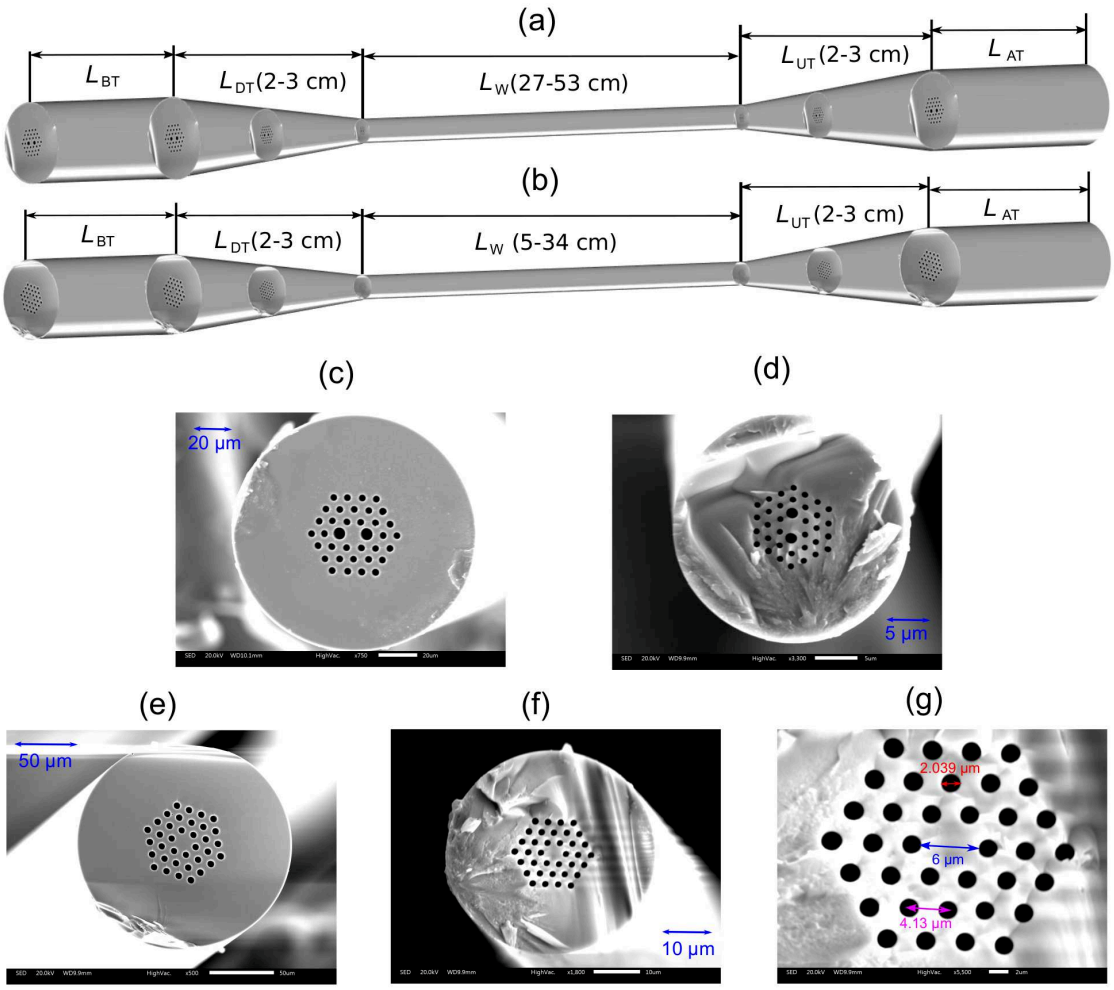

Figure 4.8: (a) & (b) Schematic of longitudinal sections of $As_{38}Se_{62}$ PM-PCF tapers and $Ge_{10}As_{22}Se_{68}$ PCF tapers, respectively: length before taper (L_{BT}), length of down-taper section (L_{DT}), length of uniform taper-waist section (L_W), length of up-taper section (L_{UT}), and length after taper (L_{AT}). (c) & (d) Cross-section images of normal section and taper-waist section of $As_{38}Se_{62}$ PM-PCF with respective outer diameter (d_{out}) of 162 µm and 28.74 µm and respective core diameter (d_{core}) of 10 µm and 1.77 µm. (e) Cross-section image of normal section of $Ge_{10}As_{22}Se_{68}$ PCF with d_{out} of 166.5 µm and d_{core} of 14.59 µm. (f) Cross-section image of taper section of $Ge_{10}As_{22}Se_{68}$ PCF with d_{out} of 68.47 µm and an expanded view of the taper waist region in (g) showing d_{core} = 6 µm, d_{SA} =2.039 µm, and Λ = 4.131 µm.

0.499 and 0.478 for the normal section and the taper section, respectively for the $As_{38}Se_{62}$ PM-PCF taper and values of 0.504 and 0.494 for $Ge_{10}As_{22}Se_{68}$ PCF taper.

4.3/ OPTICAL TRANSMISSION AND ATTENUATION OF FIBERS

In this section, we will discuss about the optical attenuation and transmission of the $As_{38}Se_{62}$ PM-PCF, $Ge_{10}As_{22}Se_{68}$ PCF, and the PCF tapers, which are described in the previous section. The attenuation of the drawn $As_{38}Se_{62}$ PM-PCF with a core diame-

ter of 8.11 µm and $Ge_{10}As_{22}Se_{68}$ PCF with a core diameter of 14.9 µm were measured with a Bruker Tensor 37 FTIR spectrometer equipped with a liquid nitrogen cooled mercury–cadmium–tellurite (MCT) detector having a sensitivity from 1.2 to 14 µm, as shown in Fig. 4.9. The attenuation of the fibers were precisely measured using the standard cut-back technique and guidance of cladding modes was eliminated by applying a layer of graphite on the surface of the fiber during the measurement. Figure 4.9(a) shows light transmission in the $As_{38}Se_{62}$ PM-PCF between 2 µm and 9.4 µm with a minimum attenuation of 0.25 dB/m at 6.64 µm. Two absorption peaks can be observed in the attenuation spectrum of the fiber including a peak at 4.56 µm due to the presence of Se-H bonds (as in the bulk sample, see Fig. 4.5(a)) and another peak at 6.3 µm due to the presence of H_2O molecules. The attenuation spectrum of $Ge_{10}As_{22}Se_{68}$ PCF, as can be seen from

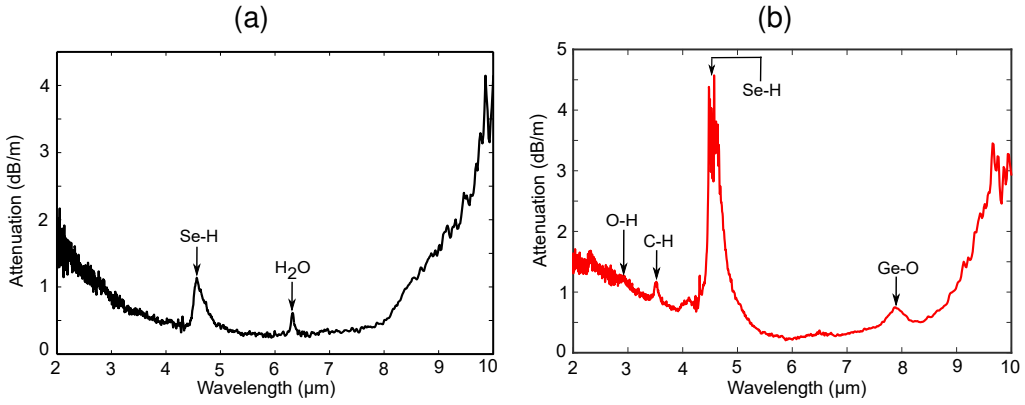

Figure 4.9: Attenuation spectrum of (a) $As_{38}Se_{62}$ PM-PCF with cut-back length of 3.35 m and (b) $Ge_{10}As_{22}Se_{68}$ PCF with cut-back length of 4.3 m, measured with a Bruker Tensor 37 FTIR spectrometer.

Fig. 4.9(b), shows light transmission from 2 µm up to 10 µm with a minimum attenuation of 0.204 dB/m at 5.88 µm. The attenuation spectrum also shows four notable absorption peaks as follows: first small peak from left at 2.9 µm due to the presence of O–H bonds, second peak at 3.5 µm due to surface contamination by C–H bonds of non-cyclic organic compounds, the third peak at 4.56 µm due to the presence of Se-H bonds (as in the bulk sample, see Fig. 4.5(b)), and the fourth peak at 7.9 µm due to the presence of Ge-O bonds.

The power transmission (i.e., the percentage of incident power (at the input facet of the fiber) that is transmitted at the output of the fiber) of a tapered $As_{38}Se_{62}$ PM-PCF with taper-waist of 1.77 µm and taper-waist length of 27 cm was measured to be 13% at 1.55 µm using an 1 mW continuous wave (CW) laser and a Thorlabs power meter. Then, the transmission spectra of all three $As_{38}Se_{62}$ PM-PCF tapers with a taper-waist length of 27 cm, 40 cm, and 53 cm were measured with the same FTIR spectrometer as previous, which is shown in Fig. 4.10(a). The tapers transmit light from 1.84 to 5.23 µm (at the 3 dB level of maximum transmission) and there is no significant change in transmission window with taper length. However, the transmission bandwidth is significantly reduced compared to the untapered PM-PCF (see Fig. 4.9(a)) and there are three transmission dips clearly visible because of the presence of three new absorption bands at 2.9 µm due to O–H bonds, at 3.5 µm due to surface contamination by C–H Bonds of non-cyclic organic compounds, and at 4.25 due to CO_2 molecules. These are mainly due to the contamination of the taper-waist, non-adiabatic taper transitions during taper drawing process, and high

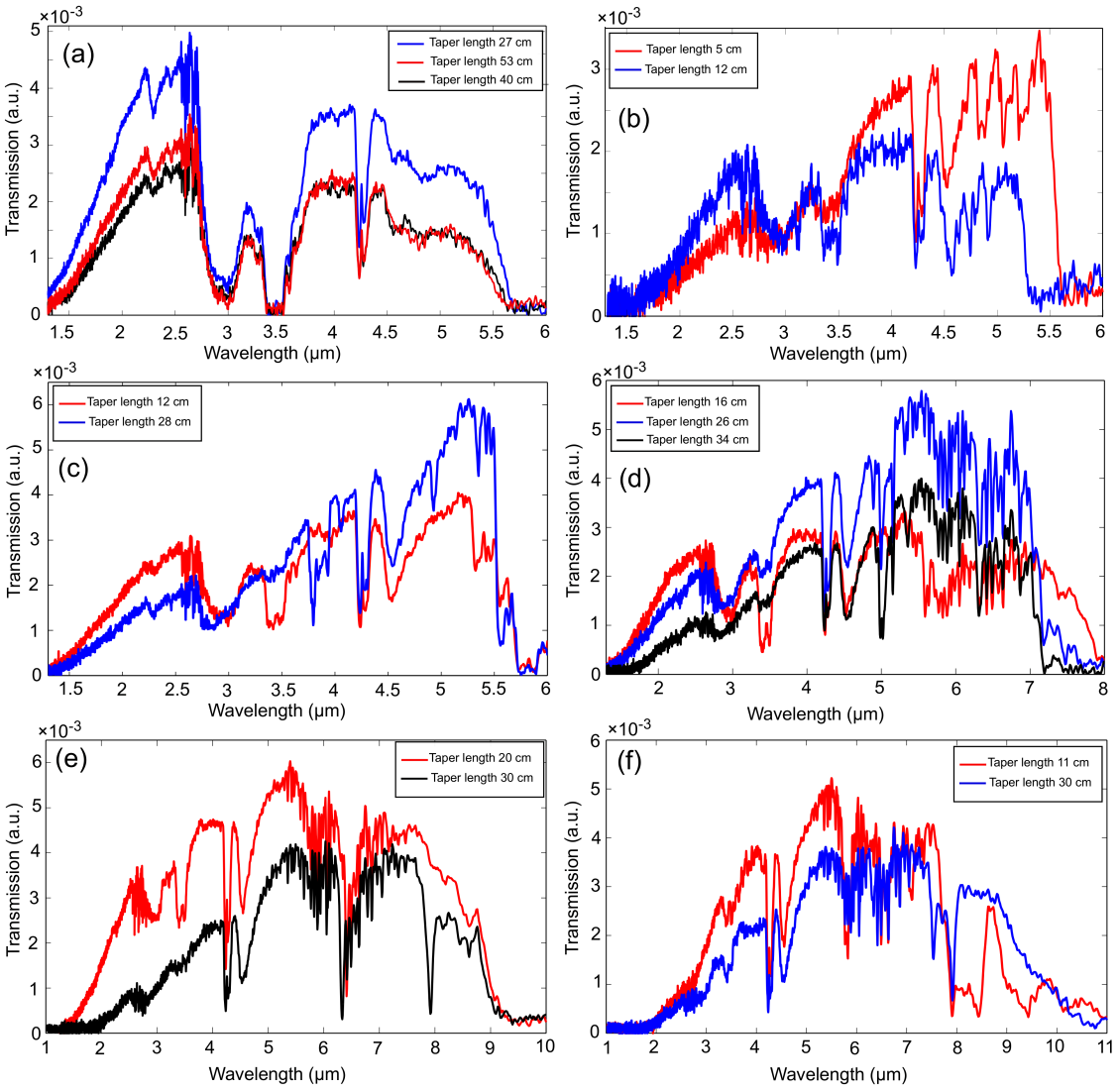

Figure 4.10: Qualitative transmission spectra of different chalcogenide tapered fibers measured with a Bruker Tensor 37 FTIR spectrometer: (a) $As_{38}Se_{62}$ PM-PCF tapers with different taper-waist length having a waist diameter 1.77 µm. (b-f) $Ge_{10}As_{22}Se_{68}$ PCF tapers with different taper-waist length having a waist diameter of (b) 2.5 µm, (c) 3 µm, (d) 4 µm, (e) 5 µm, and (f) 6 µm.

confinement loss for non-uniform and small taper-waist. This unfortunately prevents the use of the $As_{38}Se_{62}$ PM-PCF tapers for mid-IR SC generation beyond 5.5 µm and we will therefore in Section 4.6 focus on the straight $As_{38}Se_{62}$ PM-PCF for mid-IR SC generation.

The transmission spectra of $Ge_{10}As_{22}Se_{68}$ PCF tapers with 5 different taper-waist core diameters, such as 2.5 µm, 3 µm, 4 µm, 5 µm, and 6 µm having different set of taper-waist length are further measured, which are shown in Figs. 4.10(b-f). The transmission spectra are recorded to be compared to the untapered initial fiber attenuation and in order to check the transmission windows which is strongly linked to the core size. Indeed, when the core size is smaller than the propagated wavelength, additional confinement losses appear due to the structure of the PCF. From Figs. 4.10(b-f), we can see that, the transmission window inside the tapers increases with increasing taper-waist core di-

ameter and we obtained maximum transmission window from 3.3 µm up to 9.1 µm (at the 3 dB level of maximum transmission) for the tapers with taper-waist core diameter of 6 µm. Furthermore, transmission window decreases with increasing taper-waist length for the same taper-waist core diameter due to increasing propagation losses in the taper section as shown in Figs. 4.10(b-f). The transmission spectra of tapers also show several new dips such at 4.26 µm due to the presence of CO_2 molecules, at 4.94 µm due to Ge-H bonds, at 6.3 µm due to H_2O molecules, along with already present attenuation peaks in the untapered PCF (see Fig. 4.9(b)). Since, the $Ge_{10}As_{22}Se_{68}$ PCF tapers with taper-waist of 6 µm have the broadest transmission window up to 9.1 µm (similar to the untapered fiber), therefore, they will be tested for mid-IR SC generation in Section 4.6.

4.4/ COMPUTATION OF DISPERSION AND BIREFRINGENCE

Group-velocity dispersion (GVD) and birefringence properties of the PM-PCF and the PM-PCF taper are computed using COMSOL software based on a full vector finite-element method from the cross-section images shown in Fig. 4.7(c) and Fig. 4.8(d). The refractive index of the air holes is set to 1 and the refractive index of the glass was calculated using a standard Sellmeier equation with the following form [10]

$$n^2(\lambda) = A_0 + \frac{A_1\lambda^2}{\lambda^2 - a_1^2} + \frac{A_2\lambda^2}{\lambda^2 - a_2^2}, \tag{4.4.1}$$

where, A_0, A_1, and A_2 are dimensionless coefficients and a_1 and a_2 are the material resonant wavelengths. For $As_{38}Se_{62}$ glass, the values of the coefficients used in the simulation are: $A_0 = 3.7464$, $A_1 = 3.9057$, $A_2 = 0.9466$, $a_1 = 0.4073$ µm, and $a_2 = 40.082$ µm [216]. The PM-PCFs are assumed to be single-mode (HE_{11}) in the mid-IR as the second-order and higher-order modes have much higher confinement loss (18 dB/m at 3 µm, 56 dB/m at 4 µm, and 176 dB/m at 5 µm, obtained using Eq. 2.1.45 from Chapter 2) than HE_{11} mode over the wavelength range under investigation. Therefore, the effective refractive index (n_{eff}) is calculated for the fundamental mode of PM-PCF followed by computation of group-velocity dispersion (D) and phase birefringence ($B(\lambda)$) of the fundamental mode using Eqs. 2.1.50 and 2.1.53 from Chapter 2. The computed GVD and phase birefringence are plotted in Fig. 4.11(a) for the PM-PCF with a d_{core} of 8.11 µm and in Fig. 4.11(b) for a PM-PCF taper with a taper-waist d_{core} of 1.77 µm. The PM-PCF has a zero-dispersion wavelength (ZDW) at 4.56 µm for the fast axis and 4.68 µm for the slow axis and, at average ZDW, a large phase birefringence of $6.5 \cdot 10^{-4}$ such that strong polarization maintaining properties are expected. This is in excellent agreement with the experimental measurement recently reported in [216] using crossed-polarizers technique. By tapering the PM-PCF core from 8.11 µm to 1.77 µm, we are able to bring down the ZDW from 4.56 µm to 2.507 µm for the fast axis and from 4.68 µm to 2.75 µm for the slow axis along with a second ZDW at 3.51 µm for the fast axis and 3.78 µm for the slow axis. The PM-PCF taper also shows quite high phase birefringence of $9 \cdot 10^{-3}$ and $1.93 \cdot 10^{-2}$ at two respective average ZDWs.

As mentioned before, out of all the $Ge_{10}As_{22}Se_{68}$ PCF tapers with different taper-waist core diameter as reported in Table. 4.1, the taper with taper-waist d_{core} of 6 µm is used for experimental SC generation. Therefore, its group-velocity dispersion for the fundamental mode (see inset of Fig. 4.11(c)) is computed following the same procedure, as that of $As_{38}Se_{62}$ PM-PCF taper discussed above, using the SEM image shown in Fig. 4.8(g). In this case the refractive index of the glass was calculated using the following form of

standard Sellmeier equation,

$$n^2(\lambda) = 1 + B_0 + \frac{B_1\lambda^2}{\lambda^2 - b_1^2} + \frac{B_2\lambda^2}{\lambda^2 - b_2^2}, \tag{4.4.2}$$

where the values of the coefficients in Eq. 4.4.2 for $Ge_{10}As_{22}Se_{68}$ glass are: $B_0 = 2.774$, $B_1 = 2.892$, $B_2 = 0.7320$, $b_1 = 0.4047$ µm, and $b_2 = 38.53$ µm [236]. Figure 4.11(c) shows the computed group-velocity dispersion of the PCF taper, which exhibits a zero-dispersion wavelength at 3.541 µm.

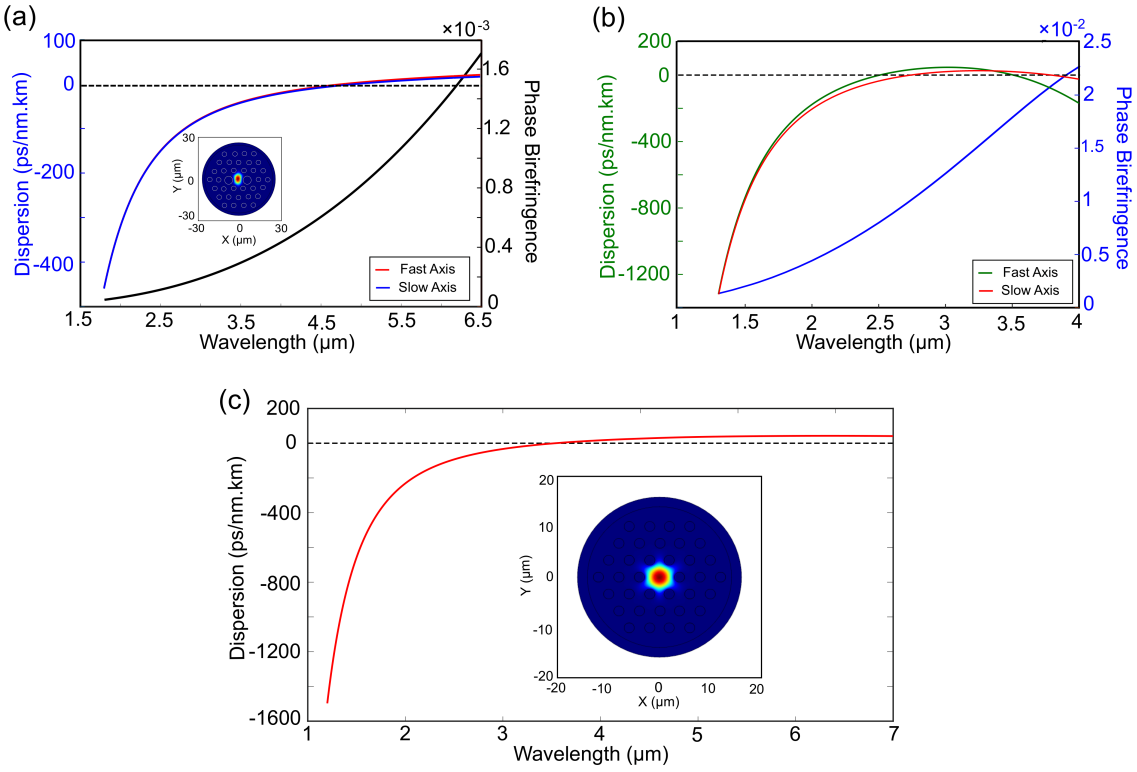

Figure 4.11: Dispersion and birefringence characteristics of the $As_{38}Se_{62}$ PM-PCF, taper, and $Ge_{10}As_{22}Se_{68}$ PCF taper simulated for the fundamental mode from SEM image. (a) $As_{38}Se_{62}$ PM-PCF with d_{core} of 8.11 µm. Blue and red curve: group-velocity dispersion of PM-PCF sample for different polarization axis. Inset: optical power density of the fundamental mode for the fast axis at a wavelength of 2 µm inside the core of the fiber. Black curve: phase birefringence of PM-PCF. (b) PM-PCF taper with a taper-waist core diameter 1.77 µm. Green curve: group-velocity dispersion of taper-waist section. Blue curve: phase birefringence of the taper-waist section. (c) $Ge_{10}As_{22}Se_{68}$ PCF taper with d_{core} of 6 µm. Inset: optical power density of the fundamental mode at a wavelength of 1.7 µm inside the core of the fiber. Red curve: group-velocity dispersion of taper-waist section.

4.5/ EXPERIMENTAL SETUP FOR MID-INFRARED PUMP AND SC GENERATION

Figure 4.12 outlines the experimental setup for mid-IR pumping of the chalcogenide glass based PM-PCF and non-PM taper and measuring the generated SC infrared light [236]. The experiment was performed at the Technical University of Denmark as part of author's PhD secondment in the framework of the European program H2020-MSCA-ITN SUPUVIR. The mid-IR pump was generated through a single-pass parametric generation process using a 10 mm periodically-poled fan-out MgO:$LiNbO_3$ crystal (MgO:PPLN). The nonlinear crystal was pumped by a continuous-wave (CW) seed laser (tunable from 1350 to 1450 nm) along with a 1.04 µm mode-locked Yb:KYW solid-state laser (having a full width half maximum pulse duration of 250 fs at 21 MHz repetition rate) to stimulate quasi phase-matched parametric anti-Stokes generation. The phase-matching relation was achieved by selecting the appropriate poling period of the fan-out structure using a linear translation stage, and the crystal was kept in an oven at a constant temperature of 150 ℃ to avoid photorefraction. The combination of tunable seed and tunable poling

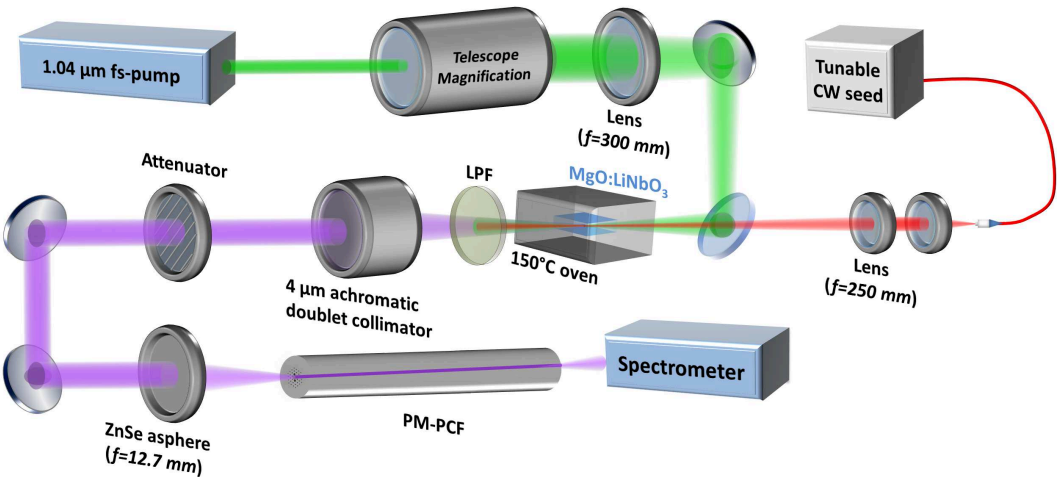

Figure 4.12: Schematic of the experimental setup for mid-IR pump laser and supercontinuum infrared light generation. LPF, long-pass filter; PM-PCF, polarization maintaining photonic crystal fiber. Polarization dependency of SC light was studied by rotating the fiber at fixed input power.

period of the crystal provides a tunable MIR output between 3.7 µm and 4.53 µm whose spectrum corresponds to a 252 fs transform limited pulse train at 4 µm (see [213] for the first use of the laser). Any residual pump and other radiation below 3.5 µm was eliminated by placing a reflective long pass filter (LPF) after the crystal system. The mid-IR output beam was then collimated by an achromatic air-space lens doublet, which is optimized for a central wavelength of 4 µm and anti-reflection (AR) coated for the 3–5 µm range. The pump beam was then injected into the PM-PCF or the PCF taper through an AR coated ZnSe aspheric lens with a focal length of 12 mm and the coupling power was controlled by rotating a variable attenuator. The generated SC light was measured using a fiber-coupled Fourier transform infrared (FTIR) spectrometer (FOSS) covering from 1–10 µm (low sensitivity below 3 µm) and a grating-based spectrometer covering from 1–5 µm (Spectro 320, Instrument Systems), depending on the wavelength. The output power was measured with a thermal power meter.

4.6/ RESULTS

In this section, at first we reported the SC spectra generated in 8.11 µm core diameter $As_{38}Se_{62}$ PM-PCF with 4 µm and 4.53 µm pumping and also its polarization dependency. In order to have better understanding of the underlying physical phenomena behind the experiment, these results were then compared with a numerical simulation performed with a two-polarization code based on two coupled generalized nonlinear Schrödinger equations (CGNLSE). Finally the SC spectra generated with a 6 µm core diameter $Ge_{10}As_{22}Se_{68}$ PCF taper was further investigated to show the influence of taper-waist core diameter and taper-waist length on SC bandwidth.

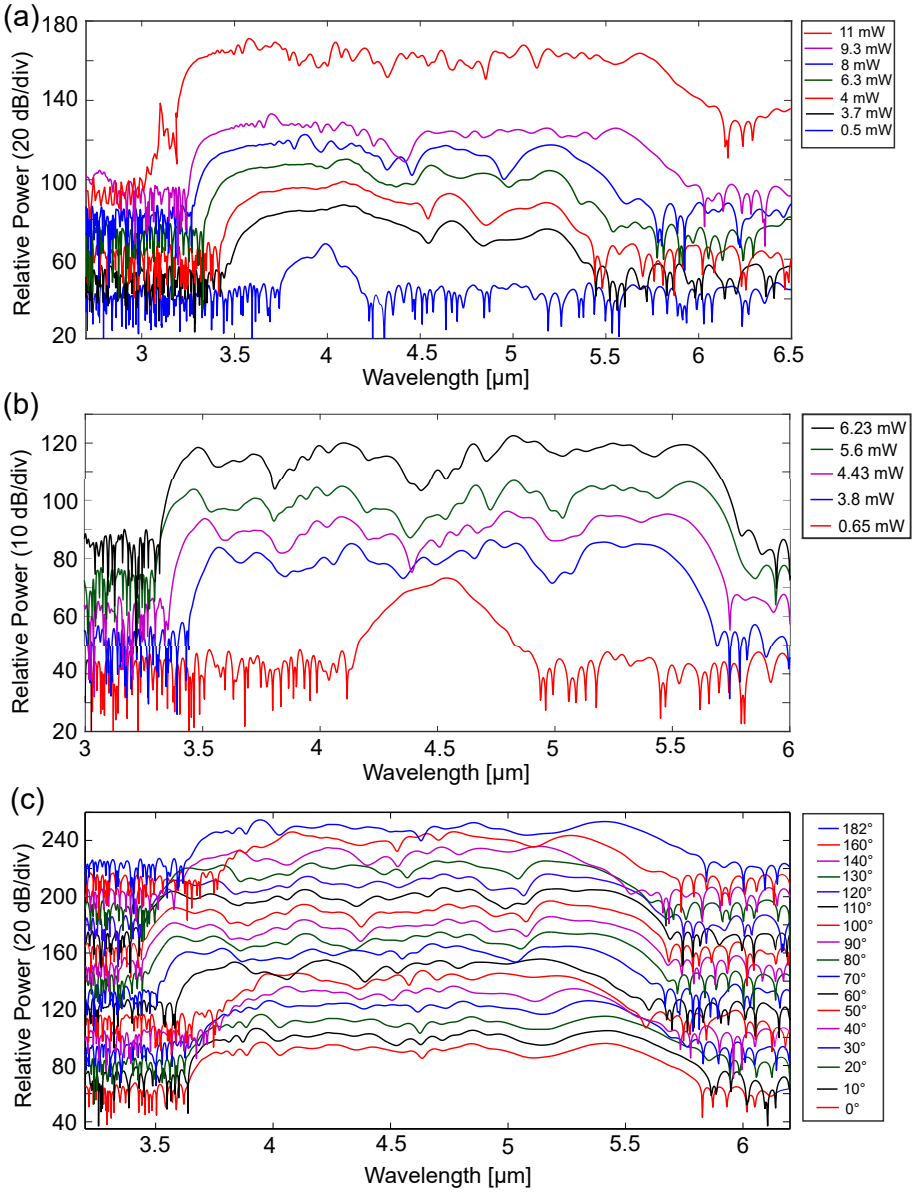

Figure 4.13: Supercontinuum spectra generated in a 25 cm long PM-PCF sample with 252 fs pulses. Different spectra are all shifted by 10 dB. (a) & (b) SC spectra generated with 4 µm and 4.53 µm pump, respectively, as a function of mean output power. (c) Dependency of SC spectra with incident angle of polarization from 0° to 182° for pumping at 4.53 µm.

4.6.1/ SC GENERATION IN A UNTAPERED $As_{38}Se_{62}$ PM-PCF

Figure 4.13(a) shows the generated SC spectra with increasing pump power in a 25 cm long PM-PCF with the pump tuned to 4 µm central wavelength. For a maximum available pump power of 135 mW, we obtained a SC spectrum spanning from 3.1 to 6.02 µm (at the -30 dB level) with an average output power of 11 mW. Then we tuned the pump wavelength close to the ZDW at 4.53 µm and the obtained SC spectra with different output power are shown in Fig. 4.13(b). An available maximum power of 98 mW provided a spectral broadening from 3.33 to 5.78 µm (at the -30 dB level) with an average output power of 6.23 mW. However, the spectrum at 4.53 µm has a lower bandwidth than the spectrum at 4 µm due to available lower input power from the laser in spite of pumping closer to the ZDW. Furthermore, with a constant input power of 62 mW at 4.53 µm, we were able to measure the polarization dependency of the SC spectra by rotating the fiber, which amounts to turning the input pump polarization with respect to the principal axes of the PM fiber. Using the measured output power, Fresnel loss from the output end face of the fiber, and intrinsic attenuation of the fiber in Eqs. 2.1.35 and 2.1.36 from Chapter 2, we estimated the coupling efficiency to be $\sim 11\%$ and $\sim 9\%$, the coupling peak power as 2.74 kW and 1.59 kW at 4 µm pumping and 4.53 µm pumping, respectively. Figure 4.13(c) shows the recorded SC spectra when tuning the fiber angle from 0° till 182° with 10° steps and with constant output power of 3.8 mW. As it can be seen from Fig. 4.13(c), the input pump polarization strongly affects the SC generation in the PM-PCF. The obtained SC bandwidth reduces from 2140 nm down to 1620 nm (at the -20 dB level) with an angular periodicity of about 90°. Polarization-maintaining property of the PM-PCF could be further investigated efficiently by placing an analyzer after the PM-PCF output in order to check the polarization of the SC spectra. Unfortunately, it was not performed due to the absence of a mid-IR polarizer during the experiment.

4.6.2/ COMPARISON WITH NUMERICAL SIMULATIONS

Detailed modelling of the polarization and modal properties of mid-IR SC generation in multi-mode step-index non-PM chalcogenide fibers was studied in [222], which demonstrated how important it is to control the polarization and the number of modes participating in the SC generation process. Here the uniform PM-PCF is single-mode at the pump wavelength, which means that we can restrict ourselves to consider only the fundamental mode with both polarizations. Nonlinear pulse propagation and SC generation in the highly-birefringent PM-PCF was therefore modelled using a two-polarization code based on the two coupled generalized nonlinear Schrödinger equations (CGNLSEs) [121, 128, 131, 166]. These equations can be written in following reduced form in a linearly polarized basis

$$\frac{\partial A_{x,y}}{\partial z} + \frac{\alpha}{2}A_{x,y} + \beta_{1x,y}\frac{\partial A_{x,y}}{\partial T} - \sum_{k\geq 2}\frac{i^{k+1}}{k!}\beta_k^{x,y}\frac{\partial^k A_{x,y}}{\partial T^k} = i\gamma\left(1 + i\tau_{\text{shock}}\frac{\partial}{\partial T}\right)\times$$
$$\left[(1-f_R)\left(|A_{x,y}|^2 + \frac{2}{3}|A_{y,x}|^2\right) + f_R A_{x,y}(z,T)\int_{-\infty}^{T} h_R(T-T')|A_{x,y}(z,T-T')|^2 dT'\right], \qquad (4.6.1)$$

where A_x and A_y are the slow and fast axis field amplitudes, α is the wavelength-dependent propagation loss taken from Fig. 4.9(a), $\beta_k^{x,y}$ is the k^{th} Taylor expansion of the propagation constants for the two linearly polarized field amplitudes. It accounts for the phase birefringence of the PM-PCF plotted in green in Fig. 4.11(a). The second-order dispersion $\beta_2^{x,y}(\omega)$ is also shown in Fig. 4.11(a) as the D parameter. We also included

higher order dispersion coefficients from Fig. 4.11(a). Nonlinear coefficient γ was calculated from effective mode area of PM-PCF and nonlinear index of the $As_{38}Se_{62}$ glass using $\gamma = \frac{2\pi n_2}{\lambda A_{\text{eff}}(\lambda)}$. This gives $\gamma = 358.6$ $W^{-1}km^{-1}$ and 301 $W^{-1}km^{-1}$ at the two pumping wavelengths, 4 µm and 4.53 µm, respectively [73]. The time derivative term in RHS of Eq. 4.6.1 models the effects such as self-steepening and optical shock formation with $\tau_{\text{shock}} = \frac{1}{\omega_0}$. The bottom first term in the RHS represents the nonlinear response function, which includes both instantaneous self-phase modulation (SPM) and degenerate cross-phase modulation (DXPM) between the two cross-polarized fields with the coupling factor 2/3 [131, 121]. The coherent coupling term between the two cross-polarized fields is here neglected because of the high birefringence [128]. f_R is the Raman fractional contribution to the Kerr effect and we find $f_R = 0.1$, using the parameter reported in [120] for chalcogenide glass. The Raman response delayed function $h_R(t)$ in the last term of Eq. 4.6.1 can be expressed in the time domain as follows:

$$h_R(t) = \frac{\tau_1^2 + \tau_2^2}{\tau_1^2 \tau_2^2} \exp\left(\frac{-T}{\tau_2}\right) \sin\left(\frac{T}{\tau_1}\right). \tag{4.6.2}$$

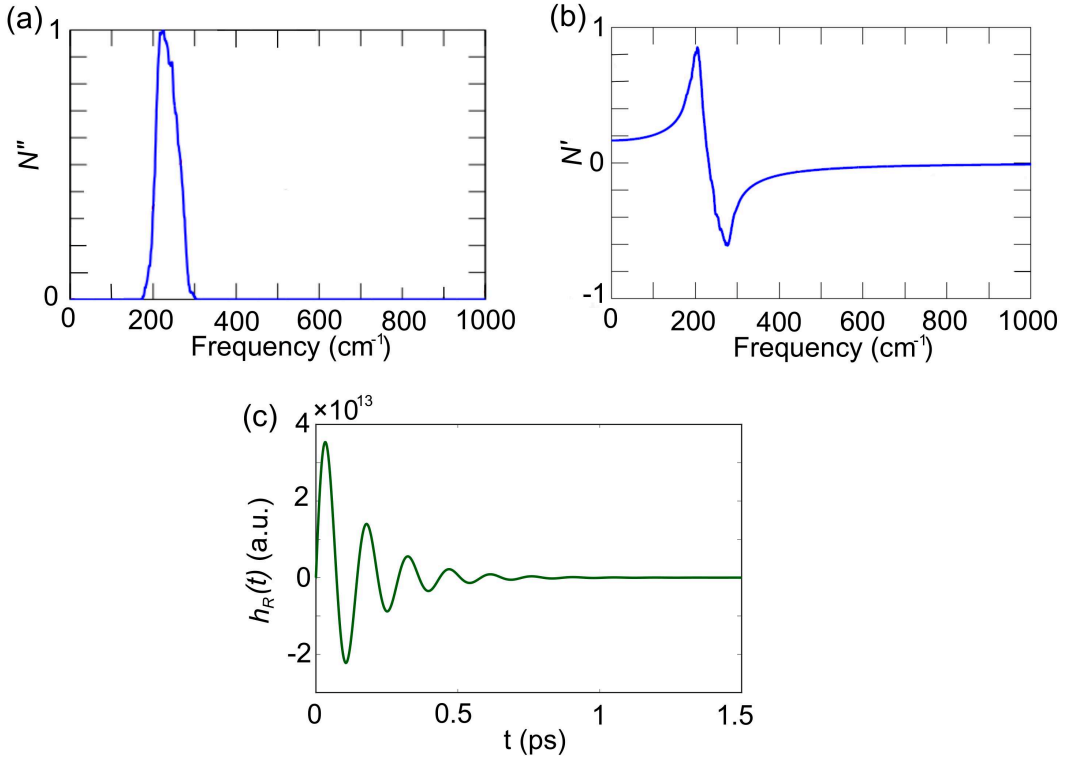

Figure 4.14: (a) The imaginary part of third-order susceptibility for an As_2Se_3 chalcogenide fiber, whose Raman gain was measured at the Naval Research Laboratory, taken and adapted from [168]. The third-order susceptibility is proportional to the Raman gain. It has been normalized to 1 at the peak gain. (b) The real part of the third-order susceptibility, adapted from [168]. (c) Raman response delayed function for $As_{38}Se_{62}$ fiber.

Raman gain can be obtained as $g(\Omega) = (2\omega_p/c)n_2 f_R \text{Im}[H_R(\Omega)]$, where ω_p and

$\mathrm{Im}[H_R(\Omega)]$ denote the pump frequency and the imaginary part of the Fourier transform of $h_R(t)$, respectively [43]. Then $\mathrm{Re}[H_R(\Omega)]$, whose inverse Fourier transform yields $h_R(t)$, can be then determined from $\mathrm{Im}[H_R(\Omega)]$ using the Kramers-Kronig relations (Hilbert transformation) [43]. Figure 4.14(a) shows the imaginary part of third-order susceptibility $N''(\Omega)$, which is proportional to $\mathrm{Im}[H_R(\Omega)]$ and has been normalized to 1 at the peak gain. The real part of the third-order susceptibility $N'(\Omega)$, which is the corresponding Hilbert transforms of $N''(\Omega)$ is shown in Fig. 4.14(b), as reported in [168]. In our case τ_1 and τ_2 in Eq. 4.6.2 are 23.14 fs and 157 fs, respectively, which was fitted for the Raman gain peak of 230 cm^{-1} or 6.9 THz (see Fig. 4.14(a)) for $As_{38}Se_{62}$ fiber whose Raman gain peak was measured in [168]. The Raman response delayed function is shown in Fig. 4.14(b). The same Raman function was used for both fiber axes because the perpendicular Raman gain is almost negligible [131]. For the PM-PCF sample with pump at 4 µm and 4.53 µm, we used a fiber length of 25 cm and pump pulse duration of 252 fs for both cases. The coupling peak power at the input of the fiber was considered to be 1.33 kW and 0.40 kW for the pump at 4 µm and 4.53 µm, respectively, in order to have the best fit with experimental results. Figures 4.15(c)&(d) show the evolution of numerically

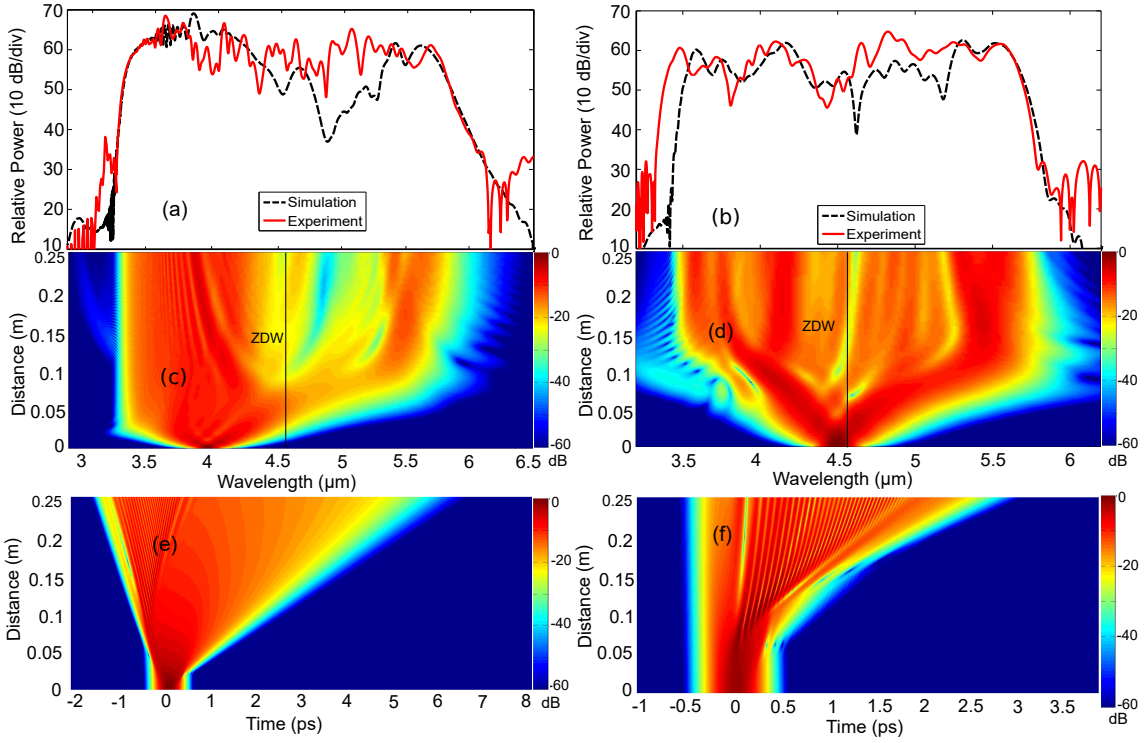

Figure 4.15: Numerical simulation:(a) and (b) Comparison between numerically and experimentally generated SC spectra in the PM-PCF for pumping at 4 µm (a) and 4.53 µm (b). (c) and (d) Numerically generated evolution of SC spectra along the fiber length at the respective pumping wavelength. The vertical black line represents the zero-dispersion wavelength (ZDW). (e) and (f) Corresponding temporal distribution along the fiber length.

computed SC spectra along fiber length for a pump wave polarized along one of the principal axis at 4 µm and 4.53 µm, respectively. The temporal counterparts are shown in Figs. 4.15(e)&(f). The comparisons between simulated and experimental SC spectra for respective pump wavelength of 4 µm and 4.53 µm are shown in Figs. 4.15(a)&(b). The simulated and experimental SC spectra are in qualitative agreement in terms of band-

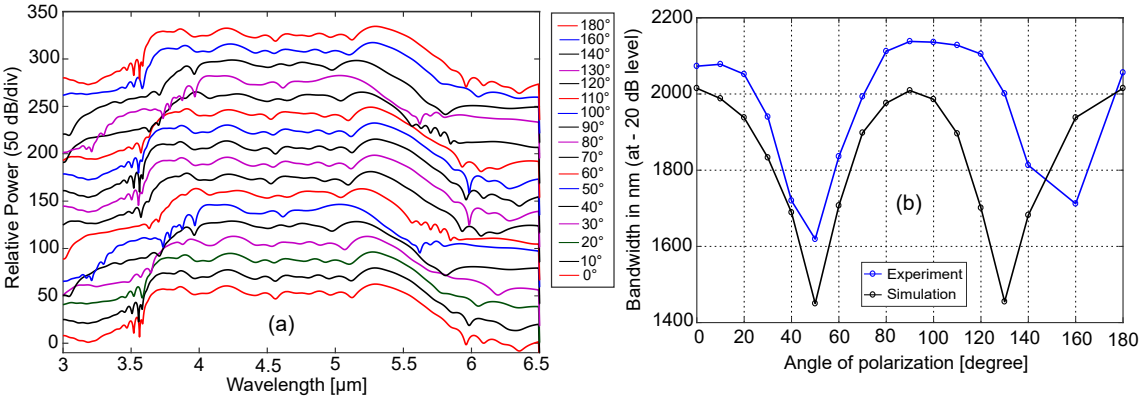

Figure 4.16: Numerical simulation: (a) Polarization dependency of numerically generated SC spectra at 4.53 µm pumping when tuning the input polarization angle from 0° up to 180° from the fast axis. (b) Comparison of bandwidth (at -20 dB) between experimental and simulated SC spectra at different polarization angle for 4.53 µm pumping.

width, but in terms of structure of the spectrum, they are quite different. In 4 µm pumping, since the pump was located in the strong normal dispersion regime but far from the ZDW, therefore, initial SC generation was driven mainly by self-phase modulation (SPM). From both the numerical and experimental observations (see Figs. 4.15(a)&(c)), we can see due to SPM, pumping below the ZDW initiates a large build-up of power in the 3.3-4.3 µm region. Therefore, it limits the amount of power which crosses the ZDW to generate the long-wavelength part of the spectrum. However, after just 2 cm of propagation in the fiber, the spectrum extends beyond the ZDW, which then initiates soliton formation and fission followed by Raman soliton self-frequency shifting (SSFS). As a result, we could observe multiple soliton generation towards the infrared up to 6 µm. Simultaneously there are dispersive waves that are emitted from solitons in the short wavelength range down to 3 µm. The cross phase modulation (XPM) interaction between dispersive waves and Raman solitons could be observed around 3.3 µm of the spectra in Fig. 4.15(a). Figure 4.16(a) shows a series of computed SC spectra as a function of input polarization angle θ, from 0° to 180° with respect to the fast axis. This leads to SC bandwidth reduction from 2010 nm down to 1450 nm with an angular periodicity of around 90°, as shown in Fig. 4.16(b), as a black curve. This can be explained by the fact that when tuning the polarization angle from one principal axis to the other, the degenerate cross-phase modulation between the A_x and A_y vector fields is lower than the self-phase modulation (SPM) itself by a factor 2/3, giving rise to less SC broadening when pumping off axis with a minimum at 45°. The agreement with experimental measurements (blue curve) is quite satisfactory, except the small offset that is due to the different SC bandwidth shown in Fig. 4.15(b). It is well known that SC generated in a fiber pumped in the anomalous group velocity dispersion regime usually contains large amount of intensity noise due to soliton dynamics and stimulated Raman scattering, which is the basis of SC generation. However, here the PM-PCF pumped in the anomalous group velocity dispersion regime only maintains the polarization of generated SC but it anyway does not contribute to the reduction of noise unlike ANDi PM-PCF [231].

4.6.3/ SC GENERATION IN $Ge_{10}As_{22}Se_{68}$ PCF TAPER

The zero-dispersion wavelength of a tapered fiber is much lower compared to the non-tapered section and it allows coupling of more pump power into the anomalous dispersion regime in order to improve efficiency of SC generation in the taper. However tapering a fiber has a drawback as it also pushes the confinement loss edge towards short-wavelengths. Therefore, it introduces a trade-off between efficiency and long-wavelength loss. As previously explained in Section 1.2, mid-IR SC spectra in optical fiber can be generated in two ways: direct pumping and cascaded pumping. Therefore, we will focus on both methods in the following sections.

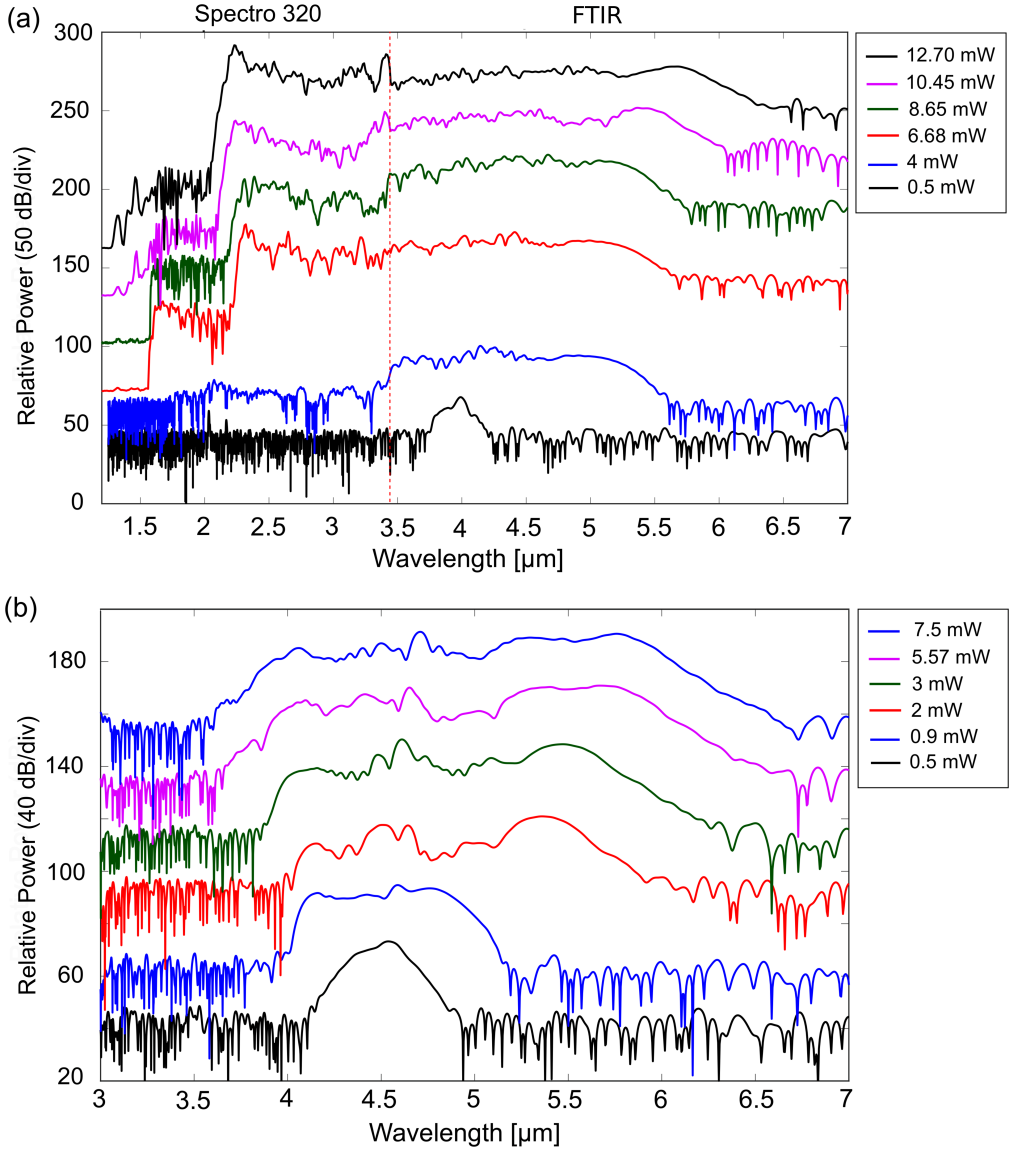

Figure 4.17: Supercontinuum spectra generated in a $Ge_{10}As_{22}Se_{68}$ taper sample (taper-waist core diameter of 6 μm) with 252 fs pulses as a function of mean output power. (a) SC spectra generated with a 4 μm pump. (b) SC spectra generated with a 4.53 μm pump.

4.6.3.1/ DIRECT PUMPING

Here a $Ge_{10}As_{22}Se_{68}$ PCF taper (see Fig. 4.8(b) and Table 4.2) with a taper-waist d_{core} of 6 µm and a total length of 45 cm, which consists a taper-waist length (L_W) of 11 cm, before taper section length ($L_B = L_{BT} + L_{DT}$) of 15 cm, and after taper section length ($L_A = L_{AT} + L_{UT}$) of 19 cm, was directly pumped in the anomalous GVD region at 4 µm central wavelength, above the ZDW of 3.541 µm using the same experimental setup demonstrated in Section 4.5. The variation of measured spectra with output power is shown in Fig. 4.17(a). We obtained a SC spectrum spanning from 1.3 to 6.3 µm with an average output power of 12.70 mW for an input pump power of 195 mW. Figure 4.17(b) shows the measured SC spectra with different output power when the pump wavelength is tuned to 4.53 µm in the strong anomalous GVD region. An available maximum input power of 98 mW provided a spectral broadening from 3.61 to 6.56 µm (at the -30 dB level) with an average output power of 7.5 mW. In this case, we were able to extend the SC broadening towards the long-wavelength edge by few 100 nm by pumping far in the anomalous GVD region but in the same time, the SC broadening was shortened in the short-wavelength edge as we were limited by low input power compared to 4 µm pumping. The estimated coupling efficiency using Eq. 2.1.36 are $\sim 9\%$ and $\sim 14\%$, the coupling peak power using Eq. 2.1.35 are 3.26 kW and 2.62 kW at 4 µm pumping and 4.53 µm pumping, respectively.

4.6.3.2/ CASCADED PUMPING

In a recent study on SC generation in tapered $Ge_{10}As_{22}Se_{68}$ PCFs using direct pumping by Petersen et al [236], it was found that generated SC bandwidth is greatly influenced by the length of uniform fiber before taper section (L_B) and after taper section (L_A). In this section, an investigation of the influence of taper-waist core diameter to the SC generation is performed using cascaded fiber system, as reported in [254]. In this investigation, the two same 6 µm (d_{core}) $Ge_{10}As_{22}Se_{68}$ PCF tapers with taper-waist length (L_w) of 11 and 30 cm as described in Table 4.1 & Table 4.2 along with other tapers (d_{core} between 6.5 and 7.5 µm) from the same $Ge_{10}As_{22}Se_{68}$ glass were pumped in a cascaded SC system. The structural parameters of all the tapers together are reported in Table 4.3.

Table 4.3: Structural parameters of $Ge_{10}As_{22}Se_{68}$ PCF tapers, reproduced from [254].

Taper ID	d_{core} [µm]	L_B [cm]	L_w [cm]	L_A [cm]	L_{total} [cm]
A	6	6	11	18	35
B	6.5	10	15	11	36
C	7	2	12	19	33
D	7.5	9	15	18	42
E	6	27	30	12	69

The pump source for the cascaded system was a SC source based on 7 µm core diameter ZBLAN (ZrF_4–BaF_2–LaF_3–AlF_3–NaF) fiber with a spectral coverage from 1-4.2 µm. The ZBLAN fiber was pumped with a four-stage all-fiberized master oscillator power amplifier (MOPA) configuration [249], as shown in Fig. 4.18. The MOPA is based on erbium-ytterbium (Er-Yb) and other co-ion-doped fibers. The first stage of MOPA is comprised of a directly modulated laser diode at 1556 nm with a variable pulse repetition rate

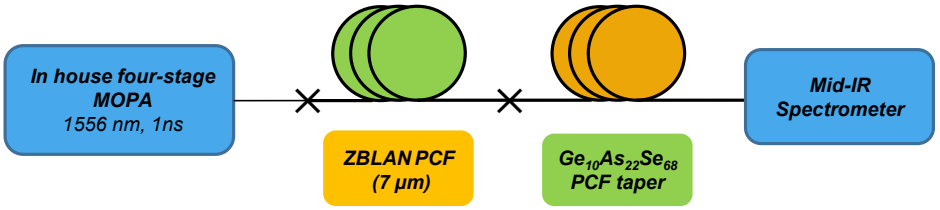

Figure 4.18: Schematic of the experimental setup for mid-IR SC generation in cascaded pumping configuration, reproduced from [249, 254]. MOPA, master oscillator power amplifier.

and 1 ns pulse duration acting as a seed source. The signal was further amplified in three stages where the first two stages have Er-doped fiber and the third stage has an Er-Yb-doped fiber. The MOPA generates the above mentioned 1-4.2 µm SC in ZBLAN fiber and it was then injected into the chalcogenide PCF taper to extend the long wavelength edge of the SC.

Furthermore, the generated SC light at the output of tapers A-E was measured with a grating-based Spectro 320 spectrometer and a custom version of the FTIR spectrometer (FOSS, with extended coverage from 2.8-14 µm) as described in Section 4.5. For an average pump power of ~ 270 mW at 1 MHz repetition rate, the generated SC spectra at the output of tapers A-D is shown in Fig. 4.19(a) with total measured output power for each taper. We obtained total transmission between 31-38$\%$ in tapers A-D and managed to achieve highest output power of 103 mW in taper D. It can be seen from Fig. 4.19(a) that the taper A-C show similar spectra with SC bandwidth up to 8 µm at -30 dB level, despite having different taper-waist core diameter. However, the SC spectrum in taper D was limited to 7.5 µm and the flatness in the SC spectra was much less compared to tapers A-C. The pump SC source (1-4.2 µm) has a cut off at around 4 µm, therefore, for taper D ($d_{\text{core}} = 7.5$ µm and estimated ZDW around 4 µm), the coupled solitons in the PCF initially experience self phase modulation in the normal dispersion regime and the part which crosses ZDW and broadens in the anomalous dispersion regime contributes to long-wavelength in the spectra. As a result, in taper D, the amount of power above 3.5 µm is $\sim 21\%$ (22.2 mW), lower than compared to $\sim 29\%$ (25.8) in taper C (ZDW is lower compared to taper D).

Another taper E (same $d_{\text{core}} = 6$ µm as taper A but twice the length of L_w and longer L_B) was tested in order to investigate whether the spectral extension of SC was limited by taper-waist length (L_w). The long-wavelength region of generated SC spectrum in taper E is shown in Fig. 4.19(a) and the full SC spectrum is reported in Fig. 4.19(b). From Fig. 4.19(a), we can see that the long taper-waist length in taper E increases the bandwidth in the long-wavelength region but in the same time output power decreases significantly due to increasing propagation losses in the taper section. From the full spectrum of taper E in Fig. 4.19(b), it is observed that the maximum SC broadening covers from 1.07-7.94 µm (at -20 dB level) with a total output power of a 41 mW for an input pump power of 350 mW. Furthermore, we were not able to increase the long-wavelength edge of the SC spectrum by increasing the input pump power in taper E and the SC broadening was limited to around 8 µm as can be seen from Fig. 4.19(c). The same behavior was found in all other tapers B-D and it suggests that further broadening in the long-

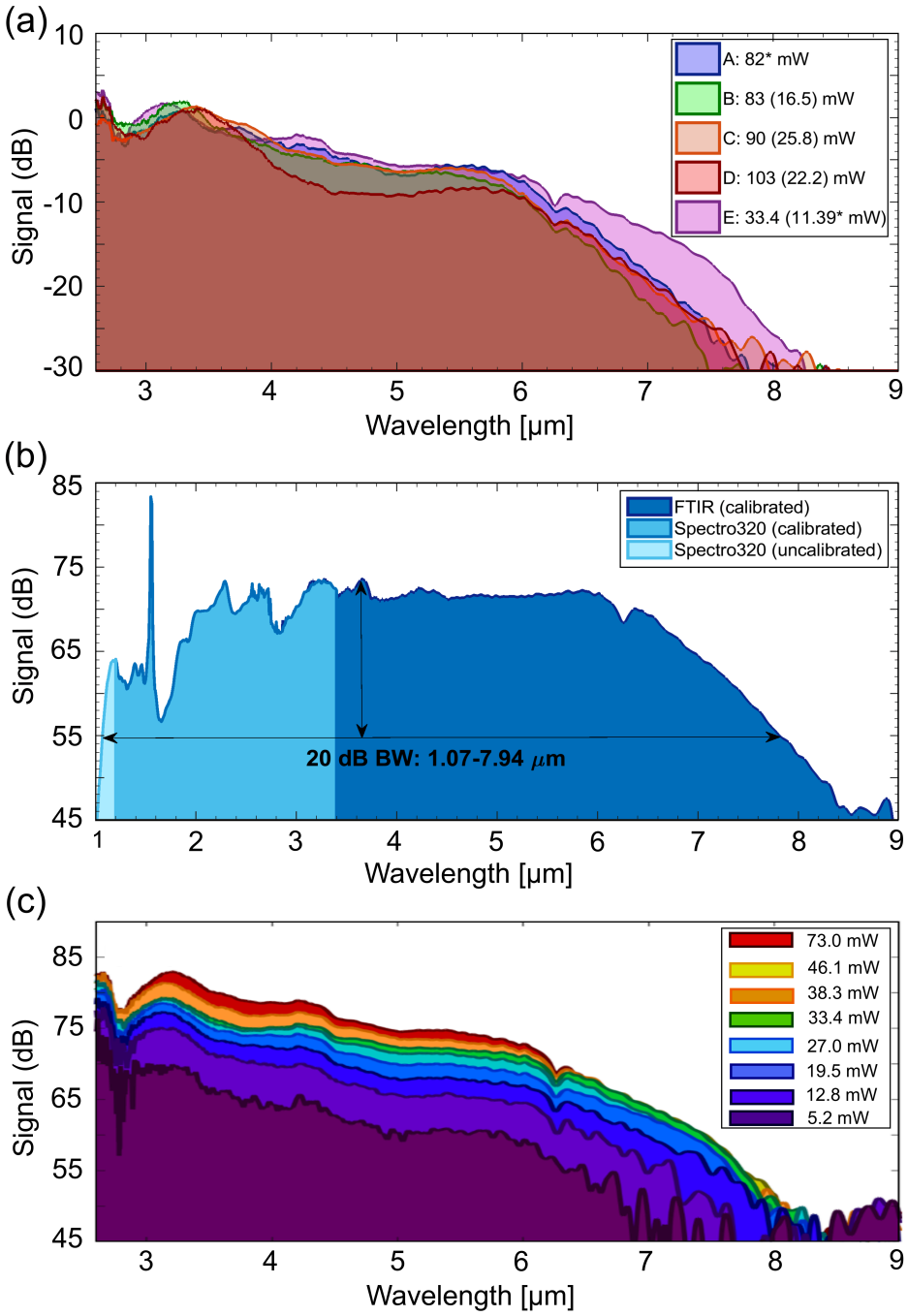

Figure 4.19: (a) SC spectra of the long-wavelength edge obtained for tapers A–E for a pump power of ~ 270 mW. The corresponding measured total output power (power > 3.5 μm in brackets) is indicated in the legend ($*$ = estimated). (b) Output spectrum (total) of taper E showing a spectral broadening from 1.07–7.94 μm at -20 dB level with a total output power of a 41 mW for a pump power of 350 mW. (c) Spectral broadening in taper E with increasing output power, reproduced from [254]. Courtesy of C.R. Petersen from the Technical University of Denmark.

wavelength edge is limited mainly by the absorption barrier in the transmission spectrum of the taper as shown in Fig. 4.10(f).

4.7/ PRELIMINARY INVESTIGATIONS OF DAMAGE THRESHOLD IN CHALCOGENIDE FIBERS

In many application like air pollution monitoring and hyperspectral imaging, the mid-IR supercontinuum light sources require to have high brightness with several mW/nm of spectral density in addition to the broad spectral coverage. It is very difficult to increase the output SC power after certain limit due to the laser induced damage threshold in chalcogenide glass. In recent years, several research has been done to investigate laser damage characteristics of several chalcogenide glasses with the aim to acquire glass materials with high laser damage resistance [188, 237]. Zhang et al. recently reported power damage threshold measurement in Ge-As-S glasses [255].

It is well known that all of the nonlinear phenomena occurring in an optical fiber are extensively dependent on optical power. From this perspective, chalcogenide index guiding PCFs have a major disadvantage in nonlinear applications due to their low power-damage threshold property. Therefore, in this chapter, the power-handling capability of chalcogenide fibers is verified by a set of measurements using As_xSe_y and $Ge_xAs_ySe_z$ PCFs with different glass compositions, mainly increasing the germanium (Ge) content in the glass. The fibers were provided by the University of Rennes for a collaboration project as a part of European Union H2020 SUPUVIR consortium. These measurements include the evolution of the output power of fixed length PCFs with variable input power or over time with fixed input power at different wavelengths, which will be described and analyzed in this section.

4.7.1/ DETAILS OF CHALCOGENIDE PCFS USED FOR TESTING

Microstructured optical fibers with 3 hexagonal rings of air holes organised in a triangular lattice containing 36 air holes are used for this power handling capacity measurements. One of the PCFs with a core diameter of 11 µm is shown in the optical microscope image in Fig. 4.20(a). In the matter of glass composition, we have used $Ge_{10}As_{22}Se_{68}$, $Ge_{14}As_{20}Se_{66}$, and $Ge_{16}As_{20}Se_{64}$ glass PCFs as well as $As_{38}Se_{62}$ glass PCF in order to test both the effect of different germanium content and also the presence and absence of germanium content in the glass. The geometrical parameters of the drawn PCFs with the above mentioned glass compositions used for the power handling capacity measurements, are given in Table. 4.4. The d/Λ ratio of all the PCFs are greater than 0.4, which emphasizes that the PCFs are not endlessly single mode. This was confirmed

Table 4.4: Characteristics of chalcogenide PCFs used for power handling capacity measurements.

Glass Composition	Core diameter [µm]	d/Λ	Attenuation [dB/m] at 1750 nm	Attenuation [dB/m] at 2100 nm
$Ge_{10}As_{22}Se_{68}$	11	0.47	~ 2	~ 1.2
$Ge_{14}As_{20}Se_{66}$	11.1	0.50	~ 6.5	~ 5
$Ge_{16}As_{20}Se_{64}$	11.1	0.49	~ 6.5	~ 5
$As_{38}Se_{62}$	11.2	0.49	~ 2.5	~ 2

by Figs. 4.20(b)&(c), which show the presence of LP_{11} and LP_{01} modes, respectively, at

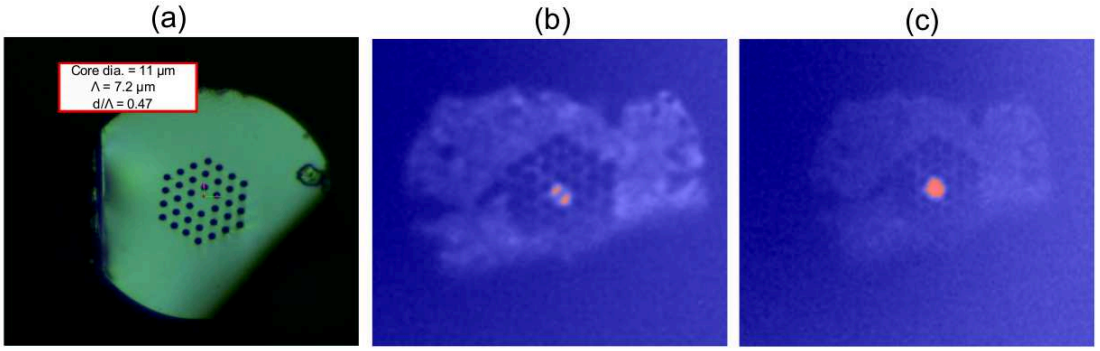

Figure 4.20: (a) Optical microscope image of a $Ge_{10}As_{22}Se_{68}$ PCF with core diameter of 11 µm. LP_{11} (b) and LP_{01} (c) modes exited in one of the PCF under test at 1750 nm.

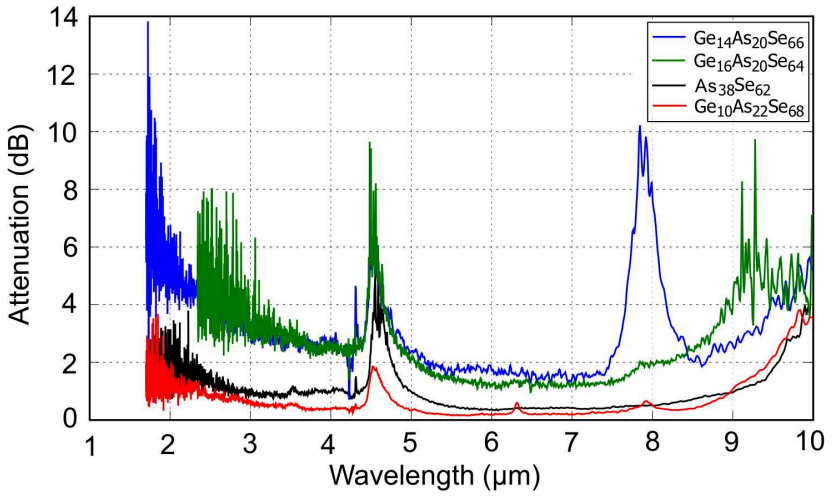

Figure 4.21: Attenuation spectra of different chalcogenide PCFs tested for power handling capacity.

1750 nm, and obtained from the experiment described in the following section. Therefore, in order to have a proper comparison between all the measurements, it is made sure to excite always the same mode. In our case, we have chosen to excite the fundamental (LP_{01}) mode for our power handling capacity measurements as only this mode can transmit in the mid-IR spectral region where the application of chalcogenide fibers mainly takes place.

The measured attenuation spectra of the PCFs are shown in Fig. 4.21. The estimated optical attenuation of the PCFs at the measurement wavelengths 1750 nm and 2100 nm are also provided in Table 4.4 with high degree of approximation due to the low sensitivity of the detector below 2.5 µm. It can be seen from Fig. 4.21 that the fibers with different glass composition show quite different attenuation. This could be due to scattering effect rather than absorption and it should not affect the thermal load that will be put on the fiber while injecting light in to it. Furthermore, power handling properties are related to absorption, which is expected to be similar between the drawn fibers.

4.7.2/ EXPERIMENTAL SETUP

The experimental setup for power damage threshold and power handling capacity measurement of chalcogenide fibers is shown in Fig. 4.22. It is similar to the experimental setup described in Section 3.4 of Chapter 3 excluding the measurement part with the spectrometer. Since the transmission range of chalcogenide PCF is in the mid-IR spectral region, idler output of the OPO with tunability from 1.7-4 µm is chosen for the pump laser. However, the power output of the OPO idler beyond 2100 nm was very low and not sufficient for power damage measurement, hence we have tested the above-mentioned chalcogenide PCFs using our OPO at two different pumping wavelengths (1750 nm and 2100 nm) and we have observed dramatically different power damage effects. It is noted that in the above mentioned test wavelength range, our chacogenide PCFs show high linear and nonlinear absorption coefficients. Therefore, the performance of the tested PCFs in terms of power handling capacity is expected to be significantly better in the mid infrared compared to our chosen wavelengths due to insufficient power of our laser system. The light from the OPO was injected into the PCF through an IR-coated focusing objective (20X magnification) and the input power was controlled via a variable attenuator. The input power after the attenuator was measured with a Thorlabs thermal power

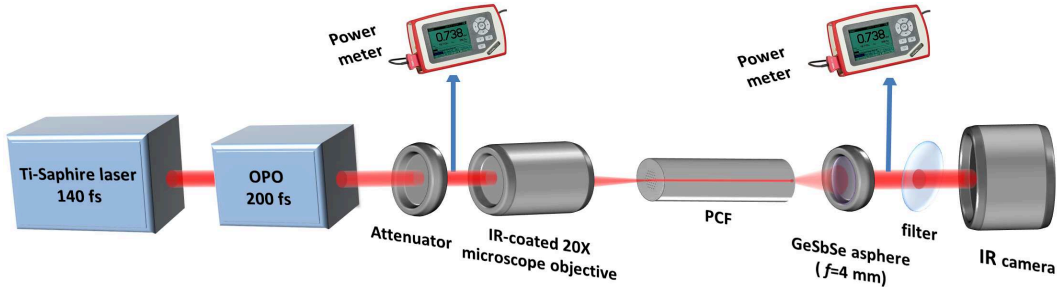

Figure 4.22: Schematic of the experimental setup for measuring power damage threshold and power handling capacity of chalcogenide PCFs. OPO, optical parametric oscillator.

meter (operating range: 1-10 µm). The light at the fiber output was collimated by a D-coated GeSbSe aspheric lens with an effective focal length of 4 mm and the power was then measured with Thorlabs S132c Ge photodiode (operating range: 700 to 1800 nm) or with a Thorlabs thermal power meter S401C (operating range 0.2-10.6 µm), depending on the wavelength. The coupling efficiency and the coupling power were calculated from the ratio between output and input powers taking into account the fiber's intrinsic attenuation and Fresnel losses. Furthermore, before measurement with every fiber, the second power meter was replaced with an IR camera combined with neutral density (ND) filters to study the light guidance inside the fiber core and excitation of only the fundamental mode as shown in Fig. 4.20(c).

4.7.3/ POWER HANDLING BEHAVIOR OF CHALCOGENIDE PCFS WITH DIFFERENT COMPOSITIONS

The maximum peak power delivered by the laser system can reach up to 15 kW, which leads to an optical intensity up to several tens of GW/cm^2 in the fiber core with few µm^2 effective mode area. Although the laser has low pulse energy (few nJ) due to low average power and high repetition rate (80 MHz), but the high optical intensity combined with high repetition rate can leads to power related damage in the chalcogenide fiber due to

a number of thermal effects such as thermally induced stress, fatigue effects, cumulative pulse effects, and melting, which are caused because of the local increase in temperature given by linear, nonlinear, and free carrier absorption.

The amount of launched input power coupled to the core of the fiber, that is the coupled input power (P_c), is different for every PCF sample in our experiment due to non-reproducible cleaving and low idler beam quality. Since, the length of the fiber, wavelength dependent attenuation in dB/m and Fresnel loss from the fiber's output facet are known, the coupled input power P_c and the coupling efficiency C_{eff} were calculated using P_{out} and P_{in} in Eqs. 2.1.35 and 2.1.36 from Chapter 2. The estimated coupling efficiency are reported in Table 4.5. From Table 4.5, it can be seen that $Ge_{10}As_{22}Se_{68}$ and $Ge_{14}As_{20}Se_{66}$ fiber offers the worst and best coupling, respectively. The coupling efficiency was lower at 2100 nm than 1750 nm for each individual fiber due to lower beam quality (wavelength dependent) of idler at 2100 nm.

Table 4.5: Coupling efficiency for different sets of measurements.

Glass Composition	Wavelength [nm]	Fiber length (m)	Estimated C_{eff} [%]
$Ge_{10}As_{22}Se_{68}$	1750	0.25	21.4
	2100	0.24	17.2
$Ge_{14}As_{20}Se_{66}$	1750	0.65	48.9
	2100	0.59	26.4
$Ge_{16}As_{20}Se_{64}$	1750	0.45	38.3
	2100	0.43	22.1
$As_{38}Se_{62}$	1750	0.47	37.4
	2100	0.44	19.7

During the measurement, it was noticed that the idler power was a little bit unstable with a fluctuation of around 10-15 mW, directly coming from the OPO. So the error on the obtained data should be regarded as quite large, however, with large number of collected points, the accuracy has been deemed sufficient for deriving at least trends in the fibers' behavior under laser power. In order to minimize the effects due to accumulation of damage in the fiber, the P_{out} data was taken for shortest possible beam exposure time by using a beam blocker on the beam path. Figure 4.23 shows the measured output power with increasing input coupled power for the four fiber samples with four different compositions. From Fig. 4.23, we can see a common trend for all the fiber. At first for both pump at 1750 nm and 2100 nm, output power increases linearly for a certain value of coupled input power. After this value of P_c, the slope in P_{out} vs P_c plot (see red curves in Fig. 4.23) for 1750 nm started to decrease. This value is defined as power damage threshold, which is reported in Table 4.6 for all four fiber samples at 1750 nm. This change in slope at different P_c for different glass composition (see Table 4.6) suggests that at shorter wavelength, the germanium contain in the glass increases the power handling capabilities of the fiber. However, for $Ge_{10}As_{22}Se_{68}$ fiber, poor quality data collection restrains us from correct estimation of a power damage threshold but the value seems to be in the same range as the one of $As_{38}Se_{62}$. The power damage at 1750 nm seems to

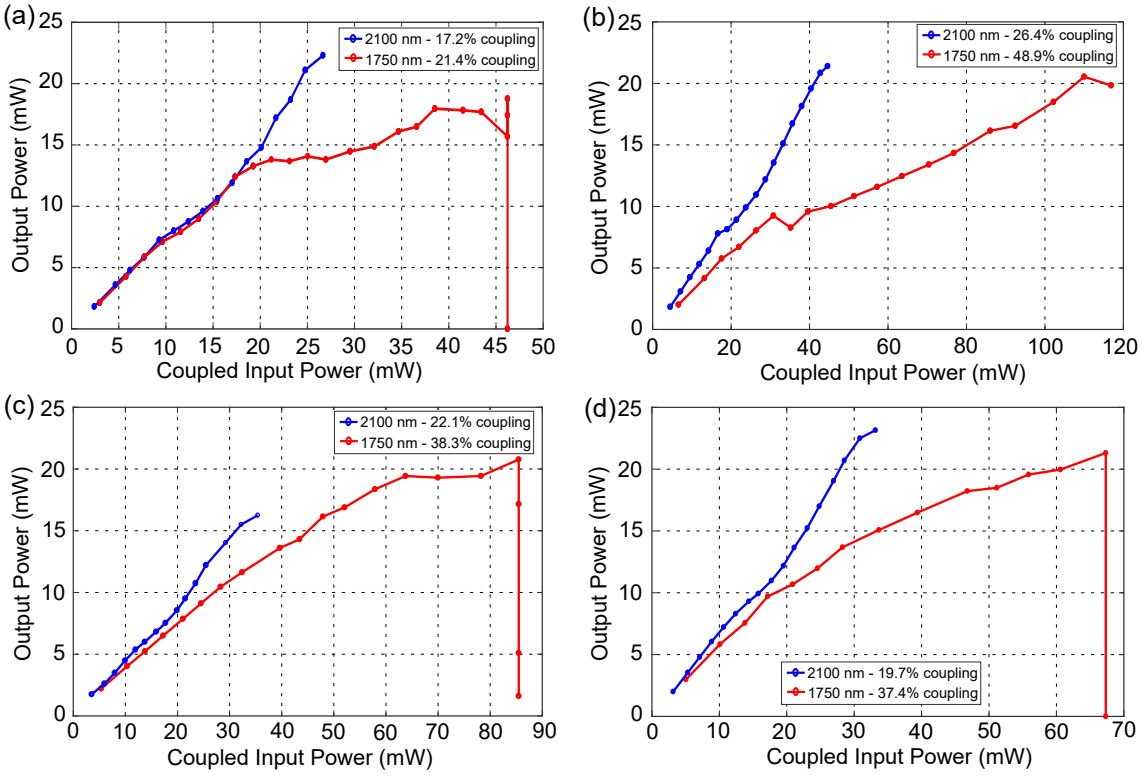

Figure 4.23: Attenuation spectra of different chalcogenide PCFs tested for power handling capacity: (a) $Ge_{10}As_{22}Se_{68}$ PCF, (b) $Ge_{14}As_{20}Se_{66}$ PCF, (c) $Ge_{16}As_{20}Se_{64}$ PCF, and (d) $As_{38}Se_{62}$ PCF.

happen in the beginning part of the fiber's input end as the original slope was possible to retrieve again by removing the first few centimeters of fiber's input end. In 1750 nm case, just before the fiber burns, we can observe a sharp fall of P_{out} over a few seconds at a certain high value of P_c (see red curves in Fig. 4.23) for all the fibers except $Ge_{14}As_{20}Se_{66}$. After checking the input fiber end with a fiberscope, the fiber surface appeared to be completely melted with the holes closed, which suggests that not only the coupled power but also the whole launched power was involved in this phenomena. The input/coupled power at which the fiber burns is denoted as burning power, which is reported in Table 4.6 for all four fiber samples. Here, we can see no trend relating the coupled burning power to the amount of germanium in the glass composition but when comparing the values of P_{in} with respect to fiber burning, there is a clear distinction between $As_{38}Se_{62}$ ($\sim$ 180 mW) and the germanium containing compositions (>216 mW). A comparison between the compositions containing germanium would not be satisfactory due the above mentioned sources of errors.

At the 2100 nm pumping case, we did not observe any permanent change in slope of P_{out} and P_c plots (see blue curves in Fig. 4.23) due to insufficient power but it seems that such changes in slope, if present, would occur in much higher input power than those at 1750 nm. This being consistent with the attenuation data of the fibers, suggested a significantly higher band-gap related absorption (thus more thermal load) at 1750 nm than that of 2100 nm. High peak power related two photon absorption (TPA) is also more significant at wavelengths closer to the band-gap.

For better understanding of power damage phenomena happening in the fiber, an

Table 4.6: Estimation of damage threshold and burning power for the different fibers pumped at 1750 nm.

Glass Composition	Damage threshold [mW]	Burning power (mW)	
		Total	Coupled
$Ge_{10}As_{22}Se_{68}$	10-17	216	46
$Ge_{14}As_{20}Se_{66}$	22-31	> 239	> 117
$Ge_{16}As_{20}Se_{64}$	~ 39	223	85
$As_{38}Se_{62}$	13-20	180	67

extensive study of the output power with time at fixed input power under continuous exposure of laser was performed for the fiber samples with all the compositions. At 1750 nm, for the coupled input power lower than the damage threshold value of the individual fibers mentioned in Table 4.6, no variation in output power over time could be seen. When the fixed coupled input power reaches above the damage threshold value, output power decreases by a significant amount over in few minutes as shown in Fig. 4.24 for all four fibers with four different compositions. From Fig. 4.24, we can see that the decrease in output power is not linear and there are few changes in the slope, which could be at least partially due to the cumulative effect of the power absorbed while collecting the points and also due to the very small movement of the centre of laser beam in our experiment, despite the necessary precautions taken to avoid it. After these experiments, the laser beam was stopped to cool down the fiber. Then after one hour, without modifying the

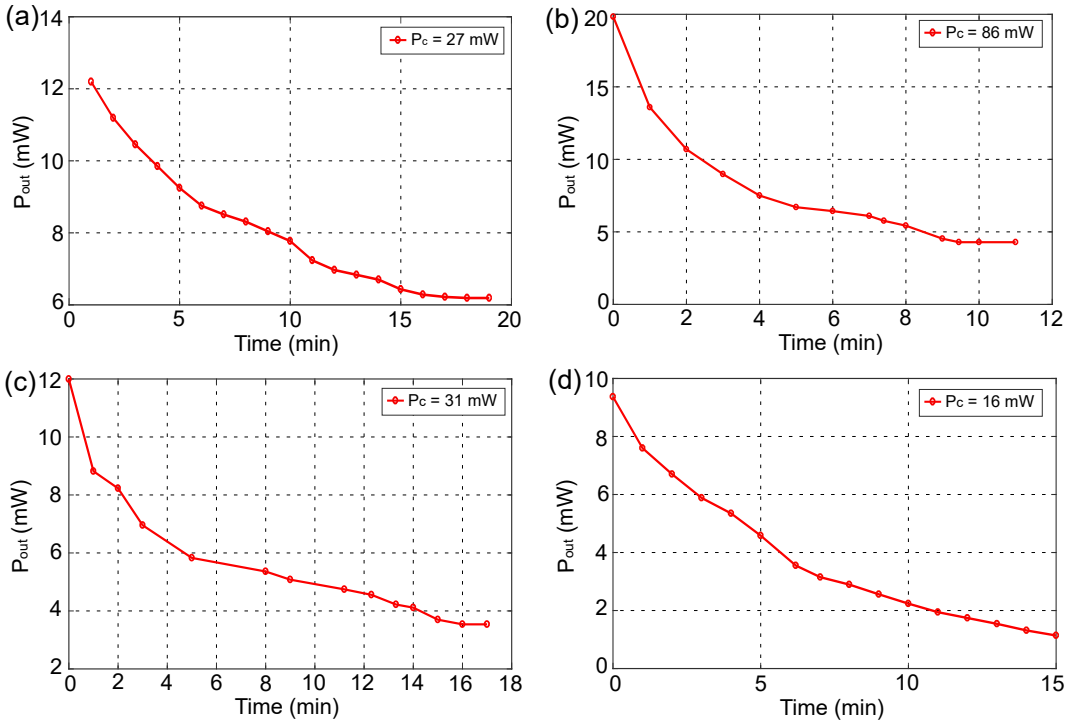

Figure 4.24: Output power vs time at 1750 nm for fixed input power for (a) $Ge_{10}As_{22}Se_{68}$, (b) $Ge_{14}As_{20}Se_{66}$, (c) $Ge_{16}As_{20}Se_{64}$, and (d) $As_{38}Se_{62}$ fibers.

input power, injection of light into the fibers leads to retrieval of only a few percentage ($\sim 33\% - 70\%$) of the initial output power suggested that the loss in transmittance induced in the fibers due to power damage experiment is partially reversible as well as partially permanent. At 2100 nm, for the similar length of the fiber, no significant change in output power over time could be observed even for maximum amount of available coupled input power. This means that the power drop in time is mainly due to two-photon absorption.

4.8/ CONCLUSIONS

In Section 4.6, polarization-preserving supercontinuum generation in the mid-infrared from 3.1 to 6.02 µm and from 3.33 to 5.78 µm with output power of 11 mW and 6.23 mW, respectively, has been demonstrated by pumping a highly-birefringent photonic crystal fiber made of chalcogenide glass with femtosecond pulses at 4 µm and 4.53 µm, respectively. It has been further shown that tuning the input polarization angle with respect to the fiber principle axes affects the supercontinuum bandwidth and this was checked against numerical simulations based on two coupled generalized nonlinear Schrödinger equations. The chalcogenide glass was fabricated using standard melt-quenching method and the fiber was drawn using the casting method from $As_{38}Se_{62}$ glass, which features a transmission window from 2 to 10 µm and a high nonlinear index of $1.13 \cdot 10^{-17}$ m^2/W. It has a large birefringence of $6.5 \cdot 10^{-4}$ at 4.6 µm enabling strong polarization maintaining properties. Long tapered optical fibers have also been designed and fabricated from the same polarization-maintaining fiber with taper-waist core diameter down to a 1.77 μm that increases the birefringence up to 10^{-2}. This work constitutes an important step towards stable and linearly-polarized supercontinuum generation for mid-IR applications.

By tapering a 15 µm core diameter $Ge_{10}As_{22}Se_{68}$ PCF (non-PM) down to a core diameter of 6 µm over a 11 cm taper-waist section, a SC spectrum covering from 1.3-6.3 µm with output power of 12.7 mW was obtained by direct pumping at 4 µm and a SC spectrum covering from 1-7.4 µm with 82 mW of output power was achieved by pumping in a cascaded system with pump source covering 1-4.2 µm. The SC spectrum in the cascaded system was further broadened in the long-wavelength edge from 1.03-7.94 µm with output power of 41 mW using 30 cm of taper-waist section. We have shown that the taper-waist core diameter mainly influences the maximum output power and power in the long-wavelength region, but has negligible influence on the SC bandwidth. The length before taper section also appears to have negligible impact on the SC bandwidth within the range of tested lengths. However using a combination of much longer length before taper section and longer length of taper-waist, a significant impact on the output spectrum was observed suggesting the importance of the length of taper-waist section. In this case, although the output power is significantly lower due to the longer length of fiber, however, the percentage of the power in the longer wavelength region is higher.

In Section 4.7, we have demonstrated power damage threshold measurements in chalcogenide fiber with glass compositions such as $Ge_{10}As_{22}Se_{68}$, $Ge_{14}As_{20}Se_{66}$, $Ge_{16}As_{20}Se_{64}$, and $As_{38}Se_{62}$. The power damage effect visible in these fibers at 1750 nm are due to band-gap related absorption and two-photon absorption. These fibers showed power damage threshold of between 10-40 mW of coupled input power. PCF made from $Ge_{14}As_{20}Se_{66}$ composition is the best among the other three compositions in terms of both the burning coupled power (117 mW) and coupling efficiency (48.9%) at 1750 nm. $Ge_{16}As_{20}Se_{64}$ fiber showed the highest damage threshold of 39 mW. No significant damage was seen for the fibers pumped at 2100 nm due to insufficient laser

power. Surprisingly, the $Ge_{10}As_{22}Se_{68}$ fiber showed the worst coupling efficiency with respect to the other fibers for unknown reason and we need to test it again in the future for much better estimation of its damage threshold. In addition to this, further measurements with much higher and stable pump power in the mid-IR region will be needed to have a better and clear understanding of the physical origin of the difference in power handling behavior between these fibers made from different compositions. Finally, the fibers with higher scattering losses appear to exhibit the best properties, which further confirms that the power-related damage experienced by fibers as can be seen from our measurements were not affected by the presence of particles inside the glass.

5

GENERAL CONCLUSION AND OUTLOOK

IN this thesis, our goal was to develop mid-IR SC light sources in soft glass microstructured photonic crystal fiber platform for numerous practical applications like optical sensing, material processing, biomedical imaging and microscopy cell and tissue analysis using OCT, confocal and fluorescence imaging, and infrared spectroscopy for molecular fingerprints. The combination of enhanced nonlinearities and tailorable dispersion characteristics enables small core microstructured fibers to efficiently generate ultra-broad supercontinua spanning from near-IR to mid-IR wavelengths. SC generation in microstructured PCFs through various nonlinear processes had been studied in details for different pump pulse parameters such as width, wavelength, and power.

In the project, strong collaboration with various national and international universities and companies had provided us incredible resources to achieve our goal. Towards our goal, in collaboration with the Institute of Electronic Materials Technology in Poland, we achieved a record SC bandwidth covering the near-IR from 891 nm - 2466 nm in heavy metal-oxide glass based suspended core microstructured PCF using femtosecond pulses pumped at 1580 nm. This suspended-core PCF structure offers tight light confinement and very small effective mode area. This geometry also prevents from glass recrystallization during fiber drawing using stack-and-draw method and provides higher mechanical durability. Using femtosecond pulses with peak power higher than the one used in this project, the SC bandwidth in these fibers could be increased until their transmission cut-off up to 2800 nm. This result demonstrates the strong potential of heavy metal-oxide suspended-core PCF for SC generation.

Our main goal of extending the SC bandwidth to mid-IR was achieved in a collaboration with the SelenOptics company, the University of Rennes, and the DTU Fotonik, where we obtained a polarization-preserving supercontinuum generation with a record broadening from 3.1 to 6.02 µm with output power of 11 mW by pumping a highly-birefringent microstructured photonic crystal fiber made of chalcogenide glass ($As_{38}Se_{62}$) with femtosecond pulses at 4 µm. Effects of polarization on SC bandwidth have also been investigated. This work constitutes an important step towards stable and linearly-polarized supercontinuum generation for various mid-IR applications such as gas and pressure sensing, integrated-optic devices and polarization-sensitive OCT. In spite of featuring a transmission window up to 10 µm, the SC bandwidth in $As_{38}Se_{62}$ PCF in this project was limited to 6 µm due to the unavailability of sufficiently high peak power of our laser pulses at desired pump wavelength and low coupling efficiency because of poor beam quality of our laser and difficulty to achieve smooth cleaving of chalcogenide fiber facet. The high purity $As_{38}Se_{62}$ glass was fabricated using standard melt-quenching method, fiber

preform was prepared using moulding method and the final PCF was drawn using the casting method. All these methods have been demonstrated in great details. Furthermore, to extend the SC bandwidth beyond 6 µm, $As_{38}Se_{62}$ PCF tapers, which increase the nonlinearity while maintaining a moderate damage threshold, were realized and investigated for efficient SC generation with relatively short pump wavelengths (around 2 µm). However, various factors like contamination of the taper-waist, crystallization of $As_{38}Se_{62}$ glass and non-adiabatic taper transitions during taper drawing process, high confinement loss for non-uniform and small taper-waist (1.77 µm diameter) unfortunately limit the transmission window of these tapers to around 5.5 µm and as a result they were not efficient for mid-IR SC generation beyond 6 µm for our project.

The above mentioned limitations were overcome in a collaboration with the SelenOptics Company and the DTU Fotonik where several microstructured PCF tapers with core diameters between 2.5-6 µm were fabricated from $Ge_{10}As_{22}Se_{68}$ glass and a SC spectrum covering from 1.3-6.3 µm with output power of 12.7 mW was obtained by direct pumping at 4 µm and the same taper with core diameter of 6 µm and 11 cm taper-waist section generated another SC spectrum covering from 1-7.4 µm with output power of 82 mW by pumping in a cascaded system with pump source covering 1-4.2 µm. The latter was further broadened up to 7.94 µm with output power of 33.4 mW using 30 cm of taper-waist section. Furthermore, the investigation also showed that taper-waist core diameter had negligible influence on the SC bandwidth, however, it influences the maximum output power and power in the long-wavelength region. Near-IR pumped cascaded system have made a revolutionary change in mid-IR SC generation to allow us to build compact and low cost all fiber SC sources. SC bandwidth has been further broadened up to 10 µm by using short length chalcogenide fiber in an all fiber cascaded system, which was realized in another collaboration with SelenOptics, LEUKOS, and Le Verre Fluoré companies, McGill University and the University of Rennes.

Lastly, in a collaboration with the University of Rennes, the power handling capabilities of chalcogenide fiber had been investigated in the near-IR wavelengths in PCFs with different glass compositions (mainly increasing the germanium content in the glass) such as $Ge_{10}As_{22}Se_{68}$, $Ge_{14}As_{20}Se_{66}$, $Ge_{16}As_{20}Se_{64}$, and $As_{38}Se_{62}$. Power damage effect in chalcogenide fibers usually occurs due to a number of thermal effects such as thermally induced stress, fatigue effects, cumulative pulse effects, and melting that are caused as a result of the local increase in temperature given by linear, nonlinear and free carrier absorption. At 1750 nm, band-gap related absorption and two-photon absorption were the main contributor to the power damage effect. $Ge_{16}As_{20}Se_{64}$ had showed the highest damage threshold behaviour where as $Ge_{14}As_{20}Se_{66}$ PCFs had showed to support the highest burning coupled power and coupling efficiency than the rest of the fibers. Due to insufficient laser power, fibers pumped at 2100 nm did not show any significant damage. Therefore, we do require further measurements with much higher and stable pump power in the mid-IR region for a better and clear understanding of the physical origin of the difference in power handling behavior between these different compositions.

From the experimental evidence, in my opinion cascaded pumping system is the best and efficient way to develop mid-IR SC sources up to 10 µm and beyond. Here we will provide several recommendations to improve the performance of mid-IR SC sources. We will recommend for telluride-glass fibers as a final fiber to further broaden the cascaded spectrum beyond 10 µm. Another recommendation is the use of anti-reflection coating or nanoimprinting of the chalcogenide fibers that could significantly reduce the Fresnel losses and the input damage threshold, which in turns allow us to considerably increase

both the output power and the power spectral density. Polarization and coherence properties of the mid-IR SC light are the key parameters for some applications such as mid-IR OCT and interferometric measurements. Therefore, polarization property could be maintained for example by replacing the fiber laser and the cascaded system with polarization-maintaining fibers. All the anomalous dispersion regime SC generation demonstrated in this thesis do not maintain the initial temporal coherence of the input laser. Therefore, in order to maintain the coherence property, we could consider all-normal dispersion (ANDi) chalcogenide fibers directly pumped with mid-IR femtosecond fiber lasers.

BIBLIOGRAPHY

[1] RAMAN, C. V. **A new radiation**. *Indian J. Phys. 2* (1928), 387–398.

[2] MORSE, P. M., AND FESHBACH, H. **Methods of Theoretical Physics**. McGraw-Hill, New York, 1953.

[3] SUTTON, L. E., AND STAVROUDIS, O. N. **Fitting refractive index data by least squares**. *J. Opt. Soc. Am. 51*, 8 (1961), 901–905.

[4] MILLER, R. C. **Optical second harmonic generation in piezoelectric crystals**. *Appl. Phys. Lett. 5*, 17 (1964), 17–19.

[5] TATIAN, B. **Interpolation of glass indices with applications to first order axial chromatic aberration**. *Itek Corp. Report OR-63-20, Lexington, Mass. 51* (1964).

[6] DEMARTINI, F., TOWNES, C. H., GUSTAFSON, T. K., AND KELLEY, P. L. **Self-steepening of light pulses**. *Phys. Rev. 164*, 2 (1967), 312–323.

[7] SHIMIZU, F. **Frequency broadening in liquids by a short light pulse**. *Phys. Rev. Lett. 19*, 19 (1967), 1097–1100.

[8] ALFANO, R. R., AND SHAPIRO, S. L. **Observation of self-phase modulation and small-scale filaments in crystals and glasses**. *Phys. Rev. Lett. 24*, 11 (1970), 592–594.

[9] KAPRON, F. P., KECK, D. B., AND MAURER, R. D. **Radiation losses in glass optical waveguides**. *Appl. Phys. Lett. 17*, 10 (1970), 423–425.

[10] MARCUSE, D. **Light Transmission Optics**. New York: Wiley, 1972.

[11] ZAKHAROV, V. E., AND SHABAT, A. B. **Exact theory of two-dimensional self-focusing and one-dimensional self-modulation of waves in nonlinear media**. *Sov. Phys. JETP 34*, 12 (1972), 62–69.

[12] GRISCHKOWSKY, D., COURTENS, E., AND ARMSTRONG, J. A. **Observation of self-steepening of optical pulses with possible shock formation**. *Phys. Rev. Lett. 31*, 7 (1973), 422–425.

[13] IPPEN, E. P., SHANK, C. V., AND GUSTAFSON, T. K. **Self-phase modulation of picosecond pulses in optical fibers**. *Appl. Phys. Lett. 24*, 4 (1974), 190–192.

[14] KAISER, P., AND ASTLE, H. W. **Low-loss single material fibers made from pure fused silica**. *Bell Syst. Tech. J. 53* (1974), 1021–1039.

[15] STOLEN, R. H., BJORKHOLM, J. E., AND ASHKIN, A. **Phase-matched three-wave mixing in silica fiber optical waveguides**. *Appl. Phys. Lett. 24*, 7 (1974), 308–310.

[16] FISHER, R. A., AND BISCHEL, W. K. **Numerical studies of the interplay between self-phase modulation and dispersion for intense plane-wave laser pulses**. *J. Appl. Phys. 46*, 11 (1975), 4921–4934.

[17] FEIT, M. D., AND FLECK, J. A. **Light propagation in graded-index optical fibers**. *Appl. Opt. 17*, 24 (1978), 3990–3998.

[18] STOLEN, R. H., AND LIN, C. **Self-phase modulation in silica optical fibers**. *Phys. Rev. A 17*, 4 (1978), 1448–1453.

[19] HOSAKA, T., OKAMOTO, K., MIYA, T., SASAKI, Y., AND EDAHIRO, T. **Low-loss single polarization fibers with asymmetrical strain birefringence**. *Electron. Lett. 17*, 15 (1981), 530–531.

[20] BIRCH, R. D., PAYNE, D. N., AND VARNHAM, M. P. **Fabrication of polarisation-maintaining fibres using gas-phase etching**. *Electron. Lett. 18*, 24 (1982), 1036–1038.

[21] MARCUSE, D. **Light Transmission Optics**. Van Nostrand Reinhold, New York, 1982.

[22] RASHLEIGH, S. C. **Measurement of fiber birefringence by wavelength scanning: effect of dispersion**. *Opt. Lett. 8*, 6 (1983), 336–338.

[23] SHIBATA, N., SASAKI, Y., OKAMOTO, K., AND HOSAKA, T. **Fabrication of polarization-maintaining and absorption-reducing fibers**. *J. Light. Technol. 1*, 1 (1983), 38–43.

[24] SNYDER, A. W., AND LOVE, J. D. **Optical Waveguide Theory**. Chapman and Hall, London, 1983.

[25] ANDERSON, D., AND LISAK, M. **Modulational instability of coherent optical-fiber transmission signals**. *Opt. Lett. 9*, 10 (1984), 468–470.

[26] HASEGAWA, A. **Generation of a train of soliton pulses by induced modulational instability in optical fibers**. *Opt. Lett. 9*, 7 (1984), 288–290.

[27] JAIN, R. K., AND STENERSEN, K. **Phase-matched four-photon mixing processes in birefringent fibers**. *Appl. Phys. B 35* (1984), 49–57.

[28] SHEN, Y. R. **Principles of Nonlinear Optics**. Wiley, New York, 1984.

[29] TATIAN, B. **Fitting refractive-index data with the Sellmeier dispersion formula**. *Appl. Opt. 23*, 24 (1984), 4477–4485.

[30] YANG, G., AND SHEN, Y. R. **Spectral broadening of ultrashort pulses in a nonlinear medium**. *Opt. Lett. 9*, 11 (1984), 510–512.

[31] MANASSAH, J. T., MUSTAFA, M. A., ALFANO, R. R., AND HO, P. P. **Induced supercontinuum and steepening of an ultrafast laser pulse**. *Phys. Lett. 113A*, 5 (1985), 242–247.

[32] GORDON, J. P. **Theory of the soliton self-frequency shift**. *Opt. Lett. 11*, 10 (1986), 662–664.

[33] MITSCHKE, F. M., AND MOLLENAUER, L. F. **Discovery of the soliton self-frequency shift**. *Opt. Lett. 11*, 10 (1986), 659–661.

[34] NODA, J., OKAMOTO, K., AND SASAKI, T. **Polarization-maintaining fibers and their applications**. *J. Lightwave Technol. 4*, 8 (1986), 1071–1089.

[35] TAI, K., HASEGAWA, A., AND TOMITA, A. **Observation of modulational instability in optical fibers**. *Phys. Rev. Lett. 56*, 2 (1986), 135–138.

[36] WAI, P. K. A., MENYUK, C. R., LEE, Y. C., AND CHEN, H. H. **Nonlinear pulse propagation in the neighborhood of the zero-dispersion wavelength of monomode optical fibers**. *Opt. Lett. 11*, 7 (1986), 464–466.

[37] BEAUD, P., HODEL, W., ZYSSET, B., AND WEBER, H. P. **Ultrashort pulse-propagation, pulse breakup, and fundamental soliton formation in a single-mode optical fiber**. *IEEE J. Quantum Electron. 23*, 11 (1987), 1938–1946.

[38] KODAMA, Y., AND HASEGAWA, A. **Nonlinear pulse-propagation in a monomode dielectric guide**. *IEEE J. Quantum Electron. 23*, 5 (1987), 510–524.

[39] KODAMA, Y., AND NOZAKI, K. **Soliton interaction in optical fibers**. *Opt. Lett. 12*, 12 (1987), 1038–1040.

[40] NODA, J., OKAMOTO, K., AND YOKOHAMA, I. **Fiber devices using polarization-maintaining fibers**. *Fiber and Integrated Opt. 6*, 4 (1987), 309–329.

[41] THÉVENAZ, L., COULON, V. D., AND DER WEID, J.-P. V. **Polarization-mode interferometry in birefringent single-mode fibers**. *Opt. Lett. 12*, 8 (1987), 619–621.

[42] BLOW, K. J., AND WOOD, D. **Theoretical description of transient stimulated Raman-scattering in optical fibers**. *IEEE J. Quantum Electron. 25*, 12 (1989), 2665–2673.

[43] STOLEN, R. H., GORDON, J. P., TOMLINSON, W. J., AND HAUS, H. A. **Raman response function of silica-core fibers**. *J. Opt. Soc. Am. B 6*, 6 (1989), 1159–1166.

[44] TAJIMA, K., AND SASAKI, Y. **Transmission loss of a 125 µm diameter PANDA fiber with circular stress-applying parts**. *J. Lightwave Technol. 7*, 4 (1989), 674–679.

[45] BUTCHER, P. N., AND COTTER, D. N. **The Elements of Nonlinear Optics**. Cambridge University Press, Cambridge, UK, 1990.

[46] DONG, A., HUANG, P., AND CAUGHEY, W. S. **Protein secondary structures in water from second-derivative amide I infrared spectra**. *Biochemistry 29*, 13 (1990), 3303–3308.

[47] HERMANSSON, B., YEVICK, D., VARDYSZEWSKI, W., AND GLASNER, M. **The unitarity of split-operator finite difference and finite-element methods: Applications to longitudinally varying semiconductor rib waveguides**. *J. Lightwave Technol. 8*, 12 (1990), 1866–1873.

[48] MAMYSHEV, P. V., AND CHERNIKOV, S. V. **Ultrashort-pulse propagation in optical fibers**. *Opt. Lett. 15*, 19 (1990), 1076–1078.

[49] CAPPELLINI, G., AND TRILLO, S. **Third order three-wave mixing in single-mode fibers: Exact solutions and spatial instability effects**. *J. Opt. Soc. Amer. B 8*, 4 (1991), 824–838.

[50] MARCUSE, D. **Theory of Dielectric Optical waveguides**. Academic Press, San Diego, CA, 1991.

[51] KODAMA, Y., AND HASEGAWA, A. **Theoretical foundation of optical-soliton concept in fibers**. *Prog. Optics 30* (1992), 205–259.

[52] LUCEK, J. K., AND BLOW, K. J. **Soliton self-frequency shift in telecommunications fiber**. *Phys. Rev. A 45*, 9 (1992), 6666–6674.

[53] SCHMIDT, F. **An adaptive approach to the numerical solution of Fresnel's wave equation**. *J. Lightwave Technol. 11*, 9 (1993), 1425–1434.

[54] AKHMEDIEV, N., AND KARLSSON, M. **Cherenkov radiation emitted by solitons in optical fibers**. *Phys. Rev. A 51*, 3 (1995), 2602–2607.

[55] KNIGHT, J. C., BIRKS, T. A., RUSSELL, P. S. J., AND ATKIN, D. M. **All-silica single-mode optical fiber with photonic crystal cladding**. *Opt. Lett. 21*, 19 (1996), 1547–1549.

[56] SAUTER, E. G. **Nonlinear Optics**, 1st ed. John Wiley & Sons, New York, 1996.

[57] BIRKS, T. A., KNIGHT, J. C., AND RUSSELL, P. S. **Endlessly single-mode photonic crystal fiber**. *Opt. Lett. 22*, 13 (1997), 961–963.

[58] LIU, Q. D., SHI, L., HO, P. P., ALFANO, R. R., ESSIAMBRE, R. J., AND AGRAWAL, G. P. **Degenerate-cross-phase modulation of femtosecond laser pulses in a birefringent single-mode optical fiber**. *IEEE Photon. Technol. 9*, 8 (1997), 1107–1109.

[59] TSUJI, Y., KOSHIBA, M., AND SHIRAISHI, T. **Finite element beam propagation method for three-dimensional optical waveguide structures**. *J. Lightwave Technol. 15*, 9 (1997), 1728–1734.

[60] ALLEN, M. G. **Diode laser absorption sensors for gas-dynamic and combustion flows**. *Meas. Sci. Technol. 9*, 4 (1998), 545–562.

[61] JACKSON, J. D. **Classical Electrodynamics**, 3rd ed. Wiley, New York, 1998.

[62] KNIGHT, J. C., BIRKS, T. A., CREGAN, R. F., RUSSELL, P. S., AND DE SANDRO, J. P. **Large mode area photonic crystal fibre**. *Electron. Lett. 34*, 13 (1998), 1347–1348.

[63] KNIGHT, J. C., BROENG, J., BIRKS, T. A., AND RUSSEL, P. S. J. **Photonic band cap guidance in optical fibers**. *Science 282*, 5393 (1998), 1476–1478.

[64] MILAM, D. **Review and assessment of measured values of the nonlinear refractive-index coefficient of fused silica**. *Appl. Opt. 37*, 3 (1998), 546–550.

[65] RUSSELL, P. S. J., BIRKS, T. A., KNIGHT, J. C., CREGAN, R. F., MANGAN, B., AND SANDRO, J. P. D. **Silica/air photonic crystal fibres**. *Jpn. J. Appl. Phys. 37* (1998), 45–48.

[66] BARKOU, S. E., BROENG, J., AND BJARKLEV, A. **Silica-air photonic crystal fiber design that permits waveguiding by a true photonic bandgap effect**. *Opt. Lett. 24*, 1 (1999), 46–48.

[67] BENNETT, P. J., MONRO, T. M., AND RICHARDSON, D. J. **Toward practical holey fiber technology: fabrication, splicing, modeling, and characterization**. *Opt. Lett. 24*, 17 (1999), 1203–1205.

[68] BRODERICK, N. G. R., MONRO, T. M., BENNETT, P. J., AND RICHARDSON, D. J. **Nonlinearity in holey optical fibers: measurement and future opportunities**. *Opt. Lett. 24*, 20 (1999), 1395–1397.

[69] BROENG, J., MOGILEVSTEV, D., BARKOU, S. E., AND BJARKLEV, A. **Photonic crystal fibers: A new class of optical waveguides**. *Opt. Fiber Technol. 5*, 3 (1999), 305–330.

[70] FERRANDO, A., SILVESTRE, E., MIRET, J. J., MONSORIU, J. A., ANDRES, M. V., AND RUSSELL, P. S. **Designing a photonic crystal fibre with flattened chromatic dispersion**. *Electron. Lett. 35*, 4 (1999), 325–327.

[71] BIRKS, T. A., WADSWORTH, W. J., AND RUSSELL, P. S. J. **Supercontinuum generation in tapered fibers**. *Opt. Lett. 25*, 19 (2000), 1415–1417.

[72] KNIGHT, J. C., ARRIAGA, J., BIRKS, T. A., ORTIGOSA-BLANCH, A., WADSWORTH, W. J., AND RUSSELL, P. S. **Anomalous dispersion in photonic crystal fiber**. *IEEE Photonics Technol. Lett. 12*, 7 (2000), 807–809.

[73] LENZ, G., ZIMMERMANN, J., KATSUFUJI, T., LINES, M. E., HWANG, H. Y., SPÄLTER, S., SLUSHER, R. E., CHEONG, S.-W., SANGHERA, J. S., AND AGGARWAL, I. D. **Large Kerr effect in bulk Se-based chalcogenide glasses**. *Opt. Lett. 25*, 4 (2000), 254–256.

[74] MIDRIO, M., SINGH, M. P., AND SOMEDA, C. G. **The space filling mode of holey fibers: an analytical vectorial solution**. *J. Lightwave Technol. 18*, 7 (2000), 1031–1037.

[75] MONRO, T. M., WEST, Y. D., HEWAK, D. W., BRODERICK, N. G. R., AND RICHARDSON, D. J. **Chalcogenide holey fibres**. *Electron. Lett. 36*, 24 (2000), 1998–2000.

[76] ORTIGOSA-BLANCH, A., KNIGHT, J. C., WADSWORTH, W. J., ARRIAGA, J., MANGAN, B. J., BIRKS, T. A., AND RUSSELL, P. S. J. **Highly birefringent photonic crystal fibers**. *Opt. Lett. 25*, 18 (2000), 1325–1327.

[77] ORTIGOSA-BLANCH, A., KNIGHT, J. C., WADSWORTH, W. J., ARRIAGA, J., MANGAN, B. J., BIRKS, T. A., AND RUSSELL, P. S. J. **Highly birefringent photonic crystal fibers**. *Opt. Lett. 25*, 18 (2000), 1325–1327.

[78] ZHELTIKOV, A. M. **Holey fibers**. *PHYS-USP 43*, 11 (2000), 1125–1136.

[79] BAGGETT, J. C., MONRO, T. M., FURUSAWA, K., AND RICHARDSON, D. J. **Comparative study of large-mode holey and conventional fibers**. *Opt. Lett. 26*, 4 (2001), 1045–1047.

[80] BIRKS, T. A., KNIGHT, J. C., MANGAN, B. J., AND RUSSELL, P. S. **Photonic crystal fibres: An endless variety**. *IEICE Trans. Electron. E84C*, 5 (2001), 585–592.

[81] HANSEN, T. P., BROENG, J., LIBORI, S. E. B., KNUDSEN, E., BJARKLEV, A., JENSEN, J. R., AND SIMONSEN, H. **Highly birefringent index-guiding photonic crystal fibers**. *IEEE Photonics Technol. Lett. 13*, 6 (2001), 588–590.

[82] HECHT, J. **Holes in photonic crystal fibers open new possibilities**. *Laser Focus World 37* (2001), 207–216.

[83] KARASAWA, N., NAKAMURA, S., NAKAGAWA, N., SHIBATA, M., MORITA, R., SHIGEKAWA, H., AND YAMASHITA, M. **Comparison between theory and experiment of nonlinear propagation for a-few-cycle and ultrabroadband optical pulses in a fused silica fiber**. *IEEE J. Quantum Electron. 37*, 3 (2001), 398–404.

[84] LIZIER, J. T., AND TOWN, G. E. **Splice losses in holey optical fibers**. *IEEE Photonics Technol. Lett. 13*, 8 (2001), 794–796.

[85] MOGILEVTSEV, D., BROENG, J., BARKOU, S. E., AND BJARKLEV, A. **Design of polarization-preserving photonic crystal fibres with elliptical pores**. *J. Opt. A: Pure Appl. Opt. 3* (2001), s141–s143.

[86] SORENSEN, T., BROENG, J., BJARKLEV, A., KNUDSEN, E., AND LIBORI, S. E. B. **Macro-bending loss properties of photonic crystal fibre**. *Electron. Lett. 37*, 5 (2001), 287–289.

[87] SUZUKI, K., KUBOTA, H., KAWANISHI, S., TANAKA, M., AND FUJITA, M. **High-speed bi-directional polarization division multiplexed optical transmission in ultra low-loss (1.3 dB/km) polarization-maintaining photonic crystal fiber**. *Electron. Lett. 37*, 23 (2001), 1399–1401.

[88] SUZUKI, K., KUBOTA, H., KAWANISHI, S., TANAKA, M., AND FUJITA, M. **Optical properties of a low-loss polarization-maintaining photonic crystal fiber**. *Opt. Express 9*, 13 (2001), 676–680.

[89] WHITE, T. P., MCPHEDRAN, R. C., DE STERKE, C. M., BOTTEN, L. C., AND STEEL, M. J. **Confinement losses in microstructured optical fibers**. *Opt. Lett. 26*, 21 (2001), 1660–1662.

[90] ZHU, Z., AND BROWN, T. G. **Analysis of the space filling modes of photonic crystal fibers**. *Opt. Express 8*, 10 (2001), 547–554.

[91] BENABID, F., KNIGHT, J. C., ANTONOPOULOS, G., AND RUSSELL, P. S. J. **Stimulated Raman scattering in hydrogen-filled hollow-core photonic crystal fiber**. *Science 298*, 5592 (2002), 399–402.

[92] FERRARINI, D., VINCETTI, L., ZOBOLI, M., CUCINOTTA, A., AND SELLERI, S. **Leakage properties of photonic crystal fibers**. *Opt. Express 10*, 23 (2002), 1314–1319.

[93] HANSRYD, J., ANDREKSON, P. A., WESTLUND, M., AND HEDEKVIST, P. **Fiber-based optical parametric amplifiers and their applications**. *IEEE J. Sel. Top. Quantum Electron. 8*, 3 (2002), 506–520.

[94] HERRMANN, J., GRIEBNER, U., ZHAVORONKOV, N., HUSAKOU, A., NICKEL, D., KNIGHT, J. C., WADSWORTH, W. J., RUSSELL, P. S. J., AND KORN, G. **Experimental evidence for supercontinuum generation by fission of higher-order solitons in photonic fibers**. *Phys. Rev. Lett. 88*, 17 (2002), 173901.

[95] KIANG, K. M., FRAMPTON, K., MONRO, T. M., MOORE, R., TUCKNOTT, J., HEWAK, D. W., RICHARDSON, D. J., AND RUTT, H. N. **Extruded singlemode non-silica glass holey optical fibres**. *Electron. Lett. 38*, 12 (2002), 546–547.

[96] KNIGHT, J. C., AND RUSSELL, R. S. J. **Microstructured glass for optical fibers**. *Glass Sci. Technol. 75* (2002), 54–62.

[97] KUMAR, V., GEORGE, A. K., REEVES, W. H., KNIGHT, J. C., RUSSELL, P. S., OMENETTO, F. G., AND TAYLOR, A. J. **Extruded soft glass photonic crystal fiber for ultrabroad supercontinuum generation**. *Opt. Express 10*, 25 (2002), 1520–1525.

[98] RAO, K. J. **Structural Chemistry of Glasses**, 1st ed. Elsevier Science, 2002.

[99] REEVES, W. H., KNIGHT, J. C., RUSSELL, P. S. J., AND ROBERTS, P. J. **Demonstration of ultra-flattened dispersion in photonic crystal fibers**. *Opt. Express 10*, 14 (2002), 609–613.

[100] BJARKLEV, A., BROENG, J., AND BJARKLEV, A. S. **Photonic Crystal Fibres**, 1st ed. Kluwer Academic Publishers, Boston, 2003.

[101] FANG, X., KARASAWA, N., MORITA, R., WINDELER, R., AND YAMASHITA, M. **Nonlinear propagation of a-few-optical cycle pulses in a photonic crystal fiber—experimental and theoretical studies beyond the slowly varying-envelope approximation**. *IEEE Photonics Technol. Lett. 15*, 2 (2003), 233–235.

[102] FINAZZI, V., MONRO, T. M., AND RICHARDSON, D. J. **The role of confinement loss in highly nonlinear silica holey fibers**. *IEEE Photonics Technol. Lett. 15*, 9 (2003), 1246–1248.

[103] FROSZ, M. H., HOUGAARD, K., LIBORI, S. E. B., LAEGSGAARD, J., AND BJARKLEV, A. **Radial deformation losses in photonic crystal fibres**. *J. Opt. A-Pure Appl. Opt. 5*, 3 (2003), 268–271.

[104] HANSEN, K. P. **Dispersion flattened hybrid-core nonlinear photonic crystal fiber**. *Opt. Express 11*, 13 (2003), 1503–1509.

[105] JU, J., JIN, W., AND DEMOKAN, M. S. **Properties of a highly birefringent photonic crystal fiber**. *IEEE Photonics Technol. Lett. 15*, 10 (2003), 1375–1377.

[106] KNIGHT, J. C. **Photonic crystal fibres**. *Nature 424* (2003), 847–851.

[107] KOSHIBA, M., AND SAITOH, K. **Polarization-dependent confinement losses in actual holey fibers**. *IEEE Photonics Technol. Lett. 15*, 5 (2003), 691–693.

[108] MONRO, T. M., AND RICHARDSON, D. J. **Holey optical fibres: Fundamental properties and device applications**. *C. R. Phys. 4*, 1 (2003), 175–186.

[109] MORTENSEN, N. A., NIELSEN, M. D., FOLKENBERG, J. R., PETERSSON, A., AND SIMONSEN, H. R. **Improved large-mode-area endlessly single-mode photonic crystal fibers**. *Opt. Lett. 28*, 6 (2003), 393–395.

[110] NIELSEN, M. D., MORTENSEN, N. A., AND FOLKENBERG, J. R. **Reduced microdeformation attenuation in large-mode-area photonic crystal fibers for visible applications**. *Opt. Lett. 28*, 18 (2003), 1645–1647.

[111] OUZOUNOV, D. G., AHMAD, F. R., MÜLLER, D., VENKATARAMAN, N., GALLAGHER, M. T., THOMAS, M. G., SILCOX, J., KOCH, K. W., AND GAETA, A. L. **Generation of megawatt optical solitons in hollow-core photonic band-gap fibers**. *Science 301*, 5640 (2003), 1702–1704.

[112] RENVERSEZ, G., KUHLMEY, B., , AND MCPHEDRAN, R. **Dispersion management with microstructured optical fibers: ultraflattened chromatic dispersion with low losses**. *Opt. Lett. 28*, 12 (2003), 989–991.

[113] RUSSELL, P. S. J. **Photonic crystal fibers**. *Science 299*, 5605 (2003), 358–362.

[114] SAITOH, K., AND KOSHIBA, M. **Single-polarization single-mode photonic crystal fibers**. *IEEE Photonics Technol. Lett. 15*, 10 (2003), 1384–1386.

[115] SAITOH, K., KOSHIBA, M., HASEGAWA, T., AND SASAOKA, E. **Chromatic dispersion control in photonic crystal fibers: application to ultra-flattened dispersion**. *Opt. Express 11*, 8 (2003), 843–852.

[116] ZHELTIKOV, A. M. **Limiting efficiencies of nonlinear-optical processes in microstructure fibers**. *J. Exp. Theor. Phys. 97*, 3 (2003), 505–521.

[117] KOLESIK, M., WRIGHT, E. M., AND MOLONEY, J. V. **Simulation of femtosecond pulse propagation in sub-micron diameter tapered fibers**. *Appl. Phys. B 79* (2004), 293–300.

[118] KOSHIBA, M., AND SAITOH, K. **Applicability of classical optical fiber theories to holey fibers**. *Opt. Lett. 29*, 15 (2004), 1739–1741.

[119] OLIVIER, T., BILLARD, F., AND AKHOUAYRI, H. **Nanosecond Z-scan measurements of the nonlinear refractive index of fused silica**. *Opt. Express 12*, 7 (2004), 1377–1382.

[120] SLUSHER, R. E., LENZ, G., HODELIN, J., SANGHERA, J., SHAW, L. B., AND AGGARWAL, I. D. **Large Raman gain and nonlinear phase shifts in high-purity As_2Se_3 chalcogenide fibers**. *J. Opt. Soc. Am. B 21*, 6 (2004), 1146–1155.

[121] ZHU, Z., AND BROWN, T. G. **Polarization properties of supercontinuum spectra generated in birefringent photonic crystal fibers**. *J. Opt. Soc. Am. B 21*, 2 (2004), 249–257.

[122] KIBLER, B., DUDLEY, J. M., AND COEN, S. **Supercontinuum generation and nonlinear pulse propagation in photonic crystal fiber: influence of the frequency-dependent effective mode area**. *Appl. Phys. B 81*, 2–3 (2005), 337–342.

[123] LIMPERT, J., DEGUIL-ROBIN, N., MANEK-HÖNNINGER, I., SALIN, F., RÖSER, F., LIEM, A., SCHREIBER, T., NOLTE, S., ZELLMER, H., TÜNNERMANN, A., BROENG, J., PETERSSON, A., AND JAKOBSEN, C. **High-power rod-type photonic crystal fiber laser**. *Opt. Express 13*, 4 (2005), 1055–1058.

[124] SCHREIBER, T., RÖSER, F., SCHMIDT, O., LIMPERT, J., ILIEW, R., LEDERER, F., PETERSSON, A., JACOBSEN, C., HANSEN, K., BROENG, J., AND TÜNNERMANN, A. **Stress-induced single-polarization single-transverse mode photonic crystal fiber with low nonlinearity**. *Opt. Express 13*, 19 (2005), 7621–7630.

[125] SKRYABIN, D. V., AND YULIN, A. V. **Theory of generation of new frequencies by mixing of solitons and dispersive waves in optical fibers**. *Phys. Rev. E 72* (2005), 016619.

[126] **Supercontinuum generation in materials (solids, liquids, gases, air)**. In *The Supercontinuum Laser Source*, R. R. Alfano, Ed. Springer, New York, 2006.

[127] COUNY, F., BENABID, F., AND LIGHT, P. S. **Large pitch kagome-structured hollow-core photonic crystal fiber**. *Opt. Lett. 31*, 24 (2006), 3574–3576.

[128] DUDLEY, J. M., GENTY, G., AND COEN, S. **Supercontinuum generation in photonic crystal fiber**. *Rev. Mod. Phys. 78* (2006), 1135–1184.

[129] GORBACH, A. V., SKRYABIN, D. V., STONE, J. M., AND KNIGHT, J. C. **Four-wave mixing of solitons with radiation and quasi-nondispersive wave packets at the short-wavelength edge of a supercontinuum**. *Opt. Express 14*, 21 (2006), 9854–9863.

[130] XIA, C., KUMAR, M., KULKARNI, O. P., ISLAM, M. N., TERRY, F. L., FREEMAN, M. J., POULAIN, M., AND MAZÉ, G. **Mid-infrared supercontinuum generation to 4.5 µm in ZBLAN fluoride fibers by nanosecond diode pumping**. *Opt. Lett. 31*, 17 (2006), 2553–2555.

[131] AGRAWAL, G. P. **Nonlinear Fiber Optics**. New York: Academic, 2007.

[132] CHEN, D., AND SHEN, L. **Highly birefringent elliptical-hole photonic crystal fibers with double defect**. *J. L. Technol. 25*, 9 (2007), 2700–2705.

[133] COUNY, F., BENABID, F., ROBERTS, P. J., LIGHT, P. S., AND RAYMER, M. G. **Generation and photonic guidance of multi-octave optical-frequency combs**. *Science 318*, 5853 (2007), 1118–1121.

[134] GORBACH, A. V., AND SKRYABIN, D. V. **Light trapping in gravity-like potentials and expansion of supercontinuum spectra in photonic-crystal fibres**. *Nat. Photonics 1* (2007), 653–657.

[135] HULT, J., WATT, R. S., AND KAMINSKI, C. F. **High bandwidth absorption spectroscopy with a dispersed supercontinuum source**. *Opt. Express 15*, 18 (2007), 11385–11395.

[136] JEFFREY, A., AND ZWILLINGER, D. **Table of Integrals, Series, and Products**, 7th ed. Academic Press, San Diego, CA, 2007.

[137] MÄGI, E. C., FU, L. B., NGUYEN, H. C., LAMONT, M. R. E., YEOM, D. I., AND EGGLETON, B. J. **Enhanced Kerr nonlinearity in sub-wavelength diameter As_2Se_3 chalcogenide fiber tapers**. *Opt. Express 15*, 16 (2007), 10324–10329.

[138] PEARCE, G. J., WIEDERHECKER, G. S., POULTON, C. G., BURGER, S., AND RUSSELL, P. S. J. **Models for guidance in kagome-structured hollow-core photonic crystal fibres**. *Opt. Express 15*, 20 (2007), 12680–12685.

[139] POLI, F., CUCINOTTA, A., AND SELLERI, S. **Photonic Crystal Fibers**, 1st ed. Springer, Netherlands, 2007.

[140] PRICE, J. H. V., MONRO, T. M., EBENDORFF-HEIDEPRIEM, H., POLETTI, F., HORAK, P., FINAZZI, V., LEONG, J. Y. Y., PETROPOULOS, P., FLANAGAN, J. C., BRAMBILLA, G., FENG, X., AND RICHARDSON, D. J. **Mid-IR supercontinuum generation from nonsilica microstructured optical fibers**. *IEEE J. Sel. Top. Quantum Electron. 13*, 3 (2007), 738–749.

[141] SALEH, B. E. A., AND TEICH, M. C. **Fundamentals of Photonics**, 2nd ed. Wiley, New Jersey, 2007.

[142] WALSH, M. J., GERMAN, M. J., SINGH, M., POLLOCK, H. M., HAMMICHE, A., KYRGIOU, M., STRINGFELLOW, H. F., PARASKEVAIDIS, E., MARTIN-HIRSCH, P. L., AND MARTIN, F. L. **IR microspectroscopy: potential applications in cervical cancer screening**. *Cancer Lett. 246*, 1–2 (2007), 1–11.

[143] BOYD, R. W. **Nonlinear Optics**, 3rd ed. Academic Press, 2008.

[144] BRILLAND, L., TROLES, J., HOUIZOT, P., DESEVEDAVY, F., COULOMBIER, Q., RENVERSEZ, G., CHARTIER, T., NGUYEN, T. N., ADAM, J. L., AND TRAYNOR, N. **Interfaces impact on the transmission of chalcogenide photonic crystal fibres**. *J. Ceram. Soc. Jpn 116*, 1358 (2008), 1024–1027.

[145] DOMACHUK, P., WOLCHOVER, N. A., CRONIN-GOLOMB, M., WANG, A., GEORGE, A. K., CORDEIRO, C. M. B., KNIGHT, J. C., AND OMENETTO, F. G. **Over 4000 nm bandwidth of mid-IR supercontinuum generation in sub-centimeter segments of highly nonlinear tellurite PCFs**. *Opt. Express 16*, 10 (2008), 7161–7168.

[146] DONG, L., THOMAS, B. K., AND FU, L. **Highly nonlinear silica suspended core fibers**. *Opt. Express 16*, 21 (2008), 16423–16430.

[147] FU, H. Y., TAM, H. Y., SHAO, L. Y., DONG, X., WAI, P. K. A., LU, C., AND KHIJWANIA, S. K. **Pressure sensor realized with polarization-maintaining photonic crystal fiber-based Sagnac interferometer**. *Appl. Opt. 47*, 15 (2008), 2035–2039.

[148] HANCOCK, G., HORROCKS, S. J., RITCHIE, G. A. D., VAN-HELDEN, J. H., AND WALKER, R. J. **Time-resolved detection of the CF3 photofragment using chirped QCL radiation**. *J. Phys. Chem. A 112*, 40 (2008), 9751–9757.

[149] LORENC, D., ARANYOSIOVA, M., BUCZYNSKI, R., STEPIEN, R., BUGAR, I., VINCZE, A., AND VELIC, D. **Nonlinear refractive index of multicomponent glasses designed for fabrication of photonic crystal fibers**. *Appl. Phys. B 93* (2008), 531–538.

[150] MERGO, P., MAKARA, M., WOJCIK, J., POTURAJ, K., KLIMEK, J., SKORUPSKI, K., AND NASILOWSKI, T. **Supercontinuum generation in suspended core microstructured optical fibers**. *Proc. SPIE 7120* (2008), 712009.

[151] PRASAD, A., ZHA, C., WANG, R., SMITH, A., MADDEN, S., AND LUTHER-DAVIES, B. **Properties of $Ge_xAs_ySe_{1-x-y}$ glasses for all-optical signal processing**. *Opt. Express 16*, 4 (2008), 2804–2815.

[152] RAMPUR, A., CIACKA, P., CIMEK, J., KASZTELANIC, R., BUCZYNSKI, R., AND KLIMCZAK, M. **Development of suspended core soft glass fibers for far-detuned parametric conversion**. *J. Opt. 20*, 4 (2008), 045501.

[153] WILDANGER, D., RITTWEGER, E., KASTRUP, L., AND HELL, S. **STED microscopy with a supercontinuum laser**. *Opt. Express 16*, 13 (2008), 9614–9621.

[154] ZHANG, X., BUREAU, B., LUCAS, P., BOUSSARD-PLEDEL, C., AND LUCAS, J. **Glasses for seeing beyond visible**. *Chem. Eur. J. 14* (2008), 432–444.

[155] DIANOV, E. M., LIKHACHEV, M. E., AND FÉVRIER, S. **Solid-core photonic bandgap fibers for high-power fiber lasers**. *IEEE J Sel Top Quantum Electron 15*, 1 (2009), 20–29.

[156] FATOME, J., FORTIER, C., NGUYEN, T. N., CHARTIER, T., SMEKTALA, F., MESSAAD, K., KIBLER, B., PITOIS, S., GADRET, G., FINOT, C., TROLES, J., DESEVEDAVY, F., HOUIZOT, P., RENVERSEZ, G., BRILLAND, L., AND TRAYNOR, N. **Linear and nonlinear characterizations of chalcogenide photonic crystal fibers**. *J. Lightwave Technol. 27*, 11 (2009), 1707–1715.

[157] GOTZINGER, E., BAUMANN, B., PIRCHER, M., AND HITZENBERGER, C. K. **Polarization maintaining fiber based ultra-high resolution spectral domain polarization sensitive optical coherence tomography**. *Opt. Express 17*, 25 (2009), 22704–22717.

[158] MOSTAÇO-GUIDOLIN, L. B., MURAKAMI, L. S., NOMIZO, A., AND BACHMANN, L. **Fourier transform infrared spectroscopy of skin cancer cells and tissue**. *Appl. Spectrosc. Rev 44*, 5 (2009), 438–455.

[159] PUREUR, V., BÉTOURNÉ, A., BOUWMANS, G., BIGOT, L., KUDLINSKI, A., DELPLACE, K., ROUGE, A. L., QUIQUEMPOIS, Y., AND DOUAY, M. **Overview on solid core photonic bandgap fibers**. *Fiber Integr. Opt. 28* (2009), 27–50.

[160] SNOPATIN, G., SHIRYAEV, V., PLOTNICHENKO, V., DIANOV, E., AND CHURBANOV, M. **High purity chalcogenide glasses for fiber optics**. *Inorg. Mater. 45*, 13 (2009), 1439–1460.

[161] VODOPYANOV, K. L. **Sensing with mid-infrared frequency combs: a novel modality for ultrasensitive detection of hazardous materials**. *Proc. SPIE 7304* (2009), 73040T.

[162] AGRAWAL, G. P. **Fiber-Optic Communication Systems**, 4th ed. Wiley, 2010.

[163] AMRAOUI, M. E., FATOME, J., JULES, J.-C., KIBLER, B., GADRET, G., FORTIER, C., SMEKTALA, F., SKRIPATCHEV, I., POLACCHINI, C. F., MESSADDEQ, Y., TROLES, J., BRILLAND, L., SZPULAK, M., AND RENVERSEZ, G. **Strong infrared spectral broadening in low-loss As-S chalcogenide suspended core microstructured optical fibers**. *Opt. Express 18*, 5 (2010), 4547–4556.

[164] CARBONARO, M., AND NUCARA, A. **Secondary structure of food proteins by Fourier transform spectroscopy in the mid-infrared region**. *Amino Acids 38* (2010), 679–690.

[165] COULOMBIER, Q., BRILLAND, L., HOUIZOT, P., CHARTIER, T., N'GUYEN, T. N., SMEKTALA, F., RENVERSEZ, G., MONTEVILLE, A., MÉCHIN, D., PAIN, T., ORAIN, H., SANGLEBOEUF, J.-C., AND TROLÈS, J. **Casting method for producing low-loss chalcogenide microstructured optical fibers**. *Opt. Express 18*, 9 (2010), 9107–9112.

[166] DUDLEY, J., AND TAYLOR, J. **Supercontinuum Generation in Optical Fibers**, 1st ed. Cambridge University, 2010.

[167] FEVRIER, S., BEAUDOU, B., AND VIALE, P. **Understanding origin of loss in large pitch hollow-core photonic crystal fibers and their design simplification**. *Opt. Express 18*, 5 (2010), 5142–5150.

[168] HU, J., MENYUK, C. R., SHAW, L. B., SANGHERA, J. S., AND AGGARWAL, I. D. **Maximizing the bandwidth of supercontinuum generation in As_2Se_3 chalcogenide fibers**. *Opt. Express 18*, 7 (2010), 6722–6739.

[169] SYCH, Y., ENGELBRECHT, R., SCHMAUSS, B., KOZLOV, D., SEEGER, T., AND LEIPERTZ, A. **Broadband time-domain absorption spectroscopy with a ns-pulse supercontinuum source**. *Opt. Express 18*, 22 (2010), 22762–22771.

[170] TROLES, J., COULOMBIER, Q., CANAT, G., DUHANT, M., RENARD, W., TOUPIN, P., CALVEZ, L., RENVERSEZ, G., SMEKTALA, F., AMRAOUI, M. E., ADAM, J. L., CHARTIER, T., MECHIN, D., AND BRILLAND, L. **Low loss microstructured chalcogenide fibers for large non linear effects at 1995 nm**. *Opt. Express 18*, 25 (2010), 26647–26654.

[171] WANG, H., AL-QAISI, M. K., AND AKKIN, T. **Polarization-maintaining fiber based polarization-sensitive optical coherence tomography in spectral domain**. *Opt. Lett. 35*, 2 (2010), 154–156.

[172] ZENDEHNAM, A., MIRZAEI, M., FARASHIANI, A., AND FARAHANI, L. H. **Investigation of bending loss in a single-mode optical fibre**. *Pramana J. Phys. 74* (2010), 591–603.

[173] CAFFEY, D., RADUNSKY, M. B., COOK, V., WEIDA, M., BUERKI, P. R., CRIVELLO, S., AND DAY, T. **Recent results from broadly tunable external cavity quantum cascade lasers**. *Proc. SPIE 7953* (2011), 79531K.

[174] CEZARD, N., DOBROC, A., CANAT, G., DUHANT, M., RENARD, W., ALHENC-GELAS, C., LEFEBVRE, S., AND FADE, J. **Supercontinuum laser absorption spectroscopy in the mid-infrared range for identification and concentration estimation of a multi- component atmospheric gas mixture**. *Proc. SPIE 8182* (2011), 81820V.

[175] CIMALLA, P., WALTHER, J., MITTASCH, M., AND KOCH, E. **Shear flow-induced optical inhomogeneity of blood assessed in vivo and in vitro by spectral domain optical coherence tomography in the 1.3 µm wavelength range**. *J. Biomed. Opt. 16*, 11 (2011), 116020.

[176] GEISLER, T., AND HERSTRØM, S. **Measured phase and group birefringence in elliptical core fibers with systematically varied ellipticities**. *Opt. Express 19*, 26 (2011), B283–B288.

[177] HUDSON, D. D., DEKKER, S. A., MAGI, E. C., JUDGE, A. C., JACKSON, S. D., LI, E., SANGHERA, J. S., SHAW, L. B., AGGARWAL, I. D., AND EGGLETON, B. J. **Octave spanning supercontinuum in an As_2S_3 taper using ultralow pump pulse energy**. *Opt. Lett. 36*, 7 (2011), 1122–1124.

[178] LIAO, M., YAN, X., GAO, W., DUAN, Z., QIN, G., SUZUKI, T., AND OHISHI, Y. **Five-order SRSs and supercontinuum generation from a tapered tellurite microstructured fiber with longitudinally varying dispersion**. *Opt. Express 19*, 16 (2011), 15389–15396.

[179] LORENTZ, H. A. **The Theory of Electrons and Its Applications to the Phenomena of Light and Radiant Heat**, 2nd ed. New York:Dover Books, 2011.

[180] PRYAMIKOV, A. D., BIRIUKOV, A. S., KOSOLAPOV, A. F., PLOTNICHENKO, V. G., SEMJONOV, S. L., AND DIANOV, E. M. **Demonstration of a waveguide regime for a silica hollow-core microstructured optical fiber with a negative curvature of the core boundary in the spectral region $>$ 3.5 µm**. *Opt. Express 19*, 2 (2011), 1441–1448.

[181] AGGER, C., PETERSEN, C., DUPONT, S., STEFFENSEN, H., LYNGSØ, J. K., THOMSEN, C. L., THØGERSEN, J., KEIDING, S. R., AND BANG, O. **Supercontinuum generation in ZBLAN fibers–detailed comparison between measurement and simulation**. *J. Opt. Soc. Am. B 29*, 4 (2012), 635–645.

[182] CHIU, L.-D., SU, L., REICHELT, S., AND AMOS, W. B. **Use of a white light supercontinuum laser for confocal interference-reflection microscopy**. *J. Microsc. 246*, 2 (2012), 153–159.

[183] GATTASS, R. R., SHAW, L. B., NGUYEN, V. Q., PUREZA, P. C., AGGARWAL, I. D., AND SANGHERA, J. S. **All fiber chalcogenide-based mid-infrared supercontinuum source**. *Opt. Fiber Technol. 18* (2012), 345–348.

[184] HARTUNG, A., HEIDT, A. M., AND BARTELT, H. **Nanoscale all-normal dispersion optical fibers for coherent supercontinuum generation at ultraviolet wavelengths**. *Opt. Express 20*, 13 (2012), 13777–13788.

[185] HULT, J., WATT, R. S., AND KAMINSKI, C. F. **High bandwidth absorption spectroscopy with a dispersed supercontinuum source**. *Opt. Express 15*, 23 (2012), 11385–11395.

[186] LE, S. D., GAY, M., BRAMERIE, L., E. SILVA, M. C., LENGLE, K., CHARTIER, T., THUAL, M., SIMON, J.-C., BRILLAND, L., MECHIN, D., TOUPIN, P., AND TROLES, J. **Wavelength conversion in a highly nonlinear chalcogenide microstructured fiber**. *Opt. Lett. 37*, 22 (2012), 4576–4578.

[187] LUZI, G., EPPLE, P., SCHARRER, M., FUJIMOTO, K., RAUH, C., AND DELGADO, A. **Numerical solution and experimental validation of the drawing process of six-hole optical fibers including the effects of inner pressure and surface tension**. *J. Lightw. Technol. 30*, 9 (2012), 1306–1311.

[188] MESSADDEQ, S. H., VALLÉE, R., SOUCY, P., BERNIER, M., EL-AMRAOUI, M., AND MESSADDEQ, Y. **Self-organized periodic structures on Ge-S based chalcogenide glass induced by femtosecond laser irradiation**. *Opt. Express 20*, 28 (2012), 29882–29889.

[189] TOUPIN, P., BRILLAND, L., TROLES, J., AND ADAM, J.-L. **Small core Ge-As-Se microstructured optical fiber with single-mode propagation and low optical losses**. *Opt. Mater. Express 2*, 10 (2012), 1359–1366.

[190] WHITE, J. R. **Herschel and the puzzle of infrared**. *Am. Sci. 100*, 3 (2012), 128.

[191] BARH, A., GHOSH, S., AGRAWAL, G. P., VARSHNEY, R. K., AGGARWAL, I. D., AND PAL, B. P. **Design of an efficient mid-IR light source using chalcogenide holey fibers: a numerical study**. *J. Opt. 15* (2013), 035205.

[192] GAO, W., AMRAOUI, M. E., LIAO, M., KAWASHIMA, H., DUAN, Z., DENG, D., CHENG, T., SUZUKI, T., MESSADDEQ, Y., AND OHISHI, Y. **Mid-infrared supercontinuum generation in a suspended-core As_2S_3 chalcogenide microstructured optical fiber**. *Opt. Express 21*, 8 (2013), 9573–9583.

[193] KLIMCZAK, M., STEPNIEWSKI, G., BOOKEY, H., SZOLNO, A., STEPIEN, R., PYSZ, D., KAR, A., WADDIE, A., TAGHIZADEH, M. R., AND BUCZYNSKI, R. **Broadband infrared supercontinuum generation in hexagonal-lattice tellurite pho-**

tonic crystal fiber with dispersion optimized for pumping near 1560 nm. *Opt. Lett. 38*, 22 (2013), 4679–4682.

[194] KOLYADIN, A. N., KOSOLAPOV, A. F., PRYAMIKOV, A. D., BIRIUKOV, A. S., PLOTNICHENKO, V. G., , AND DIANOV, E. M. **Light transmission in negative curvature hollow core fiber in extremely high material loss region**. *Opt. Express 21*, 8 (2013), 9514–9519.

[195] LUCAS, P., YANG, Z., FAH, M. K., LUO, T., JIANG, S., BOUSSARD-PLEDEL, C., ANNE, M.-L., AND BUREAU, B. **Telluride glasses for far infrared photonic applications**. *Opt. Mater. Express 3*, 8 (2013), 1049–1058.

[196] RUDY, C. W., MARANDI, A., VODOPYANOV, K. L., AND BYER, R. L. **Octave-spanning supercontinuum generation in *in situ* tapered As_2S_3 fiber pumped by a thulium-doped fiber laser**. *Opt. Lett. 38*, 15 (2013), 2865–2868.

[197] YU, F., AND KNIGHT, J. C. **Spectral attenuation limits of silica hollow core negative curvature fiber**. *Opt. Express 21*, 18 (2013), 21466–21471.

[198] YU, Y., GAI, X., WANG, T., MA, P., WANG, R., YANG, Z., CHOI, D.-Y., MADDEN, S., AND DAVIES, B. L. **Mid-infrared supercontinuum generation in chalcogenides**. *Opt. Mater. Express 3*, 8 (2013), 1075–1086.

[199] ADAM, J.-L., AND ZHANG, X. **Chalcogenide Glasses: Preparation, Properties and Applications**. Oxford: Woodhead Publishing, 2014.

[200] AL-KADRY, A., EL-AMRAOUI, M., MESSADDEQ, Y., AND ROCHETTE, M. **Two octaves mid-infrared supercontinuum generation in As_2Se_3 microwires**. *Opt. Express 22*, 25 (2014), 31131–31137.

[201] GHOSH, D., ROY, S., AND BHADRA, S. K. **Efficient supercontinuum sources based on suspended core microstructured fibers**. *IEEE J. Sel. Top. Quantum Electron. 20*, 5 (2014), 597–604.

[202] KLIMCZAK, M., SIWICKI, B., SKIBINSKI, P., PYSZ, D., STEPIEN, R., SZOLNO, A., PNIEWSKI, J., RADZEWICZ, C., AND BUCZYNSKI, R. **Mid-infrared supercontinuum generation in soft-glass suspended core photonic crystal fiber**. *Opt. Quantum Electron. 46*, 4 (2014), 563–571.

[203] KUBAT, I., PETERSEN, C. R., MØLLER, U. V., SEDDON, A., BENSON, T., BRILLAND, L., MÉCHIN, D., MOSELUND, P. M., AND BANG, O. **Thulium pumped mid-infrared 0.9-9 µm supercontinuum generation in concatenated fluoride and chalcogenide glass fibers**. *Opt. Express 22*, 4 (2014), 3959–3967.

[204] LEO, F., SAFIOUI, J., KUYKEN, B., ROELKENS, G., AND GORZA, S.-P. **Generation of coherent supercontinuum in a-Si:H waveguides: experiment and modeling based on measured dispersion profile**. *Opt. Express 22*, 23 (2014), 28997–29007.

[205] MANNINEN, A., KÄÄRIÄINEN, T., PARVIAINEN, T., BUCHTER, S., HEILIÖ, M., AND LAURILA, T. **Long distance active hyperspectral sensing using high-power near-infrared supercontinuum light source**. *Opt. Express 100*, 6 (2014), 7172–7177.

[206] MOUAWAD, O., AMRANI, F., KIBLER, B., PICOT-CLÉMENTE, J., STRUTYNSKI, C., FATOME, J., DÉSÉVÉDAVY, F., GADRET, G., JULES, J.-C., HEINTZ, O.,

LESNIEWSKA, E., AND SMEKTALA, F. **Impact of optical and structural aging in As_2S_3 microstructured optical fibers on mid-infrared supercontinuum generation**. *Opt. Express 22*, 20 (2014), 23912–23919.

[207] PETERSEN, C. R., MØLLER, U., KUBAT, I., ZHOU, B., DUPONT, S., RAMSAY, J., BENSON, T., SUJECKI, S., MONEIM, N. A., TANG, Z., FURNISS, D., SEDDON, A., AND BANG, O. **Mid-infrared supercontinuum covering the 1.4–13.3 µm molecular fingerprint region using ultra-high NA chalcogenide step-index fibre**. *Nat. Photonics 8* (2014), 830–834.

[208] RUSSELL, P. S. J., HOLZER, P., CHANG, W., ABDOLVAND, A., AND TRAVERS, J. C. **Hollow-core photonic crystal fibers for gas-based nonlinear optics**. *Nat. Photonics 8* (2014), 278–286.

[209] SOBON, G., KLIMCZAK, M., SOTOR, J., KRZEMPEK, K., PYSZ, D., STEPIEN, R., MARTYNKIEN, T., ABRAMSKI, K. M., AND BUCZYNSKI, R. **Infrared supercontinuum generation in soft-glass photonic crystal fibers pumped at 1560 nm**. *Opt. Mater. Express 4*, 1 (2014), 7–15.

[210] TOUPIN, P., BRILLAND, L., MÉCHIN, D., ADAM, J.-L., AND TROLES, J. **Optical aging of chalcogenide microstructured optical fibers**. *J. Light. Technol. 32*, 13 (2014), 2428–2432.

[211] BELARDI, W. **Design and properties of hollow antiresonant fibers for the visible and near infrared spectral range**. *J. Light. Technol. 33*, 21 (2015), 4497–4503.

[212] BELLI, F., ABDOLVAND, A., CHANG, W., TRAVERS, J. C., AND RUSSELL, P. S. J. **Vacuum-ultraviolet to infrared supercontinuum in hydrogen-filled photonic crystal fiber**. *Optica 2*, 4 (2015), 292–300.

[213] MØLLER, U., YU, Y., KUBAT, I., PETERSEN, C. R., GAI, X., BRILLAND, L., MECHIN, D., CAILLAUD, C., TROLES, J., LUTHER-DAVIES, B., AND BANG, O. **Multi-milliwatt mid-infrared supercontinuum generation in a suspended core chalcogenide fiber**. *Opt. Express 23*, 3 (2015), 3282–3291.

[214] SHIRYAEV, V., CHURBANOV, M., SNOPATIN, G., AND CHENARD, F. **Preparation of low-loss core–clad As–Se glass fibers**. *Opt. Mater. 48* (2015), 222–225.

[215] YU, Y., ZHANG, B., GAI, X., ZHAI, C., QI, S., GUO, W., YANG, Z., WANG, R., CHOI, D., MADDEN, S. J., AND LUTHER-DAVIES, B. **1.8-10 µm mid-infrared supercontinuum generated in a step-index chalcogenide fiber using low peak pump power**. *Opt. Lett. 40*, 6 (2015), 1081–1084.

[216] CAILLAUD, C., GILLES, C., PROVINO, L., BRILLAND, L., JOUAN, T., FERRE, S., CARRAS, M., BRUN, M., MECHIN, D., ADAM, J.-L., AND TROLES, J. **Highly birefringent chalcogenide optical fiber for polarization-maintaining in the 3-8.5 µm mid-IR window**. *Opt. Express 24*, 8 (2016), 7377–7986.

[217] CHENG, T., NAGASAKA, K., TUAN, T. H., XUE, X., MATSUMOTO, M., TEZUKA, H., SUZUKI, T., AND OHISHI, Y. **Mid-infrared supercontinuum generation spanning 2.0 to 15.1 µm in a chalcogenide step-index fiber**. *Opt. Lett. 41*, 9 (2016), 2117–2120.

[218] CHU, K. K., UNGLERT, C., FORD, T. N., CUI, D., CARRUTH, R. W., SINGH, K., LIU, L., BIRKET, S. E., SOLOMON, G. M., ROWE, S. M., AND TEARNEY, G. J. **In vivo**

imaging of airway cilia and mucus clearance with micro-optical coherence tomography. *Biomed. Opt. Express 7*, 7 (2016), 2494–2505.

[219] HASAN, M. I., AKHMEDIEV, N., AND CHANG, W. **Mid-infrared supercontinuum generation in supercritical xenon-filled hollow-core negative curvature fibers**. *Opt. Lett. 41*, 21 (2016), 5122–5125.

[220] HUGHES, C., AND BAKER, M. J. **Can mid-infrared biomedical spectroscopy of cells, fluids and tissue aid improvements in cancer survival? A patient paradigm**. *Analyst 141*, 2 (2016), 467–475.

[221] JAIN, D., SIDHARTHAN, R., MOSELUND, P. M., YOO, S., HO, D., AND BANG, O. **Record power, ultra-broadband supercontinuum source based on highly GeO_2 doped silica fiber**. *Opt. Express 24*, 23 (2016), 26667–26677.

[222] KUBAT, I., AND BANG, O. **Multimode supercontinuum generation in chalcogenide glass fibres**. *Opt. Express 24*, 3 (2016), 2513–2526.

[223] OU, H., DAI, S., ZHANG, P., LIU, Z., WANG, X., CHEN, F., XU, H., LUO, B., HUANG, Y., AND WANG, R. **Ultrabroad supercontinuum generated from a highly nonlinear Ge–Sb–Se fiber**. *Opt. Lett. 41*, 14 (2016), 3201–3204.

[224] PETERSEN, C. R., MOSELUND, P. M., PETERSEN, C., MØLLER, U., AND BANG, O. **Mid-IR supercontinuum generation beyond 7 µm using a silica-fluoride-chalcogenide fiber cascade**. *Proc. SPIE 9703* (2016), 97030A.

[225] TU, H., LIU, Y., TURCHINOVICH, D., MARJANOVIC, M., LYNGSØ, J. K., LÆGSGAARD, J., CHANEY, E. J., ZHAO, Y., YOU, S., WILSON, W. L., XU, B., DANTUS, M., AND BOPPART, S. A. **Stain-free histopathology by programmable supercontinuum pulses**. *Nat. Photon. 10* (2016), 534–540.

[226] ZHAO, P., REICHERT, M., ENSLEY, T. R., SHENSKY, W. M., MOTT, A. G., HAGAN, D. J., AND STRYLAND, E. W. V. **Nonlinear refraction dynamics of solvents and gases**. *Proc. SPIE 9731*, 97310F (2016).

[227] AMIOT, C., AALTO, A., RYCZKOWSKI, P., TOIVONEN, J., AND GENTY, G. **Cavity enhanced absorption spectroscopy in the mid-infrared using a supercontinuum source**. *Appl. Phys. Lett. 111* (2017), 061103.

[228] CALVEZ, L. **Chalcogenide glasses and glass-ceramics: Transparent materials in the infrared for dual applications**. *C. R. Phys. 18*, 5-6 (2017), 314–322.

[229] CIMEK, J., LIAROS, N., COURIS, S., STEPIE, R., KLIMCZAK, M., , AND BUCZYNSKI, R. **Experimental investigation of the nonlinear refractive index of various soft glasses dedicated for development of nonlinear photonic crystal fibers**. *Opt. Mater. Express 7*, 10 (2017), 3471–3483.

[230] DÉSÉVÉDAVY, F., GADRET, G., JULES, J. C., KIBLER, B., AND SMEKTALA, F. **Supercontinuum generation in tellurite optical fibers**, vol. 254. Technological Advances in Tellurite Glasses, Springer Ser. Mater. Sci., Berlin, 2017.

[231] HEIDT, A. M., FEEHAN, J. S., PRICE, J. H. V., AND FEURER, T. **Limits of coherent supercontinuum generation in normal dispersion fibers**. *J. Opt. Soc. Am. B 34*, 4 (2017), 764–775.

[232] HUDSON, D. D., ANTIPOV, S., LI, L., ALAMGIR, I., HU, T., AMRAOUI, M. E., MESSADDEQ, Y., ROCHETTE, M., JACKSON, S. D., AND FUERBACH, A. **Toward all-fiber supercontinuum spanning the mid-infrared**. *Optica 4*, 10 (2017), 1163–1166.

[233] JIANG, L., WANG, X., GUO, F., WU, B., ZHAO, Z., MI, N., LI, X., DAI, S., LIU, Z., NIE, Q., AND WANG, R. **Fabrication and characterization of chalcogenide polarization-maintaining fibers based on extrusion**. *Opt. Fiber Technol. 39* (2017), 26–31.

[234] KUDINOVA, M., HUMBERT, G., AUGUSTE, J. L., AND DELAIZIR, G. **Multimaterial polarization maintaining optical fibers fabricated with the powder-in-tube technology**. *Opt. Mater. Express 7*, 10 (2017), 3780–3790.

[235] MICHALSKA, M., HLUBINA, P., AND SWIDERSKI, J. **Mid-infrared supercontinuum generation to ~4.7 µm in a ZBLAN fiber pumped by an optical parametric generator**. *IEEE Photon. J. 9*, 2 (2017), 3200207.

[236] PETERSEN, C. R., ENGELSHOLM, R. D., MARKOS, C., BRILLAND, L., CAILLAUD, C., TROLES, J., AND BANG, O. **Increased mid-infrared supercontinuum bandwidth and average power by tapering large-mode-area chalcogenide photonic crystal fibers**. *Opt. Express 25*, 13 (2017), 15336–15347.

[237] YOU, C., DAI, S., ZHANG, P., XU, Y., WANG, Y., XU, D., AND WANG, R. **Mid-infrared femtosecond laser-induced damages in As_2S_3 and As_2Se_3 chalcogenide glasses**. *Sci. Rep. 7*, 1 (2017), 6497.

[238] ZHAO, Z., WU, B., WANG, X., PAN, Z., LIU, Z., ZHANG, P., SHEN, X., NIE, Q., DAI, S., AND WANG, R. **Mid-infrared supercontinuum covering 2.0–16 µm in a low-loss telluride single-mode fiber**. *Laser Photonics Rev. 11*, 2 (2017), 1700005.

[239] DAI, S., WANG, Y., PENG, X., ZHANG, P., WANG, X., AND XU, Y. **A review of mid-infrared supercontinuum generation in chalcogenide glass fibers**. *Appl. Sci. 8*, 707 (2018), 1–28.

[240] GONZALO, I. B., ENGELSHOLM, R. D., SØRENSEN, M. P., AND BANG, O. **Polarization noise places severe constraints on coherence of all-normal dispersion femtosecond supercontinuum generation**. *Sci. Rep. 8*, 6579 (2018).

[241] MARTINEZ, R. A., PLANT, G., GUO, K., JANISZEWSKI, B., FREEMAN, M. J., MAYNARD, R. L., ISLAM, M. N., TERRY, F. L., ALVAREZ, O., CHENARD, F., BEDFORD, R., GIBSON, R., AND IFARRAGUERRI, A. I. **Mid-infrared supercontinuum generation from 1.6 to >11 µm using concatenated step-index fluoride and chalcogenide fibers**. *Opt. Lett. 43*, 2 (2018), 296–299.

[242] PETERSEN, C. R., MOSELUND, P. M., HUOT, L., HOOPER, L., AND BANG, O. **Towards a table-top synchrotron based on supercontinuum generation**. *Infrared Phys. Techn. 91* (2018), 182–186.

[243] PETERSEN, C. R., PRTLJAGA, N., FARRIES, M., WARD, J., NAPIER, B., LLOYD, G. R., NALLALA, J., STONE, N., AND BANG, O. **Mid-infrared multispectral tissue imaging using a chalcogenide fiber supercontinuum source**. *Opt. Lett. 43*, 5 (2018), 999–1002.

[244] STEPNIEWSKI, G., PNIEWSKI, J., PYSZ, D., CIMEK, J., STEPIEN, R., KLIMCZAK, M., AND BUCZYNSKI, R. **Development of dispersion-optimized photonic crystal fibers based on heavy metal oxide glasses for broadband infrared supercontinuum generation with fiber lasers**. *Sensors 18* (2018), 4127.

[245] THEBERGE, F., BERUBE, N., POULAIN, S., COZIC, S., CHATIGNY, S., ROBICHAUD, L.-R., PLEAU, L.-P., BERNIER, M., AND VALLEE, R. **Infrared supercontinuum generated in concatenated InF_3 and As_2Se_3 fibers**. *Opt. Express 26*, 11 (2018), 13952–13960.

[246] ZORIN, I., SU, R., PRYLEPA, A., KILGUS, J., BRANDSTETTER, M., AND HEISE, B. **Mid-infrared Fourier-domain optical coherence tomography with a pyroelectric linear array**. *Opt. Express 26*, 25 (2018), 33428–33439.

[247] BLINDER, S. M. **Lorentz oscillator model for refractive index**. https://demonstrations.wolfram.com/LorentzOscillatorModelForRefractiveIndex/, 2019. [valid; 3 August-2020].

[248] ISRAELSEN, N. M., PETERSEN, C. R., BARH, A., JAIN, D., JENSEN, M., HANNESSCHLÄGER, G., TIDEMAND-LICHTENBERG, P., PEDERSEN, C., PODOLEANU, A., AND BANG, O. **Real-time high-resolution mid-infrared optical coherence tomography**. *Light Sci. Appl. 8*, 11 (2019).

[249] JAIN, D., SIDHARTHAN, R., WOYESSA, G., MOSELUND, P. M., BOWEN, P., YOO, S., AND BANG, O. **Scaling power, bandwidth, and efficiency of mid-infrared supercontinuum source based on a GeO_2-doped silica fiber**. *J. Opt. Soc. Am. B 36*, 2 (2019), A86–A92.

[250] KLIMCZAK, M., DOBRAKOWSKI, D., GHOSH, A. N., STEPNIEWSKI, G., PYSZ, D., HUSS, G., SYLVESTRE, T., AND BUCZYNSKI, R. **Nested capillary anti-resonant silica fiber with mid-infrared transmission and low bending sensitivity at 4000 nm**. *Opt. Lett. 44*, 17 (2019), 4395–4398.

[251] LEMIÈRE, A., DÉSÉVÉDAVY, F., MATHEY, P., FROIDEVAUX, P., GADRET, G., JULES, J.-C., AQUILINA, C., KIBLER, B., BÉJOT, P., BILLARD, F., FAUCHER, O., AND SMEKTALA, F. **Mid-infrared supercontinuum generation from 2 to 14 µm in arsenic- and antimony-free chalcogenide glass fibers**. *J. Opt. Soc. Am. B 36*, 2 (2019), A183–A192.

[252] LI, J., ZHAO, F., AND HU, Z. **Mid-infrared supercontinuum generation in dispersion-engineered highly nonlinear chalcogenide photonic crystal fiber**. *MOD PHYS LETT B 33*, 19 (2019), 1950211–1–14.

[253] MENEGHETTI, M., CAILLAUD, C., CHAHAL, R., GALDO, E., BRILLAND, L., ADAM, J.-L., AND TROLES, J. **Purification of Ge-As-Se ternary glasses for the development of high quality microstructured optical fibers**. *J. Non-Cryst. Solids 503-504* (2019), 84–88.

[254] PETERSEN, C. R., LOTZ, M. B., WOYESSA, G., GHOSH, A. N., SYLVESTRE, T., BRILLAND, L., TROLES, J., JAKOBSEN, M. H., TABORYSKI, R., AND BANG, O. **Nanoimprinting and tapering of chalcogenide photonic crystal fibers for cascaded supercontinuum generation**. *Opt. Lett. 44*, 22 (2019), 5505–5508.

[255] ZHANG, M., LI, L., LI, T., WANG, F., TIAN, K., TAO, H., FENG, X., YANG, A., AND YANG, Z. **Mid-infrared supercontinuum generation in chalcogenide fibers with high laser damage threshold**. *Opt. Express 27*, 20 (2019), 29287–29296.

[256] DASA, M. K., NTEROLI, G., BOWEN, P., MESSA, G., FENG, Y., PETERSEN, C. R., KOUTSIKOU, S., BONDU, M., MOSELUND, P. M., PODOLEANU, A., BRADU, A., MARKOS, C., AND BANG, O. **All-fibre supercontinuum laser for in vivo multispectral photoacoustic microscopy of lipids in the extended near-infrared region**. *Photoacoustics 18* (2020), 100163.

[257] LEUKOS. **Scientific supercontinuum lasers**. https://leukos-laser.com/products/supercontinuum-lasers/scientific/#nir-midir, 2020. [valid; 3 August-2020].

[258] NKT PHOTONICS. **Supercontinuum white light lasers**. https://nktphotonics.com/lasers-fibers/product-category/supercontinuum-lasers/, 2020. [valid; 3 August-2020].

[259] NORBLIS. **Mid-IR supercontinuum laser**. https://https://norblis.com/index.php/products/aurora-supercontinuum-laser, 2020. [valid; 3 August-2020].

[260] VENCK, S., ST-HILAIRE, F., BRILLAND, L., GHOSH, A. N., CHAHAL, R., CAILLAUD, C., MENEGHETTI, M., TROLES, J., JOULAIN, F., COZIC, S., POULAIN, S., HUSS, G., ROCHETTE, M., DUDLEY, J. M., AND SYLVESTRE, T. **2-10 µm mid-infrared fiber-based supercontinuum laser source: experiment and simulation**. *Laser Photonics Rev. 14*, 6 (2020), 2000011.

List of Figures

LIST OF TABLES

Document generated with LaTeX and:
the LaTeX style for PhD Thesis created by S. Galland — http://www.multiagent.fr/ThesisStyle
the tex-upmethodology package suite — http://www.arakhne.org/tex-upmethodology/

Optics Letters

Cross-phase modulation instability in PM ANDi fiber-based supercontinuum generation

Etienne Genier,[1,2,*] Amar N. Ghosh,[2] Swetha Bobba,[2] Patrick Bowen,[1] Peter M. Moselund,[1] Ole Bang,[1,3] John M. Dudley,[2] and Thibaut Sylvestre[2]

[1]NKT Photonics A/S, Blokken 84, DK-3460, Birkerød, Denmark
[2]Institut FEMTO-ST, UMR 6174 CNRS-Université Bourgogne Franche-Comté, 25030 Besançon, France
[3]DTU Fotonik, Department of Photonics Engineering, Technical University of Denmark, 2800 Kgs. Lyngby, Denmark
*Corresponding author: etienne.genier@nktphotonics.com

Received 7 May 2020; revised 22 May 2020; accepted 22 May 2020; posted 26 May 2020 (Doc. ID 397106); published 24 June 2020

We demonstrate broadband supercontinuum generation in an all-normal dispersion polarization-maintaining photonic crystal fiber and report the observation of a cross-phase modulation instability sideband generated outside of the supercontinuum bandwidth. We demonstrate that this sideband is polarized on the slow axis and can be suppressed by pumping on the fiber's fast axis. We theoretically confirm and model this nonlinear process using phase-matching conditions and numerical simulations, obtaining good agreement with the measured data. © 2020 Optical Society of America

https://doi.org/10.1364/OL.397106

All-normal dispersion (ANDi) optical fibers have recently emerged as attractive platforms to improve the noise and coherence of supercontinuum generation (SC/SCG) beyond the limits of anomalous SC generation [1–4]. ANDi SCG is based on two fully coherent nonlinear effects: self-phase modulation (SPM) and optical wave breaking (OWB) [2,5] while anomalous SCG is typically susceptible to or even generated by incoherent nonlinear effects [6]. Despite this, ANDi SCG has its own limitations, being both very sensitive to Raman noise [2–4,7] and requiring low and flat fiber dispersion engineering that is technically challenging to achieve [1]. When pumping with femtosecond pulses, it has been shown that other factors should be considered including polarization modulation instability (PMI) or the amplitude noise of the laser, both of which can drastically degrade the relative intensity noise (RIN) and coherence [3,4,8]. These factors limit the available parameter space for coherent SCG; however, fs-pumped ANDi SC generation still has significant potential to generate temporally coherent SC with realistic laser parameters, a feature hard to come by in the anomalous dispersion regime. This gives such systems potential in a range of fields including optical coherence tomography (OCT), optical metrology, photoacoustic imaging, and spectroscopy [9–11].

In this work, we investigate SCG in a polarization-maintaining (PM)-ANDi silica photonic crystal fiber (PCF) with a femtosecond stable optical parametric oscillator (OPO) with intention to suppress PMI. However, in doing this, we discovered the generation of a sideband outside the SC bandwidth that was not observed in previous PM-ANDi SCG [12,13]. We identify this sideband as the result of a cross-phase modulation instability (XPMI) process that builds up from coherent SCG and OWB. As described in [14,15], XPMI is usually observed when a beam is launched at a 45° angle from the principal axis of a highly birefringent fiber. This beam is then split into two linearly polarized modes on each axis that will nonlinearly interact with each other to generate two frequency-detuned and cross-polarized four-wave mixing (FWM) sidebands [14]. However, this XPMI process has never been observed before through the stimulation of fs-SC generation but only via spontaneous generation of the interaction of picosecond or nanosecond pulses.

Our results show that we can generate a stimulated XPMI sideband in a PM-ANDi PCF using femtosecond pulses. As expected, this sideband is most powerful while pumping the fiber at 45° off the axes. We also demonstrate this sideband can be completely suppressed when pumping the fiber on the fast axis.

The experimental setup used to observe and analyze SC and XPMI generation in the PM-ANDi PCF is shown in Fig. 1. As a pump laser, we used a Ti:Sa femtosecond pulsed laser (Coherent Chameleon) tunable from 680–1080 nm, delivering 200 fs pulse duration at an 80 MHz repetition rate with a maximum average power of 450 mW at 1040 nm. The output power is controlled using a variable neutral density filter (ND). A half-wave plate is used to turn the input polarization state , while the polarizer at the fiber's output is used to observe the spectral content on the light of each axis. A 40x microscope objective is used to couple the light into the 40 cm of PM ANDi PCF—the NL-1050-NE-PM from NKT Photonics. This fiber has a relative hole size of $d/L = 0.45$, a small hole-to-hole pitch of 1.44 μm, and a nonlinear coefficient of $\gamma = 26.8\ \mathrm{W^{-1}\ km^{-1}}$ at 1040 nm. A set of two aspheric lenses is used to collimate the output beam and then focus it to the multimode pick-up fiber.

The dispersion was measured using white-light interferometry and calculated for an idealized structure with a uniform hole structure with fixed pitch and hole diameter using COMSOL.

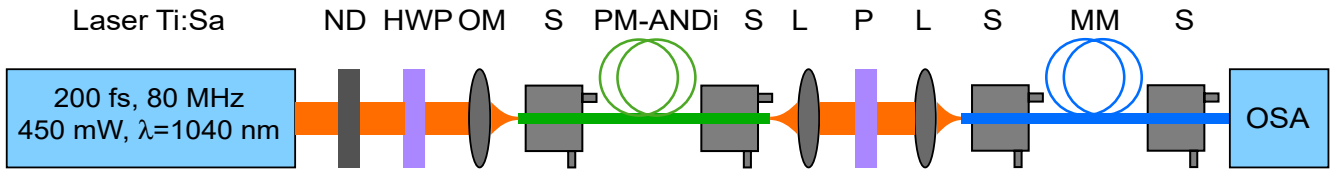

Fig. 1. Schematic of the setup, including a wavelength tunable Ti:Sa femtosecond laser, variable neutral density filter (ND), half-wave plate (HWP), 40x microscope objective (OM), aspheric lenses (L), 3D translation stages (S), 40 cm of all-normal dispersion PCF (PM-ANDi), a polarizer (P), 2 m of multimode pick-up fiber (MM), and an optical spectrum analyzer (OSA).

The calculation fits the measurements well and is shown as the blue curve in Fig. 2. The numerical modeling using the experimental dispersion data did not reproduce the experimental results; this is probably due to the uncertainties on this dispersion curve that increase when the dispersion is close to zero. We therefore considered the dispersion given by the brown curve, which is shifted upwards in the center as the dispersion approaches zero. This is still within the measurement uncertainties and is able to reproduce the experiments as we will demonstrate. As expected, the small holes of the PCF give a confinement loss edge wavelength significantly below the material loss edge wavelength, calculated to be at 1450 nm using COMSOL (see Fig. 2, green curve). The dispersion profile has a minimum of −13 ps/nm/km at 1040 nm and is rather symmetrical within the low-loss window. The PM effect of this fiber is stress-rod induced, with a slight degree of core-ellipticity that causes a linearly increasing birefringence [16], which goes from $2.5 \cdot 10^{-4}$ at 850 nm to $6.8 \cdot 10^{-4}$ at 1300 nm, as shown in Fig. 2 (red circles).

We pumped the fiber at 1040 nm, at the minimum dispersion wavelength (MDW); thus we should expect the broadest SC. Figure 3 shows the spectral evolution while pumping on the slow axis, fast axis, and at 45°. The broadest SC spectrum (bandwidth at −20 dB is 460 nm) is obtained by pumping on the slow axis, while the narrowest is obtained by pumping at 45° because only half the power is available for spectral broadening in each axis and due to the temporal walk-off, which tends to eliminate the influence of cross-phase modulation [17]. Also, the SC spectrum is quite symmetric whatever the input angle

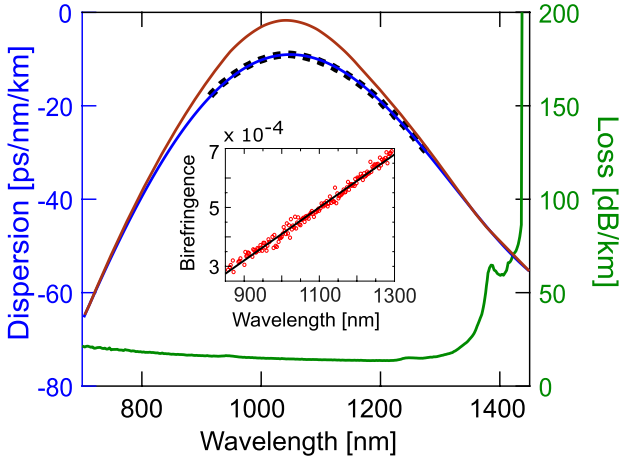

Fig. 2. Numerical (solid blue), experimental (black dots) and modeled (dashed brown) dispersion profiles, and fiber losses (solid green) of the NL-1050-NE-PM ANDi PCF. The inset shows the group birefringence: linear fitting (solid black) and measured data (circles red).

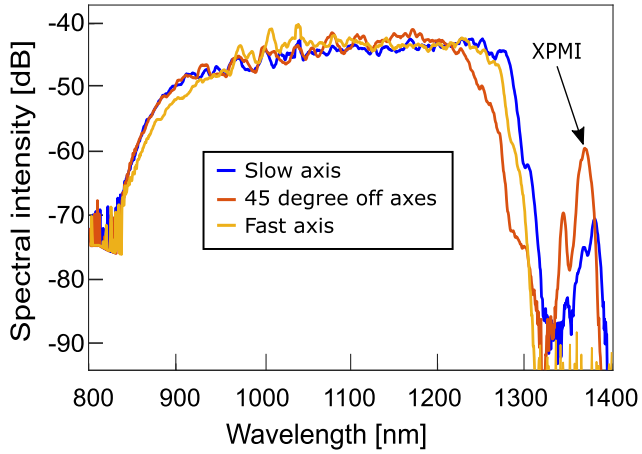

Fig. 3. Experimental SC spectra for different input polarizations with 220 mW output power.

due to the parabolic shape of the fiber dispersion. Interestingly a sideband appears at 1360 nm, which is strongest when pumping at 45° and which we identify as XPMI. When pumping on the slow axis, the sideband intensity is reduced by 12 dB but is still clearly observable. Finally, when pumping on the fast axis, the sideband appears to be completely suppressed with an extinction of at least 25 dB. To understand the appearance of this sideband and the efficiencies regarding the input polarization angle, let us recall that the phase-matching condition for XPMI should give rise to a Stokes sideband on the slow axis and an anti-Stokes sideband on the fast axis because of positive (normal) group-velocity dispersion (GVD) [6,18]. This means to stimulate the generation of an idler-pumped sideband in the Stokes side of the spectrum, we need energy in the pump (on both axes) and energy in the anti-Stokes sideband (aligned to the fast axis). Experimentally, we use a pump laser with a polarization extinction ratio (PER) of 40 dB and inject the light into the PM-ANDi fiber, whose input face was end-collapsed to remove back reflections into the Ti:Sa laser. At the output, we measure a maximum achievable PER of 17 dB, which has a relatively even distribution over the whole SC bandwidth. This shows that at some point in the propagation, light has deviated from the input axis to become distributed more over both axes, probably due to the collapse of the fiber holes. This can explain why it is possible to observe a Stokes sideband at 1360 nm even when the input beam is almost aligned on the slow axis, as shown in Fig. 3.

Figure 4 shows the evolution of the SC spectrum as a function of the pump power for an input polarization at 45° off axes. The SC bandwidth is 430 nm at −20 dB (845–1275 nm) for an average output power of 220 mW. The XPMI sideband grows

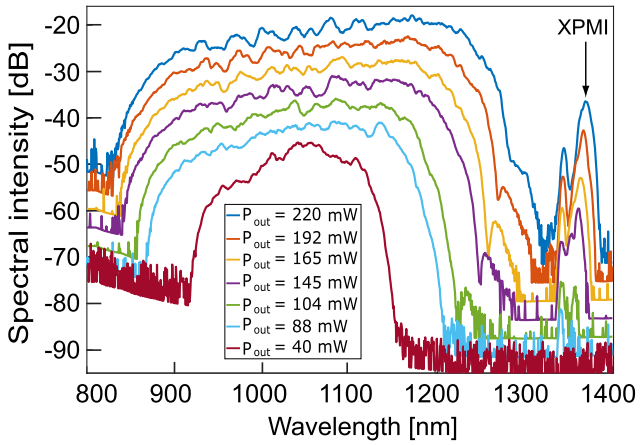

Fig. 4. SC evolution for different pump powers while pumping at 45° from the two axes (power offset for clarity).

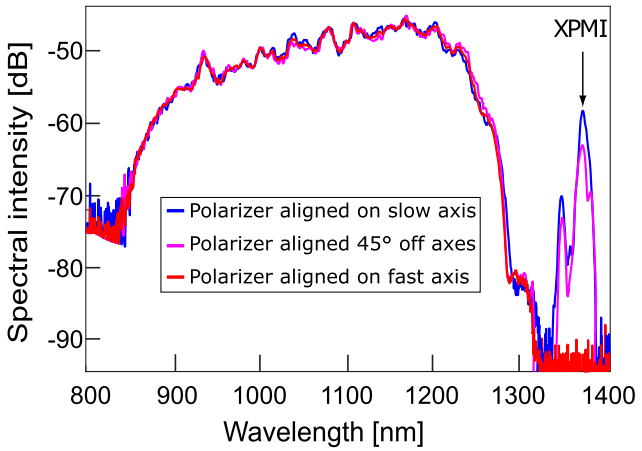

Fig. 5. SC evolution for different polarizer orientations while pumping at 45° from the two axes.

and slightly broadens to longer wavelengths when increasing the coupled power. It starts to appear only when SC extends past 1200 nm and when the OWB also starts to appear (see the green spectrum in Fig. 4). In addition, there is no observable anti-Stokes sideband outside the SC, even when observing the spectrum over a wide bandwidth (600–2000 nm).

Adding a polarizer at the output of the fiber to analyze the sideband polarization angle, we show in Fig. 5 the SC spectrum measured after the polarizer as a function of the polarizer angle at maximum output power (220 mW average power). We notice that the three spectra obtained by aligning the polarizer on the slow axis (blue curve), fast axis (red curve), and at 45° of the axes (pink curve) have a similar bandwidth and shape. We observe the most powerful sideband when the polarizer is aligned on the slow axis and a 10 dB suppression when aligning the polarizer at 45° of the axes. Finally, aligning the polarizer on the fast axis totally suppresses the sideband, confirming that the sideband is polarized along the slow axis.

To simulate the SCG in the PM-ANDi fiber, we use a MATLAB code solving the two coupled generalized nonlinear Schrodinger equations (CGNLSEs) for highly birefringent fibers as described in [19]. We used as input parameters a pump wavelength of 1040 nm, a sech-shaped pump pulse with duration of 200 fs (full width half maximum intensity), 12 kW peak power, a longer fiber length of 60 cm for better visibility, the loss profile as described in Fig. 2 (green curve), and the birefringence values taken from the inset. One-photon-per-mode noise and intensity noise of 1% was added to our input condition, and the results were sampled average over 20 simulations. Using these parameters, we obtain a quite good agreement between simulation and experimental results. This is shown in Figs. 6(a)–6(d), which depict both the spectral and temporal intensity dynamics on each axis when pumping the PM-ANDi fiber at 45°. First, the numerical SC bandwidth at −20 dB level is estimated to be 450 nm, which is very close to the experimental one (430 nm). Second, we can clearly see the generation of a small signal at 1360 nm polarized on the slow axis, which fits with the experimentally observed XPMI sideband [see Fig. 6(b)]. We also notice that the sideband appears after 20 cm of propagation exactly where the OWB sets in and stops the red-shift of the SPM lobes. Interestingly, the temporal trace plotted in Fig. 6(d) reveals that the signal at 1360 nm behaves as a small dispersive wave (DW) shed by the pump pulse on the slow axis, in a way akin to the DW emission by OWB in the anomalous dispersion region [20,21].

To go further into detail, in Fig. 7, we plot the theoretical XPMI sidebands as a function of pump wavelength using the well-known formula for the XPMI frequency shift [22]

$$\Omega_s(\lambda, z) = \frac{\delta n(\lambda)}{2c\beta_2(\lambda)}\left(1 + \sqrt{1 - 4\beta_2(\lambda)\gamma P_0(z)\left(\frac{c}{\delta n(\lambda)}\right)^2}\right),$$

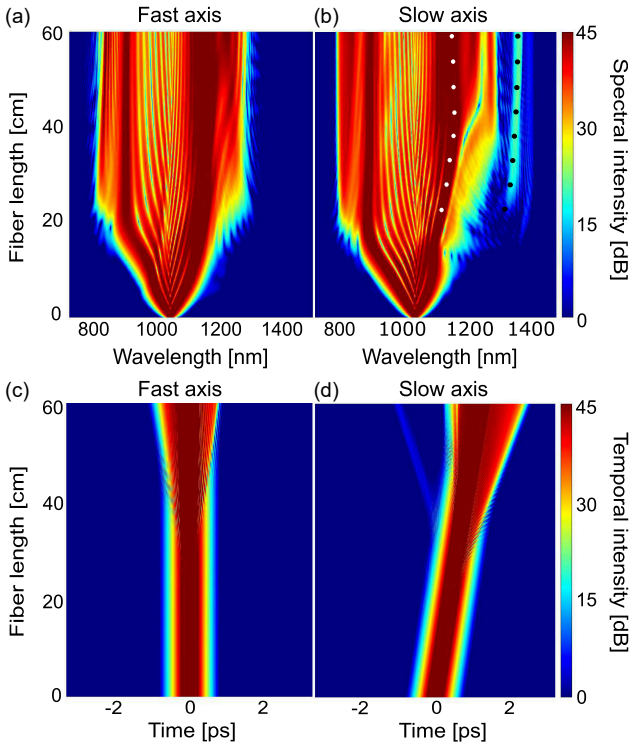

Fig. 6. Simulated spectral (top) and temporal (bottom) SC evolution on each fiber axis as a function of fiber length. The dots represent the theoretical XPMI wavelength (black) using the redder SPM wavelength (white) as a pump.

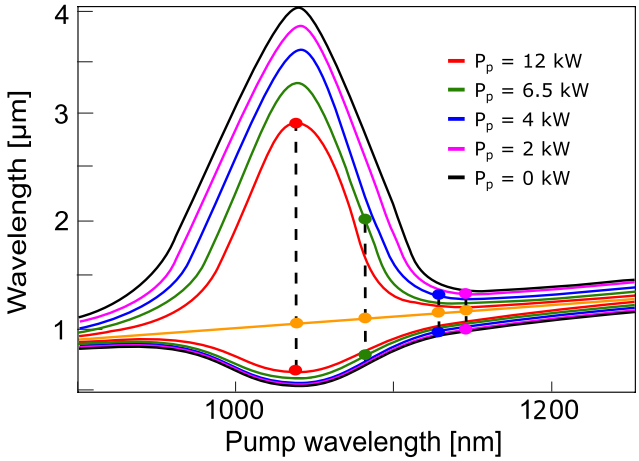

Fig. 7. Phase-matching map as a function of total peak power, 12 kW (red), 6.5 kW (green), 4 kW (blue), 2 kW (pink), and 0 kW (black). The orange dots on the straight line for the pump wavelength show the numerically observed red SPM wavelength [white dots in Fig. 6(b)], and the other colored dots mark the corresponding XPMI wavelength.

where δn is the group birefringence, P_0 the total peak power, and β_2 the wavelength-dependent GVD. The XPMI wavelengths are plotted in Fig. 7 for different peak powers. From the modeling, the slow axis XPMI generation is seen to be closely linked to the long wavelength SPM lobe in the slow axis, marked with white dots. According to this conjecture, the XPMI gain is efficient only when the red shift of the SPM lobe, acting as the pump, slows down, and for lengths not much longer than the walk-off length of 22 cm. This is exactly what is observed: the XPMI peak is first growing after about 20 cm when the red-shift of the SPM lobe is stopped by OWB, and after about 30 cm, the power in the XPMI peak does not grow anymore. Looking into more detail, we find that the peak power decreases from 12 kW at $z = 0$ to 1.5 kW at $z = 60$ cm. From the corresponding phase-matching curves in Fig. 7, we see that the XPMI phase-matches to the center wavelength of the SPM lobe initially at 2787 nm ($P_0 = 12$ kW, $\lambda_{\mathrm{SPM}} = 1040$ nm), then it rapidly decreases because of the red-shift of the SPM lobe. The observed final SPM lobe wavelength of 1152 nm is seen to generate XPMI at 1360 nm in the valley of the linear phase-matching curve, which corresponds nicely to the numerically and experimentally observed XPMI wavelength, for the adjusted dispersion profile. The observed SCG-induced XPMI generation thus requires a delicate balance between strong SPM stopped sufficiently before, say, twice the walk-off length by OWB.

In conclusion, we have reported the observation of XPMI while pumping a PM-ANDi PCF with a femtosecond laser. A sideband was generated through a XPMI process at 1360 nm during coherent SCG from SPM and OWB. We demonstrated this sideband cannot be generated while pumping on the fast axis and is itself polarized along the fiber's slow axis. Further clarifying that we were observing XPMI, theoretical calculation and simulation performed solving the CGNLSE confirmed the degenerate FWM between a pump corresponding to the red edge of the SPM on the fiber's slow axis, an anti-Stokes idler pump in the central SPM area on the fiber fast's axis, and a signal at 1360 nm polarized on the fiber's slow axis. Our study is of substantial value to potential applications, such as OCT and metrology, which require ultra-low-noise SC light sources. To achieve low noise in these future SC sources, a high degree of suppression of XPMI will be required and for this a solid understanding of the underpinning physics. Indeed, this study shows that controlling the input polarization is very important to avoid noise the amplification effect and thus keep the noise-free/stability given by fs PM-ANDi SCG.

Funding. Horizon 2020 Framework Programme (722380); Agence Nationale de la Recherche (ANR-15-IDEX-0003).

Disclosures. The authors declare no conflicts of interest.

REFERENCES

1. A. Hartung, A. M. Heidt, and H. Bartelt, Opt. Express **19**, 7742 (2011).
2. A. M. Heidt, J. S. Feehan, J. H. V. Price, and T. Feurer, J. Opt. Soc. Am. B **34**, 764 (2017).
3. I. B. Gonzalo, R. D. Engelsholm, M. P. Sørensen, and O. Bang, Sci. Rep. **8**, 6579 (2018).
4. E. Genier, P. Bowen, T. Sylvestre, J. M. Dudley, P. Moselund, and O. Bang, J. Opt. Soc. Am. B **36**, A161 (2019).
5. C. Finot, B. Kibler, L. Provost, and S. Wabnitz, J. Opt. Soc. Am. B **25**, 1938 (2008).
6. J. M. Dudley, G. Genty, and S. Coen, Rev. Mod. Phys. **78**, 1135 (2006).
7. U. Møller and O. Bang, Electron. Lett. **49**, 63 (2013).
8. A. Loredo-Trejo, Y. López-Diéguez, L. Velázquez-Ibarra, A. Díez, E. Silvestre, J. M. Estudillo-Ayala, and M. V. Andrés, IEEE Photon. J. **11**, 7104208 (2019).
9. M. K. Dasa, C. Markos, M. Maria, C. R. Petersen, P. M. Moselund, and O. Bang, Biomed. Opt. Express **9**, 1762 (2018).
10. C. R. Petersen, N. Prtljaga, M. Farries, J. Ward, B. Napier, G. R. Lloyd, J. Nallala, N. Stone, and O. Bang, Opt. Lett. **43**, 999 (2018).
11. B. Povazay, K. Bizheva, A. Unterhuber, B. Hermann, H. Sattmann, A. Fercher, W. Drexler, A. Apolonski, W. Wadsworth, J. Knight, P. St.J. Russell, M. Vetterlein, and E. Scherzer, Opt. Lett. **27**, 1800 (2002).
12. K. Tarnowski, T. Martynkien, P. Mergo, K. Poturaj, A. Anuszkiewicz, P. Béjot, F. Billard, O. Faucher, B. Kibler, and W. Urbanczyk, Opt. Express **25**, 27452 (2017).
13. K. Tarnowski, T. Martynkien, P. Mergo, J. Sotor, and G. Soboń, Sci. Rep. **9**, 1 (2019).
14. A. Kudlinski, A. Bendahmane, D. Labat, S. Virally, R. Murray, E. Kelleher, and A. Mussot, Opt. Express **21**, 8437 (2013).
15. P. Drummond, T. Kennedy, J. Dudley, R. Leonhardt, and J. Harvey, Opt. Commun. **78**, 137 (1990).
16. P. Hlubina, D. Ciprian, and M. Kadulová, Meas. Sci. Technol. **20**, 025301 (2008).
17. T. Sylvestre, H. Maillotte, E. Lantz, and D. Gindre, J. Nonlinear Opt. Phys. Mater. **6**, 313 (1997).
18. J. Chen, G. Wong, S. Murdoch, R. Kruhlak, R. Leonhardt, J. Harvey, N. Joly, and J. Knight, Opt. Lett. **31**, 873 (2006).
19. A. N. Ghosh, M. Meneghetti, C. R. Petersen, O. Bang, L. Brilland, S. Venck, J. Troles, J. M. Dudley, and T. Sylvestre, J. Phys. Photon. **1**, 044003 (2019).
20. M. Conforti and S. Trillo, Opt. Lett. **38**, 3815 (2013).
21. K. E. Webb, Y. Q. Xu, M. Erkintalo, and S. G. Murdoch, Opt. Lett. **38**, 151 (2013).
22. G. P. Agrawal, *Nonlinear Fiber Optics* (Springer, 2000), pp. 195–211.

2–10 μm Mid-Infrared Fiber-Based Supercontinuum Laser Source: Experiment and Simulation

*Sébastien Venck, François St-Hilaire, Laurent Brilland, Amar N. Ghosh, Radwan Chahal, Céline Caillaud, Marcello Meneghetti, Johann Troles, Franck Joulain, Solenn Cozic, Samuel Poulain, Guillaume Huss, Martin Rochette, John M. Dudley, and Thibaut Sylvestre**

Mid-infrared supercontinuum (mid-IR SC) sources in the 2–20 μm molecular fingerprint region are in high demand for a wide range of applications including optical coherence tomography, remote sensing, molecular spectroscopy, and hyperspectral imaging. Herein, mid-IR SC generation is investigated in a cascaded silica-ZBLAN-chalcogenide fiber system directly pumped with a commercially available pulsed fiber laser operating in the telecommunications window at 1.55 μm. This fiber-based system is shown to generate a flat broadband mid-IR SC covering the entire range from 2 to 10 μm with several tens of mW of output power. This technique paves the way for low cost, practical, and robust broadband SC sources in the mid-IR without the requirement of mid-infrared pump sources or Thulium-doped fiber amplifiers. A fully realistic numerical model used to simulate the nonlinear pulse propagation through the cascaded fiber system is also described and the numerical results are used to discuss the physical processes underlying the spectral broadening in the cascaded system. Finally, recommendations are provided for optimizing the current cascaded system based on the simulation results.

1. Introduction

Fiber-based supercontinuum (SC) sources have become enormously useful in the last decade for a wide range of industrial and scientific applications.[1,2] New uses are also constantly emerging due to their unique properties that combine high brightness, multioctave frequency bandwidth, fiber delivery and single-mode output. Applications include optical coherence tomography (OCT), material processing, chemical sensing, gas monitoring, broadband imaging, and absorption spectroscopy. Currently, there is a significant research effort focused on extending the wavelength coverage toward the mid-Infrared (mid-IR) in the 2–20 μm molecular fingerprint region.[3–18] Various soft glasses based on chalcogenide (As_2S_3, As_2Se_3, GeAsSe),[3,8] tellurite (TeO_2),[19] telluride (GeTe, GeAsTeSe),[20,21] heavy-metal oxide (PbO-Bi_2O_3-Ga_2O_3-SiO_2-CdO),[10] and ZBLAN (ZrF_4 –BaF_2 –LaF_3 –AlF_3 –NaF),[22–25] have been used for drawing highly nonlinear infrared fibers, and experiments have shown efficient mid-IR SC generation up to 14 μm in chalcogenide optical fibers[3] and up to 16 μm in telluride fibers.[21] However, most of these mid-IR SC sources have been demonstrated using bulky mid-IR pump sources such as optical parametric oscillators (OPO) and amplifiers (OPA). Mid-IR fiber lasers and cascaded fiber systems have recently emerged as attractive and promising solutions for practical and commercial applications.[25–35] These fiber lasers-based systems indeed open routes to practical, table-top, and robust mid-IR supercontinuum sources with high spectral power density. Of particular interest are cascaded fiber systems as they are pumped by standard pulsed fiber lasers at telecommunication wavelength. In cascaded SC generation, an initial pulsed fiber laser at a wavelength of 1550 nm is progressively red-shifted in a cascade of silica and soft-glass fibers, enabling a stepwise extension toward the Mid-IR. From a fundamental point of view, the overall objective is to strongly enhance the soliton self-frequency shift (SSFS) using dispersion-tailored highly nonlinear fiber segments to push forward the SC generation far in the mid-IR.[29–31]

S. Venck, Dr. L. Brilland, R. Chahal, C. Caillaud
SelenOptics
Campus Beaulieu
Rennes 35000, France

F. St-Hilaire, A. N. Ghosh, Prof. J. M. Dudley, Dr. T. Sylvestre
Institut FEMTO-ST, CNRS UMR 6174
Université Bourgogne Franche-Comté
Besançon 25030, France
E-mail: thibaut.sylvestre@univ-fcomte.fr

F. St-Hilaire, Prof. M. Rochette
Department of Electrical and Computer Engineering
McGill University
Montréal H3A 0E9, Canada

M. Meneghetti, Prof. J. Troles
Université de Rennes
CNRS, ISCR-UMR 6226, Rennes 35000, France

F. Joulain, S. Cozic, S. Poulain
Le Verre Fluoré
Campus Kerlann
Bruz 35170, France

Dr. G. Huss
LEUKOS
37 rue Henri Giffard Limoges 87280, France

DOI: 10.1002/lpor.202000011

 © 2020 WILEY-VCH Verlag GmbH & Co. KGaA, Weinheim

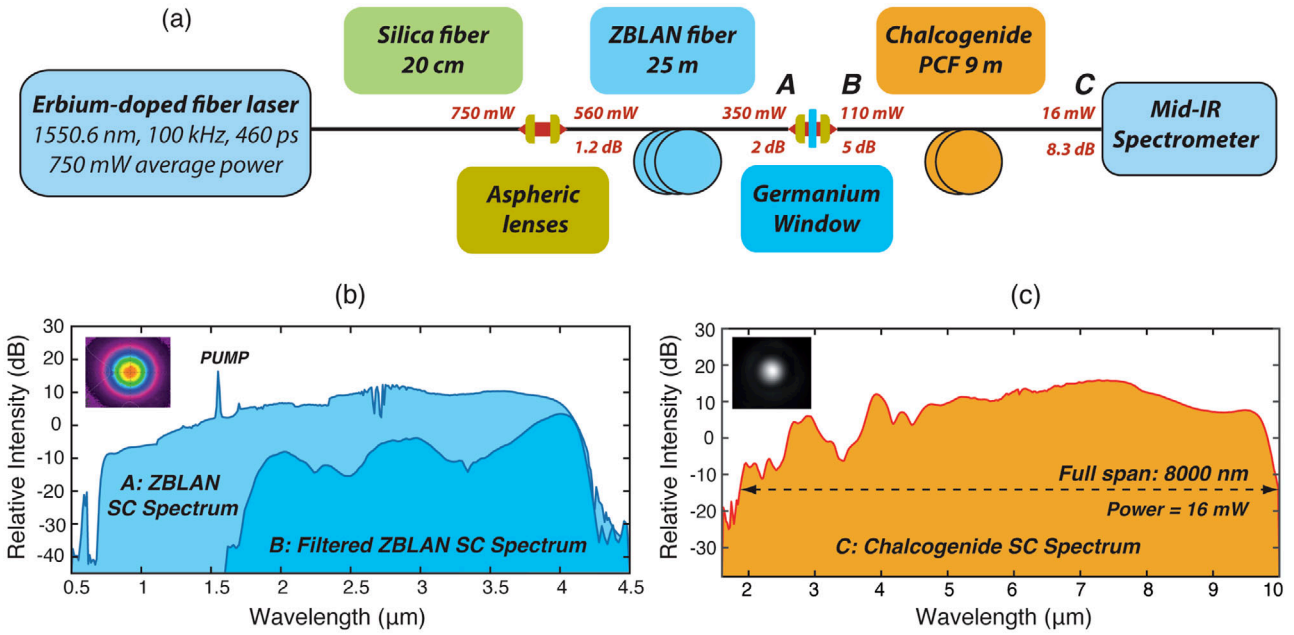

Figure 1. a) Experimental setup for mid-infrared SC generation in a cascaded silica-ZBLAN-chalcogenide optical fiber system. b) Experimental SC spectra at the ZBLAN fiber output (light blue) and after the long-pass filter (dark blue). c) Experimental SC spectrum at the chalcogenide fiber output (yellow). The insets show the optical mode profiles out of both the ZBLAN (b) and chalcogenide (c) optical fibers.

Among the most advanced fiber-based systems, Martinez et al. recently demonstrated a mid-IR SC from 2 to 11 μm with 139 mW average power by concatenating solid-core ZBLAN, arsenic sulfide, and arsenic selenide fibers, pumped by a master oscillator power amplifier and three thulium-doped fiber amplifier stages.[29,30] Hudson et al. combined a 2.9 μm ultrafast fiber laser based on holmium with an environmentally stable, polymer-protected chalcogenide fiber taper. By launching femtosecond, 4.2 kW peak power pulses into the As_2Se_3/As_2S_3 tapered fiber, they demonstrated a SC spectrum spanning from 1.8 to 9.5 μm with an average power of more than 30 mW.[27] C.R. Petersen et al. also demonstrated in 2016 Mid-IR SC generation beyond 7 μm using a silica–fluoride–chalcogenide fiber cascade pumped by a 1.55 μm seed laser and a thulium-doped fiber amplifier. By pumping a commercial $Ge_{10}As_{22}Se_{68}$-glass photonic crystal fiber with 135 mW of the pump continuum from 3.5–4.4 μm, they obtained a continuum up to 7.2 μm with a total output power of 54.5 mW, and 3.7 mW above 4.5 μm.[33] Commercially available mid-IR SC source with an extended bandwidth up to 10 μm and with 50 mW output power is now on sale at Norblis.[36]

In this paper, we demonstrate mid-IR SC generation from 2 to 10 μm in a cascaded silica-ZBLAN-As_2Se_3 fiber system directly pumped with a commercially available 460-ps pulsed fiber laser at 1.55 μm without any fiber amplifier stage. We provide details of the experimental cascaded fiber system and discuss the choice of the parameters such as chromatic dispersion and nonlinear coefficients used for optimal spectral broadening. We further report a fully realistic numerical model based on cascaded generalized nonlinear Schrödinger equations with an adaptive step size method. The model includes all the linear and nonlinear responses of the fibers, the infrared filtering function, and the effective mode area variation across the full SC spectrum. We then use our numerical results to discuss the physical processes underlying the spectral broadening in the cascaded system, such as modulation instability (MI), soliton fission, dispersive wave generation, and intrapulse Raman scattering (IRS).[37,38] We conclude with recommendations to optimize the current cascaded systems based on the simulation results.

2. Experimental Section

A diagram of the experimental setup for cascaded mid-IR SC generation is shown in **Figure 1a**. It consists of a concatenation of three commercially available optical fibers including a 20 cm-long single-mode silica fiber (SMF-28), a 25 m-long ZBLAN fiber, and a 9 m-long chalcogenide–glass photonic crystal fiber. Detailed specifications for each fiber segment are given in the next section including all parameters used in numerical simulations. This cascaded fiber arrangement was directly pumped by a compact ($90 \times 70 \times 15$ mm^3 only) pulsed fiber laser providing 460 ps-width pulse train at 100 kHz repetition rate and at a center wavelength of 1550.6 nm, a high peak power per pulse (18 kW), an average output power of 750 mW, and a near diffraction limited randomly polarized beam ($M^2 < 1.1$). These compact lasers are mainly commercialized for range-finding and LIDAR applications. Light coupling between each fiber was achieved using high-numerical aperture aspheric lenses matching the fiber numerical apertures and their effective mode areas. A key element in the cascaded fiber system is a mid-IR long pass filter (LPF) placed in between the ZBLAN and the chalcogenide fibers. This filter rejects wavelengths below 1.9 μm. This prevents from two-photon absorption (TPA) and optical damage in the chalcogenide fiber, enabling a better long-term stability of the mid-IR SC source. The long-pass filter is a Germanium (Ge) Ar-coated broadband window inserted in between two aspheric lenses. The generated SC

© 2020 WILEY-VCH Verlag GmbH & Co. KGaA, Weinheim

spectra have been recorded using a mid-IR optical spectrometer including a monochromator (ORIEL 7240) and a highly sensitive Hg-Cd-Te detector. The chalcogenide fiber output face was terminated with an end cap fiber and connectorized using an FC/PC connector for practical applications.

Experimental data for the spectra measured are provided at three key points in the cascaded fiber setup (A, B, C). The first spectrum, shown in Figure 1b (light blue), was measured at the output of the ZBLAN fiber at point A, before the long-pass infrared filter. The supercontinuum spans from 0.7 up to 4.1 μm. The inset in Figure 1b shows the ZBLAN fiber's mode profile measured with an IR camera. The second spectrum, also shown in Figure 1b (dark blue), was measured after the filter at point B. This is the filtered IR spectrum injected into the chalcogenide fiber. The final SC spectrum at the output of the chalcogenide fiber is shown in Figure 1c in yellow. As can be seen, the full SC spans from 2 up to 9.8 μm with a relatively smooth and flat bandwidth. The measured spectrum however shows a decrease in spectral intensity for shorter wavelengths and significant modulations in intensity (especially from 2 to 4 μm). Our simulations will show that those are not entirely a result of SC dynamics, but presumably artefacts from the wavelength sensitivity of the spectrometers used for measurement. The measured average power at the output is 16 mW, which corresponds to roughly 2% of the pump's average power (750 mW). Significant losses occur in the cascaded system, mainly from the free-space optics between the ZBLAN fiber and the chalcogenide fiber, including Fresnel reflections and coupling losses due to mode field diameter mismatch, aspheric lenses, cleaving imperfections, and optical misalignment. All these losses and the output power of every stage of the cascade fiber system are mentioned in red in Figure 1a. Despite this low conversion efficiency, the brightness of this source of a few microwatt per nanometer is sufficient for practical applications. It is worth mentioning that the experimental spectra are provided only at maximum pump power (750 mW) at the output of every fiber-stage, which look very flat and therefore hard to tell what actual broadening mechanism is dominant. However, it was observed that when decreasing the input pump laser current (from 4600 to 3600 mA), the SC in the ZBLAN fiber considerably reduces its lateral extension at long wavelength from 4.2 μm to 3.5 μm, thus limiting the additional extension in stages in the chalcogenide fiber. In such a cascade system, it is indeed crucial to obtain the most efficient SC extension in the ZBLAN fiber, as will be seen thereafter using numerical simulations.

3. Numerical Method

To simulate nonlinear pulse propagation in the cascaded fiber system, we used the generalized nonlinear Schrödinger equation (GNLSE) and solved the propagation equation numerically with the split-step Fourier method (SSFM)[37,38] combined with an adaptive step size.[39] The GNLSE can be written in the following form:

$$\frac{\partial A(z,T)}{\partial z} = -\frac{\alpha}{2}A + \mathrm{i}\sum_{k=2}^{\infty}\frac{\mathrm{i}^k\beta_k}{k!}\frac{\partial^k}{\partial T^k}A + \mathrm{i}\gamma\left(1+\mathrm{i}\tau_0\frac{\partial}{\partial T}\right) \times \left[A\cdot R(T)\circledast|A|^2\right] \quad (1)$$

This equation models the evolution of the complex pulse envelope $A(z,T)$ as it propagates inside an optical fiber in a frame of reference moving with the group velocity of the pulse: $T = t-\beta_1 z$. The first term on the right models optical losses with the linear loss coefficient α. The second term models dispersion with a Taylor expansion of the propagation constant $\beta(\omega)$, where $\beta_k = \frac{\partial^k\beta(\omega)}{\partial\omega^k}$. The third term models Kerr nonlinearity, including the Raman response of the material and a first-order correction for the frequency dependence of the nonlinear parameter γ, $\gamma(\omega) = \frac{\omega n_2(\omega)}{cA_{\mathrm{eff}}(\omega)}$. The first-order correction is referred to as the "shock" term and is characterized by a time-scale τ_0, which can include the frequency-dependence of A_{eff}, n_2, and n_{eff} (see ref. [40] for more details).

$$\tau_0 = \frac{1}{\omega_0} - \left[\frac{1}{n_{\mathrm{eff}}(\omega)}\frac{\mathrm{d}n_{\mathrm{eff}}}{\mathrm{d}\omega}\right]_{\omega_0} - \left[\frac{1}{A_{\mathrm{eff}}(\omega)}\frac{\mathrm{d}A_{\mathrm{eff}}}{\mathrm{d}\omega}\right]_{\omega_0} + \left[\frac{1}{n_2(\omega)}\frac{\mathrm{d}n_2}{\mathrm{d}\omega}\right]_{\omega_0} \quad (2)$$

The nonlinear response of the fiber is modeled with a convolution (denoted by $\circledast$) of the nonlinear response function $R(T)$ and the pulse power profile $|A(z,T)|^2$. $R(T)$ is commonly divided into an instantaneous electronic response (Kerr) and a delayed molecular response (Raman), and reads as $R(T) = (1-f_R)\delta(T) + f_R h_R(T)$, where f_R is the fractional contribution of the delayed Raman response, $\delta(T)$ is the Dirac delta function that models the instantaneous Kerr response, and $h_R(T)$ is the delayed Raman response function. $R(T)$ is normalized such that $\int_{-\infty}^{\infty} R(T)\mathrm{d}T = 1$. The Raman response function $h_R(T)$ is modeled using two characteristic times related to phonon dynamics in the material, τ_1 and τ_2 (see ref. [38] for more details):

$$h_R(T) = (\tau_2^{-2}+\tau_2^{-2})\tau_1\exp(-T/\tau_2)\sin(T/\tau_1) \quad (3)$$

We will use Equation (3) for both the silica and chalcogenide fibers (See **Table 1** for parameters). However, as the ZBLAN fiber has a dual-peak Raman gain spectrum, we will use another model based on Equation (5). A crucial step in modeling nonlinear pulse propagation in a cascaded fiber system is defining the longitudinal step size h. To accurately model the effects of nonlinearity and dispersion, h must be much smaller than both the dispersion length and the nonlinear length, defined as, $L_{\mathrm{NL}} = \frac{1}{\gamma P_0}$ and $L_{\mathrm{D}} = \frac{T_0^2}{|\beta_2|}$, respectively, where P_0 is the peak power, and T_0 is the $1/e$ pulse width. These two conditions must hold throughout the propagation length. Pumping with a quasi-continuous-wave laser (i.e., 460 ps pulses) leads to the break-up of the initial pulse via modulation instability (MI) into a vast collection of ultrashort soliton-like pulses with variable peak powers P_0 and durations T_0. The choice of h is therefore not as straightforward in this case. Our simulations show that the nonlinear length L_{NL} is a much more limiting factor than the dispersion length L_{D} for the step size h because of the high peak power reached within the soliton train. When the soliton train starts propagating, the maximal peak power varies significantly along the propagation distance z because of randomly occurring soliton collisions. This means that the condition $h \ll L_{\mathrm{NL}}$ can change drastically along z. To account for this, we used an adaptive step size method for the SSFM algorithms: the nonlinear phase-rotation method (see

© 2020 WILEY-VCH Verlag GmbH & Co. KGaA, Weinheim

Table 1. Nonlinear parameters for the cascaded fiber system.

Fiber	L [cm]	n_2 [cm^{2}W^{-1}]	A_{eff} [μm^2]	γ [W^{-1} km^{-1}]	f_R	τ_1 [fs]	τ_2 [fs]
SMF-28	20	2.4×10^{-16}	85	1.3	0.18	12.2	32
ZBLAN	2500	2.1×10^{-16}	43	2	0.2	Equation (5)	Equation (5)
Chalcogenide	900	1.1×10^{-13}	62	720	0.1	23.2	195

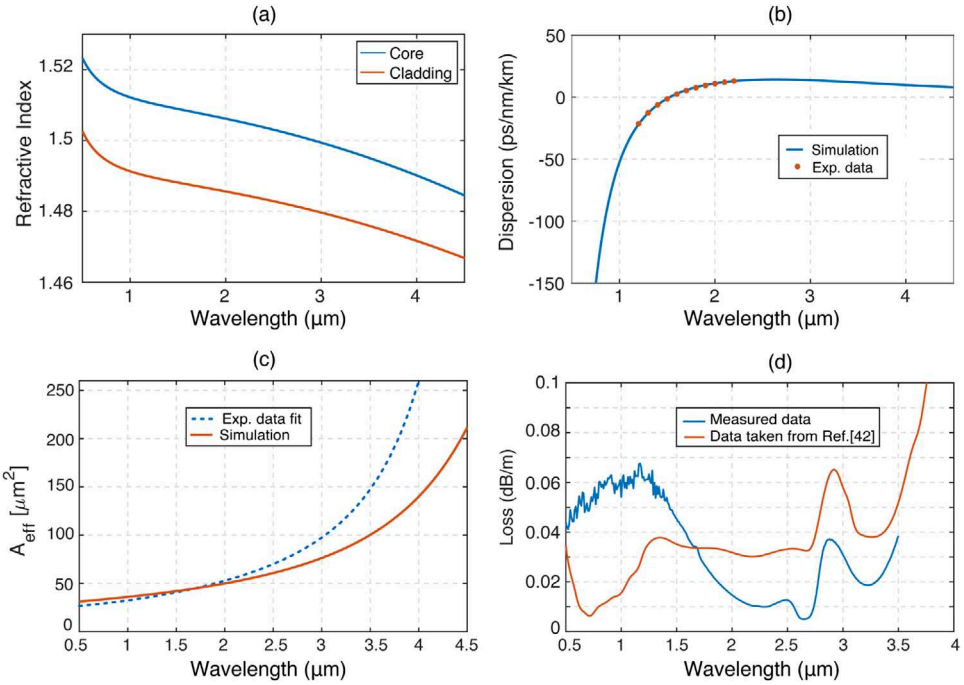

Figure 2. ZBLAN step-index optical fiber specifications: a) Core (blue) and cladding (red) refractive indices versus wavelength. b) Computed dispersion (blue curve) and experimental data (red dots). c) Simulated (red) and experimental (blue) effective mode area. d) Loss spectrum: blue, measured data; red, data from ref. [42].

ref. [39] for more details). This method consists of limiting the nonlinear phase-shift $\phi_{\text{NL}} = \gamma P_0 h$ to a sufficiently small value at each iteration, that is, the step size h is adapted at each iteration to optimize computing time and accuracy. For a train of soliton pulses, the maximal phase-shift is calculated from the maximal soliton peak power P_0^{max}. Every iteration i, the step size $h(i)$ is determined by $h(i) = \frac{\phi_{\text{NL}}^{max}}{\gamma_0 P_0^{max}(i)}$. For our simulations, we found that a maximal nonlinear phase-shift of $\phi_{\text{NL}}^{max} = 1/50$ rad is enough for convergence and allows for reasonable computing times.

3.1. Cascaded Fiber System

This section provides all linear and nonlinear parameters of the cascaded fiber system used in numerical simulations. The first fiber segment consists of a length of 20 cm of standard SMF-28. Although this fiber plays little role in SC broadening, it serves as a nonlinear modulation instability stage that triggers the soliton dynamics in both the ZBLAN and chalcogenide fibers. The nonlinear parameters for fused silica fiber are taken from ref. [38] and are shown in Table 1.

The wavelength dependence of A_{eff} and n_2 is negligible over the spectral bandwidth along this first fiber segment. The dispersion characteristics of SMF-28 are modeled using a Taylor series expansion. The following values are used: $\beta_2 = -21.4\times10^{-27}$ s^{2}m^{-1}, $\beta_3 = 0.12\times10^{-39}$ s^{3}m^{-1} (from ref. [38]). The 1550 nm pump is in the anomalous dispersion regime. Optical losses were neglected for this fiber segment given the short length (20 cm) and low absorption of silica fibers at 1550 nm (0.2 dB km^{-1}).

The second fiber consists of a length of 25 m of a commercially available step-index fluoride (ZBLAN) fiber from Le Verre Fluoré.[41] The core and cladding diameters are 8.5 μm and 125 μm, respectively. The refractive index of core and cladding are plotted in **Figure 2a** and the dispersion curve is shown in Figure 2b in blue. Experimental data of dispersion from 1.2 to 2.2 μm are provided in red dots. To obtain the dispersion of the fiber over the full bandwidth, we solved the characteristic equation for a step-index fiber with the wavelength-dependent core and cladding indices shown in Figure 2a. Results show that the zero dispersion wavelength (ZDW) is 1525 nm. Therefore, the 1550 nm pump wave is in the slightly anomalous dispersion regime.

© 2020 WILEY-VCH Verlag GmbH & Co. KGaA, Weinheim

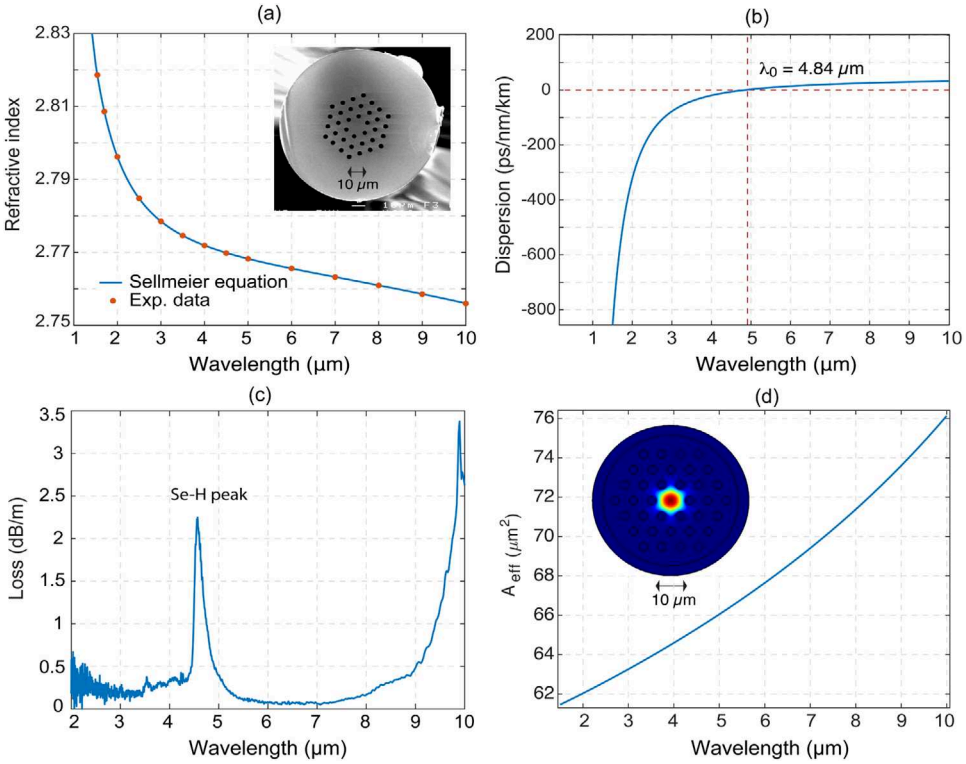

Figure 3. a) Refractive index of $As_{38}Se_{62}$ glass calculated with the Sellmeier model. Inset shows the cross-section image of the microstructured chalcogenide fiber. b) Computed dispersion curve for the microstructured chalcogenide fiber with a zero dispersion wavelength near 5 μm. c) Absorption loss of the chalcogenide-based microstructured fiber. d) Computed effective mode area. Inset shows the fundamental optical HE_{11} mode.

The strong effective mode area variation from 0.5 to 5 μm was also considered. We calculated A_{eff} over the same bandwidth by solving the characteristic equation for a step-index fiber with the wavelength-dependent core and cladding indices. The results are compared with the experimental data in Figure 2c. Our simulated results were used instead of the measured data because it provided a better fit with the experimental SC when the wavelength dependence of A_{eff} was included.

Figure 2d shows the optical losses of the ZBLAN fiber. The measurements are shown in blue, and the data used in the simulations (taken from ref. [42]) is shown in orange. The data from ref. [42] was used in our simulations to better model the limit of the transmission window in the infrared, which ends between 4 and 4.5 μm. As we will show in our results, the transmission window limit of the ZBLAN fiber is the only feature of the loss curve that has a significant impact on spectral nonlinear dynamics. The small discrepancies with the measured loss curve should not affect the overall SC mechanisms.

The nonlinear parameters for the ZBLAN fiber are listed in Table 1. The wavelength dependence of the nonlinear index is neglected. The Raman response function h_R was obtained with the model developed in ref. [24], where the measured Raman gain spectrum $g_R(\Omega)$ is approximated by a sum of two Gaussian functions, and the response function is extracted from the imaginary part of the Fourier transform as

$$h_R(T>0) = C \cdot \int_0^{\infty} g_R(\Omega)\sin(\Omega T)\mathrm{d}\Omega \quad (4)$$

where C is a normalization constant chosen such that $\int_{-\infty}^{\infty} h_R(T)\mathrm{d}T = 1$. The following equation was used in our simulations to model $g_R(\Omega)$:

$$g_R(\Omega) = a_1 \exp\left(\frac{(\Omega/(2\pi)-\nu_1)^2}{2\omega_1^2}\right) + a_2 \exp\left(\frac{(\Omega/(2\pi)-\nu_2)^2}{2\omega_2^2}\right) \quad (5)$$

with $a_1 = 0.54\times10^{-11}$cm W^{-1}, $a_2 = 0.25\times10^{-11}$cm W^{-1}, $\nu_1 =$ 17.4 THz, $\nu_2 = 12.4$ THz, $\omega_1 = 0.68$ THz, $\omega_2 = 3.5$ THz.[24]

The third fiber sample is a chalcogenide–glass solid-core microstructured optical fiber. It was fabricated from $As_{38}Se_{62}$ glass using the casting method.[45] It has a core diameter of 11.2 μm, a pitch of 7.11 μm, and an air-hole diameter of 3.23 μm. **Figure 3** shows in inset a cross section of the microstructure with dimensions for the air hole structure as well as the refractive index of $As_{38}Se_{62}$ glass. The following Sellmeier model was used, $n^2 = A_0 + \frac{A_1\lambda^2}{\lambda^2-a_1^2} + + \frac{A_2\lambda^2}{\lambda^2-a_2^2}$, with $A_0 = 3.7464$, $A_1 = 3.9057$, $A_2 = 0.9466$, $a_1 = 0.4073$ μm, and $a_2 = 40.082$ μm. These values were chosen to obtain the best fit with the refractive index measured data shown in Figure 3a.

The dispersion curve for the fundamental mode was calculated by the finite-element method using the COMSOL software. The result is shown in Figure 3b. The zero-dispersion wavelength is at 4.84 μm. The calculated effective mode area is shown in Figure 3d. Optical losses for the chalcogenide fiber are shown in Figure 3c. The transmission window ends near 10 μm, and there is an absorption peak around 4.56 μm due to the presence of Se–H

© 2020 WILEY-VCH Verlag GmbH & Co. KGaA, Weinheim

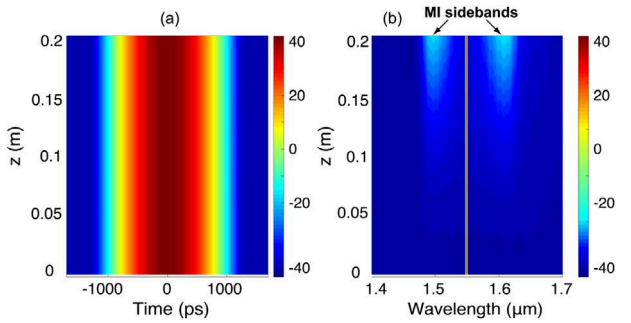

Figure 4. a) Temporal and b) spectral evolution in the silica fiber (SMF-28) for a 460 ps pulse and a 6 kW peak power.

chemical bonds in the glass. The nonlinear parameters considered for this $As_{38}Se_{62}$ glass fiber are summarized in Table 1. The nonlinear index n_2 is very large and is taken from refs. [45, 46]. The Raman response is modelled with Equation (3) and the Raman parameters are taken from ref. [27]. This gives Raman gain peak centered around 6.9 THz with a linewidth of about 3.2 THz.

3.2. Infrared Optical Filter

The short-wavelength filtering of the ZBLAN fiber output is achieved experimentally with a combination of a germanium window and lenses with IR antireflective (AR) coatings for infrared. This filtering window aims to cut all the energy <1.9 μm in the ZBLAN fiber output spectrum to prevent two-photon absorption and optical damage in the chalcogenide optical fiber. The global transmission function of this filtering system was modelled with a supergaussian function of the following form,

$$T = \exp\left(-\left(\frac{\lambda - \Lambda_0}{\Delta\lambda}\right)^m\right) \tag{6}$$

The parameters Λ_0, m, and $\Delta\lambda$ were adjusted to obtain the best fit with the experimental spectrum measured after the filtering system. The following values where used: $\Lambda_0 = 11.87\,\mu m$, $m = 80$, and $\Delta\lambda = 10\,\mu m$.

4. Simulation Results

In this section, we present simulation results for three different pump pulse durations: 50, 200, and 460 ps (the measured experimental duration). All the spectral and temporal evolutions shown thereafter are plotted with colormaps of relative intensity with a 80 dB range from blue to red (**Figure 4**). For the simulations, a Gaussian pulse was used. Quantum noise was added to the initial pulse following the one photon per mode model (see ref. [44] for more details). The numerical models used for each fiber are also presented, including dispersion, nonlinear parameters, and losses. A peak power of 6 kW was chosen for the three pump pulses to get the best match with experimental results. For this type of simulation, we typically use a lower peak power than the experimental peak power, which is around 18 kW in this case. This is due to the fact that the simulation model considers perfectly polarized and single-mode propagation. In experimental conditions, random polarization and multimode behavior is generally detrimental to spectral broadening mechanisms, hence the need for more peak power than in simulations. Simulations were carried out for the three pump pulse durations in the SMF-28 fiber and the ZBLAN fiber. As expected from the theory of SC generation with quasi-CW pulses, we show that the same mechanisms occur for the three different pump pulse durations, and that the experimental SC bandwidths at the output of the ZBLAN and chalcogenide fibers can be achieved with pump pulses as short as 50 ps. The SSFM algorithm requires high longitudinal precision in the chalcogenide fiber because of high nonlinearity ($\gamma_0 = 720\,km^{-1}\,W^{-1}$). As a result, simulations for 200 ps and 460 ps pump pulses, which require at least $Nt = 2^{21}$ sampling points, would require unrealistic computing times. Therefore, simulations in the chalcogenide fiber were only carried out with the intermediate ZBLAN results from the 50 ps pump pulse.

5. Silica Fiber

The simulation results for 20 cm of propagation in the single-mode silica fiber are shown in Figure 4 in colormap and for a 460 ps pulse. The pulse shape remains virtually unchanged throughout this fiber segment. The only notable feature is the apparition of weak MI Stokes and anti-Stokes sidebands in the spectrum around 1.51 and 1.59 μm, respectively. They can be seen appearing on either side of the pump in the spectral evolution, as shown in top of Figure 4b. Their specific frequencies relative to the pump ($\Omega_{MI} = \omega_P - \omega_S$) are given by the scalar phase-matching relation that reads as $\beta_2\Omega_{MI}^2 + \frac{\beta_4}{12}\Omega_{MI}^4 + 2\gamma P_0 = 0$, where P_0 is the peak power, γ is the nonlinear parameter, β_2 is the GVD parameter, and β_4 is the fourth-order dispersion.[38] A more detailed view is shown in Figure 6. It is worth noting, however, that our simulations show this first fiber segment has little to no effect on the overall SC evolution in the ZBLAN and chalcogenide fibers.

6. ZBLAN Fiber

The simulated spectral and temporal evolutions in both the silica and the ZBLAN fibers are shown in **Figure 5**. In Figure 5c, the final spectrum after 25 m of propagation is compared to the experimental spectrum. The agreement is particularly excellent. This is due to the fact that the total bandwidth and soliton self-frequency shift (SSFS) are only limited by the transmission window of the fiber in the mid-infrared which ends between 4 and 4.5 μm (Figure 2d). The break-up of the pulse into a train of solitons can be seen from 2 m in Figure 5b. Beyond this point, the continuous Raman-induced self-frequency shift of the solitons is clearly seen in both the spectral and temporal evolutions as they gradually separate from the main pulse due to their dispersion increasing with the SSFS. Events of soliton collision can also be observed in the spectral evolution. They manifest themselves as sharp increases in the spectrum bandwidth on the long-wavelength side (e.g., around 16 m in the 50 ps spectral evolution). Dispersive waves can be seen rapidly drifting away from the main pulse in the time evolution beyond 1000 ps. In

© 2020 WILEY-VCH Verlag GmbH & Co. KGaA, Weinheim

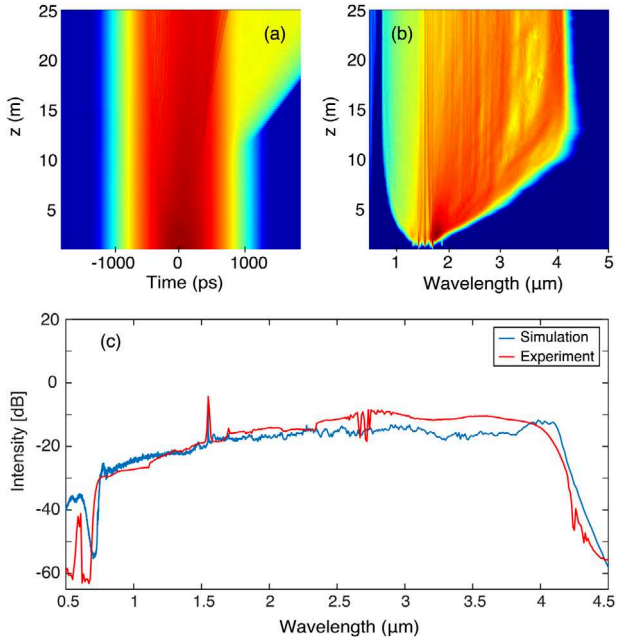

Figure 5. a) Spectral and b) time-domain evolution for the 460 ps pump pulse with the output experimental and numerical spectra shown in (c).

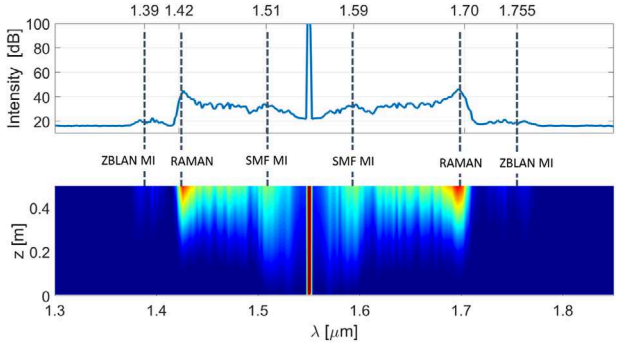

Figure 6. Initial spectral evolution in the ZBLAN fiber. The wavelengths marked with the dotted lines correspond to the theoretical MI and Raman wavelengths calculated with phase-matching equation in the text and the Raman gain peak at 17.4 THz, respectively.

terms of bandwidth, the simulation provide a nearly perfect match with the experimental spectrum (within 0.05 μm at the –20 dB level of the maximum intensity).

From Figure 5b, we see that the SC in ZBLAN reached a maximum extension at 4.2 μm around 13 m. At longer distance, the SC becomes slightly narrower due to the absorption edge around 4–4.2 μm in ZBLAN, and since there is not much spectral evolution between 15 and 25 m in the ZBLAN fiber, this might indicate that the peak power of the solitons are not very high, nonlinear effects are not very important and the dispersion continue to increase the pulse duration of these solitons. Therefore, it might be more efficient to cut the ZBLAN fiber at 13–15 m to inject its output SC (which is broader and maybe more intense soliton train) in the following chalcogenide fiber.

To gain insight on the processes initiating SC generation in the ZBLAN fiber, we show in **Figure 6** the details of the first 50 cm of

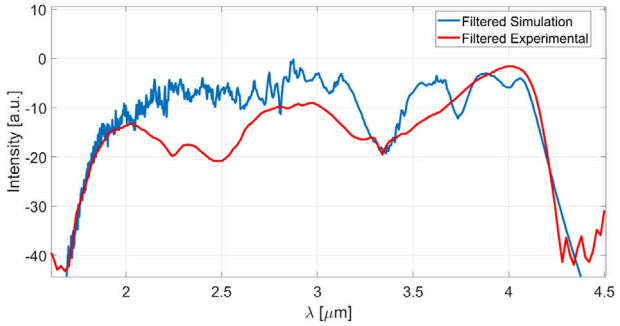

Figure 7. Filtered spectrum injected in the chalcogenide fiber.

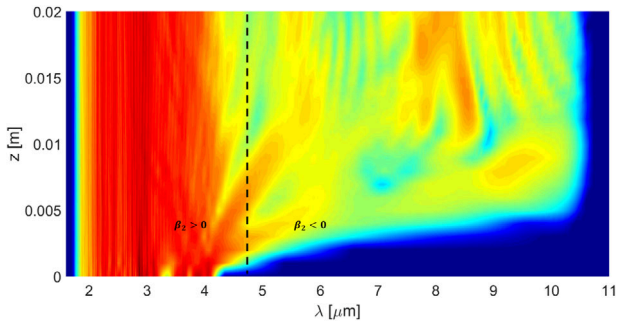

Figure 8. Initial spectral evolution in the chalcogenide fiber.

spectral evolution. The strongest sidebands correspond to the MI-enabled Stokes and anti-Stokes Raman sidebands around 1.42 and 1.70 μm.[43] Around 1.51 and 1.59 μm are the residual MI sidebands from the silica fiber. Weak MI ZBLAN sidebands are visible around 1.39 and 1.755 μm. Each of the wavelength pairs given here and identified on the plot were calculated theoretically. The MI wavelengths can be derived from the same equation as for the silica fiber, and the Raman wavelengths correspond to the peak of the ZBLAN Raman gain at 17.4 THz.

From theory and simulation, we confirm that the time and spectral domain evolutions of the 460 ps pulse is well approximated by the 50 ps pulse. Longer pulses simply provide a longer collection of solitons but that will not change the statistical distribution of peak powers and pulse widths. Therefore, from now on, simulations are carried out only with the 50 ps pump pulse to save computing time. **Figure 7** shows the filtered simulated spectrum compared with the experimental filtered spectrum using 50-ps input pulse. This is the spectrum injected in the chalcogenide fiber.

7. Chalcogenide Fiber

The simulation results for the first 2 cm of propagation in the chalcogenide fiber are shown in **Figure 8**. The injected spectrum from the filtered ZBLAN output lies entirely in the normal dispersion regime of the chalcogenide fiber which has its ZDW at 4.838 μm (marked by the dotted line). The initial spectral evolution shows that, from the train of thousands of pulses injected in the chalcogenide fiber, a fraction of them have a small enough width T_0 to drift through the zero-dispersion via intrapulse Raman scattering (IRS). The pulses crossing the ZDW evolve into

© 2020 WILEY-VCH Verlag GmbH & Co. KGaA, Weinheim

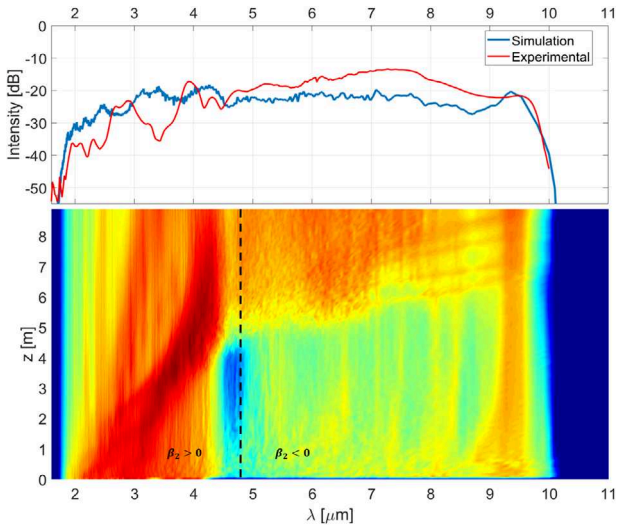

Figure 9. Full spectral evolution in the chalcogenide fiber with final output spectrum.

solitons and create an initial low-intensity continuum on the long-wavelength side through SSFS.

The spectral evolution over the full length of chalcogenide fiber is shown in **Figure 9**. The top of the figure shows the final simulated output spectrum compared to the experimental spectrum. In terms of spectral bandwidth, our numerical result matches nearly perfectly with the experimental measurement. If we compare the numerical and experimental SC bandwidth at –20 dB of maximum intensity, we get a deviation of only 0.04 μm over the full 8 μm width. As for the ZBLAN fiber, spectral broadening in the chalcogenide fiber is only limited by its transmission window and the confinement losses.

The spectral evolution of Figure 9 shows interesting SC dynamics. From 0 to 5 m, most of the energy remains in the normal dispersion regime ($\beta_2 > 0$). Energy rapidly accumulates at the limit of the transmission window (around 9.5 μm) from the pulses that initially crossed the ZDW. These solitons tend to accumulate around this wavelength as their SSFS is stopped by the upper limit of the transmission window. The effect of the absorption peak at around 4.6 μm (Figure 3) can be clearly seen on the low-energy continuum. From the beginning, the main train of pulses can be seen drifting through intrapulse Raman scattering toward the ZDW. After 5 m, most of the pulses remain trapped by the ZDW barrier and stop their frequency drift. From 5 m onward, a fraction of the pulses cross the ZDW barrier and start evolving as solitons on the anomalous dispersion side ($\beta_2 < 0$). This gradually adds energy to the initial low-energy continuum via the SSFS of the solitons. The spectrum evolves toward thermalization, where energy is equally distributed throughout the transmission bandwidth. The output is therefore a relatively flat spectrum from 2 to 9.7 μm.

8. Conclusion and Recommendations

In this work, we have developed a broadband fiber-based supercontinuum source spanning from 2 to 10 μm with 16 mW output power. This was achieved using cascaded ZBLAN-chalcogenide optical fibers directly pumped by a compact 1550-nm pulsed fiber laser without using thulium-doped fiber amplifiers. We have further carried numerical simulations for broadband mid-infrared SC generation in a cascaded fiber system. Our simulations were consistent with the theory of quasi-CW SC generation. We show that noise amplification through MI and Raman gain leads to the break-up of the pulse envelope into a chaotic train of solitons which broadens the spectrum through Raman-induced self-frequency shift and dispersive waves. In terms of bandwidth, our numerical results are nearly identical to the experimentally measured spectra, both at the output of the ZBLAN fiber (within 0.05 μm at −20 dB level) and the chalcogenide fiber (within 0.04 μm at −20 dB level). The final output spectrum is a flat broadband spectrum covering the mid-IR from 2 to 10 μm. Further broadening is only limited by the transmission window of the chalcogenide fiber. Our main recommendation drawn from our numerical simulations would consist of using a shorter ZBLAN fiber (around 13 m) and a chalcogenide microstructured fiber with a smaller core diameter (ideally 7 μm).[47] This would shift its zero-dispersion wavelength toward shorter wavelengths (<4 μm) and allow to fill the desired window (from 2 to 10 μm) with a few centimeters of fiber only (based on numerical simulations, See Supporting Information), while reducing the linear loss (8.3 dB). Our second recommendation consists into exploring different options for the infrared filtering system and to avoid free-space optics. Free-space optics and recoupling to the chalcogenide fiber induces considerable losses in the system. An all-fiber filtering system, for example, would provide improved robustness and reduced losses. Anti-reflection coating or nanoimprinting of the chalcogenide fibers could also significantly reduce the Fresnel losses and the input damage threshold.[48,49] This would allow to considerably increase both the output power and the spectral power density. Another way to reduce free-space optics in this cascaded fiber setup is to use a fusion splice between the silica and the ZBLAN fiber, as demonstrated in refs. [50, 51]. Finally, we also recommend exploring telluride-glass fibers as a fourth fiber to add to the system. This would potentially allow to further broaden the spectrum and reach wavelengths beyond 10 μm.[52] Polarization and coherence properties of the mid-IR cascaded SC light are further key parameters for some applications such as mid-IR OCT and interferometric measurements. We could for instance replace the fiber laser and the cascaded system with polarization-maintaining fibers.[53,54] About coherence, it is evident that this cascaded fiber system does not maintain the initial temporal coherence of the input laser but we could consider all-normal dispersion (ANDi) chalcogenide fibers directly pumped with mid-IR femtosecond fiber lasers to improve this feature.[44] Nevertheless, we believe that, despite the mentioned weaknesses, current mid-infrared supercontinuum all-fiber sources will find several applications and represent a landmark to foster the improvement of such broadband sources in other fiber or chip-based photonic platforms.

Acknowledgements

The project received funding from the European Union H2020 programme MSCA-ITN-SUPUVIR under grant agreement 722380 and the Agence

 © 2020 WILEY-VCH Verlag GmbH & Co. KGaA, Weinheim

Nationale de la Recherche (ANR) (I-SITE BFC: ANR-15-IDEX-0003, EIPHI Graduate School: ANR-17-EURE-0002).

Conflict of Interest

The authors declare no conflict of interest.

Keywords

chalcogenide fibers, fiber lasers, nonlinear optics and solitons, soft-glass fibers, supercontinuum generation, ZBLAN fibers

Received: January 13, 2020
Revised: February 28, 2020
Published online:

[1] R. R. Alfano, *The Supercontinuum Laser Source: The Ultimate White Light*, Springer, New York **2016**.
[2] J. M. Dudley, J. R. Taylor (Eds.), *Supercontinuum Generation in Optical Fibers*, Cambridge University Press, Cambridge **2010**.
[3] C. R. Petersen, U. Møller, I. Kubat, B. Zhou, S. Dupont, J. Ramsay, T. Benson, S. Sujecki, N. Abdel-Moneim, Z. Tang, D. Furniss, A. Seddon, O. Bang, *Nat. Photonics* **2014**, *8*, 830.
[4] Y. Yu, B. Zhang, X. Gai, C. Zhai, S. Qi, W. Guo, Z. Yang, R. Wang, D. Choi, S. J. Madden, B. Luther-Davies, *Opt. Lett.* **2015**, *40*, 1081.
[5] T. Cheng, K. Nagasaka, T. H. Tuan, X. Xue, M. Matsumoto, H. Tezuka, T. Suzuki, Y. Ohishi, *Opt. Lett.* **2016**, *41*, 2117.
[6] U. Møller, Y. Yu, I. Kubat, C. R. Petersen, X. Gai, L. Brilland, D. Mechin, C; Caillaud, J. Troles, B. Luther-Davies, O. Bang, *Opt. Express* **2015**, *23*, 3282.
[7] A. Lemière, F. Désévédavy, P. Mathey, P. Froidevaux, G. Gadret, J.-C. Jules, C. Aquilina, B. Kibler, P. Béjot, F. Billard, O. Faucher, F. Smektala, *J. Opt. Soc. Am. B* **2019**, *36*, 183.
[8] C. R. Petersen, R. D. Engelsholm, C. Markos, L. Brilland, C. Caillaud, J. Troles, O. Bang, *Opt. Express* **2017**, *25*, 15336.
[9] S. Dai, Y. Wang, X. Peng, P. Zhang, X. Wang, Y. Xu, *Appl. Sci.* **2018**, *8*, 707.
[10] A. N. Ghosh, M. Klimczak, R. Buczynski, J. M. Dudley, T. Sylvestre, *J. Opt. Soc. Am. B* **2018**, *35*, 2311.
[11] F. Belli, A. Abdolvand, W. Chang, J. C. Travers, P. St. J. Russell, *Optica* **2015**, *2*, 292.
[12] N. M. Israelsen, C. R. Petersen, A. Barh, D. Jain, M. Jensen, G. Hannesschläger, P. T. -Lichtenberg, C. Pedersen, A. Podoleanu, O. Bang, *Light: Sci. Appl.* **2019**, *8*, 11.
[13] I. Zorin, R. Su, A. Prylepa, J. Kilgus, M. Brandstetter, B. Heise, *Opt. Express* **2018**, *26*, 33428.
[14] J. Hult, R. S. Watt, C. F. Kaminski, *Opt. Express* **2007**, *15*, 11385.
[15] C. Amiot, A. Aalto, P. Ryczkowski, J. Toivonen, G. Genty, *Appl. Phys. Lett.* **2017**, *111*, 061103.
[16] C. R. Petersen, P. M. Moselund, L. Huot, L. Hooper, O. Bang, *Infrared Phys. Technol.* **2018**, *91*, 182.
[17] A. B. Seddon, in *Deep Imaging in Tissue and Biomedical Media* (Eds: L. Shi, R. R. Alfano), Pan Stanford Publishing, Singapore **2016**, pp. 231–294.
[18] C. R. Petersen, N. Prtljaga, M. Farries, J. Ward, B. Napier, G. R. Lloyd, J. Nallala, N. Stone, O. Bang, *Opt. Lett.* **2018**, *43*, 999.
[19] F. Désévédavy, G. Gadret, J.-C. Jules, B. Kibler, F. Smektala, *Supercontinuum Generation in Tellurite Optical Fibers*, Technological Advances in Tellurite Glasses, Springer Ser. Mater. Sci., Vol. *254*, Springer, **2017**.
[20] P. Lucas, Z. Yang, M. K. Fah, T. Luo, S. Jiang, C. Boussard-Pledel, M.-L. Anne, B. Bureau, *Opt. Mater. Express* **2013**, *3*, 1049.
[21] Z. Zhao, B. Wu, X. Wang, Z. Pan, Z. Liu, P. Zhang, X. Shen, Q. Nie, S. Dai, R. Wang, *Laser Photonics Rev.* **2017**, *11*, 1700005.
[22] C. Xia, M. Kumar, O. P. Kulkarni, M. N. Islam, F. L. Terry, M. J. Freeman, M. Poulain, G. Mazé, *Opt. Lett.* **2006**, *31*, 2553.
[23] M. Michalska, P. Hlubina, J. Swiderski, *IEEE Photonics J.* **2017**, *9*, 3200207.
[24] C. Agger, C. Petersen, S. Dupont, H. Steffensen, J. K. Lyngsø, C. L. Thomsen, J. Thøgersen, S. R. Keiding, O. Bang, *J. Opt. Soc. Am. B* **2012**, *29*, 635.
[25] C. L. Hagen, J. W. Walewski, S. T. Sanders, *IEEE Photonics Technol. Lett.* **2006**, *18*, 91.
[26] C. Xia, M. Kumar, M.-Y. Cheng, R. S. Hegde, M. N. Islam, A. Galvanauskas, H. G. Winful, F. L. Terry, M. J. Freeman, M. Poulain, G. Mazé, *Opt. Express* **2007**, *15*, 865.
[27] D. D. Hudson, S. Antipov, L. Li, I. Alamgir, T. Hu, M. El Amraoui, Y. Messaddeq, M. Rochette, S. D. Jackson, A. Fuerbach, *Optica* **2017**, *4*, 1163.
[28] F. Theberge, N. Berube, S. Poulain, S. Cozic, S. Chatigny, L.-R. Robichaud, L.-P. Pleau, M. Bernier, R. Vallee, *Opt. Express* **2018**, *26*, 13952.
[29] R. A. Martinez, G. Plant, K. Guo, B. Janiszewski, M. J. Freeman, R. L. Maynard, M. N. Islam, F. L. Terry, O. Alvarez, F. Chenard, R. Bedford, R. Gibson, A. I. Ifarraguerri, *Opt. Lett.* **2018**, *43*, 296.
[30] R. A. Martinez, K. Guo, T. Zhai, F. L. Terry, L. E. Pierce, M. N. Islam, R. Gibson, J. M. Reed, R. G. Bedford, L. Maksymiuk, M. J. Freeman, B. A. Gorin, N. P. Christian, A. I. Ifarraguerri, *J. Lightwave Technol.* **2019**, *37*, 3626.
[31] I. Kubat, C. R. Petersen, U. Visbech Møller, A. Seddon, T. Benson, L. Brilland, D. Méchin, P. M. Moselund, O. Bang, *Opt. Express* **2014**, *22*, 3959.
[32] C. R. Petersen, P. M. Moselund, C. Petersen, U. Møller, O. Bang, *Opt. Express* **2016**, *24*, 749.
[33] C. R. Petersen, P. M. Moselund, Ch. Petersen, U. Møller, O. Bang, in *Proc. SPIE 9703, Optical Biopsy XIV: Toward Real-Time Spectroscopic Imaging and Diagnosis, 97030A*, **2016**.
[34] L.-R. Robichaud, V. Fortin, J.-C. Gauthier, S. Châtigny, J.-F. Couillard, J.-L. Delarosbil, R. Vallée, M. Bernier, *Opt. Lett.* **2016**, *41*, 4605.
[35] J. Yao, B. Zhang, K. Yin, J. Hou, *Chin. Phys. B* **2019**, *28*, 084209.
[36] NORBLIS homepage, http://norblis.com/ (accessed: March 2020).
[37] J. M. Dudley, G. Genty, S. Coen, *Rev. Mod. Phys.* **2006**, *78*, 1135.
[38] G. P. Agrawal, *Nonlinear Fiber Optics*, 4th ed., Academic Press, Elsevier, San Diego **2007**.
[39] O. V. Sinkin, R. Holzlohner, J. Zweck, C. R. Menyuk, *J. Lightwave Technol.* **2003**, *21*, 61.
[40] B. Kibler, J. M. Dudley, S. Coen, *Appl. Phys. B* **2005**, *81*, 337.
[41] ZFG singlemode, https://leverrefluore.com/products/passive-fibers/zfg-singlemode/ (accessed: March 2020).
[42] Fluoride fiber technology, https://www.fiberlabs.com/glossary/technology/ (accessed: March 2020).
[43] A. D. Sánchez, P. I. Fierens, S. M. Hernandez, J. Bonetti, G. Brambilla, D. F. Grosz, *J. Opt. Soc. Am. B* **2018**, *35*, 2828.
[44] E. Genier, P. Bowen, T. Sylvestre, J. M. Dudley, P. Moselund, O. Bang, *J. Opt. Soc. Am. B* **2019**, *36*, 161.
[45] Q. Coulombier, L. Brilland, P. Houizot, T. Chartier, T. N. NGuyen, F. Smektala, G. Renversez, A. Monteville, D. Mechin, T. Pain, H. Orain, J.-C. Sangleboeuf, J. Troles, *Opt. Express* **2010**, *18*, 9107.
[46] G. Lenz, J. Zimmermann, T. Katsufuji, M. E. Lines, H. Y. Hwang, S. Spälter, R. E. Slusher, S.-W. Cheong, J. S. Sanghera, I. D. Aggarwal, *Opt. Lett.* **2000**, *25*, 254.
[47] H. Saghaei, M. Ebnali-Heidari, M. K. Moravvej-Farshi, *Appl. Opt.* **2015**, *54*, 2072.
[48] L.-R. Robichaud, S. Duval, L.-P. Pleau, V. Fortin, S. T. Bah, S. Châtigny, R. Vallée, M. Bernier, *Opt. Express* **2020**, *28*, 107.

 © 2020 WILEY-VCH Verlag GmbH & Co. KGaA, Weinheim

[49] C. R. Petersen, M. B. Lotz, G. Woyessa, A. N. Ghosh, T. Sylvestre, L. Brilland, J. Troles, M. H. Jakobsen, R. Taboryski, O. Bang, *Opt. Lett.* **2019**, *44*, 5505.
[50] K. Yin, B. Zhang, J. Yao, L. Yang, S. Chen, J. Hou, *Opt. Lett.* **2016**, *41*, 946.
[51] Z. Zheng, D. Ouyang, J. Zhao, M. Liu, S. Ruan, P. Yan, J. Wang, *Photonics Res.* **2016**, *4*, 135.
[52] S. Cui, C. Boussard-Plédel, J. Troles, B. Bureau, *Opt. Mater. Express* **2016**, *6*, 971.
[53] S. A. Rezvani, Y. Nomura, K. Ogawa, T. Fuji, *Opt. Express* **2019**, *27*, 24499.
[54] A. N. Ghosh, M. Meneghetti, C. R. Petersen, O. Bang, L. Brilland, S. Venck, J. Troles, J. M. Dudley, T. Sylvestre, *J. Phys.: Photonics* **2019**, *1*, 044003.

© 2020 WILEY-VCH Verlag GmbH & Co. KGaA, Weinheim

Research Article Vol. 3, No. 1 / 15 January 2020 / OSA Continuum 31

Silica-based photonic crystal fiber for the generation of broad band UV radiation

S. Perret,[1,*] C. Poudel,[3] A. N. Ghosh,[1] G. Fanjoux,[1] L. Provino,[2] T. Taunay,[2] A. Monteville,[2] D. Landais,[2] C. F. Kaminski,[3] J. M. Dudley,[1] and T. Sylvestre[1]

[1]Institut FEMTO-ST, UMR 6174 CNRS, Université Bourgogne Franche-Comté, Besançon, France
[2]Photonics Bretagne, Lannion, France
[3]Department of Chemical Engineering and Biotechnology, University of Cambridge, UK
[*]solveig.perret@femto-st.fr

Abstract: We report a small-core UV-grade silica multimode photonic crystal fiber for nonlinear frequency conversion in the ultraviolet spectral region. The fiber has been fabricated using F110 UV-Grade glass from Heraeus, which features excellent transmission and low solarization in the UV window. Pumping the fiber core at 355 nm with picosecond laser pulses, we observe the appearance of parametric sidebands in several spatial modes up to 380 nm. We modelled this process using intermodal phase-matching conditions and obtained excellent agreement between calculations and the measured data. We further report frequency conversion pumping into the fiber microstructured cladding where broadband cascaded Raman scattering spanning up to 391 nm is observed. These results represent a significant step towards the efficient and stable generation of UV supercontinuum spectra in an all-silica fiber platform.

© 2019 Optical Society of America under the terms of the OSA Open Access Publishing Agreement

1. Introduction

A major current challenge in supercontinuum (SC) generation is the generation of spectral components in the ultraviolet (UV) wavelength range below 400 nm [1]. There is particular need for UV broadband light sources in applications such as fluorescence microscopy for the simultaneous coherent excitation of multiple fluorophores, and in UV absorption spectroscopy [2]. However, UV generation in conventional silica-core fibers has proven to be extremely difficult because of factors such as high material electronic absorption, increased Rayleigh scattering, glass solarization (photo-darkening and optically-induced color centers), and large normal dispersion which limits the generated bandwidth from nonlinear frequency conversion processes [3]. These factors have stimulated much recent work on alternative approaches, primarily using gas-filled hollow-core photonic crystal fibers (PCFs) [4–10]. Although these efforts show great promise for deep UV generation down to 110 nm [8], compatibility with the ubiquitous silica platform remains a problem. There is therefore great interest in generating UV-light using modified UV-resistant glasses instead.

In this work, we report on the design and fabrication of a UV-resistant silica-based multimode photonic crystal fiber (PCF) for broadband UV generation below 400 nm exploiting intermodal nonlinear wave mixing. The fiber was fabricated using F110 UV-Grade glass from Heraeus, selected for its excellent transmission and low solarization in the UV-A range (260 nm-400 nm). Using a picosecond UV pump laser at 355 nm, we demonstrate a number of intermodal four-wave mixing (FWM) processes in the UV, which extend beyond the pump wavelength to 380 nm. The generated FWM signal and idler sidebands were carefully analyzed and imaged to determine their modal content. We determine the intermodal phase-matching conditions from the computed first and second-order dispersion parameters obtained from finite-element method (FEM) modelling, and obtain good agreement between experimental results and calculations.

#381628 https://doi.org/10.1364/OSAC.3.000031
Journal © 2020 Received 11 Nov 2019; accepted 4 Dec 2019; published 20 Dec 2019

OSA CONTINUUM

Significantly, we also observe a broadband Raman cascade from 355–391 nm when pumping the fiber directly in the microstructured cladding. This observation is interpreted using generalized nonlinear Schrödinger equation simulations of propagation in one bridge of the microstructure. We specifically show that the tight optical confinement allows for strong enhancement of the Raman effect with few intermodal FWM.

2. UV-Grade silica photonic crystal fiber

Figures 1(a-c) show, respectively, the UV-grade PCF design, a scanning electron microscope (SEM) image of the fabricated fiber cross-section, and a contrast-enhanced black and white image for improved visibility. The fiber was designed using a finite element method approach (COMSOL Software) to support multiple spatial modes with effective indices and dispersion profiles suitable to enable intermodal nonlinear FWM in the UV range. The fiber was then drawn at Photonics Bretagne in Lannion using the F110 UV-Grade silica glass from Heraeus. This glass has a high OH content up to 400 ppm and features good transmission in the UV-A range, from 260 nm to 400 nm. It also possesses a low solarization threshold around 300 nm and has a good transmission near the OH absorption band minima around 670, 800 and 1030 nm. The typical measured fiber attenuation provided by the manufacturer was 100 dB/km at 300 nm. This compares with an attenuation as large as 1000 dB/km at this wavelength for standard (low-OH) F300 silica glass used in conventional telecommunications fibers (SMF-28).

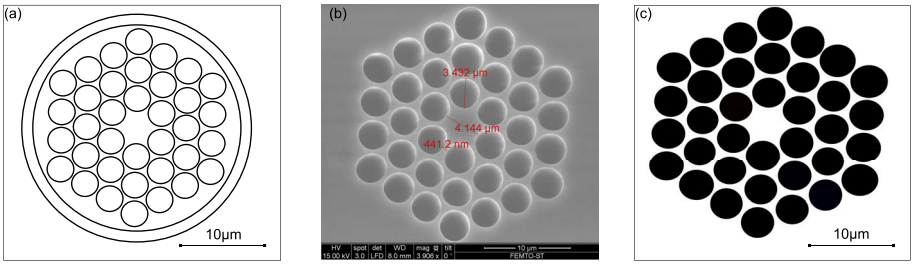

Fig. 1. (a) Design of the UV-grade solid-core microstructured fiber for nonlinear UV generation. (b) SEM image of the PCF manufactured by Photonics Bretagne using F110 UV-grade silica glass. (c) Contrast-enhanced black and white image from the SEM image (b).

The design in Fig. 1(a) was based on a triangular photonic lattice with core diameter of 4.26 µm, hole diameter d = 3.5 µm, pitch Γ = 3.88 µm, and air-fill fraction d/Γ = 0.902. The UV fiber theoretically supports the first eight LP modes at 355 nm including the fundamental mode LP01 and 7 higher-order modes from LP11 up to LP22. They are plotted in Fig. 2(a) in colormap.

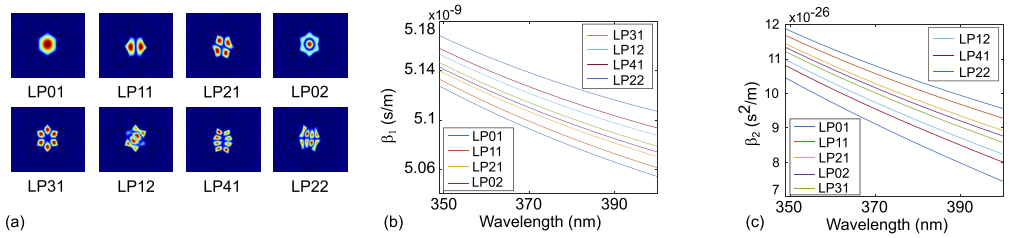

Fig. 2. (a) Computed mode profiles of the 8 main guided modes from LP01 to LP22. (b) Computed inverse group velocity β_1 for 8 spatial modes versus wavelength. (c) Computed group velocity dispersion parameter β_2 for 8 spatial modes versus wavelength.

OSA CONTINUUM

Figures 2(b) and (c) show their inverse group velocity β_1 and their second-order dispersion β_2 in the UV range, respectively. As can be seen, the second-order dispersion is highly normal for all modes at 355 nm (up to 12×10^{-26} s^2 m^{-1} for the LP22 mode) because it is mainly dominated by material dispersion. This strong normal dispersion in turn precludes standard soliton and dispersive wave dynamics usually involved in anomalous-dispersion supercontinuum generation [11–13], and it this limitation which motivates the design of a multimode fiber for intermodal FWM in the UV [14–20].

3. Experimental setup

Figure 3 shows the experimental setup used to investigate intermodal FWM and Raman scattering in the UV. As a pump source, we used a passively Q-switched Nd:YAG microchip laser (Teemphotonics PowerchipTM series) at 355 nm with a repetition rate of 1 kHz, a pulse duration (FWHM) of 350 ps, and an output mean power of 18 mW (peak power of ~50 kW). The laser power was further controlled by a variable density filter and the laser beam was injected into the fiber using a UV-coated aspherical injection lens controlled by a 3-axis translation stage. We used several different injection lenses with focal lengths f of 7.5 mm, 8 mm, 11 mm and 15.3 mm and numerical aperture (N.A.) of 0.3, 0.5, 0.3 and 0.16. This allowed a change of beam waist diameter from 3.4 µm, 3.6 µm, 4.9 µm to 6.8 µm, modifying the fiber injection conditions and modal properties, allowing us to explore the various intermodal FWM processes. A coupling efficiency of 20 % was obtained using aspherical lenses with focal length f = 7.5 mm, f = 8 mm and f = 11 mm, respectively, and of 28 % for an aspherical lens with f = 15.3 mm. These measurements of optimal injection efficiency were measured using a short fibre length of 75 cm, but we note that in the experiments described below to excite particular mode combinations, the coupling efficiency could be significantly less than the optimal. The fiber output beam was then imaged using a CCD camera after a diffraction grating to record the modal profiles of the generated parametric sidebands. Another part of the fiber output beam was deflected using a beam splitter and recorded with an UV-visible optical spectral analyzer (OSA) operating in the wavelength range 350-1200 nm (Yokogawa AQ6373).

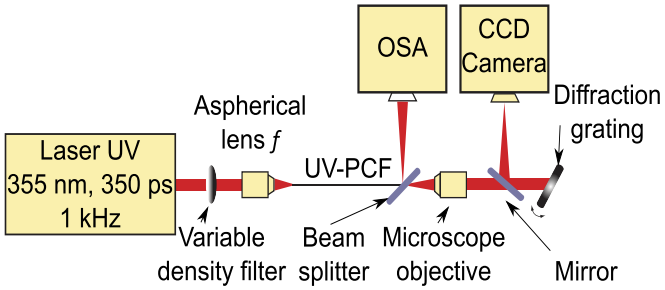

Fig. 3. Experimental setup for intermodal FWM and Raman generation in the UV-Grade fiber (UV-PCF).

4. Experimental results

4.1. Intermodal four-wave mixing

Initial experiments were carried out using a 4 m long fiber sample and a coupling lens with focal distance f = 7.5 mm. Figure 4 shows two typical optical spectra recorded out of the fiber for two different coupling powers and injection conditions. We can clearly see a series of intermodal FWM sidebands around the pump wavelength at 355 nm. In Fig. 4(a), a first Stokes sideband is generated at 359 nm with a weaker anti-Stokes idler at 350.5 nm. The modal content of the

OSA CONTINUUM

Stokes signal (shown in inset) reveals that it propagates in the LP31 mode. We can further notice the onset of the first-order stimulated Raman scattering sideband at 360.8 nm, which matches with the Raman frequency shift of fused silica (13.2 THz). Figure 4(b) shows, for different transverse coupling conditions, two new FWM processes involving a Stokes signal at 357.3 nm in the LP41 mode, and an anti-Stokes sideband below the pump at 352 nm, respectively. The second FWM involves a Stokes signal at 363.1 nm, still in the LP41, due to the coupling with the Raman Stokes at 360.8 nm. The image in the middle shown in Fig. 4(b) is a mix between the first Raman order at 360.8 nm and an intermodal FWM process at 361 nm [21].

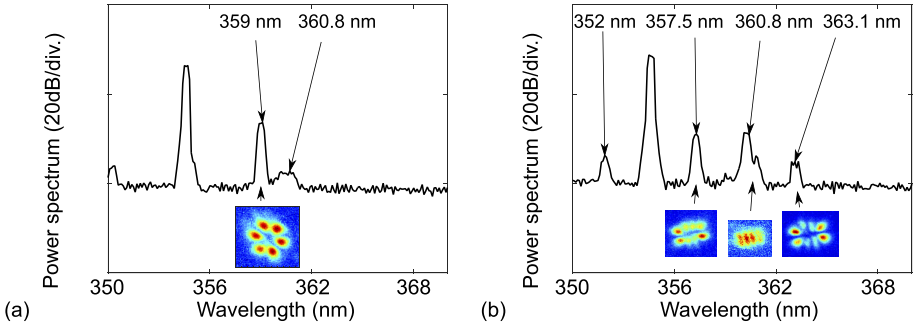

Fig. 4. Experimental output spectrum showing intermodal FWM sidebands for (a) an output power of 23 µW and (b) a fiber output power of 31 µW. The spectral resolution is 0.5 nm and the images in the inset show the modal content of each component of interest (f = 7.5 mm for both).

Next, we investigated in the same fiber sample the intermodal FWM with a focal length f = 8 mm. In Fig. 5, we show an output optical spectrum for a mean output power of 14 µW. It features different intermodal FWM and modal content. A first FWM signal appears at 358.1 nm in the LP11 mode, a second signal at 359.8 nm in the LP21, a third signal at 363.4 nm in the LP21, and a fourth signal is at 369 nm in the LP11 mode, respectively, while the pump beam at 354.8 nm has a complex mixed-mode profile.

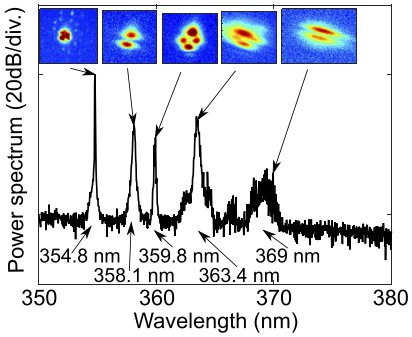

Fig. 5. Intermodal FWM spectrum for a fiber output power of 14 µW with the modal images of each FWM component of interest. The spectral resolution is 0.1 nm (f = 8 mm).

Other intermodal FWM sidebands have been observed using the coupling lens with f = 15.3 mm with a beam waist of 6.8 µm that over matches the core diameter of around 4.14 µm. One can first see in Fig. 6(a), in addition to the Raman line at 360.8 nm, a new FWM sideband generated at 364.9 nm in the LP02 mode. Figures 6(b-d) also shows more FWM spectra. We retrieve the FWM signals at 358.1 nm and 359.9 nm as in Fig. 5. However, new FWM Stokes signals are

OSA CONTINUUM

now generated at 358.9 nm and 363.7 nm with a modal image of LP11. The fifth peak at 366 nm with a large modal image of LP01 is similar to a Raman second order. In Fig. 6(c), there is only one FWM case with an anti-Stokes sideband at 351.1 nm in the LP01 and a Stokes sideband at 358.3 nm in the LP11 mode. In Fig. 6(d), we again show four FWM. A first signal wavelength is at 358.6 nm with a modal image of LP31, a second signal wavelength is at 359.2 nm, a third signal wavelength is at 361.1 nm without any clear modal image, a fourth signal wavelength is at 364.2 nm with a modal image of LP31. The first modal image is the one of the pump at 355 nm. The other peak at 360 nm with a modal image of LP21 corresponds to the first Raman line involved with the FWM process.

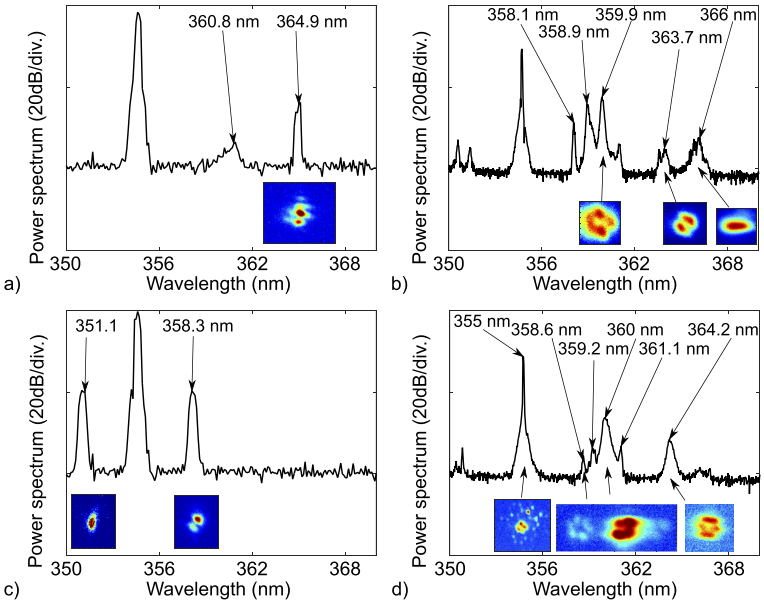

Fig. 6. Experimental results of intermodal FWM spectra in the UV-grade photonic crystal fiber pumped at 355 nm with the aspherical lens of f = 15.3 mm and for different fiber output power and fiber length (a) L = 1 m, P_{out} = 187 µW, (b) L = 4 m, P_{out} = 21 µW, (c) L = 1 m, P_{out} = 145 µW, (d) L = 4 m, P_{out} = 23.5 µW.

Finally, using the coupling lens with f = 11 mm with a beam waist of 4.9 µm we observed the broadened intermodal FWM spectrum generated with a pump at 355 nm (see Fig. 7). Fig. 7 shows three strong intermodal FWM bands at 359.5 nm in LP21, at 363.6 nm in LP02 and at 364.9 nm in LP02, respectively. It also shows the broadened peak generated via intermodal FWM at 379.7 nm in the LP22 mode. These results have been further compared to the theoretical calculations of intermodal phase-matching conditions (see Table 1 in the next section).

4.2. *Intermodal FWM theory*

Here we briefly review the basic theory of degenerate intermodal FWM and the related phase matching conditions [22–28]. First, we consider energy conservation,

$$\frac{2}{\lambda_p} = \frac{1}{\lambda_i} + \frac{1}{\lambda_s}, \tag{1}$$

OSA CONTINUUM

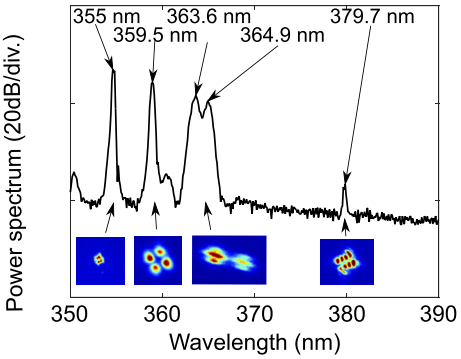

Fig. 7. Intermodal FWM spectrum for a fiber output power of 34 μW, with a resolution of 0.5 nm and with the modal images of each component of interest (f = 11 mm).

Table 1. Comparison between theory and experiment for a number of intermodal FWM processes. The experimental values listed correspond to results shown in different figures as follows: Wavelengths shown in black correspond to the results in Fig. 6(a) or (b) or (c) or (d). Wavelengths shown in Blue correspond to the results in Fig. 5; Wavelengths in Green correspond to the results in Fig. 9(b); Wavelengths in Red correspond to the results in Fig. 7; Wavelengths in Purple correspond to the results in Fig. 4(a) or (b). Those idler wavelengths marked (*) have been calculated from the experimental signal wavelengths.

	Theory		Experiment	
modes [LP_{xx}]	Idler	Signal	Idler	Signal
LP_{01}/LP_{11}	351.6 nm	358.5 nm	351.1 nm	358.3 nm
			351.3 nm	358.1 nm
			351.3 nm*	**358.1 nm**
			351.3 nm*	358.1 nm
LP_{11}/LP_{21}	350.5 nm	359.7 nm	350.3 nm*	359.8 nm
			350.2 nm*	**359.9 nm**
			350.6 nm*	359.5 nm
LP_{21}/LP_{31}	351.4 nm	358.7 nm	351.5 nm*	358.6 nm
			351 nm*	359 nm
LP_{11}/LP_{31}	346.9 nm	363.5 nm	346.2 nm*	364.2 nm
LP_{11}/LP_{02}	349.1 nm	361.1 nm	349.1 nm*	361.1 nm*
LP_{01}/LP_{02}	345.8 nm	364.7 nm	345.6 nm*	364.9 nm
LP_{01}/LP_{21}	347.1 nm	363.3 nm	346.9 nm*	363.4 nm
LP_{31}/LP_{41}	347.6 nm	362.7 nm	**347.3 nm***	**363.1 nm**
LP_{12}/LP_{41}	352 nm	358 nm	**352 nm**	**357.5 nm**
LP_{31}/LP_{22}	341.1 nm	370.1 nm	342 nm*	369 nm
			340.7 nm*	370.5 nm
LP_{11}/LP_{22}	333.5 nm	379.4 nm	333.3 nm*	379.7 nm

with λ the wavelength in nm, p, i and s denote the pump, idler and signal, respectively. Similarly, momentum conservation yields a phase-matching condition expressed as:

$$\Delta\beta = (\beta_1^{k(p)} - \beta_1^{j(p)})\Omega + (\beta_2^{k(p)} + \beta_2^{j(p)})\frac{\Omega^2}{2} = 0, \tag{2}$$

OSA CONTINUUM

with $\Omega = \omega_p - \omega_s \geq 0$, ω the angular frequency, β_1 is the reciprocal group velocity and β_2 the group-velocity dispersion (GVD) coefficient. The superscripts k and j are mode indices and (p) indicates that all parameters are calculated at the pump wavelength. Curves of β_1 and β_2 are plotted in Fig. 2(b) and Fig. 2(c) respectively for all spatial modes. Both β_1 and β_2 are obtained from the propagation constant through a Taylor expansion around the pump angular frequency (ω_p). Then, one finds the idler and signal angular frequencies of the involved intermodal FWM process as:

$$\omega_i^k = \frac{2(\beta_1^{j(p)} - \beta_1^{k(p)})}{(\beta_2^{k(p)} + \beta_2^{j(p)})} + \omega_p, \quad \omega_s^j = \omega_p - \frac{2(\beta_1^{j(p)} - \beta_1^{k(p)})}{(\beta_2^{k(p)} + \beta_2^{j(p)})}, \tag{3}$$

where k and j are again the different mode indices. Equation 3 is used in the theoretical intermodal FWM calculations from the computed data such as the inverse group velocity and the group velocity dispersion coefficients plotted in Fig. 2.

Table 1 summarizes the theoretical FWM signal and idler wavelengths for different modal combinations and compares them with results obtained from experiment. The agreement between theory and experiments is particularly good for all FWM signal sidebands, confirming the intermodal FWM processes occurring in the UV-grade multimode PCF. Note however that most of the calculated idler sidebands are absent in the experimental spectra shown in Figs. (4–7) due to the wavelength limitation of our spectrometer.

4.3. Cascaded Raman scattering

We investigated the stimulated Raman scattering (SRS) response of the fiber using an aspherical lens with f = 8 mm, with a beam waist diameter of 3.6 µm and a N.A. of 0.5. Figure 8 shows two different coupling conditions that allow for the generation of a Raman cascade until the sixth-order. The fiber output image shown in Fig. 8(a) shows, surprisingly, a coupling of the pump in several bridges of the fiber with no propagation in the core. In Fig. 8(b) an example is shown where coupling occurs only over a few bridges. The bridges, which have a diameter around 1.6 µm, allow a tight confinement of the light. Despite the strong attenuation of this 4 m long fibre sample, a cascaded Raman response of six orders is generated through cladding mediated modal coupling.

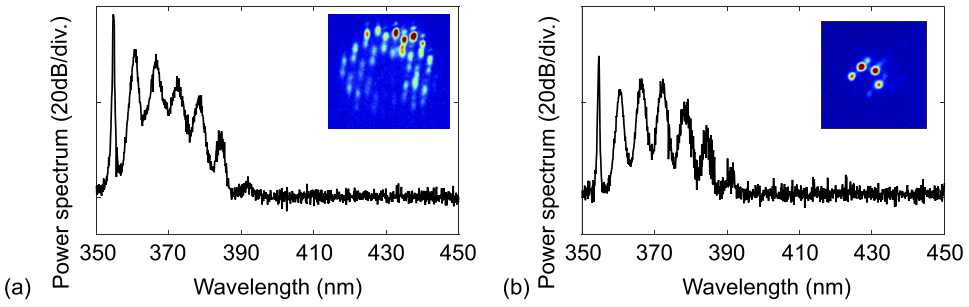

Fig. 8. (a) Experimental output spectrum for a fiber length of 4 m showing wideband cascaded Raman scattering from 355 nm to 391 nm. The fiber output image shows pump coupling in almost all the bridges. (b) Experimental output spectrum for a fiber length 4 m showing similar results but with pump coupling in only a few bridges (f = 8 mm for both).

Then the aspherical lens with f = 15.3 mm and N.A. = 0.15 was used in order to broaden the Raman cascade since the coupling efficiency with this lens is better than with the two other aspherical lenses. However, the experiments revealed a decreasing Raman cascade, which is mixed with intermodal FWM processes to generate a continuum (see Fig. 9).

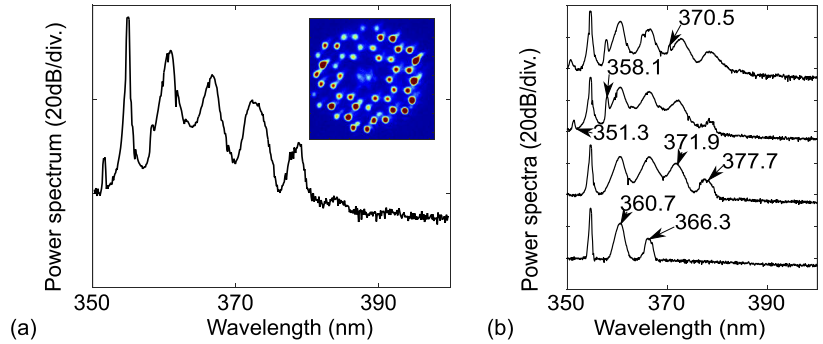

Fig. 9. (a) Experimental output spectrum for a 4 m long fiber showing wideband cascaded Raman scattering from 355 nm to 385 nm. The fiber output image shows where the pump is coupled in the fiber, here in all bridges and the core. (b) Experimental output spectra for a fiber length 4 m showing wideband cascaded Raman scattering from 355 nm to 377.7 nm and intermodal FWM effects at 358.1 nm and 370.5 nm. Output power level varies from 0.1 to 0.2 mW from bottom to top (f = 15.3 mm for both).

Figure 9(a) shows the fiber output spectrum with a cascaded Raman until the fourth order mixed with an intermodal FWM with an idler wavelength at 351.3 nm (see Figs. 9(a) and (b)) and a signal wavelength at 358.1 nm (not visible in Fig. 9(a) but visible in Fig. 9(b)). Perhaps the most surprising result is shown in the inset of Fig. 9(a) where light is seen to couple both into the whole photonic cladding as well as into the solid core.

Figure 9(b) shows the spectral evolution as a function of the fiber output power for the generation of the Raman cascade mixed with two FWM processes. At low power only the Raman cascade is generated. Then at high power one can see two FWM peaks, one with the signal wavelength at 358.1 nm and the idler wavelength at 351.3 nm and a second one with the signal wavelength at 370.5 nm. These combined effects generate a continuum from 350 nm to 377.7 nm. We performed additional FEM-based numerical simulations that confirm that the light can be indeed guided in the silica bridges (cladding modes) [5,29,30] in the UV-Grade PCF. Typical computed mode profiles are shown in Figs. 10(a-c) where we plotted three cases with their effective indices and losses, respectively.

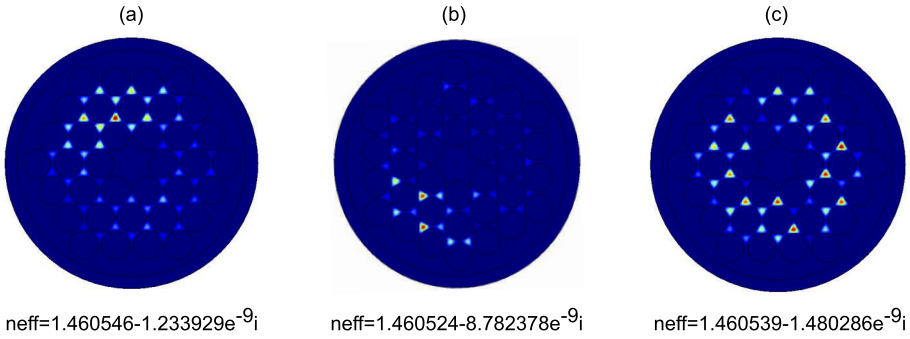

Fig. 10. Typical computed cladding mode profiles with (a) an effective index (n_{eff}) of 1.460546 with 0.1897 dB/m losses, (b) n_{eff} = 1.460524 and 1.3501 dB/m losses. (c) n_{eff} = 1.460539 with 0.2276 dB/m losses.

Figures 10(a) and (b) show the first two computed cladding modes with their effective indices that match with the modal images from Fig. 8(a) and (b), respectively. The mode losses are

OSA CONTINUUM

0.1897 dB/m and 1.3501 dB/m, respectively. Figure 10(c) shows the computed cladding mode involved in the mixing process between cascaded Raman and intermodal FWM seen in the experimental modal image in Fig. 9(a). The discrete cascaded Raman of six orders from 350 nm to 391 nm is generated through cladding modal coupling in a few bridges (see Fig. 8(b)). When the number of bridges involved in the cladding mode increases, the Raman cascade of six orders from 350 nm to 391 nm evolves towards a continuum, as shown in Fig. 8(a). Then the cladding modes are mixed with core modes. This is shown in Fig. 9(b) where we can see both cascaded Raman scattering and intermodal FWM from 350 nm to 380 nm. To interpret the cascaded Raman spectra shown in Fig. 8, we simulated the nonlinear pulse propagation and Raman cascade in one silica bridge of the microstructured cladding, using the computed first and second-order dispersion parameters for the fundamental mode (see Figs. 11(a) and (b)) from a finite-element method (FEM) computation. The generalized nonlinear Schrödinger equation (GNLSE) [31,32] was used to perform this simulation:

$$\frac{\partial A}{\partial z}+\frac{\alpha}{2}A-\sum_{k\geqslant 2}\frac{i^{k+1}}{k!}\beta_k\frac{\partial^k A}{\partial T^k}=i\gamma\left(1+i\tau_{shock}\frac{\partial}{\partial T}\right)\times\left(A(z,T)\int_{-\infty}^{+\infty}R(T')|A(z,T-T')|^2\mathrm{d}T'\right),\quad(4)$$

with the nonlinear parameter $\gamma(\omega_0)=[n_2(\omega_0)\,\omega_0]/(cA_{eff})=0.8474\,\mathrm{m}^{-1}\cdot\mathrm{W}^{-1}$ and the effective mode area $A_{eff}=6.6838\times10^{-13}\,\mathrm{m}^2$ for the fundamental mode at 355 nm. The normalized pulse amplitude $|A|^2$ represents the optical power in Watt. The second term in the left-hand side accounts for a linear loss with loss coefficient α. The dispersion data such as β_k come from COMSOL. On the right-hand side, $\tau_{shock}=1/\omega_0$ with $\lambda_0=(2\pi c)/\omega_0$ and c the speed of light. The term $R(T)=(1-f_R)\delta(t)+f_R h_R(t)$ is the response function of the Raman contribution including both a delayed and an instantaneous electronic Raman contribution. Here the silica glass is doped with high content of OH^- but its characteristics such as f_R and $h_R(t)$ are very close to the standard silica glass ($f_R=0.18$) [31–34]. The input pulse shape was considered as Gaussian. Experimentally the estimated peak power for the Raman cascade in the silica bridges is around 300 W. For a peak power $P_0=100$ W a pulse width of 300 ps and a fiber length of 4 m and 1 dB/m loss, the numerical result is shown in Fig. 12.

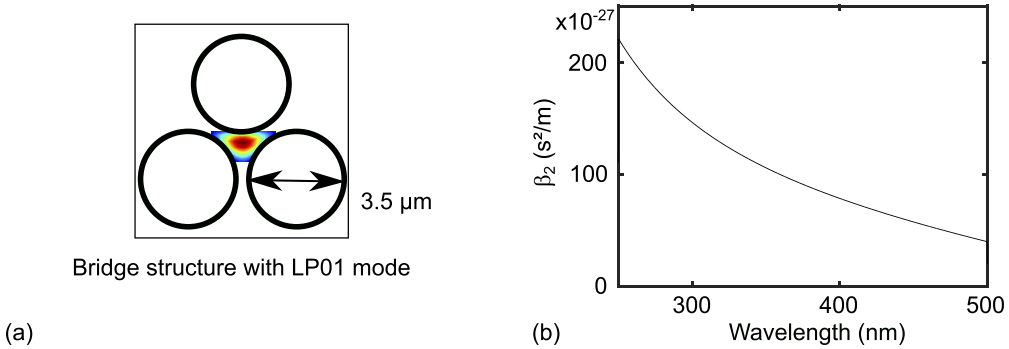

Fig. 11. (a) To calculate the dispersion properties of the PCF bridges, we performed FEM modelling of the structure as shown with each large air hole having diameter of 3.5 µm. The figure shows the computed fundamental mode in the bridge region between the air holes. (b) Computed group velocity dispersion parameter β_2 for the fundamental mode versus wavelength.

The colormap in Fig. 12 shows the evolution of the continuum generation versus distance in the silica bridge function of the length of the fiber (4 m in total). We see a typical Raman cascade generation over the propagation in one bridge until the sixth order. The result of the simulation in Fig. 12 supports well the experimental spectra in Fig. 8 as a Raman cascade is generated through

OSA CONTINUUM

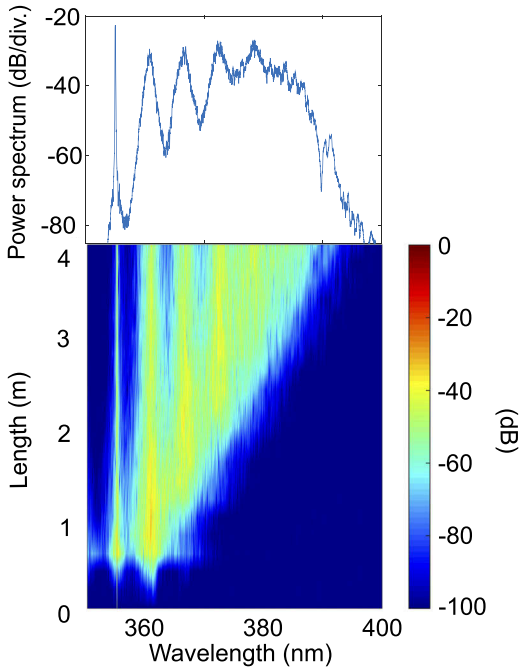

Fig. 12. Simulation with a peak power of 100 W and a loss of 1 dB/m with under a colormap of the simulation of the continuum generation over 4 m of the fiber length.

the bridge in the simulation and the spectral broadening is also reached. However, as it is a simulation in only one bridge, we cannot go further in the interpretation of losses, peak power or number of bridges involved in the experimental results.

5. Conclusion

We have designed and manufactured a new photonic crystal fiber made of UV-grade silica glass for broadband light generation in the UV range. The fiber has been drawn from F110 UV-Grade silica glass for its low loss and solarization in the UV-A band. We have observed intermodal FWM and cascaded Raman scattering in the UV-Grade silica multimode PCF, which is enabled by the modal properties of the fiber core and the tight confinement in the fiber bridges, respectively. These results are highly promising in the search of new optical fibres, which feature both a high nonlinearity and UV-resistance thus opening the way toward supercontinuum generation in the strong normal dispersion regime, which does not rely on soliton dynamics and dispersive wave generation. However, further research is needed to improve the fabrication methods with this material to reduce absorption in the UV and to improve design parameters such as a smaller core size, which would lead to improved optical confinement.

Funding

European Union's H2020 Research and Innovation Programme (722380); Agence Nationale de la Recherche (ANR-17EURE-0002, ANR-15-IDEX-0003); Conseil régional de Bourgogne-Franche-Comté.

OSA CONTINUUM

Acknowledgments

The authors thank L Gauthier-Manuel, G. Soro, A. Mosset, F. Devaux, E. Dordor, M. Raschetti, J. Chretien and C. Billet for technical support.

Disclosures

Disclosures: L.P., T.T., A.M., D.L. (Photonics Bretagne, E). All other authors (S.P., C.P., A.N.G., G.F., C.F.K., J.M.D., T.S.) declare no conflict of interest.

References

1. J. C. Travers, "Blue extension of optical fiber supercontinuum generation," J. Opt. **12**(11), 113001 (2010).
2. C. Poudel and C. F. Kaminski, "Supercontinuum radiation in fluorescence microscopy and biomedical imaging applications," J. Opt. Soc. Am. B **36**(2), A139–A153 (2019).
3. T. Sylvestre, A. R. Ragueh, M. W. Lee, B. Stiller, G. Fanjoux, B. Barviau, A. Mussot, and A. Kudlinski, "Black-light continuum generation in a silica-core photonic crystal fiber," Opt. Lett. **37**(2), 130–132 (2012).
4. F. Yu, M. Cann, A. Brunton, W. Wadsworth, and J. Knight, "Single-mode solarization-free hollow-core fiber for ultraviolet pulse delivery," Opt. Express **26**(8), 10879–10887 (2018).
5. X. Jiang, N. Y. Joly, M. A. Finger, F. Babic, G. K. Wong, J. C. Travers, and P. S. J. Russell, "Deep-ultraviolet to mid-infrared supercontinuum generated in solid-core ZBLAN photonic crystal fiber," Nat. Photonics **9**(2), 133–139 (2015).
6. F. Belli, A. Abdolvand, W. Chang, J. C. Travers, and P. S. J. Russell, "Vacuum-ultraviolet to infrared supercontinuum in hydrogen-filled photonic crystal fiber," Optica **2**(4), 292–300 (2015).
7. S. P. Stark, J. C. Travers, and P. S. J. Russell, "Extreme supercontinuum generation to the deep UV," Opt. Lett. **37**(5), 770–772 (2012).
8. J. C. Travers, F. T. Grigorova, C. Brahms, and F. Belli, "High-energy pulse self-compression and ultraviolet generation through soliton dynamics in hollow capillary fibers," Nat. Photonics **13**(8), 547–554 (2019).
9. Y. Y. Wang, F. Couny, P. S. Light, B. J. Mangan, and F. Benabid, "Compact and portable multiline UV and visible Raman lasers in hydrogen-filled HC-PCF," Opt. Lett. **35**(8), 1127–1129 (2010).
10. P. Hosseini, A. Ermolov, F. Tani, D. Novoa, and P. S. J. Russell, "UV soliton dynamics and Raman-enhanced supercontinuum generation in photonic crystal fiber," ACS Photonics **5**(6), 2426–2430 (2018).
11. Z. Zhu, L. G. Wright, D. N. Christodoulides, and F. W. Wise, "Observation of multimode solitons in few-mode fiber," Opt. Lett. **41**(20), 4819–4822 (2016).
12. W. H. Renninger and F. W. Wise, "Optical solitons in graded-index multimode fibres," Nat. Commun. **4**(1), 1719 (2013).
13. L. G. Wright, S. Wabnitz, D. N. Christodoulides, and F. W. Wise, "Ultrabroadband dispersive radiation by spatiotemporal oscillation of multimode waves," Phys. Rev. Lett. **115**(22), 223902 (2015).
14. H. Pourbeyram, G. P. Agrawal, and A. Mafi, "Stimulated Raman scattering cascade spanning the wavelength range of 523 to 1750 nm using a graded-index multimode optical fiber," Appl. Phys. Lett. **102**(20), 201107 (2013).
15. M. A. Eftekhar, Z. S. Eznaveh, J. E. Antonio-Lopez, J. C. A. Zacarias, A. Schulzgen, M. kolesik, F. W. Wise, R. A. Correa, and D. Christodoulides, "Broadband supercontinuum generation in tapered multimode graded-index optical fibers," in *Conference on Lasers and Electro-Optics*, (Optical Society of America, 2017), p. STh1K.7.
16. G. Lopez-Galmiche, Z. Sanjabi Eznaveh, M. A. Eftekhar, J. Antonio Lopez, L. G. Wright, F. Wise, D. Christodoulides, and R. Amezcua Correa, "Visible supercontinuum generation in a graded index multimode fiber pumped at 1064 nm," Opt. Lett. **41**(11), 2553–2556 (2016).
17. K. Krupa, C. Louot, V. Couderc, M. Fabert, R. Guenard, B. M. Shalaby, A. Tonello, D. Pagnoux, P. Leproux, A. Bendahmane, R. Dupiol, G. Millot, and S. Wabnitz, "Spatiotemporal characterization of supercontinuum extending from the visible to the mid-infrared in a multimode graded-index optical fiber," Opt. Lett. **41**(24), 5785–5788 (2016).
18. J. M. Stone and J. C. Knight, "Visibly white light generation in uniform photonic crystal fiber using a microchip laser," Opt. Express **16**(4), 2670–2675 (2008).
19. G. Prabhakar, P. Gregg, L. Rishoj, P. Kristensen, and S. Ramachandran, "Octave-wide supercontinuum generation of light-carrying orbital angular momentum," Opt. Express **27**(8), 11547–11556 (2019).
20. R. Dupiol, K. Krupa, A. Tonello, M. Fabert, D. Modotto, S. Wabnitz, G. Millot, and V. Couderc, "Kerr and Raman beam cleanup with supercontinuum generation in multimode fiber," in *Conference on Lasers and Electro-Optics*, (2018), paper SM3D.6
21. R. H. Stolen, "Modes in fiber optical waveguides with ring index profiles," Appl. Opt. **14**(7), 1533–1537 (1975).
22. G. P. Agrawal, *Nonlinear Fiber Optics*, 5th ed (Academic Press, 2013).
23. S. Perret, G. Fanjoux, L. Bigot, J. Fatome, G. Millot, J. M. Dudley, and T. Sylvestre, "Supercontinuum generation by intermodal four-wave mixing in a step-index few-mode fibre," APL Photonics **4**(2), 022905 (2019).
24. A. Mafi, "Pulse propagation in a short nonlinear graded-index multimode optical fiber," J. Lightwave Technol. **30**(17), 2803–2811 (2012).

OSA CONTINUUM

25. R. Dupiol, A. Bendahmane, K. Krupa, A. Tonello, M. Fabert, B. Kibler, T. Sylvestre, A. Barthelemy, V. Couderc, S. Wabnitz, and G. Millot, "Far-detuned cascaded intermodal four-wave mixing in a multimode fiber," Opt. Lett. **42**(7), 1293–1296 (2017).
26. E. Nazemosadat, H. Pourbeyram, and A. Mafi, "Phase matching for spontaneous frequency conversion via four-wave mixing in graded-index multimode optical fibers," J. Opt. Soc. Am. B **33**(2), 144–150 (2016).
27. M. A. Eftekhar, "Accelerated nonlinear interactions in graded-index multimode fibers," Nat. Commun. **10**(1), 1638 (2019).
28. L. G. Wright, D. Christodoulides, and F. W. Wise, "Controllable spatiotemporal nonlinear effects in multimode fibres," Nat. Photonics **9**(5), 306–310 (2015).
29. B. J. Eggleton, C. Kerbage, P. S. Westbrook, R. S. Windeler, and A. Hale, "Microstructured optical fiber devices," Opt. Express **9**(13), 698–713 (2001).
30. T. Baselt, B. Nelsen, A. F. Lasagni, and P. Hartmann, "Supercontinuum generation in the cladding modes of an endlessly single-mode fiber," Appl. Sci. **9**(20), 4428 (2019).
31. J. M. Dudley, G. Genty, and S. Coen, "Supercontinuum generation in photonic crystal fiber," Rev. Mod. Phys. **78**(4), 1135–1184 (2006).
32. J. M. Dudley and J. R. Taylor, *Supercontinuum Generation in Optical Fibers* (Cambridge University, 2010).
33. G. P. Agrawal, *Nonlinear Fibers Optics* (Academic Press Elsevier, 2007).
34. K. J. Blow and D. Wood, "Theoretical description of transient stimulated Raman scattering in optical fibers," IEEE J. Quantum Electron. **25**(12), 2665–2673 (1989).

194.57.91.238 {ts '2019-12-21 10:13:50'}

JPhys Photonics

PAPER • OPEN ACCESS

Chalcogenide-glass polarization-maintaining photonic crystal fiber for mid-infrared supercontinuum generation

To cite this article: A N Ghosh *et al* 2019 *J. Phys. Photonics* **1** 044003

View the article online for updates and enhancements.

This content was downloaded from IP address 37.165.134.228 on 02/10/2019 at 16:56

JPhys Photonics

OPEN ACCESS

RECEIVED
14 May 2019

REVISED
9 July 2019

ACCEPTED FOR PUBLICATION
14 August 2019

PUBLISHED
5 September 2019

Original content from this work may be used under the terms of the Creative Commons Attribution 3.0 licence.

Any further distribution of this work must maintain attribution to the author(s) and the title of the work, journal citation and DOI.

PAPER

Chalcogenide-glass polarization-maintaining photonic crystal fiber for mid-infrared supercontinuum generation

A N Ghosh[1], M Meneghetti[2], C R Petersen[3,4,6], O Bang[3,4,6], L Brilland[5], S Venck[5], J Troles[2], J M Dudley[1] and T Sylvestre[1]

[1] Institut FEMTO-ST, CNRS, Université Bourgogne Franche-Comté UMR 6174, Besançon, France
[2] Univ Rennes, CNRS, ISCR-UMR 6226, F-35000 Rennes, France
[3] DTU Fotonik, Dept. of Photonics Engineering, Technical University of Denmark, Lyngby, Denmark
[4] NORBLIS IVS, Virumgade 35D, 2830 Virum, Denmark
[5] SelenOptics, 263 Avenue du Gal Leclerc, Campus de Beaulieu, F-35700 Rennes, France
[6] NKT A/S, Blokken 84, 3460 Birkerød, Denmark

E-mail: amarnath.ghosh@femto-st.fr

Keywords: nonlinear optics, fiber optics, photonic crystal fibers, supercontinuum (SC) generation, mid-infrared (MIR) photonics, chalcogenide glass

Abstract

In this paper, we report the design and fabrication of a highly birefringent polarization-maintaining photonic crystal fiber made from chalcogenide glass, and its application to linearly-polarized supercontinuum generation in the mid-infrared region. The fiber was drawn using the casting method from $As_{38}Se_{62}$ glass which features a transmission window from 2 to 10 μm and a high nonlinear index of 1.13×10^{-17} $m^2\,W^{-1}$. It has a zero-dispersion wavelength (ZDW) at 4.56 μm for the fast axis and 4.68 μm for the slow axis and, at average ZDW, a large birefringence of 6.5×10^{-4} and consequently strong polarization maintaining properties are expected. Using this fiber, we experimentally demonstrate supercontinuum generation spanning from 3.1 to 6.02 μm and 3.33–5.78 μm using femtosecond pumping at 4 μm and 4.53 μm, respectively. We further investigate the supercontinuum bandwidth versus the input pump polarization angle and we show very good agreement with numerical simulations of the two-polarization model based on two coupled generalized nonlinear Schrödinger equations.

1. Introduction

Supercontinuum (SC) generation towards the mid-infrared (MIR) range is a very active field of research motivated by a wide range of applications including optical coherence tomography (OCT), material processing, optical sensing and absorption spectroscopy [1–17]. Although much progress in this field has been reported recently, state-of-the-art mid-IR SC systems are still in their infancy and considerable effort is required before mature broadband IR SC light sources beyond 5 μm are made available for industrial applications. Soft glasses, such as chalcogenide (As_2S_3, As_2Se_3, GeAsSe) [1–5], Tellurite (TeO_2), chalcohalides (GeTe, GeAsTeSe) [18, 19], heavy metal oxide ($PbO–Bi_2O_3–Ga_2O_3–SiO_2–CdO$) [9] and ZBLAN ($ZrF_4$ –BaF_2 –LaF_3 –AlF_3 –NaF) [20–22] have been widely used for drawing highly nonlinear infrared fibers, and experiments have shown efficient SC generation in the mid-IR up to 15 μm [1, 2], and up to 11 μm using all-fiber cascaded systems [23, 24]. Among the wide variety of infrared fibers, chalcogenide-glass-based optical fibers (composed of S, Se or Te) are excellent photonic platforms for nonlinear applications in the mid-IR due to their wider transmission window, tailorable dispersion in the mid-IR, and high optical nonlinearity up to hundred times greater than silica or ZBLAN glasses [1–5].

On the other hand, there is particular interest in combining the chalcogenide fiber platform with polarization-preserving properties as this will enable polarization-dependent applications in interferometric techniques, gas and pressure sensing, integrated-optic devices and also polarization-sensitive OCT [25–30]. Polarization-maintaining fibers also help in minimizing detrimental effects such as polarization noise and

© 2019 The Author(s). Published by IOP Publishing Ltd

instability [31]. There are several ways of introducing strong birefringence in the fiber for polarization maintaining propagation. For instance, birefringence can be obtained by applying mechanical stress in the cladding thus inducing anisotropy of the refractive index in the core region, which results in a modal birefringence up to 5×10^{-4} for the so-called PANDA fibers [32–34] and close to 60% higher birefringence in *bow-tie* fibers [35]. Highly birefringent fiber can also be fabricated using the powder-in-tube process where two rods of glass material are placed on the sides of the core [36]. Another way of obtaining high birefringence is by breaking the symmetry of the fiber structure. This was achieved in photonic crystal fibers (PCFs) where an asymmetric arrangement of air holes is designed with two different diameter air holes located in orthogonal position near the core of the fiber, thus providing higher effective index difference between the two orthogonal polarization modes [37–41]. In addition to the alteration of air hole diameter in the core region of PCFs, an asymmetric structure can also be obtained by either introducing mechanical stress [42] or modifying the shape of air holes [43]. It has been shown that the birefringence of silica based polarization-maintaining photonic crystal fibers (PM-PCFs) can reach high values up to 10^{-3} [38, 40, 41], which is one order of magnitude higher than that of conventional PANDA or bow-tie silica fibers [32–35].

Here we report the design and fabrication of a chalcogenide glass-based highly birefringent PM-PCF for SC generation in the mid-infrared. Numerical modelling is carried out in order to compute the birefringence and dispersion properties of the fiber. Two supercontinuum spectra spanning from 3.1 to 6.02 μm and 3.33–5.78 μm were experimentally demonstrated using a MHz femtosecond optical parametric oscillator with a central wavelength of 4 μm and 4.53 μm, respectively. The polarization dependence of the supercontinuum when pumping at 4.53 μm was also studied, and the experimental spectra were checked against numerical simulations of the two-polarization model based on two coupled generalized nonlinear Schrödinger equations. We furthermore report on the fabrication of long PM-PCF tapers directly on the drawing tower.

The remainder of this paper is organized as follows: in section 2 we outline the methods for chalcogenide glass fabrication, preform, PCF and taper drawing. In section 3 we report numerical simulations of the microstructured optical fibers and provide both the birefringence and the group-velocity dispersion (GVD). We show in particular how we can tailor both the birefringence and the dispersion by tapering the PM PCF down to a few μm core diameter. In section 4 we provide the transmission and attenuation spectra of the PM PCFs. In section 5 we describe the experimental setup for mid-IR SC generation and in section 6 we show experimental results of broadband SC spectra at different pump wavelength. The effect of pump polarization angle is finally investigated in section 7 both experimentally and numerically using two-coupled generalized nonlinear Schrödinger equations (GNLSE).

2. Preform and fiber fabrication

2.1. Glass fabrication

The fiber preform was made at the University of Rennes from $As_{38}Se_{62}$ chalcogenide glass. It was produced using the conventional melt-quenching method where a silica ampoule is filled with high purity As (99.999%), Se (99.999%) and oxygen and hydrogen getters like $TeCl_4$ and Mg [44–46]. The silica tube is then placed in a two-stage vacuum pump (combination of oil pump and turbo molecular pump) where it is pumped for approximately 3 h. Next, the silica ampoule is sealed and then placed inside a furnace for 12 h at 850 °C. The furnace has a rotational motion that enables uniform mixture of molten materials. During the heating process, $TeCl_4$ produces HCl and CCl_4 by collecting additional hydrogen and carbon, thus increasing the purity of the glass. After that, the ampoule is cooled down to 700 °C and quenched inside water for few seconds. The ampoule is then annealed at a temperature slightly below the glass transition temperature (T_g) around 165 °C. In the next step, the chalcogenide glass rod is retrieved by breaking and removing the ampoule and put in a two-chamber distillation tube in order to purify it through several distillation processes. In the first distillation step, distillation tube is placed inside a localized heater at 600 °C and the glass rod is distilled under dynamic vacuum to remove impurity gas like HCl and CCl_4 residue [44]. In the second step, static distillation is performed at 640 °C and carbon, silica and other refractory oxides are removed from the glass. At the end of second distillation step, the glass is again homogenously heated inside a furnace for 10 h at 850 °C, then the ampoule is cooled down to 500 °C, quenched and finally annealed below T_g to get the final glass. The attenuation spectrum of bulk $As_{38}Se_{62}$ glass measured with a Bruker Tensor 37 FTIR spectrometer is shown in figure 1. This glass offers light transmission from 2 to 9 μm range with a minimum attenuation of 0.40 dB m^{-1} at 7.42 μm and an absorption peak at 4.56 μm due to the presence of Se-H chemical bonds.

2.2. Preform fabrication

The PM microstructure preform containing 3-rings of air holes shown in figure 2(a) is prepared using the molding method [47]. In this method, the above-synthesized highly purified $As_{38}Se_{62}$ glass is heated and flowed

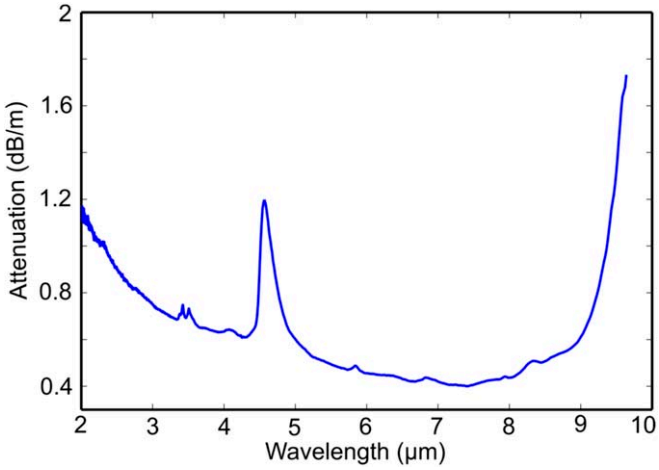

Figure 1. Attenuation spectrum of bulk $As_{38}Se_{62}$ glass.

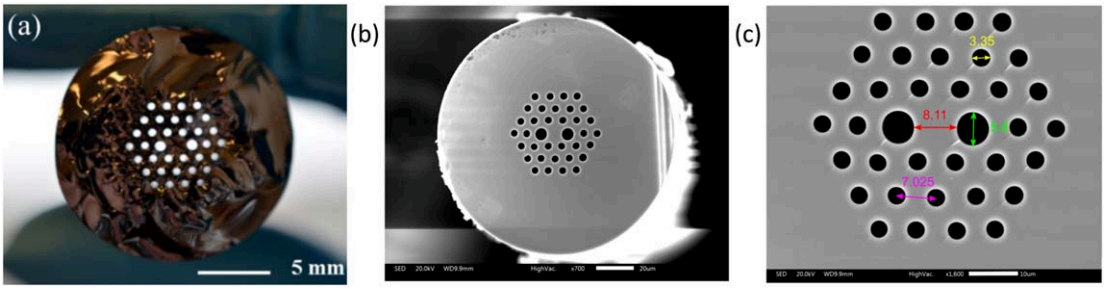

Figure 2. Cross-section images of $As_{38}Se_{62}$ preform and solid-core microstructured fiber. (a) Preform of $As_{38}Se_{62}$ glass. (b) SEM image of $As_{38}Se_{62}$ PM-PCF with an outer diameter of 125 μm. (c) Expanded view of the microstructure region showing core diameter ($d_{core} = 8.11$ μm), small air hole diameter ($d_{SA} = 3.35$ μm) and pitch ($\Lambda = 7.025$ μm).

into a silica mold, which has the negative shape of the final preform. The silica mold is made of silica-glass capillaries with a thickness of 30 μm. These capillaries are organized in a hexagonal periodical pattern, using slices of a silica microstructured preform to keep them in place. The hole diameter is 460 μm (d_{hole}) and the pitch is 1350 μm (Λ). In order to make a PM preform, the geometry of slices is modified by placing two larger holes with a diameter of 650 μm in diametrically-opposed positions in the first ring, while maintaining the d_h/Λ ratio. Both the $As_{38}Se_{62}$ glass rod and the silica mold are placed in a silica ampoule. The ampoule is then heated in a rocking furnace at 600 °C for one hour so the chalcogenide glass can flow down in to the mold having a glass viscosity about 10^{-4} Pa.s. After that, air quenching is performed on the full mold for four minutes before annealing it at 165 °C for one hour. The silica tube around the preform is then removed with a diamond tool. At the final step, the chalcogenide preform is obtained by removing the embedded silica capillaries with a hydrofluoric acid treatment. The final diameter of the $As_{38}Se_{62}$ glass preform is around 16 mm having a length of 80 mm.

2.3. Fiber fabrication

For the drawing process, the $As_{38}Se_{62}$ preform is installed in the drawing tower inside a silica glass enclosure, through which helium gas is flowed to remove any remaining moisture from inside it. An annular electrical furnace is placed around the preform in such a way that it helps to heat the lower portion of the preform. Both the preform chamber and the furnace chamber were filled with helium gas. The temperature of the furnace is increased until a drop of glass fall down from the preform due to the gravitational force (around 340 °C). Then the fiber accompanying the drop is attached to a rotating drum to continue the drawing while the preform is being fed gradually inside the annular furnace in the same time. During the drawing process, the desired air-hole diameter is obtained by controlling the helium gas pressure inside enclosure. The diameter of the fiber is further controlled by the pulling speed of the rotating drum and the feeding speed of the preform into the furnace.

Figures 2(b) and (c) show the scanning electron microscope (SEM) images of the PM-PCF drawn from the preform. As can be seen, it consists of 36 circular air holes in 3 rings with 2 larger air holes adjacent to the core

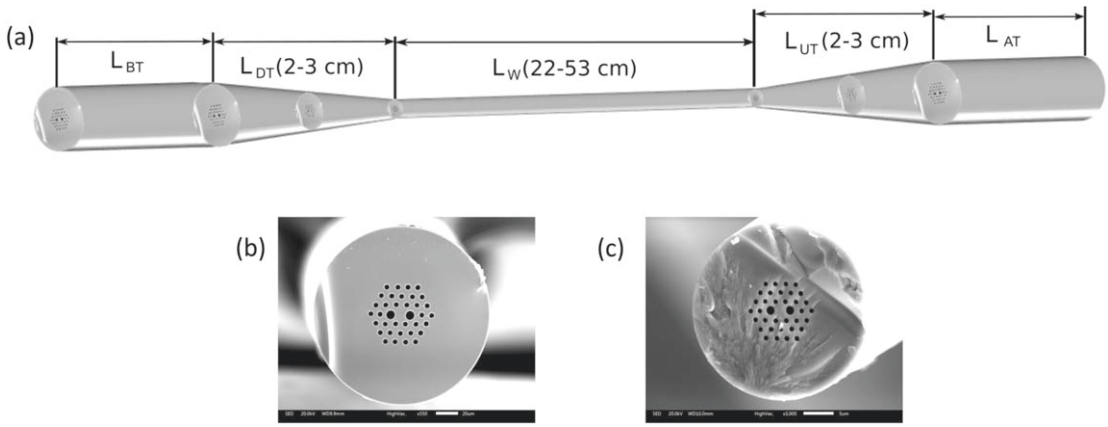

Figure 3. (a) Schematic of longitudinal sections of $As_{38}Se_{62}$ PM-PCF tapers: Length before taper (L_{BT}), length of down-taper section (L_{DT}), Length of uniform waist section (L_W), Length of up-taper section (L_{UT}), and length after taper (L_{AT}). (b) and (c) Cross-section images of normal section and taper-waist section of $As_{38}Se_{62}$ PM-PCF with respective outer diameter of 161.9 μm and 28.8 μm and respective core diameter of 9.97 μm and 1.77 μm.

Table 1. Structural parameters of a PM-PCF taper.

Initial fiber					Taper waist				
d_{core} (μm)	d_{out} (μm)	d_{SA} (μm)	Λ(μm)	d_{SA}/Λ	d_{core} (μm)	d_{out} (μm)	d_{SA} (nm)	Λ (μm)	d_{SA}/Λ
9.97	161.9	4.25	8.51	0.499	1.77	28.8	808.03	1.69	0.478

that provides strong birefringence and polarization maintaining guiding. The distance between the closest points of the two large air holes is 8.11 μm and the outer diameter of the PCF is 125 μm. The diameter of the large air holes (d_{LA}) and small air holes (d_{SA}) are 5.8 μm and 3.35 μm, respectively. The distance between two small air holes, also known as the pitch is 7.025 μm, which gives a d_{SA}/Λ ratio of 0.477, which makes the PCF with uniform holes endlessly single-moded in the mid-IR [48].

2.4. Taper fabrication

$As_{38}Se_{62}$ PM-PCF tapers were directly made on the drawing tower using the following method. One end of a previously drawn PM fiber (as described in section 2.3) with a length of 80 cm is fixed at the top of the drawing tower. In this case, the outer fibre diameter was 162 μm. Finally, the taper is obtained by drawing a second time the fiber.

Since the initial PM fiber has an outer diameter of 162 μm and core diameter of 10 μm, the output diameter of the waist should be 28.74 μm in order to have an approximate core diameter of 1.77 μm in the taper waist region. For this purpose, the pulling speed and the feeding speed are fixed at 0.05 m min^{-1} and 1.5 mm min^{-1}, respectively. The obtained PM-PCF tapers have a down-taper section length of 2–3 cm, waist section length of 22–53 cm, and up-taper section length of 2–3 cm. Figures 3(a) and (b) represent the SEM image of the normal section and tapered section of $As_{38}Se_{62}$ PM-PCF taper. The geometrical parameters of this taper are given in table 1, where d_{core}, d_{out}, d_{SA}, and Λ represent waist core diameter, outer fiber diameter, small air hole diameter and pitch, respectively. Proper maintenance of d_{SA}/Λ ratio during the taper fabrication provides closer values of 0.499 and 0.478 for the normal section and the taper section, respectively.

3. Computation of dispersion and birefringence

Dispersion and birefringence properties of the PM-PCF and the PM taper are computed from the cross-section images shown in figures 2(c) and 3(c). We calculated the effective refractive index of the fundamental mode using COMSOL software based on a full vector finite-element method. The PM-PCF fibers are assumed to be single-mode (HE_{11}) as the second-order and higher-order modes have much higher confinement loss (18 dB m^{-1} at 3 μm, 56 dB m^{-1} at 4 μm, and 176 dB m^{-1} at 5 μm) than HE_{11} mode over the wavelength range under investigation. The refractive index of the air holes is set to 1 and the refractive index of the glass was calculated using a standard Sellmeier equation with the following form [49]

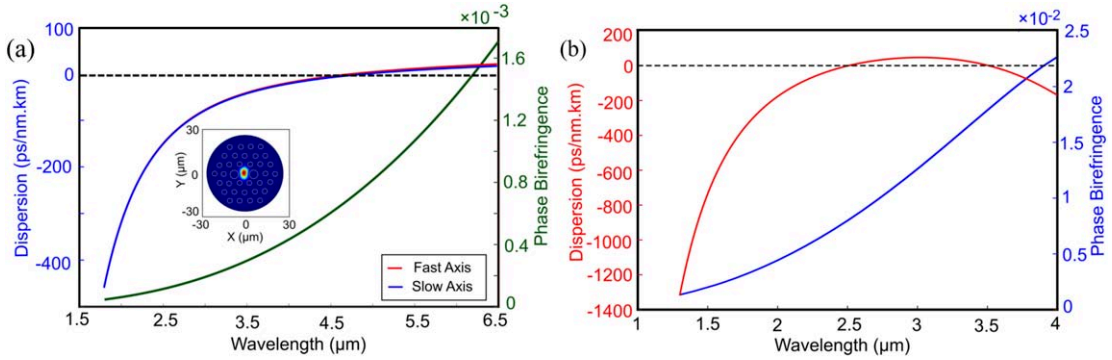

Figure 4. Dispersion and birefringence characteristics of the PM-PCF simulated for the fundamental mode from SEM image. (a) PM-PCF with core diameter of 8.11 μm. Blue and red curve: group velocity dispersion of PM-PCF sample for different polarization axis. Inset: optical power density of the fundamental mode for the fast axis at a wavelength of 2 μm inside the core of the fiber. Green curve: phase birefringence of PM-PCF. (b) PM-PCF taper with a waist core diameter 1.77 μm. Red curve: group velocity dispersion of taper-waist section. Blue curve: phase birefringence of the taper-waist section.

$$n^2(\lambda) = A_0 + \frac{A_1\lambda^2}{\lambda^2 - a_1^2} + \frac{A_2\lambda^2}{\lambda^2 - a_2^2}, \tag{1}$$

where, A_0, A_1, and A_2 are dimensionless coefficients and a_1 and a_2 are the material resonant wavelengths. For $As_{38}Se_{62}$ glass, the values of the coefficients used in the simulation are: $A_0 = 3.7464$, $A_1 = 3.9057$, $A_2 = 0.9466$, $a_1 = 0.4073$ μm, and $a_2 = 40.082$ μm [41]. The effective refractive index (n_{eff}) is then used to calculate the GVD, defined as $D = -(\lambda/c)(d^2n_{\text{eff}}/d\lambda^2)$ and the phase birefringence, defined as $B(\lambda) = (n_{\text{eff}}^y(\lambda) - n_{\text{eff}}^x(\lambda))$, where n_{eff}^x and n_{eff}^y are the effective refractive indices of x-polarized HE_{11} mode (slow axis) and of y-polarized HE_{11} mode (fast axis). The computed GVD and phase birefringence are plotted in figure 4(a) for the PM-PCF with a core diameter of 8.11 μm and in figure 4(b) for a PM-PCF taper with a waist diameter of 1.77 μm. The PM-PCF has a zero-dispersion wavelength (ZDW) at 4.56 μm for the fast axis and 4.68 μm for the slow axis and, at average ZDW, a large birefringence of 6.5×10^{-4} such that strong polarization maintaining properties are expected. This is in excellent agreement with the experimental measurement recently reported in [47]. By tapering the PM-PCF core from 8.11 μm to 1.77 μm, we are able to bring down the ZDW from 4.5 μm to 2.507 μm along with a second ZDW at 3.51 μm. The PM-PCF taper also gives higher phase birefringence of 7.97×10^{-3} and 1.79×10^{-2} at two respective ZDWs.

4. Optical transmission and attenuation

Optical attenuation of the drawn PM-PCF with a core diameter of 8.11 μm was measured with a Bruker Tensor 37 FTIR spectrometer equipped with a liquid nitrogen cooled mercury–cadmium–tellurite (MCT) detector having a sensitivity from 1.2 to 14 μm, as shown in figure 5(a). The attenuation of the fiber was precisely measured using the standard cut-back technique and guidance of cladding mode is eliminated by applying a layer of graphite on the surface of the fiber during the measurement. Figure 5(a) shows light transmission in the PM-PCF between 2 μm and 10 μm with a minimum attenuation of 0.25 dB m^{-1} at 6.64 μm. Two absorption peaks can be observed in the attenuation spectrum of the fiber including a peak at 4.5 μm due to the presence of Se-H bonds (as in the bulk sample, see figure 1) and another peak at 6.3 μm due to the presence of H_2O molecules.

The power transmission of a tapered PCF with taper waist core diameter of 1.77 μm and taper waist length of 22 cm was measured to be 13% at 1.55 μm using a 1 mW continuous wave (CW) laser and a Thorlabs power meter. Then, the transmission spectra of all four tapers were measured with the same FTIR spectrometer as previous, which is shown in figure 5(b). The tapers transmit light from 1.5 to 5.5 μm and there is no significant change in transmission window with taper length. As can be seen, the transmission bandwidth is significantly reduced compared to the untapered PM-PCF and there are three transmission dips clearly visible because of the presence of three new absorption bands at 2.9 μm due to O–H bonds, at 3.5 μm due to surface contamination by C–H Bonds of non-cyclic organic compounds, and at 4.25 due to CO_2 molecules. These are mainly due to the contamination of the taper waist, non-adiabatic taper transitions during taper drawing process, and high confinement loss for non-uniform and small taper waist. This unfortunately prevents the use of the PM tapers for mid-IR SC generation beyond 5.5 μm and we will therefore in the following sections focus on the straight PM-PCFs only.

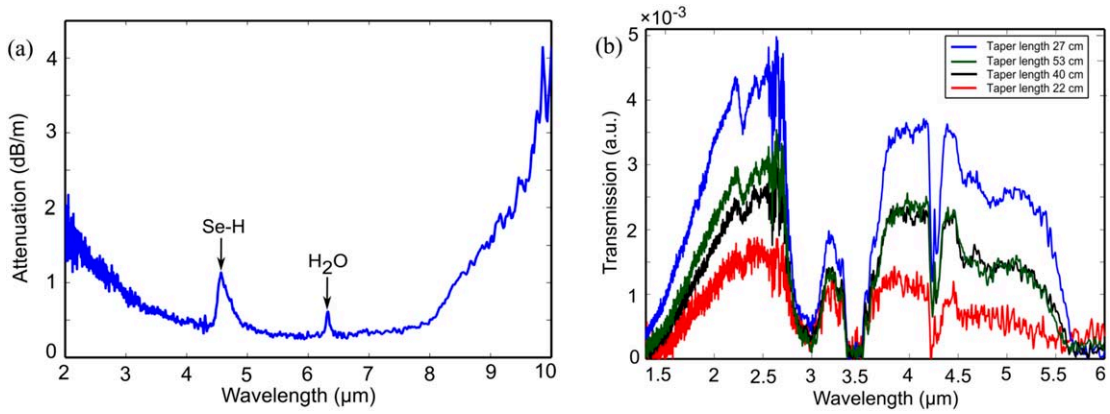

Figure 5. (a) Attenuation spectrum of $As_{38}Se_{62}$ PM-PCF with cut-back length of 3.35 m. (b) Transmission spectra of $As_{38}Se_{62}$ PM taper fibers with different taper waist length having a waist diameter 1.77 μm.

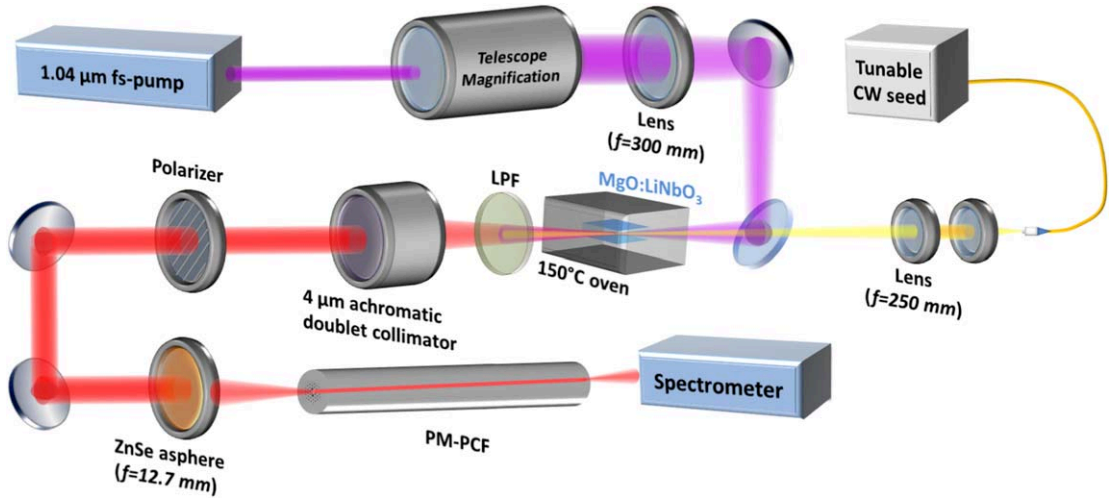

Figure 6. Scheme of the experimental setup for mid-IR pump laser and supercontinuum infrared light generation. LPF, long-pass filter; PM-PCF, polarization maintaining photonic crystal fiber.

5. Experimental setup for supercontinuum generation

Figure 6 outlines the experimental setup for mid-IR pumping of the chalcogenide-based PM-PCF and measuring the output SC infrared light [5]. The experiment was performed at the Technical University of Denmark. A 10 mm periodically-poled fan-out MgO:$LiNbO_3$ crystal (MgO:PPLN) was used to generate the mid-IR pump through a single-pass parametric generation process. The nonlinear crystal was pumped by a continuous-wave (CW) seed laser (tunable from 1350 to 1450 nm) along with a 1.04 μm mode-locked Yb: KYW solid-state laser (having a full width half maximum pulse duration of 250 fs at 21 MHz repetition rate) to stimulate quasi phase-matched parametric anti-Stokes generation. The phase-matching relation was achieved by selecting the appropriate poling period of the fan-out structure using a linear translation stage, and the crystal was kept in an oven at a constant temperature of 150 °C to avoid photorefraction. The combination of tunable seed and tunable poling period of the crystal provides a tunable MIR output between 3.7 μm and 4.53 μm whose spectrum corresponds to a 252 fs transform limited pulse train at 4 μm (see [50] for the first use of the laser). A reflective long pass filter (LPF) was used after the crystal system in order to eliminate any residual pump and other radiation below 3.5 μm. The mid-IR output beam was then collimated by an achromatic air-space lens doublet, which is optimized for a central wavelength of 4 μm and anti-reflection (AR) coated for the 3–5 μm range. The pump beam was then injected into the PM-PCF through an AR coated ZnSe aspheric lens with a focal length of 12 mm and the coupling power was controlled by rotating a wire grid polarizer relative to the linear polarization of the pump. The generated SC light was measured using an FTIR from 3 to 10 μm and a

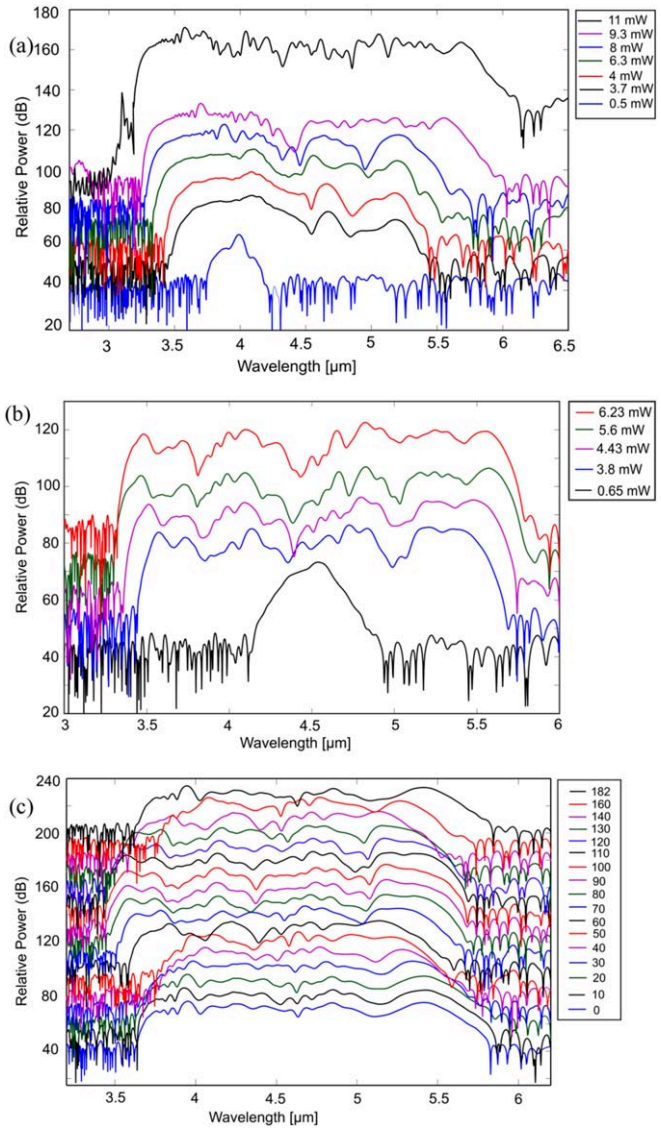

Figure 7. Supercontinuum spectra generated in a 25 cm long PM-PCF sample with 252 fs pulses as a function of mean output power. (a) SC spectra generated with a 4 μm pump. (b) SC spectra generated with a 4.53 μm pump. (c) Dependency of SC spectra with incident angle of polarization from 0° to 182° for pumping at 4.53 μm.

monochromator-based spectrometer from 1 to 5 μm. The output power was measured with a thermal power meter.

6. Results and discussions

Figure 7(a) shows the generated SC spectra with increasing pump power in a 25 cm long PM-PCF with the pump tuned to 4 μm central wavelength. For a pump power of 135 mW, we obtained a SC spectrum spanning from 3.1 to 6.02 μm (at the −30 dB level) with an average output power of 11 mW. Then we tuned the pump wavelength close to the ZDW at 4.53 μm and the obtained SC spectra with different output power are shown in figure 7(b). An available maximum power of 98 mW provided a spectral broadening from 3.33 to 5.78 μm (at the −30 dB level) with an average output power of 6.23 mW. Therefore, the spectrum at 4.53 μm has a lower bandwidth than the spectrum at 4 μm due to available lower input power from the laser in spite of pumping closer to the ZDW. Furthermore, with a constant input power of 62 mW at 4.53 μm, we were able to measure the polarization dependency of the SC spectra by rotating the input fiber, which amounts to turning the input pump polarization with respect to the principal axes of the PM fiber. Using the measured output power, Fresnel loss from both front and end surface of the fiber, and propagation loss inside the fiber, we estimated the coupling efficiency to be 18% and 13.62 %, the coupling peak power as 4.62 kW and 2.54 kW at 4 μm pumping and 4.53 μm pumping, respectively. Figure 7(c) shows the recorded SC spectra when tuning the fiber angle from 0°

till 182° with 10° steps and with constant output power of 3.8 mW. As it can be seen, the input pump polarization strongly affects the SC generation. The SC bandwidth reduces from 2140 nm down to 1620 nm (at the −20 dB level) with an angular periodicity of about 90°.

7. Numerical simulations: the vector model

Detailed modelling of the polarization and modal properties of mid-IR SC generation in multi-mode step-index non-PM chalcogenide fibers was studied in [51], which demonstrated how important it is to control the polarization and the number of modes participating in the SC generation process. Here the uniform PM-PCF is single-moded, which means that we can restrict ourselves to consider only the fundamental mode with both polarizations. Nonlinear pulse propagation and SC generation in the highly-birefringent PM-PCF was therefore modelled using a two-polarization code based on two coupled generalized nonlinear Schrödinger equations (CGNLSE) [52–55]. These equations can be written in following reduced form in a linearly polarized basis

$$\frac{\partial A_{x,y}}{\partial z} + \frac{\alpha}{2}A_{x,y} + \beta_{1x,y}\frac{\partial A_{x,y}}{\partial T} - \sum_{k\geqslant 2}\frac{i^{k+1}}{k!}\beta_k^{x,y}\frac{\partial^k A_{x,y}}{\partial T^k} = i\gamma\left(1 + i\tau_{shock}\frac{\partial}{\partial T}\right)\times$$
$$\left\{(1-f_R)\left(|A_{x,y}|^2 + \frac{2}{3}|A_{y,x}|^2\right) + f_R A_{x,y}(z,T)\int_{-\infty}^{T} h_R(T-T')\,|A_{x,y}(z,T-T')|^2 dT'\right\}, \quad (2)$$

where A_x and A_y are the slow and fast axis field amplitudes, α is the wavelength-dependent propagation loss taken from figure 5(a), $\beta_k^{x,y}$ is the kth Taylor expansion of the propagation constants for the two linearly-polarized field amplitudes. It accounts for the phase birefringence of the PM-PCF plotted in green in figure 4(a). The second-order dispersion $\beta_2^{x,y}(\omega)$ is also shown in figure 4(a) as the D parameter. We also included higher-order dispersion coefficients from figure 4(a). Nonlinear coefficient γ was calculated from effective mode area of PM-PCF and nonlinear index of the $As_{38}Se_{62}$ glass using $\gamma = \frac{2\pi n_2}{\lambda A_{eff}(\lambda)}$. This gives $\gamma = 358.6\ W^{-1}\ km^{-1}$ and $301\ W^{-1}\ km^{-1}$ at the two pumping wavelengths, 4 μm and 4.53 μm, respectively [56]. The time derivative term in RHS of equation (2) models the effects such as self-steepening and optical shock formation with $\tau_{\text{shock}} = \frac{1}{\omega_0}$. The bottom first term in the RHS represents the nonlinear response function which includes both instantaneous self and degenerate cross-phase modulation (DXPM) between the two cross-polarized fields with the factor 2/3 [54, 55]. f_R is the Raman fractional contribution to the Kerr effect and we find $f_R = 0.1$ using the parameter reported in [57] for chalcogenide glass. The Raman response delayed function $h_R(t)$ in the last term of equation (2) can be expressed in the time domain as follows:

$$h_R(t) = \frac{\tau_1^2 + \tau_2^2}{\tau_1^2\tau_2^2}\exp\left(\frac{-T}{\tau_2}\right)\sin\left(\frac{T}{\tau_1}\right), \quad (3)$$

where τ_1 and τ_2 are 23.14 fs and 157 fs, respectively, which was fitted for a Raman gain peak of 230 cm^{-1} (6.9 THz) for $As_{38}Se_{62}$ fiber whose Raman gain peak was measured in [58]. The same Raman function was used for both fiber axes because the perpendicular Raman gain is almost negligible [54]. For the PM-PCF sample with pump at 4 μm and 4.53 μm, we used a fiber length of 25 cm and pump pulse duration of 252 fs for both cases. The coupling peak power at the input of the fiber was considered to be 1.33 kW and 0.40 kW for the pump at 4 μm and 4.53 μm, respectively, in order to have the best fit with experimental results.

Figures 8(b) and (d) show the evolution of numerically computed SC spectra along fiber length for a pump wave polarized along one of the principal axis at 4 μm and 4.53 μm, respectively. The temporal counterparts are shown in figures 8(e) and (f). The comparisons between simulated and experimental SC spectra for respective pump wavelength of 4 μm and 4.53 μm are shown in figures 8(a) and (c). The simulated and experimental SC spectra are in qualitative agreement in terms of bandwidth, but in terms of structure of the spectrum, they are quite different. In figures 8(b) and (d), we plotted the SC dynamics along the propagation distance and we can clearly observe multiple soliton generation and ejection towards the infrared up to 6 μm due the Raman-self frequency shift. Simultaneously there are dispersive waves that are emitted from solitons in the short wavelength range down to 3 μm.

Figure 8(g) shows a series of computed SC spectra as a function of input polarization angle θ, from 0° to 180° with respect to the fast axis. This leads to SC bandwidth reduction from 2010 nm down to 1450 nm with an angular periodicity of around 90°, as shown in figure 8(h), as a blue curve. This can be explained by the fact that when tuning the polarization angle from one principal axis to the other, the degenerate cross-phase modulation between the A_x and A_y vector fields is lower than the self-phase modulation (SPM) itself by a factor 2/3, giving rise to less SC broadening when pumping off axis with a minimum at 45°. The agreement with experimental measurements (red curve) is quite satisfactory, except the small offset that is due to the different SC bandwidth shown in figure 8(c).

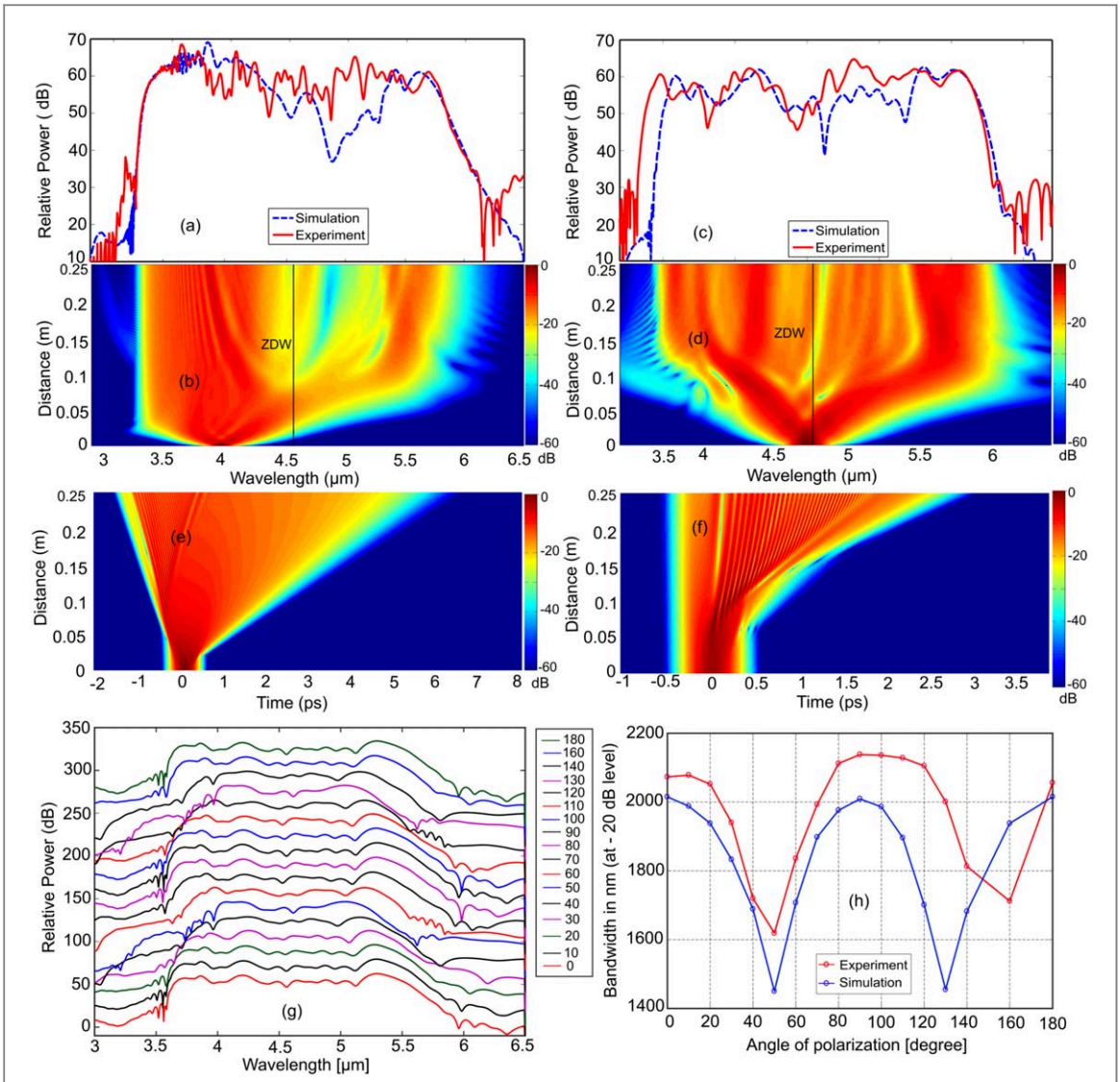

Figure 8. (a) and (c) Comparison between numerically and experimentally generated SC spectra in the PM-PCF for pumping at 4 μm (a) and 4.53 μm (c). (b) and (d) Numerically generated evolution of SC spectra along the fiber length at the respective pumping wavelength. The vertical black lines show the zero-dispersion wavelengths (ZDW). (e) and (f) Corresponding temporal distribution along the fiber length. (g) Polarization dependency of numerically generated SC spectra at 4.53 μm pumping when tuning the input polarization angle from 0° up to 180° from the fast axis. (h) Comparison of bandwidth (at −20 dB level) between experimental and simulated SC spectra at different polarization angle for 4.53 μm pumping.

8. Conclusion

In summary, polarization-preserving supercontinuum generation in the mid-infrared from 3.1 to 6.02 μm and from 3.33 to 5.78 μm have been demonstrated by pumping a highly-birefringent photonic crystal fiber made of chalcogenide glass with femtosecond pulses at 4 μm and 4.53 μm, respectively. It has been further shown that tuning the input polarization angle with respect to the fiber axes affects the supercontinuum bandwidth and this was checked against numerical simulations using vectorial two-coupled nonlinear Schrödinger equations. The fiber was drawn using the casting method from $As_{38}Se_{62}$ glass which features a transmission window from 2 to 10 μm and a high nonlinear index of 1.13×10^{-17} $m^2\,W^{-1}$. It has a large birefringence of 6.5×10^{-4} at 4.6 μm enabling strong polarization maintaining properties. Long tapered optical fibers have also been designed and fabricated from the same fiber with waist diameter down to a 1.77 μm and with ultra-high birefringence up to 10^{-2}. Finally, this work constitutes an important step towards stable and linearly-polarized supercontinuum generation for mid-IR applications.

Funding

European Union's Horizon 2020 Research and Innovation Programme under grant agreement n°722380 SUPUVIR; Agence Nationale de la Recherche (ANR) (ANR-15-IDEX-0003, ANR-17-EURE-0002), OB and CRP acknowledge support by the European Union's Horizon 2020 research and innovation program under grant agreement No. 732968 project FLAIR, and from Innovation Fund Denmark, project ShapeOCT (J. No. 4107–00011 A).

ORCID iDs

A N Ghosh https://orcid.org/0000-0002-5297-8321
C R Petersen https://orcid.org/0000-0002-2883-7908
T Sylvestre https://orcid.org/0000-0001-5849-1533

References

[1] Petersen C R *et al* 2014 Mid-infrared supercontinuum covering the 1.4–13.3 μm molecular fingerprint region using ultra-high NA chalcogenide step-index fibre *Nat. Photon.* **8** 830–4
[2] Cheng T, Nagasaka K, Tuan T H, Xue X, Matsumoto M, Tezuka H, Suzuki T and Ohishi Y 2016 Mid-infrared supercontinuum generation spanning 2.0–15.1 μm in a chalcogenide step-index fiber *Opt. Lett.* **41** 2117–20
[3] Lemière A *et al* 2019 Mid-Infrared supercontinuum generation from 2 to 14 μm in arsenic- and antimony-free chalcogenide glass fibers *J. Opt. Soc. Am.* B **36** A183–92
[4] Theberge F, Berube N, Poulain S, Cozic S, Chatigny S, Robichaud L-R, Pleau L-P, Bernier M and Vallee R 2018 Infrared supercontinuum generated in concatenated InF_3 and As_2Se_3 fibers *Opt. Express* **26** 13952–60
[5] Petersen C R, Engelsholm R D, Markos C, Brilland L, Caillaud C, Troles J and Bang O 2017 Increased mid-infrared supercontinuum bandwidth and average power by tapering large-mode-area chalcogenide photonic crystal fibers *Opt. Express* **25** 15336–47
[6] Corkum P B, Ho P P, Alfano R R and Manassah J T 1985 Generation of infrared supercontinuum covering 3-14 μm in dielectrics and semiconductors *Opt. Lett.* **10** 624–6
[7] Alfano R R 2016 *The Supercontinuum Laser Source: The Ultimate White Light* (New York: Springer)
[8] Belli F, Abdolvand A, Chang W, Travers J C and Russell P S J 2015 Vacuum-ultraviolet to infrared supercontinuum in hydrogen-filled photonic crystal fiber *Optica* **2** 292–300
[9] Ghosh A N, Klimczak M, Buczynski R, Dudley J M and Sylvestre T 2018 Supercontinuum generation in heavy-metal oxide glass based suspended-core photonic crystal fibers *J. Opt. Soc. Am.* B **35** 2311–6
[10] Hult J, Watt R S and Kaminski C F 2007 High bandwidth absorption spectroscopy with a dispersed supercontinuum source *Opt. Express* **15** 11385–95
[11] Amiot C, Aalto A, Ryczkowski P, Toivonen J and Genty G 2017 Cavity enhanced absorption spectroscopy in the mid-infrared using a supercontinuum source *Appl. Phys. Lett.* **111** 061103
[12] Israelsen N M, Petersen C R, Barh A, Jain D, Jensen M, Hannesschläger G, Lichtenberg P T, Pedersen C, Podoleanu A and Bang O 2019 Real-time high-resolution mid-infrared optical coherence tomography *Light: Science & Applications* **8** 11
[13] Zorin I, Su R, Prylepa A, Kilgus J, Brandstetter M and Heise B 2018 Mid-infrared Fourier-domain optical coherence tomography with a pyroelectric linear array *Opt. Express* **26** 33428–39
[14] Sych Y, Engelbrecht R, Schmauss B, Kozlov D, Seeger T and Leipertz A 2010 Broadband time-domain absorption spectroscopy with a ns-pulse supercontinuum source *Opt. Express* **18** 22762–71
[15] Petersen C R, Moselund P M, Huot L, Hooper L and Bang O 2018 Towards a table-top synchrotron based on supercontinuum generation *Infrared Phys. Technol.* **91** 182–6
[16] Petersen C R, Prtljaga N, Farries M, Ward J, Napier B, Lloyd G R, Nallala J, Stone N and Bang O 2018 Mid-infrared multispectral tissue imaging using a chalcogenide fiber supercontinuum source *Opt. Lett.* **43** 999–1002
[17] Seddon A B 2016 Biomedical applications in probing deep tissue using mid-infrared supercontinuum optical biopsy *Deep Imaging in Tissue and Biomedical Media* ed L Shi and R R Alfano (Singapore: Pan Stanford) pp 231–94
[18] Désévédavy F, Gadret G, Jules J-C, Kibler B and Smektala F 2017 Supercontinuum generation in tellurite optical fibers *Technological Advances in Tellurite Glasses, Springer Ser. Mater. Sci.* vol 254 (Berlin: Springer)
[19] Zhao Z, Wu B, Wang X, Pan Z, Liu Z, Zhang P, Shen X, Nie Q, Dai S and Wang R 2017 Mid-infrared supercontinuum covering 2.0–16 μm in a low-loss telluride single-mode fiber *Laser Photonics Rev.* **11** 1700005
[20] Xia C, Kumar M, Kulkarni O P, Islam M N, Terry F L, Freeman M J, Poulain M and Mazé G 2006 Mid-infrared supercontinuum generation to 4.5 μm in ZBLAN fluoride fibers by nanosecond diode pumping *Opt. Lett.* **31** 2553–5
[21] Michalska M, Hlubina P and Swiderski J 2017 Mid-infrared supercontinuum generation to ~4.7 μm in a ZBLAN fiber pumped by an optical parametric generator *IEEE Photon. J.* **9** 3200207
[22] Agger C, Petersen C, Dupont S, Steffensen H, Lyngsø J K, Thomsen C L, Thøgersen J, Keiding S R and Bang O 2012 Supercontinuum generation in ZBLAN fibers—detailed comparison between measurement and simulation *J. Opt. Soc. Am.* B **29** 635–45
[23] Hudson D D, Antipov S, Li L, Alamgir I, Hu T, Amraoui M E, Messaddeq Y, Rochette M, Jackson S D and Fuerbach A 2017 Toward all-fiber supercontinuum spanning the mid-infrared *Optica* **4** 1163–6
[24] Martinez R A *et al* 2018 Mid-infrared supercontinuum generation from 1.6 to >11 μm using concatenated step-index fluoride and chalcogenide fibers *Opt. Lett.* **43** 296–9
[25] Noda J, Okamoto K and Yokohama I 1987 Fiber devices using polarization-maintaining fibers *Fiber Integr. Opt.* **6** 3095–329
[26] Thévenaz L, Coulon V D and Von der Weid J-P 1987 Polarization-mode interferometry in birefringent single-mode fibers *Opt. Lett.* **12** 619–21
[27] Fu H Y, Tam H Y, Shao L-Y, Dong X, Wai P K A, Lu C and Khijwania S K 2008 Pressure sensor realized with polarization-maintaining photonic crystal fiber-based Sagnac interferometer *Appl. Opt.* **47** 2035–9

[28] Gotzinger E, Baumann B, Pircher M and Hitzenberger C K 2009 Polarization maintaining fiber based ultra-high resolution spectral domain polarization sensitive optical coherence tomography *Opt. Express* **17** 22704–17
[29] Wang H, Al-Qaisi M K and Akkin T 2010 Polarization-maintaining fiber based polarization-sensitive optical coherence tomography in spectral domain *Opt. Lett.* **35** 154–6
[30] Israelsen N M, Petersen C R, Barh A, Jain D, Jensen M, Hannesschläger G, Tidemand-Lichtenberg P, Pedersen C, Podoleanu A and Bang O 2019 Real-time high-resolution mid-infrared optical coherence tomography *Light: Science & Applications* **8** 11
[31] Gonzalo I B, Engelsholm R D, Sørensen M P and Bang O 2018 Polarization noise places severe constraints on coherence of all-normal dispersion femtosecond supercontinuum generation *Sci. Rep.* **8** 6579
[32] Hosaka T, Okamoto K, Miya T, Sasaki Y and Edahiro T 1981 Low-loss single polarization fibers with asymmetrical strain birefringence *Electron. Lett* **17** 530–1
[33] Shibata N, Sasaki Y, Okamoto K and Hosaka T 1983 Fabrication of polarization-maintaining and absorption-reducing fibers *J. Light. Technol.* **1** 38–43
[34] Tajima K and Sasaki Y 1989 Transmission loss of a 125 μm diameter PANDA fiber with circular stress-applying parts *J. Lightwave Technol.* **7** 674–9
[35] Birch R D, Payne D N and Varnham M P 1982 Fabrication of polarisation-maintaining fibres using gas-phase etching *Electron. Lett* **18** 1036–8
[36] Kudinova M, Humbert G, Auguste J-L and Delaizir G 2017 Multimaterial polarization maintaining optical fibers fabricated with the powder-in-tube technology *Opt. Mater. Express* **7** 3780–90
[37] Ortigosa-Blanch A, Knight J C, Wadsworth W J, Arriaga J, Mangan B J, Birks T A and Russell P S J 2000 Highly birefringent photonic crystal fibers *Opt. Lett.* **25** 1325–7
[38] Hansen T P, Broeng J, Libori S E B, Knudsen E, Bjarklev A, Jensen J R and Simonsen H 2001 Highly birefringent index-guiding photonic crystal fibers *IEEE Photonics Technol. Lett.* **13** 588–90
[39] Ju J, Jin W and Demokan M S 2003 Properties of a highly birefringent photonic crystal fiber *IEEE Photonics Technol. Lett.* **15** 1375–7
[40] Suzuki K, Kubota H, Kawanishi S, Tanaka M and Fujita M 2001 High-speed bi-directional polarization division multiplexed optical transmission in ultra low-loss (1.3 dB/km) polarization-maintaining photonic crystal fiber *Electron. Lett* **37** 1399–401
[41] Caillaud C *et al* 2016 Highly birefringent chalcogenide optical fiber for polarization-maintaining in the 3-8.5 μm mid-IR window *Opt. Express* **24** 7977–86
[42] Schreiber T *et al* 2005 Stress-induced single-polarization single-transverse mode photonic crystal fiber with low nonlinearity *Opt. Express* **13** 7621–30
[43] Chen D and Shen L 2007 Highly birefringent elliptical-hole photonic crystal fibers with double defect *J. Lightwave Technol.* **25** 2700–5
[44] Meneghetti M, Caillaud C, Chahal R, Galdo E, Brilland L, Adam J-L and Troles J 2019 Purification of Ge–As–Se ternary glasses for the development of high quality microstructured optical fibers *J. Non-Cryst. Solids* **503** 84–8
[45] Shiryaev V S, Churbanov M F, Snopatin G E and Chenard F 2015 Preparation of low-loss core-clad As-Se glass fibers *Opt. Mater.* **48** 222–5
[46] Jiang L *et al* 2017 Fabrication and characterization of chalcogenide polarization-maintaining fibers based on extrusion *Opt. Fiber Technol.* **39** 26–31
[47] Coulombier Q *et al* 2010 Casting method for producing low-loss chalcogenide microstructured optical fibers *Opt. Express* **18** 9107–12
[48] Koshiba M and Saitoh K 2004 Applicability of classical optical fiber theories to holey fibers *Opt. Lett.* **29** 1739–41
[49] Marcuse D 1982 *Light Transmission Optics* (New York: Wiley)
[50] Møller U *et al* 2015 Multi-milliwatt mid-infrared supercontinuum generation in a suspended core chalcogenide fiber *Opt. Express* **23** 3282–91
[51] Kubat I and Bang O 2016 Multimode supercontinuum generation in chalcogenide glass fibres *Opt. Express* **24** 2513–26
[52] Dudley J M, Genty G and Coen S 2006 Supercontinuum generation in photonic crystal fiber *Rev. Mod. Phys.* **78** 1135–84
[53] Dudley J and Taylor J (ed) *Supercontinuum Generation in Optical Fibers* (Cambridge: Cambridge University Press) 2010
[54] Agrawal G P 2007 *Nonlinear Fiber Optics* (New York: Academic)
[55] Zhu Z and Brown T G 2004 Polarization properties of supercontinuum spectra generated in birefringent photonic crystal fibers *J. Opt. Soc. Am.* B **21** 249–57
[56] Lenz G, Zimmermann J, Katsufuji T, Lines M E, Hwang H Y, Spalter S, Slusher R E, Cheong S-W, Sanghera J S and Aggarwal I D 2000 Large Kerr effect in bulk Se-based chalcogenide glasses *Opt. Lett.* **25** 254–6
[57] Slusher R E, Lenz G, Hodelin J, Sanghera J, Shaw L B and Aggarwal I D 2004 Large Raman gain and nonlinear phase shifts in high-purity As_2Se_3 chalcogenide fibers *J. Opt. Soc. Am.* B **21** 1146–55
[58] Hu J, Menyuk C R, Shaw L B, Sanghera J S and Aggarwal I D 2010 Maximizing the bandwidth of supercontinuum generation in As_2Se_3 chalcogenide fibers *Opt. Express* **18** 6722–39

Optics Letters

Nanoimprinting and tapering of chalcogenide photonic crystal fibers for cascaded supercontinuum generation

Christian R. Petersen,[1,6,*,†] Mikkel B. Lotz,[2,†] Getinet Woyessa,[1] Amar N. Ghosh,[3] Thibaut Sylvestre,[3] Laurent Brilland,[4] Johann Troles,[5] Mogens H. Jakobsen,[2] Rafael Taboryski,[2] and Ole Bang[1,6,7]

[1]DTU Fotonik, Technical University of Denmark, Kongens Lyngby DK–2800, Denmark
[2]DTU Nanolab, Technical University of Denmark, Kongens Lyngby DK–2800, Denmark
[3]Institut FEMTO–ST, CNRS, Université Bourgogne Franche–Comté UMR6174, Besançon, France
[4]SelenOptics, 263 Avenue du Gal Leclerc, Campus de Beaulieu, 35700 Rennes, France
[5]Glasses and Ceramics Group, ISCR UMR–CNRS 6226, University of Rennes 1, 35042 Rennes Cedex, France
[6]NORBLIS, Virumgade 35D, 2830 Virum, Denmark
[7]NKT Photonics A/S, Blokken 84, DK–3460 Birkerød, Denmark
*Corresponding author: chru@fotonik.dtu.dk

Received 26 August 2019; revised 9 October 2019; accepted 15 October 2019; posted 15 October 2019 (Doc. ID 376382); published 8 November 2019

Improved long-wavelength transmission and supercontinuum (SC) generation is demonstrated by antireflective (AR) nanoimprinting and tapering of chalcogenide photonic crystal fibers (PCFs). Using a SC source input spanning from 1 to 4.2 μm, the total transmission of a 15 μm core diameter PCF was improved from ∼53% to ∼74% by nanoimprinting of AR structures on both input and output facets of the fiber. Through a combined effect of reduced reflection and redshifting of the spectrum to 5 μm, the relative transmission of light >3.5 μm in the same fiber was increased by 60.2%. Further extension of the spectrum to 8 μm was achieved using tapered fibers. The spectral broadening dynamics and output power were investigated using different taper parameters and pulse repetition rates. © 2019 Optical Society of America

https://doi.org/10.1364/OL.44.005505

Supercontinuum (SC) light sources based on chalcogenide glass optical fibers are among the main candidates for enabling new and improved mid-infrared photonic applications within broadband imaging and spectroscopy [1–3]. Currently, the most promising method for generating SC reaching far into the mid-infrared fingerprint region is through so-called cascaded generation using a series of concatenated silica, fluoride, and chalcogenide fibers that gradually extend the spectrum from the near-infrared to the mid-infrared [4–7].

One critical point in particular is the coupling to and from the chalcogenide fiber. Due to the high refractive index of chalcogenide glasses, a significant part of the pump light is reflected at the end facets, which means that both the input and output power is substantially reduced. One way to mitigate this is by using antireflective (AR) thin-film coatings such as Al_2O_3 or diamond deposited on the fiber end facets [8]. However, deposition of thin films on fiber facets is an elaborate and time-consuming cleanroom process that requires careful sample preparation, and the resulting coating is typically narrowband, which is not ideal for cascaded generation with a broadband input source. Another way to achieve AR over a broad bandwidth is by direct thermal nanoimprinting [9–11]. Due to the low glass transition temperature (T_g) of chalcogenide glasses (∼160–280°C), the process can be performed using simple heating elements, and takes only a few minutes to complete.

Another critical aspect of coupling light to a chalcogenide fiber is avoiding damage when launching high peak power pulses. The simplest solution to allow for better power handling is to scale up the fiber core. However, when the core diameter is increased, the nonlinearity of the fiber is reduced, thus hindering further extension of the spectrum. In order to increase the nonlinearity without sacrificing the damage threshold, the fiber diameter can be gradually reduced along the propagation direction through thermal tapering, thus improving the mid-infrared generation efficiency [12,13].

In this work, we investigate these two thermal postprocessing techniques, nanoimprinting and tapering, in order to improve the output power and bandwidth of cascaded SC sources. We chose to work with single-material $Ge_{10}As_{22}Se_{68}$ photonic crystal fiber (PCF) in order to avoid issues with varying $T_g's$ and viscosities between the core and cladding in step-index fibers (SIF). The pump source for the experiments was a SC source based on a master oscillator power amplifier (MOPA) configuration with a variable pulse repetition rate and 1 ns pulse envelope [14]. The MOPA was used to pump a 7 μm core

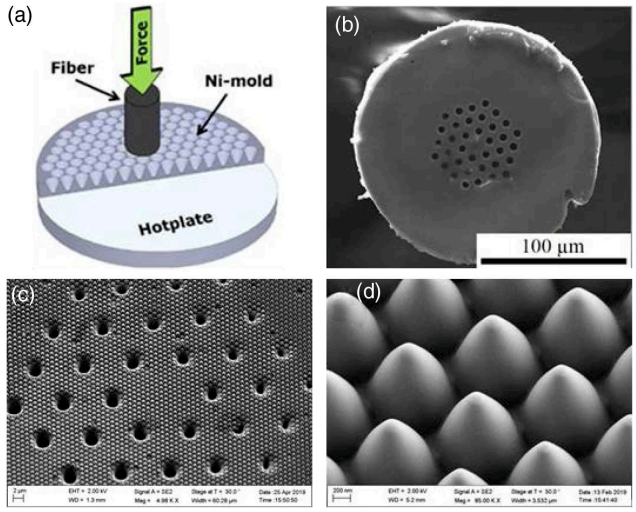

Fig. 1. (a) Principle of fiber nanoimprinting using a heated Ni mold. (b) SEM image of the PCF prior to imprinting. (c) SEM image of the imprinted core and air-clad region. (d) High-magnification SEM of the imprinted structures in the core.

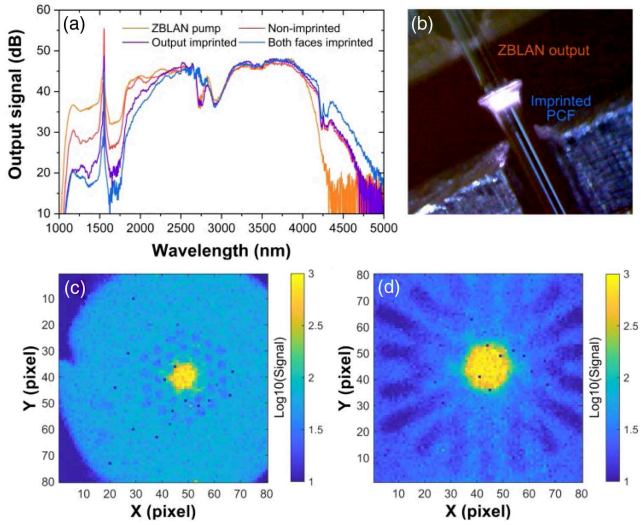

Fig. 2. (a) Comparison between the input spectrum (orange) and the nonimprinted (red), output imprinted (purple), and two-face imprinted (blue) output spectra, respectively. (b) Microscope image of the ZBLAN to PCF butt-coupling, revealing scattered light from diffraction caused by the imprinted structure. (c), (d) Output beam profile of the (c) nonimprinted and (d) imprinted fiber. Note that log scale was used on the intensity axis to better visualize the air cladding.

diameter ZrF_4-BaF_2-LaF_3-AlF_3-NaF (ZBLAN) glass fiber generating a spectrum covering 1–4.2 µm.

The principle of fiber nanoimprinting is depicted in Fig. 1(a). A nickel (Ni) mold with the negative structure is placed on a hot plate and heated to above the T_g of the chalcogenide glass (~175°C [15]). For more details regarding the fabrication of the mold, see Refs. [9,16]. The fiber is then pressed against the mold for a brief period of time, after which the fiber is quickly released to allow for the imprinted structure to settle. Force was applied by manually moving a translation stage, and the combination of force, imprint time, and temperature enabled varying degrees of structuring and deformation of the fiber. In general, higher temperatures allow for faster imprinting using low force, which also reduces the heat conduction to the rest of the fiber and thus reduces deformation.

Figure 1(b) shows the PCF used in the experiments, which has a core diameter of 15 µm and cladding diameter of 170 µm. The best imprints were achieved using a temperature between 230–250°C applying a very small translation force for just a few seconds. Figures 1(c) and 1(d) show high-magnification scanning electron microscope (SEM) images of the imprinted structures, which were designed to have a pitch of 1050 nm and a height of around 1350 nm, providing excellent antireflection from 2.6–6.2 µm (<4% reflection) peaking at 4 µm (<1% reflection) [9,16]. The size of the structure meant that for wavelengths below ~2.2 µm, the imprint acts as a diffraction grating, effectively scattering much of the light into the cladding. This effect is seen from the microscope image of Fig. 2(b), which shows the chalcogenide fiber lighting up near the butt-coupling interface with the ZBLAN fiber from the pump source. It is also apparent from the image that the imprinting procedure in this case caused significant deformation of the fiber tip, resulting in a so-called elephant's foot shape. However, this deformation affects mainly the outermost part of the cladding, leaving the core area more or less intact except for some hole shrinkage, as is apparent from Fig. 1(c). The effect of fiber tip deformation and hole shrinking on the output beam profile is seen when comparing the beam profiles of Figs. 2(c) and 2(d), which shows the near fields of the nonimprinted and imprinted fibers, respectively. The near-field images were captured using an uncooled PbSe camera covering from 1–5 µm wavelength (Tachyon 6400, NIT). In the nonimprinted fiber output beam, the PCF structure is clearly seen, while the imprinted output beam shows a significant distortion of the air-cladding structure while maintaining a circular core-guided mode. Note that the intensity scale on the figures is logarithmic in order to clearly see the air hole patterns. By optimizing the temperature, pressure, and imprinting time, it was possible to reduce the fiber tip deformation while maintaining a full imprint of the structure, but it was found to have no influence on the transmission since the core area is seemingly unaffected by the deformation.

To measure the output spectra, the PCF output was butt-coupled to a 150 µm core diameter chalcogenide patch cable (IRF–Se–150, IR Flex) and guided to a grating-based spectrometer covering from 0.2–5 µm (Spectro 320, Instrument Systems). From comparing the red output spectrum of the nonimprinted fiber in Fig. 2(a) to the purple and blue output spectra of the one-face (output) and two-face imprinted fiber, respectively, it is clear that a significant fraction of the light below 2.2 µm is lost due to diffraction. Such properties could potentially be useful for reducing the linear and nonlinear absorption of shorter wavelengths, in particular two-photon absorption, which may improve the power handling. It is also evident from the spectra that the long-wavelength transmission was improved after imprinting. In order to quantify the improvement, the total output power and output power after a 3.5 µm long-pass filter (LPF) were measured for the nonimprinted and the two-face imprinted fibers. Many fiber samples with similar lengths around 20–30 cm were prepared and measured, and because the imprinting was performed manually, the

Table 1. Measured Transmission ($T = P_{out}/P_{in}$) of Nonimprinted and Two-Face Imprinted PCFs[a]

Fiber Sample	P_{in} (mW)	P_{out} (mW)	T (%)	ΔT^b (%)
Non #1	139.8 [31.9]	74.4 [18.9]	53.2 [59.2]	–
Two-face #1	139.8 [31.9]	83.5 [23.3]	59.7 [73.0]	10.9 [18.9]
Two-face #2	139.8 [31.9]	86.5 [25.8]	61.9 [80.9]	14.1 [26.8]
Two-face #3	133.5 [31.2]	98.5 [30.7]	73.8 [98.4]	27.9 [60.2]
Non #2	160.5 [–]	72.5 [19.9]	45.2 [–]	–
Two-face #4	160.5 [–]	78.0 [22.7]	48.6 [–]	7.0 [12.3][b]

[a]The improvement in transmission is defined as ΔT = T(two-face)/T(non). Square brackets denote values >3.5 μm.
[b]Calculated using the output power >3.5 μm for Non #2 and two-face #4.

results varied from producing only minor or no improvement in transmission, to even reducing the output power compared to the nonimprinted reference. However, some samples also produced a significant increase in transmission, and these results are presented in Table 1. The total transmission improvement (ΔT) between the nonimprinted and two-face imprinted fibers ranged from 7.0–27.9%, and the maximum total transmission (T) was 73.8%. As seen from the orange curve of Fig. 2(a), a significant part of the pump spectrum is below the diffraction limit of the imprinted structure, so the transmission increase > 3.5 μm was also measured and found to range from 12.3–60.2% with a maximum transmission of 98.4%. However, this extremely high value is attributed to a combination of both reduced reflection and increased redshifting of wavelength components below 3.5 μm due to the higher transmission.

Previous work with fiber nanoimprinting has focused on large-core multimode As_2S_3SIFs (50–100 μm core diameters) [11], and so it was not clear whether the micron scale structures and especially the fiber tip deformation would affect transmission of smaller core fibers. In that respect, this work represents the first demonstration of AR nanoimprinting of a single-mode chalcogenide PCF, achieving increased transmission in a fiber suitable for SC generation (SCG) without significantly affecting the core mode of the fiber. Despite the increased transmission and redshifting in the imprinted fibers, the spectral extent was limited to 5 μm, so in order to increase the bandwidth even further, fiber tapering was, for the first time to the authors' knowledge, investigated for cascaded SCG. In a previous study on SC in tapered chalcogenide PCFs [12] using direct pumping, it was found that the length of uniform fiber before (L_b) and after (L_a) the tapered fiber section (L_t) greatly influenced the bandwidth obtained, but the influence of the tapered core diameter was never fully explored. Here we have investigated the influence of the tapered core diameter (d_c) in five different tapered fibers, whose parameters are summarized in Table 2. All tapers were designed to have around 2.5 cm adiabatic taper transitions.

Table 2. Core Diameter and Length Parameters for Tapers A–E

Taper ID	d_c (μm)	L_b (cm)	L_t (cm)	L_a (cm)	L_{tot} (cm)
A	6	6	11	18	35
B	6.5	10	15	11	36
C	7	2	12	19	33
D	7.5	9	15	18	42
E	6	27	30	12	69

When the fiber core is reduced, the zero-dispersion wavelength (ZDW) is shifted towards shorter wavelengths from around 4.9 μm at the initial 15 μm diameter to around 3.6–4 μm at 6–7.5 μm diameter, respectively [12]. But while the reduced ZDW allows for more pump power to couple into the anomalous dispersion regime for improved SCG efficiency, the confinement loss edge is also pushed towards shorter wavelengths, which introduces a trade-off between efficiency and long-wavelength loss. Figure 3(a) shows the resulting spectra from pumping tapers A–E with around 270 mW of average power at 1 MHz pulse repetition rate. The spectra were measured using a fiber-coupled Fourier transform infrared (FTIR) spectrometer (FOSS, custom) covering from 2.8–14 μm. The total transmission of the nonimprinted tapers A–D varied from 31–38%, with the highest output power of 103 mW achieved for taper D.

Despite the differences in taper parameters, tapers A–C produced very similar output spectra reaching up to around 8 μm at the −30 dB level, while taper D was limited to 7.5 μm and exhibited significantly lower flatness compared to the three

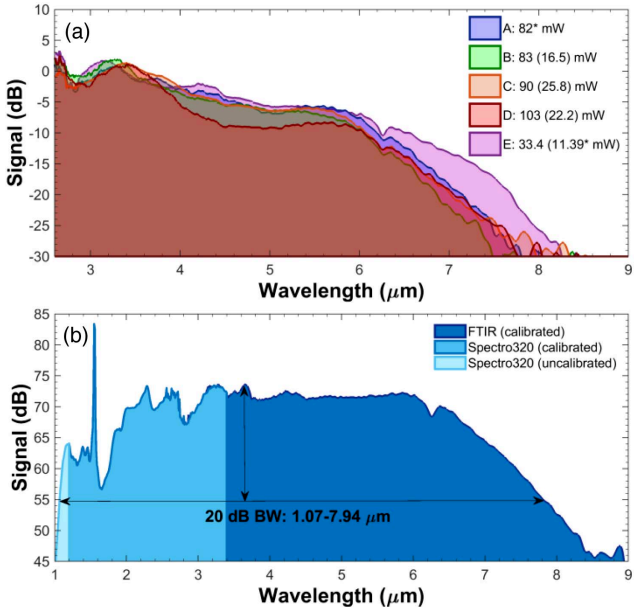

Fig. 3. (a) FTIR spectra of the long-wavelength edge obtained for tapers A–E for a pump power of ~270 mW. The corresponding measured total output power and power >3.5 μm (brackets) is indicated in the legend (* = estimated). (b) Stitched total output spectrum for taper E using 350 mW pump power and generating a 41 mW continuum with a 20 dB bandwidth from 1.07–7.94 μm.

others. For a 7.5 μm core diameter, the ZDW is estimated to be around 4 μm, which is exactly where we see a dip in the output spectrum of taper D. Such a dip followed by a peak or pedestal of lower intensity is commonly observed when pumping in the normal dispersion region close to the ZDW [17,18]. Since the SC pump starts to cut off at around 4 μm, the solitons coupled into the PCF will initially experience normal dispersion and therefore only the part that broadens into the anomalous dispersion via self-phase modulation (SPM) will then contribute to the long-wavelength edge. As a result, the amount of power >3.5 μm is only ∼21% in taper D (22.2 mW) compared to ∼29% in taper C (25.8 mW).

To investigate whether the spectral extension was limited by the taper length, another taper denoted taper E was tested. Taper E has the same 6 μm core diameter as taper A, but twice the tapered section length and a longer length of uniform fiber before the taper. It is seen in Fig. 3(a) that the longer taper improves the long-wavelength generation, but reduces the output power significantly due to increased losses. Figure 3(b) shows the entire taper E output spectrum at ∼350 mW pump power (41 mW output power), where maximum broadening was observed covering from 1.07–7.94 μm at the −20 dB level with. Further increasing the pump power did not improve the long-wavelength edge, as seen from the trend in Fig. 4(a), which shows that for these pump and taper parameters, the broadening is limited to around 8 μm.

This behavior was found in all of the tapers tested, which suggests that further broadening is limited mainly by the soliton dynamics of the MOPA source and ZBLAN fiber rather than confinement loss or dispersion in the tapers [5,7]. Lastly, the output power stability was tested. Note that at the point of this measurement (four months later), taper C had degraded significantly due to exposure to ambient lab conditions [15], and so the obtainable bandwidth and output power were reduced. Figure 4(b) shows the degradation in output power during a 116.5 h continuous power stability measurement and adjusting the coupling did not improve the output power. This highlights the need for proper sealing of the optical facets. This could for instance be realized by either fully collapsing the air holes, or by splicing an unstructured fiber end cap onto the PCF prior to imprinting.

In conclusion, we have demonstrated for the first time improved transmission and broadening in cascaded SCG through nanoimprinting and tapering of $Ge_{10}As_{22}Se_{68}$ chalcogenide PCFs. The maximum total transmission of a nanoimprinted uniform fiber was increased by 27.9% relative to the nonimprinted fiber, and the average power >3.5 μm was increased by up to 60.2%. By tapering a nonimprinted 15 μm core PCF down to a core diameter of 7 μm over a 12 cm section, a spectrum covering up to ∼8 μm with 90 mW output power and 25.8 mW > 3.5 μm was achieved. By combining the two postprocessing methods, we expect that the output power can be increased to more than 120 mW with more than 40 mW above 3.5 μm without damaging the fiber. Such power levels would enable applications such as optical coherence tomography to push further into the mid-infrared for improved inspection of ceramics, coatings, polymers, and fiber-reinforced composites [19].

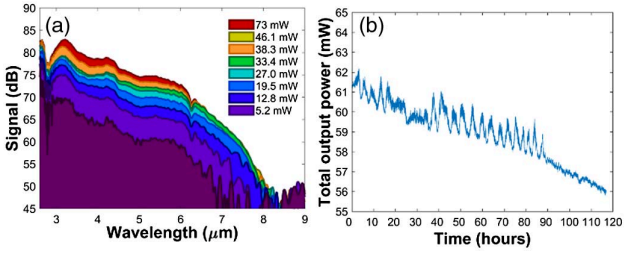

Fig. 4. (a) Spectral broadening in taper E with increasing output power (brackets, power >3.5 μm). (b) Output power degradation in Taper C during 116.5 h testing.

Funding. European Research Council (722380, 732968); Innovationsfonden (4107-00011A).

†These authors contributed equally to this work.

REFERENCES

1. C. R. Petersen, N. Prtljaga, M. Farries, J. Ward, B. Napier, G. R. Lloyd, J. Nallala, N. Stone, and O. Bang, Opt. Lett. **43**, 999 (2018).
2. C. R. Petersen, P. M. Moselund, L. Huot, L. Hooper, and O. Bang, Infrared Phys. Technol. **91**, 182 (2018).
3. R. A. Martinez, K. Guo, T. Zhai, F. L. Terry, L. E. Pierce, M. N. Islam, R. Gibson, J. M. Reed, R. G. Bedford, L. Maksymiuk, M. J. Freeman, B. A. Gorin, N. P. Christian, and A. I. Ifarraguerri, J. Lightwave Technol. **37**, 3626 (2019).
4. R. A. Martinez, G. Plant, K. Guo, B. Janiszewski, M. J. Freeman, R. L. Maynard, M. N. Islam, F. L. Terry, O. Alvarez, F. Chenard, R. Bedford, R. Gibson, and A. I. Ifarraguerri, Opt. Lett. **43**, 296 (2018).
5. C. R. Petersen, P. M. Moselund, C. Petersen, U. Møller, and O. Bang, Opt. Express **24**, 749 (2016).
6. I. Kubat, C. Rosenberg Petersen, U. V. Møller, A. Seddon, T. Benson, L. Brilland, D. Méchin, P. M. Moselund, and O. Bang, Opt. Express **22**, 3959 (2014).
7. F. Théberge, N. Bérubé, S. Poulain, S. Cozic, S. Châtigny, L.-R. Robichaud, L.-P. Pleau, M. Bernier, and R. Vallée, Opt. Express **26**, 13952 (2018).
8. A. Sincore, J. Cook, F. Tan, A. El Halawany, A. Riggins, S. McDaniel, G. Cook, D. V. Martyshkin, V. V. Fedorov, S. B. Mirov, L. Shah, A. F. Abouraddy, M. C. Richardson, and K. L. Schepler, Opt. Express **26**, 7313 (2018).
9. M. R. Lotz, C. R. Petersen, C. Markos, O. Bang, M. H. Jakobsen, and R. Taboryski, Optica **5**, 557 (2018).
10. R. J. Weiblen, C. R. Menyuk, L. E. Busse, L. B. Shaw, J. S. Sanghera, and I. D. Aggarwal, Opt. Express **24**, 10172 (2016).
11. C. Florea, J. Sanghera, L. Busse, B. Shaw, F. Miklos, and I. Aggarwal, Appl. Opt. **50**, 17 (2011).
12. C. R. Petersen, R. D. Engelsholm, C. Markos, L. Brilland, C. Caillaud, J. Trolès, and O. Bang, Opt. Express **25**, 15336 (2017).
13. D. D. Hudson, S. Antipov, L. Li, I. Alamgir, T. Hu, M. E. Amraoui, Y. Messaddeq, M. Rochette, S. D. Jackson, and A. Fuerbach, Optica **4**, 1163 (2017).
14. D. Jain, R. Sidharthan, G. Woyessa, P. M. Moselund, P. Bowen, S. Yoo, and O. Bang, J. Opt. Soc. Am. B **36**, A86 (2019).
15. P. Toupin, L. Brilland, D. Mechin, J.-L. Adam, and J. Troles, J. Lightwave Technol. **32**, 2428 (2014).
16. M. Lotz, J. Needham, M. H. Jakobsen, and R. Taboryski, Opt. Lett. **44**, 4383 (2019).
17. C. R. Petersen, U. Møller, I. Kubat, B. Zhou, S. Dupont, J. Ramsay, T. Benson, S. Sujecki, N. Abdel-Moneim, Z. Tang, D. Furniss, A. Seddon, and O. Bang, Nat. Photonics **8**, 830 (2014).
18. D. Jayasuriya, C. R. Petersen, D. Furniss, C. Markos, Z. Tang, Md. S. Habib, O. Bang, T. M. Benson, and A. B. Seddon, Opt. Mater. Express **9**, 2617 (2019).
19. N. M. Israelsen, C. R. Petersen, A. Barh, D. Jain, M. Jensen, G. Hannesschläger, P. Tidemand-Lichtenberg, C. Pedersen, A. Podoleanu, and O. Bang, Light Sci. Appl. **8**, 11 (2019).

194.57.91.238 {ts '2019-11-07 06:28:36'}

Optics Letters

Nested capillary anti-resonant silica fiber with mid-infrared transmission and low bending sensitivity at 4000 nm

Mariusz Klimczak,[1,3,*] Dominik Dobrakowski,[1,2] Amar Nath Ghosh,[3] Grzegorz Stępniewski,[1,2] Dariusz Pysz,[1] Guillaume Huss,[4] Thibaut Sylvestre,[3] and Ryszard Buczyński[1,2]

[1]Glass Department, Institute of Electronic Materials Technology, Wólczyńska 133, 01-919 Warsaw, Poland
[2]Faculty of Physics, University of Warsaw, Pasteura 5, 02-093 Warsaw, Poland
[3]Institut FEMTO-ST, CNRS, UMR 6174, Université Bourgogne Franche-Comté, Besançon, France
[4]LEUKOS, 37 rue Henri Giffard, Z.I. Nord, 87280 Limoges, France
*Corresponding author: mariusz.klimczak@itme.edu.pl

Received 17 June 2019; revised 30 July 2019; accepted 4 August 2019; posted 5 August 2019 (Doc. ID 370171); published 29 August 2019

We report a silica glass nested capillary anti-resonant nodeless fiber with transmission and low bending sensitivity in the mid-infrared around 4000 nm. The fiber is characterized in terms of transmission over 1700–4200 nm wavelengths, revealing a mid-infrared 3500–4200 nm transmission window, clearly observable for a 12 m long fiber. Bending loss around 4000 nm is 0.5 dB/m measured over three full turns with 40 mm radius, going up to 5 dB/m for full turns with 15 mm radius. Our results provide experimental evidence of hollow-core silica fibers in which nested, anti-resonant capillaries provide high bend resistance in the mid-infrared. This is obtained for a fiber with a large core diameter of over 60 µm relative to around 30 µm capillaries in the cladding, which motivates its application in gas fiber lasers or fiber-based mid-infrared spectroscopy of CO_x or N_xO analytes. © 2019 Optical Society of America

https://doi.org/10.1364/OL.44.004395

Hollow-core glass fibers (HCFs) rely on guiding mechanisms, which enable significant reduction of overlap of the guided mode with solid microstructure forming the cladding. The inhibited coupling fibers (ICFs) and hollow-core anti-resonant guiding fibers (ARFs) are two examples that have received particularly strong attention. The first reported ICFs were the Kagomé fibers, developed in 2002 [1]. The principle of light guidance in ICFs was explained in 2007 [2], revealing the fundamental difference between photonic bandgap (PBG) and inhibited coupling (IC). ARFs can be considered as simplified ICF structures, consisting of only one ring of circular capillaries in the cladding. These fibers were first reported in 2011 [3], and the anti-resonant reflecting optical waveguide model [4] is considered to be the most accurate in describing guiding in these structures. Various designs of hypocycloid-core fibers have followed since, with emphasis on fibers with the core area limited by a single ring of circular, non-touching capillaries [5,6]. Low intrinsic nonlinearity and dispersion of these fibers make them particularly attractive for high-energy pulse delivery [7]. The possibility to largely modify their optical properties by infiltration with liquids or gases opens interesting applications in optofluidics [8] or in temporal compression down to single optical cycles of laser pulses in the mid-infrared [9]. Low attenuation is the obvious advantage of any fiber for a practical application and loss below 10 dB/km in the visible and at important laser wavelengths in the near-infrared has been reported in HCFs [10,11]. More recently, an ARF with measured attenuation of 2 dB/km at a wavelength of 1512 nm made it possible to consider them for specific telecommunication applications [12]. Such applications are among the important motivations for the development of HCFs, and data transmission was demonstrated in an air core PBG fiber already in 2013 [13]. Dramatic improvement in the bringing down of attenuation—ultimately to around 1 dB/km—prompted later demonstrations of data transmission in hollow-core ARFs in the third telecommunication window, as well [14-16]. Mid-infrared guidance in silica fibers is disruptive for gas sensing and spectroscopy applications [5,17]. The feasibility to design robust multiple-pass setups is crucial for development of fiber-based cavity-enhanced spectroscopy [18]. Several-meter or longer gas-filled fibers are becoming important for fiber-based gas lasers exploiting Raman scattering [19]. More recently, mid-infrared lasers operating between 3100 and 4600 nm wavelengths and based on optical transitions between vibrational energy bands of different molecular gasses have been reported using gas-filled HCFs [20–23]. The fiber cavity length, exceeding 10 m in either case, was reported among the key parameters of optimizing laser efficiency, which puts significant pressure on bending loss performance of fibers used to build such systems. Gas-filled HCFs have also been shown as attractive experimental platforms for nonlinear propagation, broadening, and compression of ultrashort pulses across the UV to the mid-infrared [24–27]. Silica glass ARFs have been demonstrated to guide light at wavelengths up to 7900 nm, with attenuation at 3900 nm of roughly 50 dB/km [28]. Attenuation of 34 dB/km

at 3050 nm and 85 dB/km at 4000 nm was found for ARFs with a triangular cladding [29,30].

Mode confinement in HCFs is very sensitive to bending [31]. Hollow-core PBG fibers were outperforming ARFs in this regard [31]. Significant research effort has been devoted to overcoming this drawback, resulting in reported bend losses of ICFs in the order of 0.25 dB/turn [32], 0.2 dB/m of attenuation at 5 cm radius in the NIR range [33] and, finally, a result of 0.03 dB/turn bend loss for a 30 cm bend diameter at 750 nm has been reported [12]. Bend loss below 1 dB/km for $R =$ 10 cm at 1512 nm has recently been demonstrated as well [12]. An important conclusion has been drawn between low bending loss and small core diameter ARFs [34]. A variant of ARFs with nested capillaries, later commonly referred to as the nested capillary anti-resonant nodeless fiber (NANF), has been shown to alleviate the challenge of bend losses [35]. The first report on a physical NANF structure involved a 10-capillary fiber, followed by a five-capillary fiber [36,37].

In this Letter, we report on the development of a silica glass NANF, and on the characterization of its transmission, attenuation, and bending losses with a focus on the mid-infrared spectral range around wavelength of 4000 nm.

Our silica glass NANF was fabricated using the stack-and-draw technique. The microstructure of the fiber is shown in a scanning electron microscopy (SEM) image in Fig. 1. It consists of a cladding with seven nested capillaries. The criterion for the number of capillaries is usually attenuation and exceptionally low attenuation has been reported for ARFs with between five [15,38], through six–seven [10,31] to eight–10 capillaries [5] in the cladding. A seven-nested capillary ARF has been reported previously, albeit with less uniform structure, than in Fig. 1 [39] and NANFs have been numerically studied for mid-infrared transmission [40]. The outer diameter of our fiber is 162 μm, and the core diameter is 62 μm. The outer and inner capillary diameters are 29 and 16 μm, and their wall thickness is 1.6 and 0.9 μm, respectively.

All transmission measurements and mode imaging have been performed with a 150 cm long sample. Light from a Leukos Electro-250-Mir or NKT Photonics SuperK MIR supercontinuum has been coupled to the fiber with a black diamond aspheric lens (Thorlabs C036TME). At the output of the fiber, light was collimated with a parabolic off-axis silver mirror with a 10 cm focal length into a free-space input of a Fourier transform infrared (Thorlabs OSA205, FTIR) optical spectrum analyzer (OSA) for measurements in the mid-infrared or to a diffractive OSA for long-wave near-infrared measurements (Yokogawa AQ6375B). This, together with securing of both fiber ends in 9 cm long bare fiber mounts on translation stages, assured mechanical stability during measurements. In a similar way, the fiber output was collimated for characterization using an extended InGaAs beam profiler.

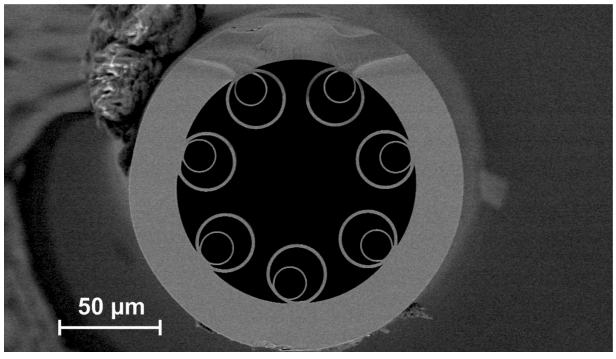

Fig. 1. SEM image of the developed fiber.

The fiber supports guidance of few modes at 2500 nm, but the fundamental mode (FM) can be selectively excited, as shown in Fig. 2(a), where light from an optical parametric oscillator has been used with around 100 nm of spectral width. Higher-order modes in this case were excited using offset launch, as shown in Fig. 2(c). We also measured numerical aperture (NA) of the fiber by registering output beam profiles in far field with a phosphor-covered CCD camera. The output of a single-mode laser diode operating at 1548 nm was coupled into the fiber with an aspheric lens (NA = 0.25). The FM or higher-order modes were selectively excited by changing the coupling conditions. The output beam size was measured at $1/e^2$ of maximum intensity. The NA was calculated from the slope of linear fitting of measurement points (beam radius as a distance function) using formulas slope $= tg(\varphi)$ and NA $= \sin(\varphi)$, obtaining NA = 0.037 for the FM and NA = 0.077 for a higher-order mode. The fiber was protected with an acrylic coating, and bending as tight as to a radius of $R =$ 0.5 cm was possible. Depending on the coupling adjustment, the LP_{11} mode could be observed, as shown in Figs. 2(c) and 2(d). Bending of the fiber with these modes excited resulted in scrambling to a structure similar to the FM.

Figure 3 contains results related to the transmission, and results of the attenuation measurements are shown in Fig. 4. Finite element method simulation results, obtained using Comsol Multiphysics (Wave optics module) for the fiber based on a vectorized image of real fiber structure, are shown in Fig. 3(a). Triangular mesh was used with a size from 0.4 to 0.015 μm over glass parts of the structure and between 0.6 and 0.06 μm over the air core. A 3 μm thick perfectly matched layer was assumed for the boundary condition. The material loss of silica was neglected. Bending loss was modeled assuming straight fiber with modified refractive index [41]. The simulations predict transmission windows in the 1800–2600 nm spectral range and over 3400–5000 nm. An attenuation penalty of around a factor of 10 at a wavelength of about 4500 nm can be anticipated, and this is related to the fact that equal capillary thickness has not been maintained in the technological process. Numerical simulations of bend loss further reveal that confinement loss penalty of about 1 dB/m can be expected, regardless of the bend radius, when comparing the developed fiber to an equal capillary thickness (0.9 μm) structure. Up to the wavelength of around 4200 nm, there is good agreement between the simulated and measured transmission spectra, as shown in Fig. 3(b). Compared to single capillary ring structure,

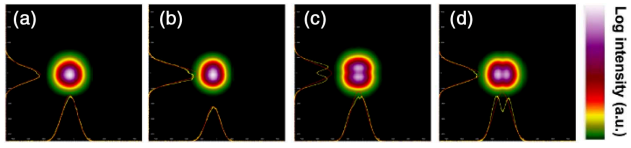

Fig. 2. Beam profiler images of fiber output recorded at 2500 nm: (a) FM in an effectively straight fiber; (b) FM in a fiber coiled at 0.5 cm radius; (c) and (d) LP_{11} modes with the fiber effectively straight and coiled at 0.5 cm radius, respectively.

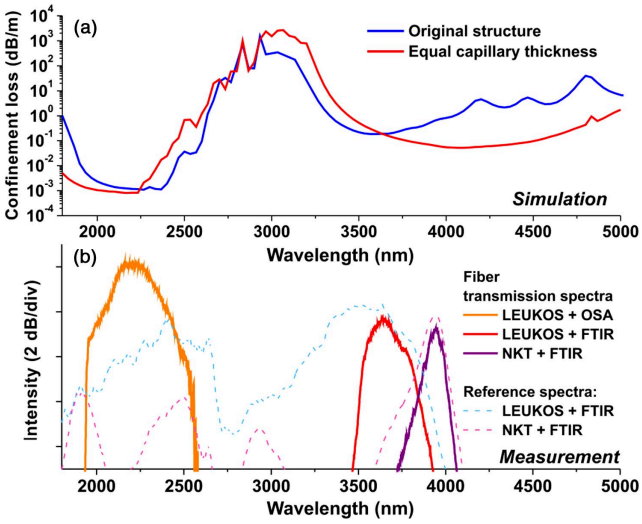

Fig. 3. (a) Finite element method simulation of the fiber transmission; (b) measured transmission spectrum for a 150 cm long fiber.

simulations show that the nested capillary design would have a magnitude lower bend loss in each of the transmission windows and, lower straight fiber attenuation, although straight fiber advantage would be lost closer to 5000 nm due to uneven capillary wall thickness. Simulations allow us to expect transmission in the mid-infrared window up to at least to 5000 nm, although we did not have light sources with spectral coverage above 4200 nm to verify this experimentally.

Attenuation of the fiber was measured by a standard cutback method starting with a 12 m long sample, which was the longest uninterrupted length of the reported fiber available. The fiber was cut by 2 m in the following measurement steps, down to 4 m of final sample length. During the measurement, he fiber was loosely looped over roughly 1 m of diameter, and no loops were made toward the end of measurement. A standard telecommunications fiber cleaver produced high-quality, repeatable cleaves and, for every fiber length, the spectrum was recorded for three consecutive cleaves, to ensure measurement repeatability. Measured attenuation from around 3600 to 4000 nm was 1.5 dB/m and between 0.5 and 1.0 dB/m in the long-wave near-infrared, as shown in Fig. 4 (thick red traces). LP_{01} mode losses obtained in simulations are up to three orders of magnitude lower around 2400 nm and a factor of two smaller around 4000 nm. This mismatch cannot be due to the inclusion of silica material loss in modeling, because the calculated power fraction in glass for this fiber is between 10^{-4} to 10^{-5}. Surface scattering loss in the considered spectral range can account for 1 dB/km and does not explain the discrepancy either [3]. The measured attenuation level is qualitatively reproduced in simulations only when the contribution of higher-order modes is assumed, especially that of LP_{02}. Thus, we relate attenuation of the fiber to content of higher-order modes, which prompts the optimization of cladding and core diameters ratio of the fiber. We note that decibel/kilometer straight-fiber loss has been reported in the HCFs of the single capillary or "ice-cream cone" designs in a similar wavelength range [10,29].

Bending loss measurement was performed by coiling of the 4 m long fiber sample into consecutive, full turns (full loops) of identical diameter, similarly to the procedure reported earlier for ARFs in Ref. [32]. Results—shown in Fig. 5—were recorded for different bending radii from 40 mm down to 7.5 mm. In the mid-infrared window between 3500 and 3900 nm, the loss remains below 5 dB/m for bending radii of 15 mm or more while, for loops with a radius of 30 or 40 mm, it remains below 2.5 dB/m down to 0.5 dB/m around 3800–3900 nm for 40 mm of bend radius. In the 1900–2600 nm window, a sharp short-wavelength transmission cutoff can be observed, which redshifts under bending with a decreasing bending radius. This is consistent with earlier reported results in low ring number Kagomé ICFs, where the redshift of short-wavelength bend loss edge has been assigned to bending-induced mode coupling between the core mode and leaky cladding modes [42] and has been numerically confirmed for NANFs as well [5]. We note that in state-of-the-art single capillary-ring ARFs, bending loss at the level of decibel/kilometer has been reported, although this related to the telecommunications wavelengths, i.e., less than 5 dB/km of loss (50 mm radius) over 1250–1650 nm [12] or over larger bending radii, i.e., 15 cm with 50 dB/km at around 3500 nm [10].

We reported the successful development of a silica nested capillary anti-resonant nodeless fiber with mid-infrared transmission up to around 4200 nm, while numerical simulations

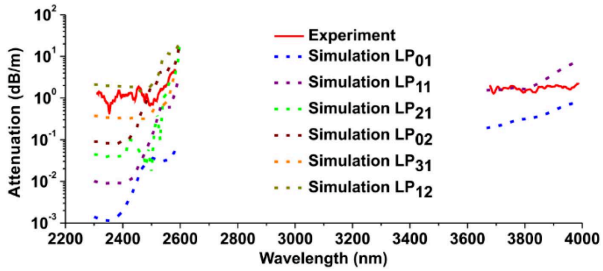

Fig. 4. Measured attenuation (solid traces) and calculated losses for different modes (dotted traces) of the developed NANF.

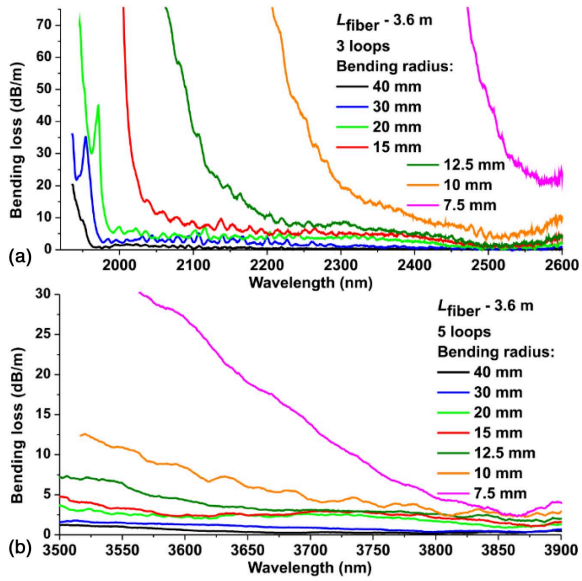

Fig. 5. Measured bend loss (a) over the long-wave infrared and (b) over the mid-infrared in the developed NANF.

allow us to anticipate this transmission to continue up to at least 5000 nm. This would cover frequencies of asymmetric stretching vibrational modes of CO_2 and N_2O molecules (around 4250 and 4500 nm). The measured mid-infrared attenuation of 1–2 dB/m prompts for improvement of both the fiber design and the technological procedure. At the design level, the cladding capillary to the core diameter ratio should be optimized for effective single-mode operation. Recent theoretical results reported for NANFs identify this ratio at around 1.129 [38], while in our case it is around 0.46. At the technological level, the pending improvement relates to maintaining of similar capillary wall thickness. Despite these imperfections, already with the demonstrated fiber were we able to achieve very low bending sensitivity corresponding to bending loss down to 0.5 dB/m at a bending radius of just 40 mm at 3800–3900 nm wavelengths, by introducing nested capillaries into the fiber microstructure. We note, that exceptional results in terms of attenuation and bending loss at a single decibel/kilometer level have been reported in hollow-core conjoined tube capillary fibers and in NANFs, in each case in the third telecommunication window [12,15]. Tens of decibel/kilometer loss in effectively straight ARFs has been reported around 3000–4000 nm, e.g., [29,30], which also identified the challenge of bend loss in this wavelength range for bending radii smaller than 20 cm. Our results provide experimental evidence for the feasibility of limiting bending loss to reasonable levels for bend radii as small as 3–4 cm and for the crucial role of the nested anti-resonant capillaries in providing high bend loss resistance in hollow-core silica fibers operating in the mid-infrared.

Funding. Fundacja na rzecz Nauki Polskiej (First TEAM/2016-1/1); Horizon 2020 Framework Programme (722380); French Government and the French Embassy in Poland; Région Bourgogne Franche-Comté.

Acknowledgment. The authors acknowledge technical support of LEUKOS, Interlab, NKT Photonics, and Prof. R. Piramidowicz from Warsaw University of Technology.

REFERENCES

1. F. Benabid, J. C. Knight, G. Antonopoulos, and P. St. J. Russell, Science **298**, 399 (2002).
2. F. Couny, F. Benabid, P. J. Roberts, P. S. Light, and M. G. Raymer, Science **318**, 1118 (2007).
3. A. D. Pryamikov, A. S. Biriukov, A. F. Kosolapov, V. G. Plotnichenko, S. L. Semjonov, and E. M. Dianov, Opt. Express **19**, 1441 (2011).
4. M. A. Duguay, Y. Kokubun, T. L. Koch, and L. Pfeiffer, Appl. Phys. Lett. **49**, 13 (1986).
5. F. Poletti, Opt. Express **22**, 23807 (2014).
6. C. Wei, R. Joseph Weiblen, C. R. Menyuk, and J. Hu, Adv. Opt. Photonics **9**, 504 (2017).
7. P. Jaworski, F. Yu, R. R. J. Maier, W. J. Wadsworth, J. C. Knight, J. D. Shephard, and D. P. Hand, Opt. Express **21**, 22742 (2013).
8. X.-L. Liu, W. Ding, Y.-Y. Wang, S.-F. Gao, L. Cao, X. Feng, and P. Wang, Opt. Lett. **42**, 863 (2017).
9. U. Elu, M. Baudisch, H. Pires, F. Tani, M. H. Frosz, F. Köttig, A. Ermolov, P. St. J. Russell, and J. Biegert, Optica **4**, 1024 (2017).
10. B. Debord, A. Amsanpally, M. Chafer, A. Baz, M. Maurel, J. M. Blondy, E. Hugonnot, F. Scol, L. Vincetti, F. Gérôme, and F. Benabid, Optica **4**, 209 (2017).
11. M. Maurel, M. Chafer, A. Amsanpally, M. Adnan, F. Amrani, B. Debord, L. Vincetti, F. Gérôme, and F. Benabid, Opt. Lett. **43**, 1598 (2018).
12. S.-F. Gao, Y.-Y. Wang, W. Ding, D.-L. Jiang, S. Gu, X. Zhang, and P. Wang, Nat. Commun. **9**, 2828 (2018).
13. M. N. Petrovich, F. Poletti, J. P. Wooler, A. M. Heidt, N. K. Baddela, Z. Li, D. R. Gray, R. Slavík, F. Parmigiani, N. V. Wheeler, J. R. Hayes, E. Numkam, L. Grűner-Nielsen, B. Pálsdóttir, R. Phelan, B. Kelly, J. O'Carroll, M. Becker, N. MacSuibhne, J. Zhao, F. C. G. Gunning, A. D. Ellis, P. Petropoulos, S. U. Alam, and D. J. Richardson, Opt. Express **21**, 28559 (2013).
14. J. R. Hayes, S. R. Sandoghchi, T. D. Bradley, Z. Liu, R. Slavík, M. A. Gouveia, N. V. Wheeler, G. Jasion, Y. Chen, E. N. Fokoua, M. N. Petrovich, D. J. Richardson, and F. Poletti, J. Lightwave Technol. **35**, 437 (2017).
15. T. D. Bradley, J. R. Hayes, Y. Chen, G. T. Jasion, S. R. Sandoghchi, R. Slavik, E. N. Fokoua, S. Bawn, H. Sakr, I. A. Davidson, A. Taranta, J. P. Thomas, M. N. Petrovich, D. J. Richardson, and F. Poletti, in *European Conference on Optical Communication (ECOC)* (2018).
16. X. Wang, D. Ge, W. Ding, Y. Wang, S. Gao, X. Zhang, Y. Sun, J. Li, Z. Chen, and P. Wang, Opt. Lett. **44**, 2145 (2019).
17. F. Benabid, F. Couny, J. C. Knight, T. A. Birks, and P. St J. Russel, Nature **434**, 488 (2005).
18. P. T. Marty, J. Morel, and T. Feurer, J. Lightwave Technol. **28**, 1236 (2010).
19. F. Couny, F. Benabid, and P. S. Light, Phys. Rev. Lett. **99**, 143903 (2007).
20. M. R. A. Hassan, F. Yu, W. J. Wadsworth, and J. C. Knight, Optica **3**, 218 (2016).
21. F. B. A. Aghbolagh, V. Nampoothiri, B. Debord, F. Gerome, L. Vincetti, F. Benabid, and W. Rudolph, Opt. Lett. **44**, 383 (2019).
22. M. Xu, F. Yu, and J. Knight, Opt. Lett. **42**, 4055 (2017).
23. M. S. Astapovich, A. V. Gladyshev, M. M. Khudyakov, A. F. Kosolapov, M. E. Likhachev, and I. A. Bufetov, IEEE Photonics Technol. Lett. **31**, 78 (2019).
24. M. S. Habib, C. Markos, O. Bang, and M. Bache, Opt. Lett. **42**, 2232 (2017).
25. M. S. Habib, C. Markos, J. E. Antonio-Lopez, and R. Amezcua-Correa, Appl. Opt. **58**, D7 (2019).
26. F. Köttig, D. Novoa, F. Tani, M. C. Günendi, M. Cassataro, J. C. Travers, and P. St. J. Russell, Nat. Commun. **8**, 813 (2017).
27. A. I. Adamu, M. S. Habib, C. R. Petersen, J. E. A. Lopez, B. Zhou, A. Schülzgen, M. Bache, R. Amezcua-Correa, O. Bang, and C. Markos, Sci. Rep. **9**, 4446 (2019).
28. A. N. Kolyadin, A. F. Kosolapov, A. D. Pryamikov, A. S. Biriukov, V. G. Plotnichenko, and E. M. Dianov, Opt. Express **21**, 9514 (2013).
29. F. Yu, W. J. Wadsworth, and J. C. Knight, Opt. Express **20**, 11153 (2012).
30. F. Yu and J. C. Knight, Opt. Express **21**, 21466 (2013).
31. M. Michieletto, J. K. Lyngsø, C. Jakobsen, J. Lægsgaard, O. Bang, and T. T. Alkeskjold, Opt. Express **24**, 7103 (2016).
32. W. Belardi and J. C. Knight, Opt. Express **22**, 10091 (2014).
33. S.-F. Gao, Y.-Y. Wang, X.-L. Liu, W. Ding, and P. Wang, Opt. Express **24**, 14801 (2016).
34. R. M. Carter, F. Yu, W. J. Wadsworth, J. D. Shephard, T. Birks, J. C. Knight, and D. P. Hand, Opt. Express **25**, 20612 (2017).
35. W. Belardi and J. C. Knight, Opt. Lett. **39**, 1853 (2014).
36. W. Belardi, J. Lightwave Technol. **33**, 4497 (2015).
37. A. F. Kosolapov, G. K. Alagashev, A. N. Kolyadin, A. D. Pryamikov, A. S. Biryukov, I. A. Bufetov, and E. M. Dianov, Quantum Electron. **46**, 267 (2016).
38. Md. S. Habib, J. E. Antonio-Lopez, C. Markos, A. Schülzgen, and R. Amezcua-Correa, Opt. Express **27**, 3824 (2019).
39. J. E. Antonio-Lopez, S. Habib, A. V. Newkirk, G. Lopez-Galmiche, Z. S. Eznaveh, J. C. Alvarado-Zacarias, O. Bang, M. Bache, A. Schülzgen, and R. A. Correa, in *IEEE Photonics Conference (IPC)* (2016), pp. 402.
40. M. S. Habib, O. Bang, and M. Bache, Opt. Express **23**, 17394 (2015).
41. H. Renner, J. Lightwave Technol. **10**, 544 (1992).
42. M. Alharbi, T. Bradley, B. Debord, C. Fourcade-Dutin, D. Ghosh, L. Vincetti, F. Gérôme, and F. Benabid, Opt. Express **21**, 28609 (2013).

Journal of the Optical Society of America B
OPTICAL PHYSICS

Supercontinuum generation in heavy-metal oxide glass based suspended-core photonic crystal fibers

A. N. Ghosh,[1] M. Klimczak,[2,3] R. Buczynski,[2,3] J. M. Dudley,[1] and T. Sylvestre[1,*]

[1]Institut FEMTO-ST, CNRS, UMR 6174, Université Bourgogne Franche-Comté, Besançon, France
[2]Institute of Electronic Materials Technology, Wolczynska 133, 01-919 Warsaw, Poland
[3]University of Warsaw, Faculty of Physics, Pasteura 5, 02-093 Warsaw, Poland
*Corresponding author: thibaut.sylvestre@univ-fcomte.fr

Received 6 June 2018; revised 27 July 2018; accepted 27 July 2018; posted 7 August 2018 (Doc. ID 334532); published 30 August 2018

In this paper we investigate supercontinuum generation in several suspended-core soft-glass photonic crystal fibers pumped by an optical parametric oscillator tunable around 1550 nm. The fibers were drawn from lead-bismuth-gallium-cadmium-oxide glass (PBG-81) featuring a wide transmission window from 0.5 to 2.7 μm and a high nonlinear refractive index up to $4.3 \cdot 10^{19}$ m^2/W. They have been specifically designed with a microscale suspended hexagonal core for efficient supercontinuum generation around 1550 nm. We experimentally demonstrate two supercontinuum spectra spanning from 1.07 to 2.31 μm and 0.89 to 2.46 μm by pumping two PCFs in both normal and anomalous dispersion regimes, respectively. We also numerically model the group velocity dispersion curves for these fibers from their scanning electron microscope images. The results are in good agreement with numerical simulations based on the generalized nonlinear Schrödinger equation including the pump frequency chirp. © 2018 Optical Society of America

OCIS codes: (320.6629) Supercontinuum generation; (060.5295) Photonic crystal fibers; (190.4370) Nonlinear optics, fibers; (260.2030) Dispersion; (140.7090) Ultrafast lasers.

https://doi.org/10.1364/JOSAB.35.002311

1. INTRODUCTION

Broadband, compact, and cost-effective supercontinuum (SC) sources in the infrared (IR) are very attractive for sensing and spectroscopy applications [1–3] because this wavelength range contains the ground tones of many molecules, yielding unique "fingerprints" of their chemical composition [4]. However, state-of-the-art mid-IR SC systems are still in their infancy, thus motivating further efforts in fiber drawing and in soft-glass chemistry to remove absorption bands while enhancing both transmission and nonlinearity. Soft glasses such as chalcogenide (As_2S_3) [4–6], tellurite [7,8], and ZBLAN (ZrF_4–BaF_2–LaF_3–AlF_3–NaF) [9–11] have been widely used for drawing highly nonlinear fibers, and experiments have shown efficient SC generation in the mid-IR up to 15 μm [4,5] and up to 11 μm using all-fiber systems [12,13]. Another approach for mid-IR SC generation is gas-filled, hollow-core photonic crystal fiber, which provides low-loss guidance and much higher effective nonlinearity than capillary-based systems [14,15]. Record output powers up to 3.2 μm have also been recently achieved in highly germanium-doped fibers [16].

An alternative to ZBLAN fibers that has recently received attention is small-core heavy metal oxide photonic crystal fibers (PCFs) [17]. They possess a number of optical and mechanical properties that make them also attractive for SC generation, despite their limited transmission window from 550 to 2800 nm compared to other soft glasses. The nonlinear index n_2 of this glass is one order of magnitude larger (4.3×10^{-19} m^2/W) than ZBLAN and silica glasses [17]. In particular, suspended core photonic crystal fibers (SC-PCF) can be readily drawn in which the microstructures enabled have tight optical confinement and a small effective mode area in the order of few μm^2 [18,19]. This results in a high nonlinear coefficient with one drawback: lower coupling efficiency to the fiber due to a small core diameter. In recent years, suspended-core fibers have received less attention in the context of supercontinuum generation than regular lattice PCFs, although existing literature reports provide evidence about the versatility of this approach, including the choice of a glass platform (silica/soft glass), spectral coverage (NIR/MIR), and the dispersion regime of SC generation (solitonic/all-normal) [20–24].

Here, we report SC generation in lead-bismuth-gallium-cadmium-oxide glass (PBG-81) based suspended-core PCF pumped by 200 fs pulses (delivered by a Ti-sapphire laser pumped OPO system) around 1550 nm.

Using two SC-PCFs (core diameter = 4.5 μm and 3.5 μm) with respective lengths of 60 cm and 180 cm, we demonstrate SC generation spanning 1.07–2.31 μm with an output mean power of 53 mW and 0.89–2.46 μm with an output mean power of 32 mW, respectively, by pumping at 1550 nm and 1580 nm. We identify a number of nonlinear phenomena such as spectral broadening due to self-phase modulation, soliton generation, and a Raman soliton self-frequency shift in the fiber at the pumping wavelengths. The experimental spectra were compared to numerical simulations of the generalized nonlinear Schrödinger equation, including the group velocity dispersion computed from the scanning electron microscope (SEM) images of the fiber samples.

2. HEAVY-METAL-OXIDE SUSPENDED-CORE PHOTONIC CRYSTAL FIBERS

The suspended-core photonic crystal fibers were drawn from lead-bismuth-gallium-cadmium-oxide (PBG81) glass. Its chemical composition contains these oxides: PbO: 39.17, Bi_2O_3: 27.26, Ga_2O_3: 14.26, SiO_2: 14.06, and CdO: 5.26. The nonlinear refractive index of PBG-81 glass was measured as $n_2 = 43 \times 10^{-20}$ m^2/W (Z-scan method at 1240 nm, bulk sample) [25,26]. The attenuation spectrum of this PBG-81 bulk glass is shown in Fig. 1. This soft glass has a transmission window from 550 to 2800 nm with typical attenuation of around 2.5 dB/m within 1000–2000 nm. Above 2800 nm, this particular glass melt shows the onset of strong attenuation assigned to OH absorption and has been subject only to standard bubbling of the glass melt with dry air (<1000 ppm of OH). As Fig. 1 shows, the attenuation curve does not feature a local peak around 1380 nm, which is the main difference between PBG-81 and previously used PBG-08 glass [17].

The microstructure of one of the five PCFs is shown in Figs. 2(a)–2(c). The PCF's outer and core diameters are 99.5 and 3.95 μm, and there are six struts or bridges supporting the hexagonal core. These thin struts result in a negligible modal confinement loss for the fundamental mode by ensuring a high degree of isolation in the core area. We fabricated five different fibers with a microscale suspended hexagonal core with dimensions chosen to yield zero-dispersion wavelengths (ZDWs) covering the range 1519–1653 nm.

The opto-geometric parameters of the five fibers are given in Table 1. From SEM images [Fig. 2(b)], we calculated the effective refractive index of the fundamental mode and the corresponding group-velocity dispersion (GVD) using COMSOL

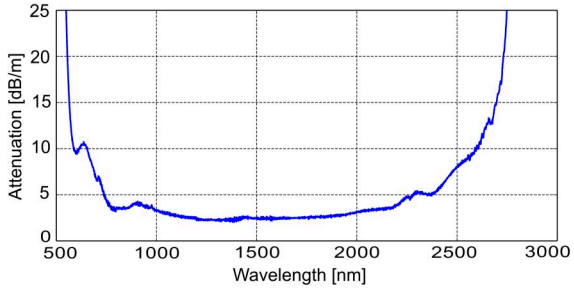

Fig. 1. Attenuation spectrum of bulk lead-bismuth-gallium-cadmium-oxide glass used for drawing SCPCFs.

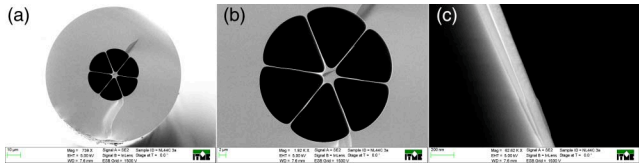

Fig. 2. Cross-section SEM images of a suspended core PCF. (a) Image of the fiber with an outer diameter of 99.5 μm. (b) Expanded view of the microstructure region (core diameter of 3.95 μm). (c) One of the six struts supporting the core with thickness of 89.7 nm.

Table 1. Geometric Parameters of SC-PCFs Used for Dispersion Calculation and Supercontinuum Generation

No.	Label	Core Diameter (μm)	Strut Thickness (nm)	ZDW (nm)
1	NL44C1a	4.5	81	1653
2	NL44C2a	4.3	99	1593
3	NL44C3a	3.95	90	1574
4	NL44C4b	3.8	40	1557
5	NL44C5c	3.51	47	1519

software. We used a standard Sellmeier equation and the coefficients used in the simulation were $B_1 = 2.30350920$, $B_2 = 0.21430548$, $B_3 = 1.73310331$, $C_1 = 0.02084623$ μm^2, $C_2 = 0.08262994$ μm^2, and $C_3 = 183.5615768$ μm^2. The numerical results are shown in Figs. 3(a) and 3(b) for our five fiber samples.

Figure 3(a) shows the group velocity dispersion curve of our five SC-PCF samples covering almost the entire transmission window of the fiber. The inset image represents the optical power density of the fundamental mode inside the core of

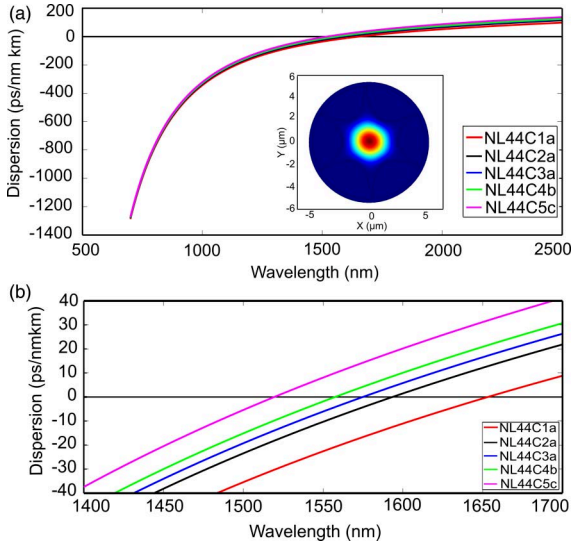

Fig. 3. Dispersion characteristics of the SC-PCFs simulated for the fundamental mode from SEM images. (a) Group velocity dispersion of five SC-PCF samples (inset: optical power density of the fundamental mode inside the core of fiber sample NL44C2a). (b) Dispersion curve of the PCFs showing zero-dispersion wavelength (ZDW).

the fiber sample NL44C2a. As shown in Fig. 3(b), the zero-dispersion wavelength shifts from 1519 nm to 1653 nm as the core diameter increases from 3.51 μm to 4.5 μm.

3. EXPERIMENTAL SETUP

The experimental setup for generating and measuring supercontinuum spectra is shown in Fig. 4. For a pump laser, we used a 200-fs optical parametric oscillator (Chameleon Compact OPO-Vis), pumped by a Ti-sapphire mode-locked laser (Chameleon Ultra II) at an 80 MHz repetition rate. The OPO signal is tunable in the range 1–1.6 μm with mean output powers 1 W–230 mW, and the idler from 1.7 μm to 4 μm with powers from 250 mW to 50 mW. The signal from the OPO was injected into the SC-PCF through a focusing objective and the coupling power was controlled via a variable attenuator. An IR camera and imaging system (another focusing objective) were combined with wavelength filters to study the mode structure and guidance inside the fiber core. The generated SC light was measured using an IR spectrometer (Ocean Optics NIRQuest512-2.5) with sensitivity in the wavelength range of 900–2500 nm. The result of the IR imaging showed that the SC was generated in the fundamental mode over the full wavelength range and no evidence for the presence of multimode operation could be observed.

4. RESULTS AND DISCUSSION

Figures 5(a)–5(d) shows the variation in the measured SC spectra for different fiber output powers as indicated for two SC-PCF samples NL44C2a (length = 60 cm, ZDW = 1593 nm) and NL44C5c (length = 180 cm, ZDW = 1519 nm) using signal wavelengths of 1550 nm (in the normal dispersion regime) and 1580 nm (in the anomalous dispersion regime), respectively.

The output spectra recorded for these two fiber samples show strong spectral broadening around the pump wavelength due to self-phase modulation at low input power. In addition to the peak contributed by pump wavelength, note that we have an additional peak due to the residual OPO idler, which otherwise does not contribute to SC generation. As the power increases, we see red-shifted solitons beyond 2 μm and simultaneous generation of upshifted dispersive waves down to 1 μm.

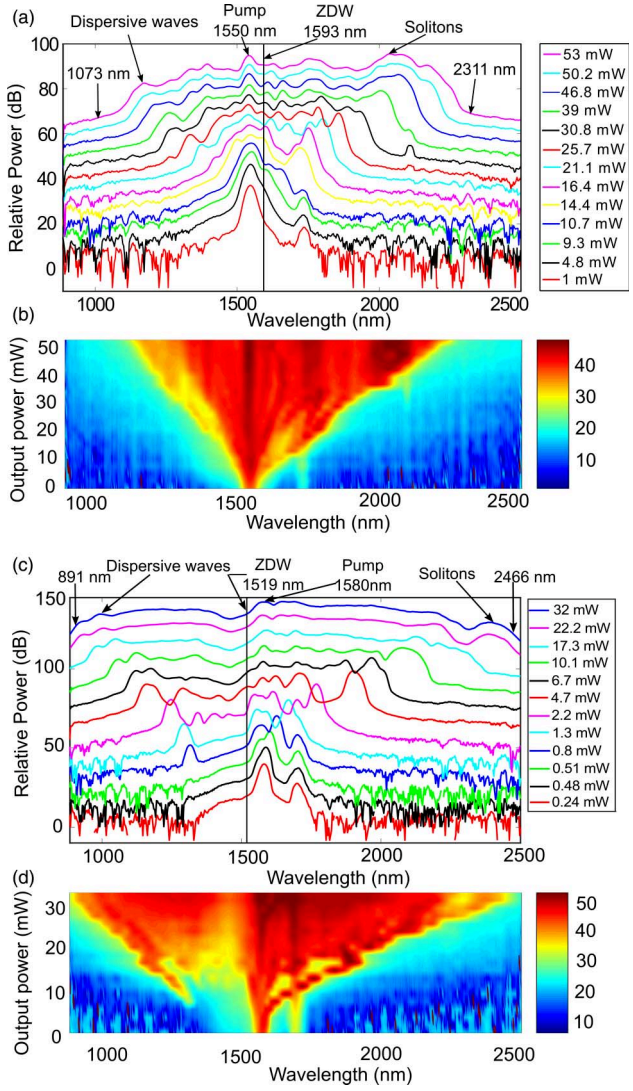

Fig. 5. Supercontinuum spectra generated in two SC-PCF samples with 200 fs pulses pumped at 1550 nm and 1580 nm, respectively, as a function of mean output power. (a) and (c) Generation of SC spectra through spectral broadening, soliton ejection, and dispersive wave generation in two fiber samples, NL44C2a and NL44C5c, respectively. (b) and (d) Evolution of SC spectrum with the fiber output power for SC-PCF samples NL44C2a and NL44C5c.

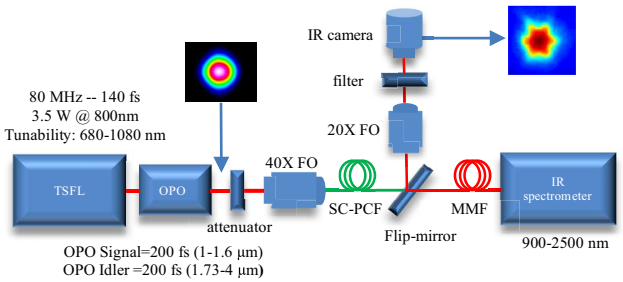

Fig. 4. Scheme of the experimental setup for generating and measuring supercontinuum infrared light. TSFL, Ti-sapphire femtosecond laser; FO, focusing objective; SC-PCF, suspended core photonic crystal fiber; MMF, multimode fiber (left inset: beam profile at OPO output; right inset: IR image at SC-PCF output).

At maximum coupling power, we obtain SC spectra of 1238 nm and 1575 nm bandwidths (at the -25 dB and -20 dB level, respectively) for fiber samples NL44C2a and NL44C5c, respectively.

A SC-PCF sample NL44C4b (length = 183 cm, ZDW = 1557 nm) is also pumped at 1740 nm in the strong anomalous dispersion regime using the idler OPO output. The variation in the measured SC spectra for different output powers for this fiber is shown in Fig. 6. As we pumped at a wavelength far away from the zero-dispersion wavelength of this fiber, we obtained three individual high-power solitons beyond 2 μm and a dispersive wave down to 1 μm instead of a smooth supercontinuum. At maximum power, the bandwidth of this broad spectrum is 1495 nm at the −25 dB level.

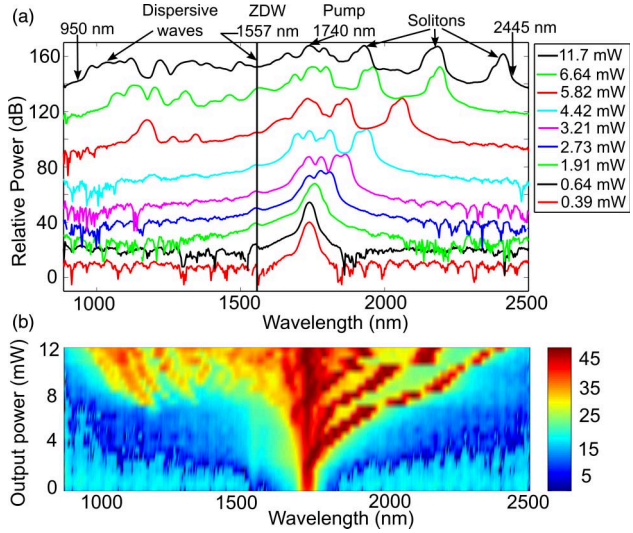

Fig. 6. Spectra generated in SC-PCF sample NL44C4b with 200 fs pulses pumped at 1740 nm. (a) Generation of broad spectra through spectral broadening, soliton ejection, and dispersive wave generation. (b) Evolution of spectrum with the fiber output power.

5. SUPERCONTINUUM SIMULATION

Nonlinear pulse propagation and supercontinuum generation was modelled using the generalized nonlinear Schrödinger equation (GNLSE) [27,28],

$$\frac{\partial A}{\partial z}+\frac{\alpha}{2}A-\sum_{k\geq 2}\frac{i^{k+1}}{k!}\beta_k\frac{\partial^k A}{\partial T^k}=i\gamma\left(1+i\tau_{\text{shock}}\frac{\partial}{\partial T}\right)\times\left(A(z,T)\int_{-\infty}^{+\infty}R(T')|A(z,T-T')|^2\mathrm{d}T'\right),\quad(1)$$

where the second term in the left-hand side accounts for a linear loss with loss coefficient α, and the third term represents the dispersion with the dispersion coefficient β_k associated with Taylor series expansion of the propagation constant $\beta(\omega)$ about central frequency ω_0. In the simulation, we introduced a linear loss of 5 dB/m (measured using a cutback method). We also used the dispersion parameters (up to the fourth order) computed from the SEM image of the SC-PCF samples. The right-hand side (RHS) of Eq. (1) models the nonlinear effects in the fiber: nonlinear coefficient $\gamma=2\pi n_2/\lambda_0 A_{\text{eff}}$, where the nonlinear refractive index n_2 was 4.3×10^{-19} m^2/W and the effective mode area A_{eff} was calculated from the SEM image of the fiber sample at pump wavelength. The time derivative term in the RHS of Eq. (1) models effects such as self-steepening and optical shock formation with $\tau_{\text{shock}}=1/\omega_0$. The term $R(T)=(1-f_R)\delta(t)+f_R h_R(t)$ represents the response function, which includes both an instantaneous electronic and a delayed Raman contribution with $f_R=0.05$. The value of f_R was measured from the Raman scattering spectra of bulk glass, and the Raman contribution to Kerr nonlinearity $h_R(t)$ was fitted from nonlinear simulation for a different type of fiber made from the same glass. The input pulse was considered to be Gaussian. Frequency-resolved optical gating measurements of our input pulses (MeasPhotonics FROGscan) showed the presence of a linear chirp (parabolic phase), which was also included in the simulation initial conditions. In the simulation for SC-PCF samples NL44C2a and NL44C5c, we used fiber lengths of 60 cm and 180 cm, and pump pulse durations of 225 fs and 220 fs, respectively. The peak power at the input of fiber was considered to be 25 kW for both cases. Figures 7(a)–7(d) shows the evolution of numerically generated supercontinuum spectra along the fiber length in spectral and time domain for the two previously mentioned fiber samples pumped at 1550 nm and 1580 nm. We only show the first beginning of pulse propagation to highlight the main nonlinear effects in SC generation. In Figs. 7(a) and 7(c), strong spectral broadening can be seen in the beginning of the fiber due to self-phase modulation. With an increase in length, we can see soliton ejection and generation of dispersive waves. The soliton distribution as a function of time is shown in Figs. 7(b) and 7(d). The comparisons between simulation and experiment in the 1550 nm and 1580 nm pump case are shown in Fig. 8. Both the simulated and experimental SC spectra almost agree with each other in terms of SC bandwidth, but they are quite different in terms of the structure of the spectrum, as can be seen from Fig. 8(a) for SC-PCF sample NL44C2a. We speculate that the observed discrepancy is accountable to some assumptions in the model. First, we did not consider the wavelength-dependent losses over the full SC span and the higher-order optical modes. Second, the dispersion profile was numerically estimated from the cross-section image of the fiber structures. It is reasonable that a small change in the slope of the normal dispersion at wavelengths blue-shifted from the pump wavelength would result in different dispersive wave phase-matching conditions, which would most reasonably explain the short-wavelength discrepancies between the theoretical and measured spectra in Fig. 8. The relatively long fiber samples used in the experiment (for soft glass fibers and femtosecond pump pulses) would suggest a significant contribution of

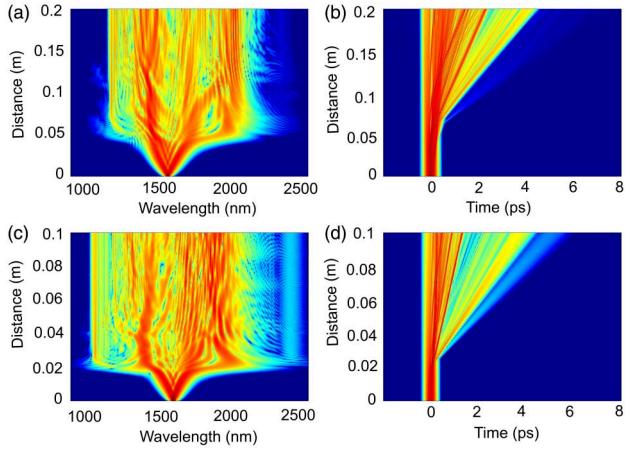

Fig. 7. (a) and (c) Numerically generated evolution of SC spectra along the fiber length for NL44C2a and NL44C5c PCFs with 1550 nm and 1580 nm pumping, respectively. (b) and (d) Corresponding temporal distribution along the fiber length for NL44C2a and NL44C5c PCFs.

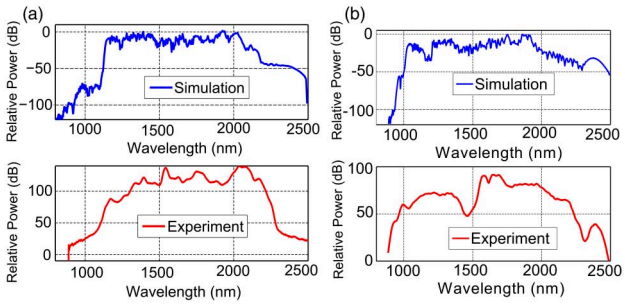

Fig. 8. Comparison between numerically and experimentally generated SC spectra for 1550 nm and 1580 nm pumping in (a) NL44C2a and (b) NL44C5c PCFs.

the OH absorption loss; however, no such features are observed at around 1380 nm in the spectra shown in Fig. 8. Bend loss of any higher-order, mode-contained blue-shifted parts of the supercontinuum spectra could also be related the observed discrepancies, but we did not observe such loss behavior for any reasonable bend radii in these fibers during the measurements.

6. CONCLUSION

Wideband SC generation from 1073 nm to 2311 nm and from 891 nm to 2466 nm was recorded by pumping two suspended core photonic crystal fibers in the both normal and anomalous dispersion regimes, respectively, with femtosecond pulses at 1550 nm and 1580 nm. These results demonstrate the utility of heavy-metal-oxide PCF for SC generation. Numerical simulations using a nonlinear Schrödinger equation and the group velocity dispersion computed from the SEM images of the SC-PCF samples show good qualitative agreement with the experimental one for 4.3 μm and 3.51 μm core diameter SC-PCF samples. It is important to stress that the SC spectra obtained using PBG-81 glass suspended-core optical fibers are limited by their transmission windows up to 2.8 μm, which may limit their potential use for applications such as infrared spectroscopy. They are actually comparable to those that can be obtained with highly nonlinear germanium-doped optical fibers [26].

Funding. Horizon 2020 Framework Programme (H2020) (722380); Agence Nationale de la Recherche (ANR) (ANR-15-IDEX-0003, ANR-11-LABX-0001); Fundacja na rzecz Nauki Polskiej (FNP) (First TEAM/2016-1/1).

Acknowledgment. The authors thank Damien Bigourd, Gil Fanjoux, and Alexis Mosset for technical support.

REFERENCES

1. J. Hult, R. S. Watt, and C. F. Kaminski, "High bandwidth absorption spectroscopy with a dispersed supercontinuum source," Opt. Express **15**, 11385–11395 (2007).
2. Y. Sych, R. Engelbrecht, B. Schmauss, D. Kozlov, T. Seeger, and A. Leipertz, "Broadband time-domain absorption spectroscopy with a ns-pulse supercontinuum source," Opt. Express **18**, 22762–22771 (2010).
3. C. Amiot, A. Aalto, P. Ryczkowski, J. Toivonen, and G. Genty, "Cavity enhanced absorption spectroscopy in the mid-infrared using a supercontinuum source," Appl. Phys. Lett. **111**, 061103 (2017).
4. C. R. Petersen, U. Møller, I. Kubat, B. Zhou, S. Dupont, J. Ramsay, T. Benson, S. Sujecki, N. A. Moneim, Z. Tang, D. Furniss, A. Seddon, and O. Bang, "Mid-infrared supercontinuum covering the 1.4–13.3 μm molecular fingerprint region using ultra-high NA chalcogenide step-index fibre," Nat. Photonics **8**, 830–834 (2014).
5. W. Gao, M. E. Amraoui, M. Liao, H. Kawashima, Z. Duan, D. Deng, T. Cheng, T. Suzuki, Y. Messaddeq, and Y. Ohishi, "Mid-infrared supercontinuum generation in a suspended-core As_2S_3 chalcogenide microstructured optical fiber," Opt. Express **21**, 9573–9583 (2013).
6. Y. Yu, X. Gai, T. Wang, P. Ma, R. Wang, Z. Yang, D.-Y. Choi, S. Madden, and B. L. Davies, "Mid-infrared supercontinuum generation in chalcogenides," Opt. Mater. Express **3**, 1075–1086 (2013).
7. F. Désévédavy, G. Gadret, J.-C. Jules, B. Kibler, and F. Smektala, "Supercontinuum generation in tellurite optical fibers," in *Technological Advances in Tellurite Glasses*, Springer Series in Material Science (Springer, 2017), Vol. **254**, pp. 277–299.
8. M. Klimczak, G. Stepniewski, H. Bookey, A. Szolno, R. Stepien, D. Pysz, A. Kar, A. Waddie, M. R. Taghizadeh, and R. Buczynski, "Broadband infrared supercontinuum generation in hexagonal-lattice tellurite photonic crystal fiber with dispersion optimized for pumping near 1560 nm," Opt. Lett. **38**, 4679–4682 (2013).
9. C. Xia, M. Kumar, O. P. Kulkarni, M. N. Islam, F. L. Terry, M. J. Freeman, M. Poulain, and G. Mazé, "Mid-infrared supercontinuum generation to 4.5 μm in ZBLAN fluoride fibers by nanosecond diode pumping," Opt. Lett. **31**, 2553–2555 (2006).
10. M. Michalska, P. Hlubina, and J. Swiderski, "Mid-infrared supercontinuum generation to ~4.7 μm in a ZBLAN fiber pumped by an optical parametric generator," IEEE Photon. J. **9**, 3200207 (2017).
11. C. Agger, C. Petersen, S. Dupont, H. Steffensen, J. K. Lyngsø, C. L. Thomsen, J. Thøgersen, S. R. Keiding, and O. Bang, "Supercontinuum generation in ZBLAN fibers—detailed comparison between measurement and simulation," J. Opt. Soc. Am. B **29**, 635–645 (2012).
12. D. D. Hudson, S. Antipov, L. Li, I. Alamgir, T. Hu, M. El Amraoui, Y. Messaddeq, M. Rochette, S. D. Jackson, and A. Fuerbach, "Toward all-fiber supercontinuum spanning the mid-infrared," Optica **4**, 1163–1166 (2017).
13. R. A. Martinez, G. Plant, K. Guo, B. Janiszewski, M. J. Freeman, R. L. Maynard, M. N. Islam, F. L. Terry, O. Alvarez, F. Chenard, R. Bedford, R. Gibson, and A. I. Ifarraguerri, "Mid-infrared supercontinuum generation from 1.6 to >11 μm using concatenated step-index fluoride and chalcogenide fibers," Opt. Lett. **43**, 296–299 (2018).
14. P. S. J. Russell, P. Holzer, W. Chang, A. Abdolvand, and J. C. Travers, "Hollow-core photonic crystal fibers for gas-based nonlinear optics," Nat. Photonics **8**, 278–286 (2014).
15. M. I. Hasan, N. Akhmediev, and W. Chang, "Mid-infrared supercontinuum generation in supercritical xenon-filled hollow-core negative curvature fibers," Opt. Lett. **41**, 5122–5125 (2016).
16. D. Jain, R. Sidharthan, P. M. Moselund, S. Yoo, D. Ho, and O. Bang, "Record power, ultra-broadband supercontinuum source based on highly GeO_2 doped silica fiber," Opt. Express **24**, 26667–26677 (2016).
17. G. Sobon, M. Klimczak, J. Sotor, K. Krzempek, D. Pysz, R. Stepien, T. Martynkien, K. M. Abramski, and R. Buczynski, "Infrared supercontinuum generation in soft-glass photonic crystal fibers pumped at 1560 nm," Opt. Mater. Express **4**, 7–15 (2014).
18. L. Dong, B. K. Thomas, and L. Fu, "Highly nonlinear silica suspended core fibers," Opt. Express **16**, 16423–16430 (2008).
19. M. Klimczak, B. Siwicki, P. Skibinski, D. Pysz, R. Stepien, A. Szolno, J. Pniewski, C. Radzewicz, and R. Buczynski, "Infrared supercontinuum generation in soft-glass suspended core photonic crystal fiber," Opt. Quantum Electron. **46**, 563–571 (2014).
20. P. Mergo, M. Makara, J. Wojcik, K. Poturaj, J. Klimek, K. Skorupski, and T. Nasilowski, "Supercontinuum generation in suspended core microstructured optical fibers," Proc. SPIE **7120**, 712009 (2008).

21. M. E. Amraoui, J. Fatome, J.-C. Jules, B. Kibler, G. Gadret, C. Fortier, F. Smektala, I. Skripatchev, C. F. Polacchini, Y. Messaddeq, J. Troles, L. Brilland, M. Szpulak, and G. Renversez, "Strong infrared spectral broadening in low-loss As-S chalcogenide suspended core microstructured optical fibers," Opt. Express **18**, 4547–4556 (2010).
22. D. Ghosh, S. Roy, and S. K. Bhadra, "Efficient supercontinuum sources based on suspended core microstructured fibers," IEEE J. Sel. Top. Quantum Electron. **20**, 597–604 (2014).
23. P. Domachuk, N. A. Wolchover, M. Cronin-Golomb, A. Wang, A. K. George, C. M. B. Cordeiro, J. C. Knight, and F. G. Omenetto, "Over 4000 nm bandwidth of mid-IR supercontinuum generation in sub-centimeter segments of highly nonlinear tellurite PCFs," Opt. Express **16**, 7161–7168 (2008).
24. A. Hartung, A. M. Heidt, and H. Bartelt, "Nanoscale all-normal dispersion optical fibers for coherent supercontinuum generation at ultraviolet wavelengths," Opt. Express **20**, 13777–13788 (2012).
25. T. Olivier, F. Billard, and H. Akhouayri, "Nanosecond Z-scan measurements of the nonlinear refractive index of fused silica," Opt. Express **12**, 1377–1382 (2004).
26. D. Lorenc, M. Aranyosiova, R. Buczynski, R. Stepien, I. Bugar, A. Vincze, and D. Velic, "Nonlinear refractive index of multicomponent glasses designed for fabrication of photonic crystal fibers," Appl. Phys. B **93**, 531–538 (2008).
27. J. M. Dudley, G. Genty, and S. Coen, "Supercontinuum generation in photonic crystal fiber," Rev. Mod. Phys. **78**, 1135–1184 (2006).
28. J. Dudley and J. Taylor, eds., *Supercontinuum Generation in Optical Fibers* (Cambridge University, 2010).

194.57.91.238 {ts '2018-08-29 11:43:30'}